Molecular simulation of flexible helical Metal-Organic Frameworks

by

Najib Ouja

A thesis submitted in partial fulfilment of the requirements for the degree of Doctor of Philosophy in Chemistry

University of Warwick, Department of Chemistry

August 2008

Table of Contents

Acknowledgments

First and foremost I'd like to thank my supervisor Prof. P. M. Rodger for his tuition and supervision. Mark has been a constant source of support and enthusiasm throughout my studies. I would also like to thank him for his support, patience and constant encouragement especially during tough times. I would also like to thank Dr Tiffany R. Walsh and Dr. Rob Deeth for their advices, for ensuring the degree criteria were met and also for their encouragement.

Thank you also to the people in the modelling room, especially David Quigley and Bibo Jiang for their help and advices. A big thank you also to my friend and housemate, Mahrez Amri, for his constant support, friendship and encouragement especially during tough times.

Finally, I would like to address a big thank you to my wonderful family, who have always believed in my ability to achieve the highest of goals. In particular, my parents who have provided me with love and continuous support throughout my time at Warwick.

Declaration

The observations and recommendations in this thesis are those of the author except where acknowledgment has been made to results and ideas previously published. The work was undertaken at the Department of Chemistry, University of Warwick between October 2004 and September 2008 and has not been previously submitted for a degree at any institution.

Abbreviations

BTC – 1,3,5-Benzene-Tricarboxylate (or trimesic acid)

CHARMM – Chemistry at HARvard Macromolecular Mechanics

DFT – Density Functional Theory

ESP – Electrostatic Potential

GCMC – Grand Canonical Monte Carlo

HF – Hartree-Fock

IRMOF – Isoreticular Metal-Organic Framework

MD – Molecular Dynamics

MNI – Nickel ions

MOF – Metal-Organic Framework

MP2 – Møller-Plesset perturbation theory 2

N6R – Nitrogen atoms of pyridine molecules

OC – Oxygen atoms of BTC molecules

OT – Oxygen atoms of alcohol molecules

RDF – Radial Distribution Function

SBU – Secondary building Unit

SCF – Self Consistent Field

Abstract

In this work, force fields were developed to model flexible helical metal-organic framework solids (MOFs). Since no suitable force fields to model flexible MOFs had been reported, the study began by benchmarking an existing organic force field, CHARMM22, against $Ni_3(BTC)_2(pyridine)_6(4,5\text{-octanediol})_3$. CHARMM22 force filed did produce a framework that retained its original three-dimensional structure for the duration of the simulations, and did so at experimentally relevant temperatures provided a minimum number of 20 solvent molecules per unit cell were included. However, important inadequacies were found between the experimental crystal structure and the simulated one. Therefore a series of refinements of the force field were performed. The three best modified force fields were then used to simulate this MOF and a detailed analysis of its physical properties produced. A key conclusion from the development and testing cycle was that hydrogen bonding between the BTC and the hydroxyl groups of both the solvent and the framework alcohol molecules played a critical role in stabilizing the MOF.

The transferability of these force-fields was tested against two new MOFs, for which experimental crystal structures had been reported: $Ni_3(BTC)_2(pyridine)_6(2,3\text{-butanediol})_3$ (called MOF-4) and $Ni_3(BTC)_2(pyridine)_6(1,2,6\text{-hexanetriol})_3$ (called MOF-6). One force-field was found to give a good description of MOF-4. For MOF-6 however, competition for framework bonding between the diol and terminal hydroxyl group on the hexanetriol destabilized the framework with all three force fields. A stable MOF was produced only when the Ni-OT bond lengths were constrained to the experimental values. It was concluded that polarisation of ligand donor atoms by the Ni^{2+} needed to be incorporated in any future refinements of the force-field.

Finally, this study showed that the $Ni_3(BTC)_2(pyridine)_6(4,5\text{-octanediol})_3$ MOF can display enantioselective properties. Solvent alcohol molecules of the same enantiomeric form as that incorporated into the framework were found to interact much more strongly with the framework

than their enantiomer, and even formed enantiomer-specific hydrogen bonds with the framework. Structural differences were also observed in solvent-BTC, solvent-Ni and solvent-pyridine geometries.

1 Introduction

1.1 Metal-organic frameworks and the concept of reticular synthesis

Metal-organic frameworks (MOFs), also referred to as metal-organic coordination networks, coordination polymers, hybrid organic inorganic materials or organic "zeolite analogues" with unavoidable overlap[1-5] are a new kind of material consisting of metal ions or clusters linked together by rigid organic molecules to form one, two or three-dimensional networks. The term "zeolite analogues" does not imply that the full functionality of zeolites should be reproduced, but refers instead to the ability of the materials to act as molecular sieves. Metal-organic frameworks are materials that have a good permeability, high void volumes, and well defined tailorable cavities of uniform size. These are precisely the qualities needed for catalysis, separation and storage-release applications. In the past ten years, the interest in Metal-organic frameworks has grown dramatically and a number of recent review articles cover the various aspects of this field of hybrid inorganic-organic materials.[6-15] The first attempts to synthesize such materials dates to the early 1990s with the work of Robson and Hoskings[16-19] who realized that the coordination of polydentate ligands to metal atoms opens the scope for the design of particular framework geometries. The final geometries depend both on the size and electronic configuration of the metal center and the structure of the organic ligands, especially the one linking these metal centers. MOFs can be assembled in a logical way from molecular building blocks from the bottom up. This method of assembling a material using molecular building blocks is called reticular synthesis. The reticular synthesis approach requires the use of secondary building units (SBUs) to direct the assembly of the resulting ordered frameworks.[20] In reticular synthesis, although Metal-organic frameworks are assembled out of molecular building blocks from the bottom up, the properties of these materials are conceived in advance in a top down design logic. Indeed, reticular synthesis allows for the design of materials with predetermined structures, compositions and properties. Therefore one major advantage of metal-organic frameworks over other porous materials such as zeolites which

are microporous aluminosilicates (microporous means that these materials have a pore diameter lower than 20 Å) or activated carbons is that it is possible when synthesizing MOFs to exert a considerable control over the formation of complex framework geometries. It appears that it will also be possible to control the host-guest chemistry of the framework by tailoring the building blocks and including binding properties of functional organic groups that are not available in zeolites. For zeolite materials, the complexity of the synthesis conditions, in which starting precursors undergo transformations, and the fact that the mechanisms that determine the final structure of these materials have not been fully understood yet impede any tailoring or control over the formation of the final geometry. The aim of reticular synthesis is to synthesize materials that would be designed a priori to get structures that would lead to desired functions. This is common in molecular chemistry but has not been yet possible in the field of solid state chemistry. Indeed, in the pharmaceutical industry, it is not unknown for molecules to be synthesized having previously been designed to have a specific physiological action. In solid-state chemistry, however new extended materials are not synthesized with prior design of a specific desired structure. Instead, new materials usually result from planned experiments that are likely to lead to materials with structures that are of possible interest. It is a much more random process than is usually done in the field of molecular chemistry ("shake and bake" method characteristic of the early days of solid state chemistry). This difference between molecular and solid-state chemistry in being able to tailor structure and properties is explained by the fact that molecules can be manipulated one step at a time whereas solids are generally assembled in a single step. However, a lot of progress has been made in tailoring the structure and properties of synthesized materials by using molecular entities as building blocks in the solution assembly of solids.[21] For example the use of polar building blocks and mixed valence metal ions for the synthesis of metal-organic frameworks has led to materials with non-linear optical and magnetic properties. Another example is the use of porphyrins and metallocrown-based solids as building blocks that leads to Metal-organic frameworks with potential for chiral separation and recognition. The molecular entities that are used as building blocks are generally referred to as secondary building units (SBU). SBUs are basically molecular complexes and cluster entities in which ligand coordination modes and the electronic structure of the metal are

used in the transformation of these fragments into extended porous networks using polytopic linkers such as 1,4-benzenedicarboxylate, 1,3,5-benzenetricarboxylate (also known as trimesic acid), 4,4'-azodibenzoate, etc.[22,23] The phrase "secondary building unit" is used to convey a conceptual unit which was not employed in the synthesis as a distinct molecular entity, at least not in the sense that metal atoms or ligand molecules are. SBUs can be used to direct the formation of desired structures as well as to design materials with specific physical properties. Generally, only a small number (about a dozen) of simple, high-symmetry structures are expected to form. These structures are well described by O'Keeffe et al.,[24] who describe the basic nets (topologies) that are most likely to form when assembling MOFs. A net is an abstract mathematical entity consisting of a collection of points (nodes or vertices) with some clearly defined connectivity (bonds).[25] Lists of existing nets has been compiled in books by Wells[26, 27] and O'Keeffe and Hyde.[28] The symbol (*N*,*M*) is generally used to describe the topology and connectivity of a given net. Figure 1-1 represents a (6,3) net. *M* refers to the number of connections to neighboring nodes that radiate from any node and *N* is the number of nodes in the smallest closed circuits in the net. This means that in the (6,3) net represented in Figure 1-1, the number 6 indicates that the smallest complete rings in the net are hexagons while the number 3 indicates that each node is connected to three other nodes. Nodes or vertices basically represent the different points in the net. The symbol (6,3) is generally referred to as the vertex symbol.

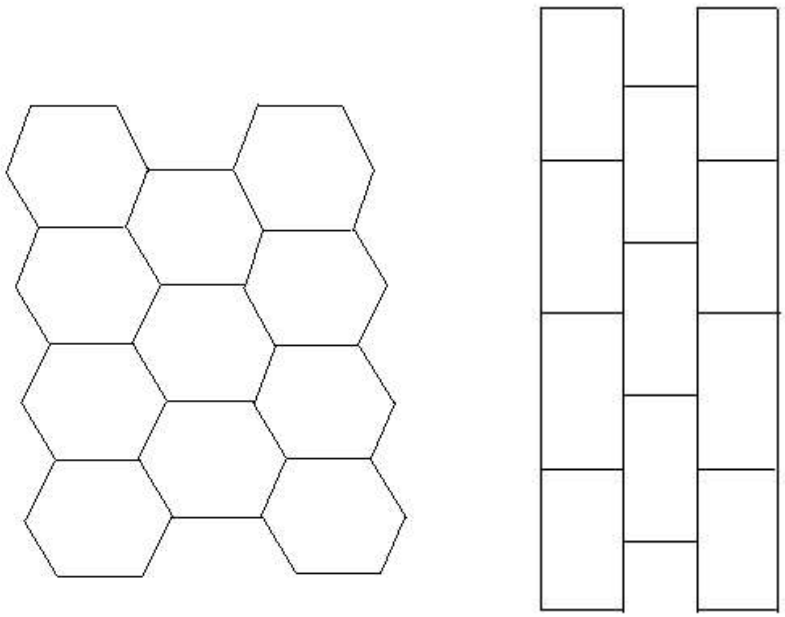

Figure 1-1 Two geometrically different forms of the (6,3) net

The net represented in Figure 1-1 is a two dimensional net. Material designers are generally more interested in three-dimensional nets. It is these three-dimensional nets that are discussed by O'Keeffe et al.[24] They classified nets by their degree of connectivity, and distinguished 3, 4, 5, 6 and 8 connected nets. The main three-dimensional, three connected nets are the $SrSI_2$ net and the $ThSi_2$ net. The framework that has been studied in this thesis can be described as the interpenetration of two $SrSi_2$ nets (also referred to as (10,3) nets). This framework is described in chapter 3 of this thesis. Figure 1-2 presents nine of the most common nets.

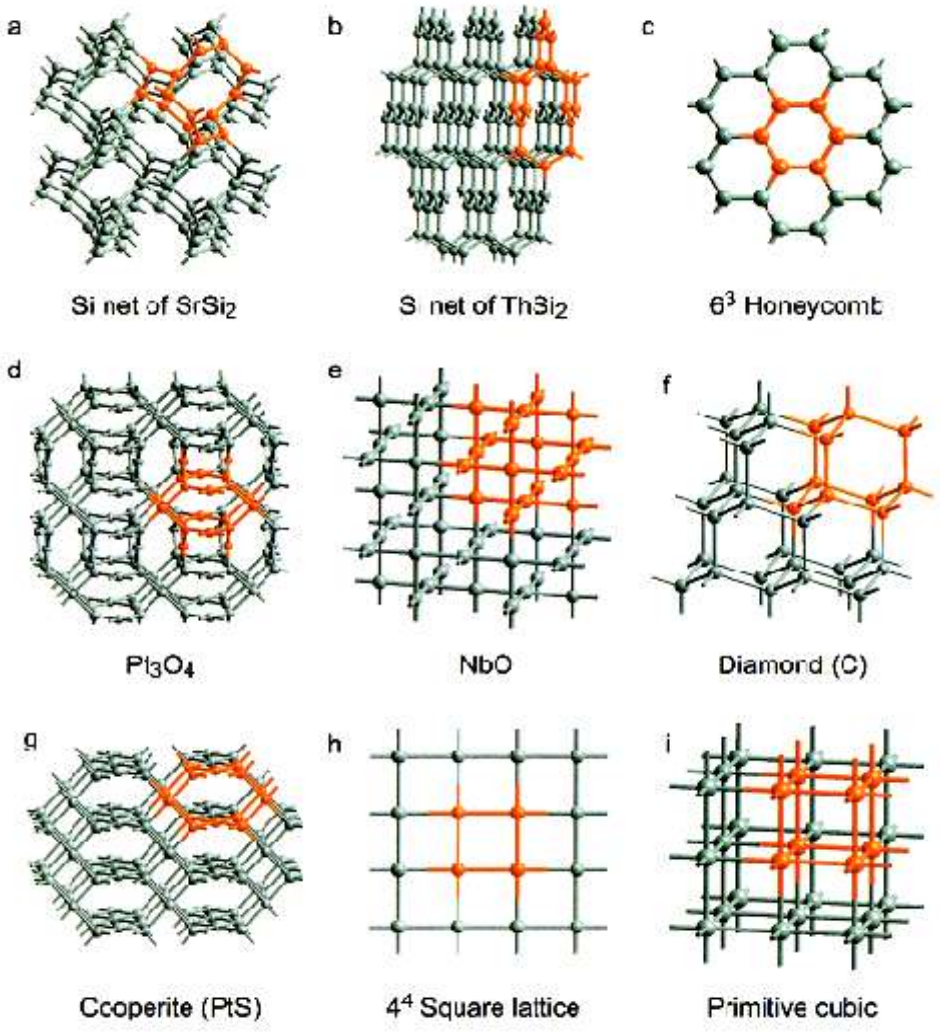

Figure 1-2 Representation of some common nets. A segment of each net has been highlighted in orange for clarity. (Structures were drawn using single crystal X-ray diffraction data).

The size of the pores of metal-organic frameworks can be controlled by varying the length of the linker molecules between vertices. This means that a bond can be replaced by a sequence of bonds so that much larger pores can be obtained. This process is called "expansion" and is well exemplified by a work done by O.M. Yaghi et al.[29] (see Figure 1-3). The reference metal-organic framework used in that work is MOF-5 also called IRMOF-1 (Isoreticular Metal-Organic Framework-1). MOF-5 can be considered as being constructed from octahedral Zn-O-C clusters at vertices linked through benzene groups. This metal-organic framework was used to demonstrate that its three-dimensional porous system can be functionalized with the organic groups such as -Br, $-NH_2$, $-OC_3H_7$, $-OC_5H_{11}$, $-C_2H_4$, and $-C_4H_4$, and that its pore size can be extended using long

molecular struts such as biphenyl, tetrahydropyrene, pyrene, and terphenyl. This work represents a very good example of material design (design of pore size and functionality) using the concept of reticular synthesis. Several metal-organic frameworks synthesized in that work have pore sizes in the mesoporous range (> 20 Å) and in the case of IRMOF-8, -12, -14, 15 and -16, the lowest crystal density of any existing materials. One of these materials, namely MOF-6 (IRMOF-6) also has the highest methane storage capacity measured thus far. The series of IRMOFs described in figure 1-3 were synthesized using the same synthesis method as the template MOF-5. The resulting general structure is the same (octahedral Zn-O-C clusters linked by linear linkers resulting in cubic cages of different sizes). All the IRMOFs have the topology of CaB_6[29] adapted from the prototype MOF-5. The only difference between these IRMOFs is the linker molecules used. The different linker molecules used to produce this series of IRMOFs are described in figure 1-4. This difference in linker molecules results in the difference of the functional groups decorating the pores of these frameworks (IRMOFs 1-7) and a difference in pore size between the different IRMOFs (IRMOFs 7-16 in which successively longer linker molecules have been used). However, expansion of the link often leads to interpenetrating frameworks. Indeed, with the exception of IRMOF-8, the other IRMOFs with longer linker molecules (IRMOF-9, -11, -13, -15) tend to have structures that doubly interpenetrate. However, Yaghi et al. [29] showed that by carrying out the synthesis under more dilute conditions, non interpenetrating IRMOFs with any of the linker molecules described in figure 1-4 could be obtained (IRMOF-10, -12, -14, -16). The percent free volume of these IRMOFs varies from 55.8 % (IRMOF-1) to 91.1 % (IRMOF-16). Remarkably the less porous of these IRMOFs (IRMOF-1) is more porous than the most open zeolites (e.g. faujasite has just 45-50 % free space).[30]

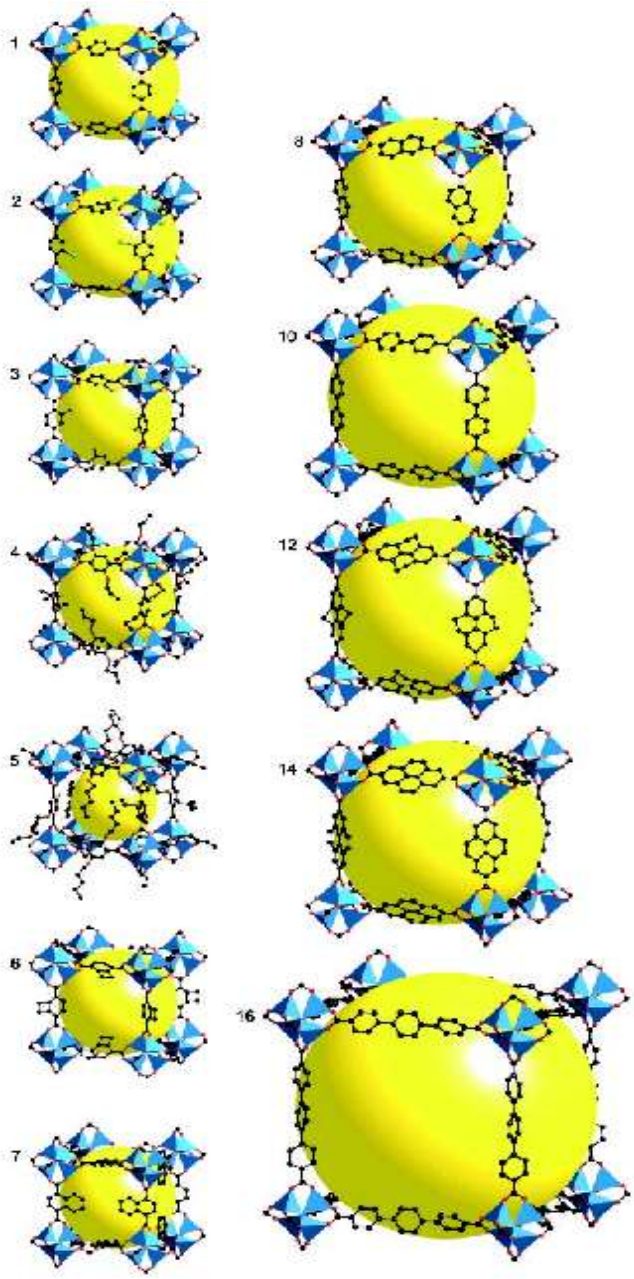

Figure 1-3 Single crystal X-ray structures of IRMOF-n (n=1 through 7,8,10,12,14 and 16. Labeled respectively. the doubly interpenetrated IRMOFs (9,11,13 and 15) are not shown. The large yellow spheres represent the largest van der Waals spheres that would fit into the cavities without touching the framework (reproduced from [29]).

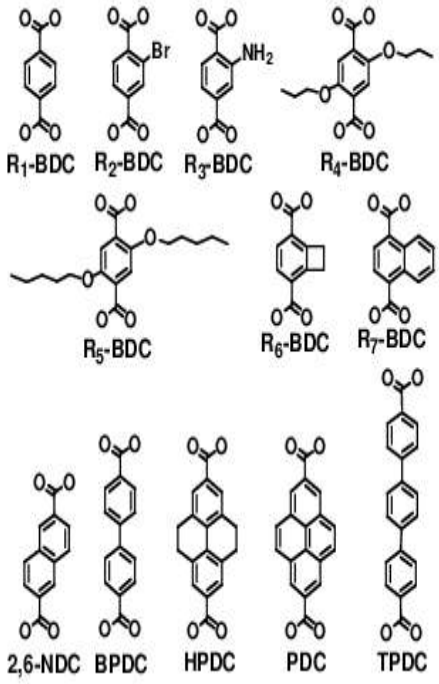

Figure 1-4 Representation of the different linker molecules used to produce the IRMOF series.

The problem with the expansion process is that materials with large void spaces are enthalpically unfavorable, and so the voids tend to be filled by a second, interpenetrating, network. This interpenetration phenomenon leads to structures which have low porosity. Other processes that can

be used for tailoring the structure of metal-organic frameworks are "decoration" and "augmentation". Decoration consists of replacing a vertex of a framework net by a group of vertices. It tends to lead to structures with high rigidity and without a tendency to interpenetrate. Augmentation is a special case of decoration. This process consists of the replacement of the vertices of an *N*-connected net by a group of *N* vertices. For example in the CaB_6 framework, B_6 units inside the cell augment the 6-connected vertices on the simple cubic net. Indeed, the CaB_6 crystal consists of a cubic cell with calcium atoms at vertices (thus 6-connected) and 6 boron atoms disposed in an octahedral way at the center of the cell. In the augmented net, the *Ca* vertices of the CaB_6 cell are replaced by vertices occupied by the 6 octahedrally disposed boron atoms. The resulting cubic cell is therefore constituted of octahedral B_6 units at the vertices and one calcium atom at the center of the cell. Decoration and augmentation are, in fact, conceptual processes that are also used for the synthesis of new metal-organic frameworks with large pores showing very simple basic topologies dictated by the shape and connectivity of their building units.

1.2 Synthesis of Metal-organic frameworks

Metal-organic frameworks combine the advantages of the low temperature host guest chemistry of biological systems with the handling and robustness of inorganic materials. One main characteristic of these metal-organic frameworks is that they are highly porous. They also have a surface area (surface/volume ratio) superior to any other known materials. Chae et al. have reported a strategy to produce metal-organic frameworks with extremely large surface area.[37] This extremely high surface area is exemplified by a material called MOF-177 which has a surface area of 4,500 m^2/g.[37,38] The porous nature of these materials and their very high surface area makes them potentially suitable for applications such as storage, catalysis or enantioselectivity.

The development of synthetic methods for new metal-organic frameworks has progressed dramatically during the last fifteen years. Numerous metal-organic frameworks with large pore size

and good stability have been synthesized. Metal-organic frameworks are generally assembled from secondary building units under mild temperature conditions. Polytopic linkers such as 1,4-benzenedicarboxylate, 4,4'-azodibenzoate and 1,3,5-benzenetricarboxylate are very good molecules for the assembly of building units. Metal atoms bind strongly to these linkers and that allows for the formation of stable frameworks. This is due to the fact that metal atoms form strong bonds with carboxylate groups. For the synthesis of these frameworks, a solution of the acid form of the organic linker and the simple metal salt (nitrate) is prepared in the desired stoichiometry. For the assembly to happen, an organic amine that will deprotonate the acid linker molecules and initiate the assembly, has to diffuse slowly into the reaction mixture. Nucleation rates and the number of nucleation sites can be controlled by adjusting the rate of amine diffusion, solvent polarity and concentration gradients. This process of diffusing a volatile amine through the reaction mixture has to be performed every time the ligand molecules have to be deprotonated before they can coordinate to the metal centers (this is especially the case for carboxylic acids). For solutions where the acid linker molecules are poorly soluble, inorganic hydroxides such as NaOH may be used instead of organic amines to deprotonate the acid.

Metal-organic frameworks are generally synthesized at temperatures lower than 250 ^{o}C. For temperatures below 100 ^{o}C, the usual routes of coordination chemistry, such as solvent diffusion methods, are used. These methods generally involve slow introduction of precursors (primary building units) to reduce the rate of crystallite nucleation. This can be done by slow evaporation of a solution of the precursors, layering of solutions, or the slow diffusion of a solution containing one building block into a solution containing another through a membrane or an immobilizing gel. For temperatures above 100 ^{o}C, it is the solvothermal synthesis route that is used. In the solvothermal synthesis route, the precursors are combined as dilute solutions in polar solvents such as water, alcohols, acetone or acetonitrile. The mixture is heated in sealed vessels such as Teflon-lined stainless steal bombs or glass tubes, generating autogenous pressure. Mixed solvent systems are also often used to adjust solvent-ligand exchange and thus enhance crystal growth. If deprotonation of the ligand molecules is required, an amide co-solvent (through thermal decomposition) can also

be used to neutralise the system. Linker molecules can also be generated in situ, for example by hydrolyzing nitriles or esters to yield carboxylates.

The main parameters to take into consideration during the synthesis are the pH which is generally acidic, the concentration and, most importantly, the temperature. A textbook example of the importance of temperature in the outcome of the synthesis is given by the reaction of the linear dicarboxylate succinate with Co (II) in water. At low temperature, dicarboxylate succinate molecules bind in a monodentate fashion to Co centers. At high temperature (> 100 ^{o}C), oxide anions condense to form inorganic networks that are bridged by multidentate carboxylic groups.[31] Besides the current methods to synthesize metal-organic frameworks, new synthetic methods are being developed. One of these methods uses an electrochemical route.[32] This method has been used for the synthesis of the Cu(BTC) metal-organic framework.[33] In this method, bulk copper plates are placed as the anodes in an electrochemical cell with BTC molecules dissolved in methanol as solvent and a copper cathode. Another method which looks very promising for the synthesis of metal-organic frameworks uses microwaves. This method has been used to synthesize inorganic porous compounds[34] but rarely for metal-organic frameworks. However, highly porous metal-organic frameworks such as chromium trimesate and terephthalate (MIL-100 and MIL-101) have been formed under microwave irradiation after less than one hour at 220 ^{o}C, instead of 96 hours using the conventional route.[35] It has also been noticed that the crystallization of some of these metal-organic frameworks using the microwave method occurs much faster than the crystallization of aluminosilicate zeolites. This is explained by the fact that metal-organic frameworks grow directly from the reactants while the formation of aluminosilicate zeolites seems to involve complex crystallization pathways via hydrolysis, hydrophobic hydration, gelation, nucleation and crystal growth.[36]

1.3 Chirality of metal-organic frameworks

Because of the importance of chirality in biological processes, there has been an increasing effort to develop chiral porous solids such as zeolites and metal-organic frameworks over the past decade. In the case of zeolites, despite all these efforts, no chiral zeolites are available in enantiopure form to date. Currently the only zeotypes that are available in chiral forms are zeolite β and titanosilicate ETS-10.[39,40] This failure to synthesize zeolites in enantiopure form is explained by the fact that zeolites are synthesized in the presence of surfactant templates which are removed through calcinations at 400-550 ^{o}C,[41] and these temperatures are sufficiently high to obscure relatively subtle discriminations in the interactions between the surfactants. Indeed, attempts to synthesize chiral zeolites have relied on chiral surfactants to organize silicate-surfactant assemblies into chiral conformations. However, calcinations at high temperature systematically destroy the chiral conformation of such assemblies to lead to, either a racemic mixture of zeolites or achiral zeolites. In contrast to zeolites, metal-organic frameworks are synthesized under mild conditions, and, as established by Yaghi et al., [29] they allow systematic engineering of their chemical and physical properties through modification of their molecular components. Chiral metal-organic frameworks are still quiet rare and most of the chiral metal-organic frameworks obtained so far were synthesized from achiral components. The chirality of these metal-organic frameworks results from the special disposition of their building blocks.[42] Indeed, chirality in metal-organic frameworks results from enantiomeric ligands and/or an asymmetric framework topology. In the case just described, since achiral components are used for the synthesis, chirality results from the three-dimensional structure of the framework. This three-dimensional structure that displays chirality is the helical structure. The two chiral forms of the structure result from the handedness (right (*P*) or left-handed (*M*) helices) of the helix. The two versions (*P* and *M*) of the handedness of the helix are shown in Figure 1-5. This figure shows that the two versions are non-identical mirror images. Therefore, if one of the versions of the helix is selectively synthesized, the resulting framework may be optically active although this framework is not constituted of chiral groups.

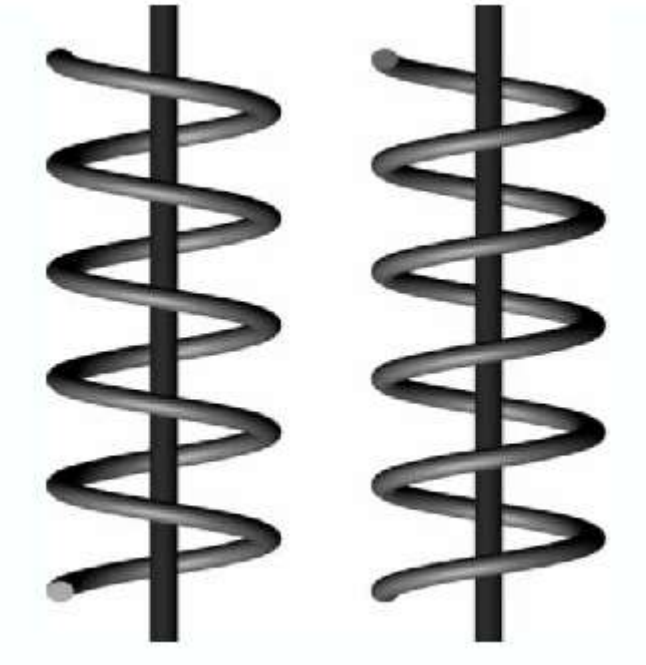

Figure 1-5 Representation of a left handed (M) and right handed (P) helices.

Helicity is a fundamental property of great interest in inorganic and coordination chemistry. A considerable amount of effort has been put in the design of metal-organic frameworks exhibiting helical architectures. Indeed, frameworks with helical architecture are of particular interest due to their potential application in some emerging fields such as asymmetric catalysis and non linear optical materials (materials in which the dielectric polarization responds non linearly to the electric field of the light). These materials are generally used in the fields of Lasers, enantioselectivity or for the aesthetically appealing topology of helical compounds.[43-47]

Helical assemblies may be finite, this is the case of helicates (helical complexes of oligomeric ligands and metals)[48,49] or infinite. Infinite assemblies of helical structures are generated upon the self-assembly of organic and metallic tectons in the crystalline phase (helical metal-organic frameworks).[43] Helicity at the supramolecular level, can be induced by conformation restrictions of macromolecules, inter-, intra-molecular hydrogen bonds, or coordination to metal ions. Single-,

double-, triple-, quadruple-stranded, as well as circular and cylindrical helical structures are reported in the literature.[50-66]

When assembling metal-organic frameworks from achiral building blocks, as it is the case for most of the chiral metal-organic frameworks synthesized to date, two outcomes may occur. Either, crystals are constituted of both *P* and *M* helices (centric space group) affording thus an internal racemate, or by a spontaneous resolution process: each crystal is enantiomerically pure but the mixture of crystals is a racemate.[67] In this latter case of resolution upon crystallization, a conglomerate is formed. A conglomerate[67] is a mechanical and racemic mixture of chiral crystals, of which each crystal is enantiopure. A more interesting possibility is homochiral crystallization. In homochiral crystallization, all the crystals are obtained in the same chiral form. Only a few examples of chiral, nonracemic, helical metal-organic frameworks have been reported to date.[20, 68-75] In these cases, chirality is induced by a stereogenic center,[76,77] atropisomerism[78] or noncovalent supramolecular interactions (hydrogen bonds, pi-pi interactions, etc).[79-81] Most homochiral metal-organic frameworks however are not robust enough to display permanent porosity and readily collapse upon removal of guest (solvent) molecules.

Coordination of transition metal atoms with 1,3,5-benzenetricarboxylate in the stoichiometry $M_3(BTC)_2$ is known to lead to chiral (10,3)-a network structures. However, bulk samples are achiral because of the presence of both *M* and *P* helices in an achiral single crystal or because of the equal probability for the formation of chiral crystals of both handedness. Rosseinsky et al. managed to synthesize homochiral metal-organic frameworks by coordinating chiral diols to the $M_3(BTC)_2$ complex.[75] These diols coordinate to the metal centers in a bidentate fashion to lead to metal-organic frameworks with reduced number of interpenetrating (10,3)-a nets. In these metal-organic frameworks, octahedral nickel centers, Ni^{2+}, are bound at their equatorial sites to one diol molecule (in a bidentate way) and two pyridine molecules while the axial sites of these octahedral Ni^{2+} centers are occupied by carboxylic oxygen atoms of the BTC molecules. In these metal-organic frameworks, the diol molecules act as a template that controls not only the handedness of the helices but all the crystals to give rise to homochiral networks with chiral pores and cavities. The

scope of this thesis is to model, using Molecular Dynamic simulations, some of the homochiral metal-organic frameworks synthesized by Rosseinsky et al. In this thesis, the effect of solvation as well as the interactions stabilizing the framework structure or the possible enantioselective properties of these homochiral metal-organic frameworks will be investigated.

1.4 Catalysis

Porous materials, especially aluminosilicate zeolites represent one of the most important classes of industrial catalysts currently used. Aluminosilicate zeolites display features that make them suitable for catalytic activity. These features include the presence of ordered, nanoscale reaction cavities that promote high selectivity, a high degree of functionalizability, good thermal and chemical stability, etc. Catalysis is also one of the most promising applications for metal-organic frameworks. However, only a few examples of metal-organic frameworks with catalytic properties have been reported to date.[82-90] Metal-organic frameworks have some disadvantages compared with aluminosilicate zeolites when considering their potential as catalysts. The main disadvantage of metal-organic frameworks when compared to aluminosilicate zeolites is that they possess weaker bonds than zeolites and are therefore less stable. Their pores often collapse upon removal of ligand molecules or increase of temperature. Indeed, organic molecules typically pyrolyze between 300 and 500^{o}C. This temperature range represents, therefore, a maximum range of thermal stability for metal-organic frameworks. The drive to investigate the potential of metal-organic frameworks in catalysis arises mainly from the fact that the size and functionality of their pores can be controlled. Another advantage of metal-organic frameworks is that they have very large pores (much larger than zeolites) allowing for complex functional groups to be added to the pores. Indeed, reactions in metal-organic frameworks could be carried out with larger molecules, and large pores allow for better diffusivities than smaller ones.

The first example of a metal-organic framework displaying catalytic activity was demonstrated by Fujita et al. in 1994.[82] Indeed, Fujita et al. first demonstrated the shape specific catalytic activity of the metal-organic framework with the formula $(Cd(NO_3)_2(4,4'\text{-bpy})_2)_n$ on the reaction of cyanosilylation of aldehydes. In that work, Fujita et al. tested several aldehydes for cyanosilation with cyanotrimethylsilane. Their results showed good yields for small molecules, but progressively poorer yields as the size of the aldehyde increased. Control experiments using only $Cd(NO_3)_2$ or 4,4'-bipyridine as catalysts resulted in no reaction, and that demonstrated the importance of the framework in the catalysis process.

Five types of catalyst systems, or active sites, can be considered when investigating potential catalytic activity in MOFs. These are:

1) homochiral metal-organic frameworks;
2) metal ions or ligands in the metal-organic frameworks;
3) coordinatively unsaturated metal (CUM) centres in metal-organic frameworks (also called open metal sites);[91-95]
4) metal complexes in supramolecular porous frameworks;[96,97]
5) highly dispersed metal or metal oxide nanoparticles loaded onto porous metal-organic framework host lattices.[98-100]

The most common type of catalysis involving metal-organic frameworks is catalysis by metal ions in the metal-organic frameworks. A number of reactions have been catalysed in this way. These reactions include cyanosilylation,[101] Diels-Alder reaction,[102] hydrogenation,[103] esterification[104] and CO oxidation.[105]

A class of metal-organic frameworks that are particularly attractive candidates for catalysis are homochiral metal-organic frameworks that look like heterogeneous enzymatic catalysts. Indeed these materials are very interesting because of their potential to display enantioselective properties and could hence be used as heterogeneous asymmetric catalysts for the production of optically

active organic compounds. This would be particularly interesting since other chiral mesoporous materials such as chiral zeolites are not available. Indeed, as discussed earlier, the few zeolites that are chiral either do not have porosity following calcination[106-109] or cannot be prepared as enantiomerically pure phases.[110,111] The difficulty in producing chiral zeolites is explained by the requirement of templating action over long distances to distinguish the two enantiomers.[112] Unfortunately, attempts to synthesize homochiral metal-organic porous materials capable of enantioselective catalysis have met with little success, and only a few preliminary studies of the potential use of homochiral porous metal-organic frameworks in enantioselective separation and catalysis have been reported.[113-116] Li et al. designed a homochiral porous metal-organic framework based on the formula $(Cd_3Cl_6L_3).X$[113] which, after chemisorption of titanium isopropoxide onto the hydroxyl units, catalyzes $ZnEt_2$ additions to aromatic aldehydes for highly enantioselective heterogeneous asymmetric catalysis. Dybtsev et al. developed a homochiral metal-organic framework consisting of metal centers coordinated to benzenedicarboxylate and lactate ligands that demonstrated size and enantioselective guest sorption properties as well as catalytic activity in the oxidation of thioethers to sulfoxides.[116] Kim et al. also demonstrated catalysis properties of a homochiral metal-organic framework. This metal-organic framework consists of tartaric acid derivatives connecting oxo-bridged trinuclear zinc carboxylate clusters forming a homochiral framework with triangular cavities of 13.4 Å sides as shown in figure 1-6.[117]

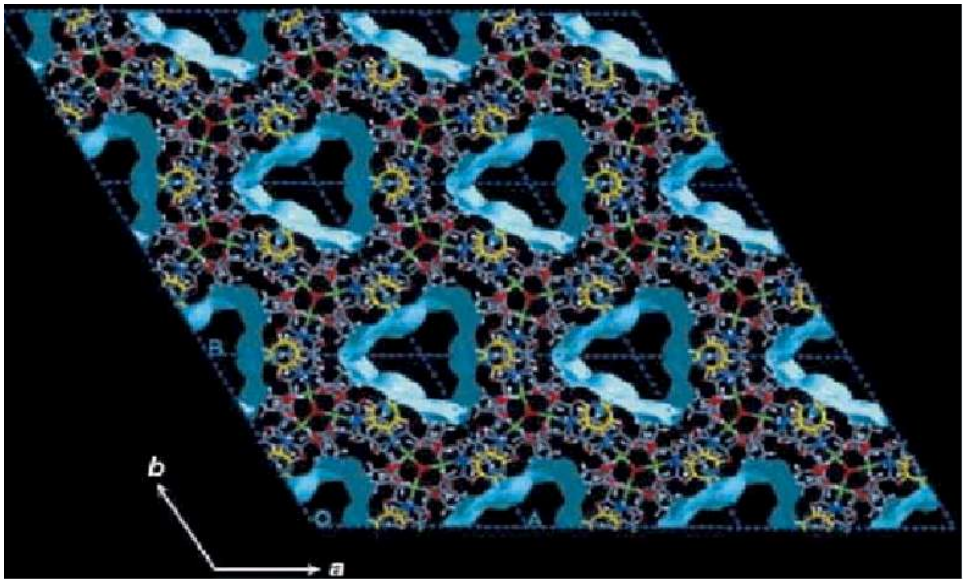

Figure 1-6 The chiral channels of the open-framework material D-POST-1 (reproduced from[56]).

This metal-organic framework, called POST-1, demonstrated catalytic activity towards transesterification reaction. POST-1 also demonstrated enantioselective properties albeit weakly: experiments with a racemic mixture of reactants resulted in an 8 % enantiomeric excess of the R or S version depending on the chirality of POST-1.

1.5 Gas storage

Metal-organic frameworks are especially interesting for their potential in the domain of gas storage. These materials, thanks to their very large surface area, pore size and the possibility of functionalizing these pores, are very promising materials for the storage of strategic gases such as H_2, CO_2, CH_4, CO and O_2. The first demonstration of this capacity of gas storage has been performed by Kitagawa et al. in 1997.[118] Because of their relevance for the energy industry, most research effort has been targeted towards developing MOFs that display large uptake of fuel gases such as methane[119-121] and hydrogen.[122,123] Some studies have also shown that by changing the linker molecules in isoreticular metal-organic frameworks, it is possible to increase their capacities for methane and hydrogen uptake.[119,121,122] Neutron scattering experiments have demonstrated the different locations of hydrogen in metal-organic frameworks.[124] However, these kinds of experiments, designed to get a better understanding of the mechanisms and thermodynamics of adsorption inside metal-organic frameworks, are still rare. Adsorption also largely depends on temperature: for example, metal-organic frameworks adsorb large amounts of hydrogen at 77 K, but at room temperature adsorption is negligible. For methane, adsorption is observed at temperatures up to about 300 K. So far, the three metal-organic frameworks that have shown the highest capabilities for hydrogen storage at 77 K are MOF-5, HKUST-1[125] and MIL-53.[123] HKUST-1 is based on the formula $(Cu_3(BTC)_2(H_2O)_3)_n$ and MIL-53 is based on the formula M (OH) (O_2C-C_6H_4-CO_2) (M = Al^{3+}, Cr^{3+}). These metal-organic frameworks show hydrogen capacities much higher than those reported for zeolites. The hydrogen capacities of these three metal-organic frameworks also compare favorably with the hydrogen capacities reported for high-grade activated carbons.[126,127]

1.6 Previous simulation studies

The predictability of the synthetic routes to metal-organic frameworks and the virtually infinite number of variations possible due to the rich coordination chemistry of transition metals and the huge variety of possible organic linker molecules make molecular modeling a particularly attractive tool for screening new structures before they are synthesised.[128] Molecular modeling can also be used to get a greater understanding of molecular level interactions that lead to observed macroscopic properties. Although molecular modeling of metal-organic frameworks is new, it seems that it will play an increasing role in the development of these materials and their applications.

Most of the simulation studies done so far consist of the study of the behavior of small molecules such as methane, carbon dioxide, argon or hydrogen inside metal-organic frameworks. However, molecular simulation of diffusion of small molecules inside metal-organic frameworks is still in its early stages. It is interesting to notice however, that simulations of diffusion in metal-organic frameworks preceded experiments by nearly two years.[129,130] Very often, the metal-organic frameworks studied in molecular modeling are isoreticular metal-organic frameworks, especially MOF-5 (also called IRMOF-1) because of their stability, simple cubic structure and very large pore volume. Vishnyakov et al. used an atomistic model and grand canonical Monte Carlo (GCMC) simulations to calculate adsorption isotherms for argon in Cu-BTC.[131] In this work, the metal-organic framework was held fixed (no possible motion of the atoms constituting the framework) and they used four different force fields derived from the UFF force field[132] to model the interactions between Ar atoms and the framework. In these simulations, the electrostatic interactions between Ar and the framework were neglected. These experiments showed reasonable agreement between adsorption isotherms obtained by experiment and through simulation at 87 K. This study also identified the adsorption sites of Ar atoms inside the framework. Skoulidas used Molecular Dynamics (MD) Simulations to study the diffusion of argon in Cu-BTC and compared it

with the diffusion of argon atoms in silica zeolites. He concluded that diffusion of argon in Cu-BTC and silica zeolites are similar in magnitude, concentration and temperature dependence.[133] Skoulidas modeled his system in a similar way to Vishnyakov et al. The framework was held rigid and Ar atoms were modeled as Lennard-Jones spheres. Similarly to what had been done by Skoulidas and Vishniakov et al., most molecular simulations of diffusion in metal-organic frameworks use the Kiselev-type potentials.[134,135] In these potentials, the atoms of the metal-organic framework are held rigid at the positions determined by crystallography. The interactions between the guest molecules and the framework are modeled by placing Lennard-Jones sites and partial charges on all atoms of the framework and the guest molecules. For non-polar molecules, the coulomb interactions of all atoms are sometimes neglected. Guest-guest interaction potentials are often taken from force fields developed for modeling vapor-liquid equilibrium.[136,137] These potentials include Lennard-Jones and partial charge parameters for the atoms of the guest molecules. They also include any necessary expressions for describing bond stretching, bond bending, and torsional potentials. Using such potentials, Johnson et al.[138] performed molecular simulations to study the adsorption of helium, argon, methane and hydrogen on a number of metal-organic frameworks including MOF-2, MOF-3, MOF-5 (IRMOF-1), IRMOF-6, IRMOF-8, IRMOF-14, Cu-BTC and manganese formate. They observed good agreement between simulation and experiment in some cases, but poor agreements in others. For these simulations, the frameworks were again held rigid with atom positions determined from X-ray diffraction experiments. They used UFF[132] and DREIDING[139] force fields for the framework atoms and Lorentz-Berthelot mixing rules to calculate the solid-fluid Lennard-Jones parameters. The gas molecules were described as spherically symmetric particles, with the exception of the hydrogen potential of Dakrim and Levesque[140] which treats hydrogen as a rigid, diatomic molecule, with the H-H distance fixed at 0.74 Å. This potential consists of a Lennard-Jones core placed at the center of mass of the molecule, point charges of magnitude $q = 0.468\ e$ at the positions of the two protons and a charge of magnitude $-2q$ at the center of mass. They used the standard Grand Canonical Monte Carlo (GCMC) method to simulate adsorption isotherms. The agreement between simulation and experimental data was reasonable for five out of nine of the systems used. For example, simulations for methane in Cu-BTC were in reasonable

agreement with the experimental data of Wag et al.,[141] with the simulation data overestimating the experimental data only by about 10 %. The simulation of H_2 in manganese at 78 K compared well with the experimental data of Dybtsev et al.,[142] although the simulated data systematically underestimated the experimental data. In the case of hydrogen adsorption in IRMOF-1, simulation results were in very good agreement with experimental values when the system was at 77 K. At room temperature however, the simulations underestimated the amount of adsorbed hydrogen by a factor of seven. In this study, they also predicted H_2 adsorbtion in MOF-2, MOF-3 and IRMOFs -6, -8 and -14 at 77 and 298 K and pressures up to 100 bar for which no experimental isotherms have yet been published. Assuming that the potentials they used were accurate, they concluded that none of these frameworks were able to meet the DOE (Department of energy) targets for hydrogen storage at room temperature. However, they showed that at 77 K IRMOF-14 demonstrated very high uptake of H_2. Skoulidas and Sholl have recently presented a set of calculations for the transport diffusivities of Ar, CH_4, CO_2, N_2 and H_2 in MOF-5 and the diffusion of Ar in MOF-2, MOF-3 and Cu-BTC.[143] They modeled the metal-organic frameworks as rigid frameworks with atomic positions obtained from X-ray diffraction data. Lennard-Jones and Coulombic potentials were used to model the interactions between the framework and the guest molecules. Adsorption isotherms of each molecule were computed using GCMC simulations. This study showed that the diffusivities in metal-organic frameworks are similar to those in zeolites and that the methods which have been widely used to measure diffusivities in zeolites should be just as applicable to metal-organic frameworks. Snurr et al. have very recently published a computational study of adsorption of methane in a number of different isoreticular metal-organic frameworks (IRMOF).[144] They found good agreement between simulations and experiments for CH4 adsorption on IRMOF-1 and IRMOF-6 at room temperature and pressures up to 40 bar. They performed GCMC simulations using an atomistic model of methane and the adsorbent. Methane was represented by the united atom model and thus was described by a single interaction site. UFF[132] and DRIEDING force fields[139] were used and both gave very similar results. They also compared simulations of adsorption of methane in metal-organic frameworks with simulations of adsorption of methane in a variety of other materials, including zeolites, MCM-41 and single walled carbon nanotubes. In this

study, they also evaluated adsorption properties of new hypothetical IRMOFs that have not been synthesized yet and predicted that one of those IRMOFs will have a capacity for methane storage that is up to 36 % higher than the best known material for methane storage. Snurr et al. also published a work on GCMC and Molecular Dynamics study of methane, n-alkanes, cyclohexane and benzene in both IRMOF-1 and bipyridine molecular squares.[145] The latter is a metal-organic framework consisting of discrete square molecules with corners formed by rhenium complexes and edges formed by bipyridine links, giving a small cavity within each square. These metal-organic frameworks were once again modeled as rigid structures. Van der Waals interactions between the framework and the guest molecules were modeled with a 12-6 Lennard-Jones potential between all pair of sites (atom or united atoms). The Lennard-Jones parameters for the interaction between the framework and the guest molecules were taken from the DRIEDING force field.[139] The DRIEDING force field is a fairly simple force field developed to handle a large number of small organic molecules, including organometallic systems. The fact that the DRIEDING force field has a small number of adjustable parameters makes it easy to extend (the force field) to more complex systems with unknown conformational behavior but also limits its accuracy. In this work, methane molecules were modeled using a united atom model. The TraPPE force field[146] was used to describe normal flexible alkanes such as pentane, hexane and heptane. This force field uses a united atom model to represent CH, CH_2 and CH_3 groups. The bond lengths between these groups are fixed and flexibility of an alkane molecule is allowed only via bond angle and torsional degrees of freedom. For cyclohexane, a six-center rigid united atom model was used with Lennard-Jones parameters for CH2 groups coming from the TraPPE force field.[146] Benzene molecules were also represented by a rigid, all atom model. The partial charges were calculated from a Mulliken charge population from a B3LYP density functional calculation. The self diffusion coefficient values for methane and n-alkanes were computed for low loadings in both the crystalline bipyridine molecular squares and IRMOF-1 (isoreticular metal-organic framework) . The values of these coefficients were in the order of 10^{-9} m^2s^{-1} for the n-alkanes and an order of magnitude faster for methane in either solid. This study also showed that the open structure of IRMOF-1 facilitates transport of normal alkanes

and cyclohexane compared to crystalline bipyridine molecular squares. In fact, diffusion of cyclohexane and benzene could not be observed for bipyridine molecular squares using molecular dynamics. In this work, no comparison with experiment was done.

Very few studies have been performed by allowing the framework atoms to move by using potential models for the framework atoms.[147,148] Greathouse and Allendorf[147] in 2006 were the first to develop a force field to model a flexible metal-organic framework. Indeed, they presented a new flexible force field for MOF-5 (IRMOF-1) that they validated by comparing the simulated lattice parameter with the structure obtained from X-ray diffraction. They also reported for the first time molecular dynamics simulations describing the interaction between water molecules and MOF-5. This work showed that MOF-5 stayed stable for very low water content. However, when the framework is exposed to more than 4 % of water content, it became unstable. No metal-organic framework specific parameters have been reported to date, therefore Greathouse and Allendorf made the hypothesis that the interaction energy between Zn ions and water O atoms was similar to the interaction energy between Zn ions and the oxygen atoms of the metal-organic framework. Because of the fact that Zn ions would interact with water molecules only through non bonded interactions (van der Waals and electrostatics), their methodology required only the use of non bonded force field parameters between Zn ions and the oxygen atoms of MOF-5. They used a general force field (CVFF[148]) for the BDC linker molecules with parameters optimized for the mineral zincite (ZnO). Simulated parameters for zincite are in good agreement with experiments. Figure 1-7 shows the evolution of the cell parameter of MOF-5 with water loading. At low water content, despite a decrease in cell parameter, the structure of MOF-5 is maintained. For higher water contents (3.9 % and 9.5 %) the structure of MOF-5 collapses within 200 ps of simulation. These results have been reported to be in good agreements with experimental studies.[149]

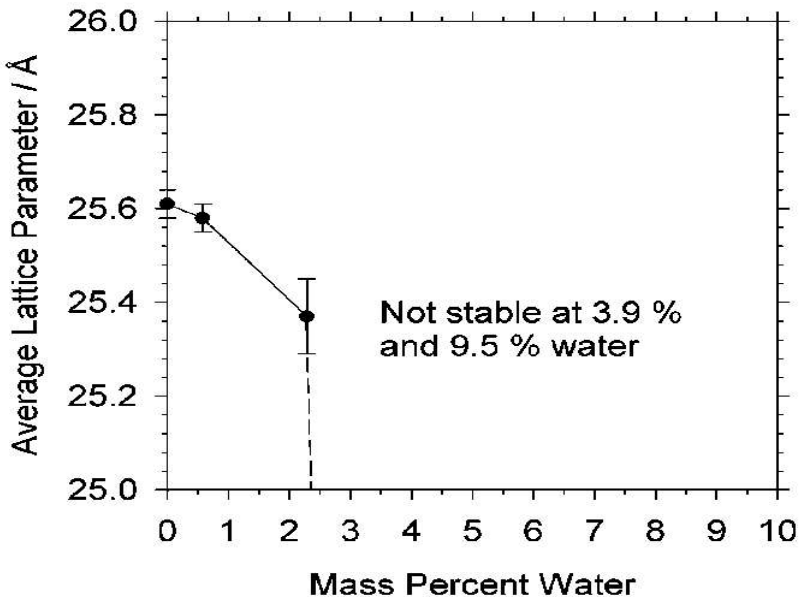

Figure 1-7 Simulated lattice parameter as a function of water content. The dashed line indicates the trend toward a much smaller lattice parameter at higher water content (reproduced from[45]).

Snurr et al.[150] have very recently modeled flexible isoreticular metal-organic frameworks, IRMOF-1 (MOF-5), IRMOF-10 and IRMOF-16. The model used in this study is similar in spirit to the model of Greathouse and Allendorf[147] but differs in the treatment of the carboxylate group. In this model, the Zn_4O cluster is modeled using only Lennard-Jones and Coulombic potentials between the individual atoms, while the linker molecule is simulated using a combination of general force field parameters (DREIDING/CVFF parameters) for bond, bend and (improper) torsion constants. This work gave good agreement with experiment and demonstrated the unusual negative thermal expansion behavior of these three IRMOFs with greater negative thermal expansion for IRMOFs with longer linker molecules. This negative thermal expansion was explained by the thermal motion of the long linker molecules (bending) and the shearing of the cages. This study also demonstrated that for low loading, increase in the sorbate loading led also to contraction of the unit cell. To our knowledge these are the only two studies on flexible MOFs reported to date.

The work presented in this thesis represents therefore one of the rare cases of study of a flexible MOF and the first simulation study of a flexible helical MOF to date. The flexible MOF studied in this work is fundamentally different from the flexible MOFs studied by Greathouse and Allendorf (published in 2006), and Snur et al. (published in 2007). Indeed, the metal centres, the SBUs and the framework topologies of the MOF studied in this work are completely different from those of the studies on flexible MOFs found in the literature. First of all, the metal constituting the MOF studied in this work is nickel while in the case of the two studies of MOFs available in the literature it is zinc. Secondly, while the MOFs in these two studies have a SBU consisting of octahedral Zn-O-C clusters at vertices linked through benzene groups, the MOF studied in this work has a SBU consisting of an octahedral nickel centre bound to, at its axial sites BTC molecules and at its equatorial sites, two cis pyridine molecules and one diol molecule (bound to the metal-center in a bidentate way). Furthermore, the topology of the flexible MOFs recently studied in the literature consists of a primitive cubic net while the topology of the MOFs studied in this work consists of two interpenetrating (10,3)-a nets. Therefore, topologically, the structure of the MOF studied in this work is a lot more complex than the simple cubic structure of the MOFs studied by Greathouse and Allendorf and Snur et al. In these two published studies respectively, Snurr et al. looked at the effect of temperature on some IRMOFs while Greathouse and Allendorf looked at the effect of water on IMOF-1 (MOF-5). In the work presented in this thesis, the effect of temperature and solvation content on helical MOFs has been studied. Furthermore, the potential enantioselective properties of these chiral helical MOFs have been investigated.

The rest of this thesis proceeds as follows: the simulation techniques used will be described in chapter 2. This is followed by a report of a temperature and solvation effect study on the MOF with 4,5-octanediol in chapter 3. This begins with a study based on the CHARMM22 force field as a benchmark, discusses a number of weaknesses identified in the CHARMM22 force field, and then reports our development of refined force fields that better reproduce experimental cell parameters and the crystal structure obtained from X-ray diffraction. This force field development phase generated a series of force fields that reproduced the structure reasonably well. In chapter 4, we report the use of these force fields to simulate two other MOFs, based on different alcohols, to

assess the transferability of our MOF potentials. Finally, MD simulations of the potential enantioselective properties of these chiral MOFs will be investigated in chapter 5.

1.7 References

[1] H. Li, M. Eddaoudi, T.L. Groy, O.M. Yaghi, *J. Am. Chem. Soc*.120 (1998) 8571.

[2] Y. Aoyama, *Topics Curr. Chem*. 198 (1998) 131.

[3] P.J. Hagrman, D. Hagrman, J. Zubieta, *Angew. Chem. Int. Ed.* 38 (1999) 2639.

[4] B. Moulton, M. J. Zaworotko, *Curr. Opin. Solid State mater. Sci*. 6 (2002) 117

[5] S.L. James, *Chem. Soc. Rev*. 32 (2003) 276

[6] M.J. Rosseinsky, *Microporous and Mesoporous Materials* 73 (2004) 15-30

[7] G. Ferey, *Chem. Soc. Rev*, 37 (2008) 191-214

[8] J.L.C. Rowsell, O.M. Yaghi, *Microporous and Mesoporous materials* 73 (2004) 3-14

[9] N.L. Rosi, M. Eddaoudi, J. Kim, M.O'Keeffe, O.M.Yaghi, *Cryst Eng Comm* 4(68) (2002) 401-404

[10] S. Kitagawa, R. Kitaura, S. Noro, *Angew. Chem. Int. Ed.* 43 (2004) 2334-2375

[11] C.N.R. Rao, S. Natarajan, R. Vaidhyanathan, *Angew. Chem. Int. Ed.* 43 (2004) 1466-1496

[12] S.L. James, *Chem. Soc. Rev*, 32 (2003) 276-288

[13] F. Fajula, A.Galarneau, F. Di Renzo, *Microporous and Mesoporous Materials* 82 (2005) 227-239

[14] C. Janiak, Dalton Trans, 2003, 2781-2804

[15] S.R. Batten, *Current Opinion in Solid State and Materials Science* 5 (2001) 107-114

[16] B.F. Hoskins, R. Robson, *Journal of the American Chemical Society* 112 (1990) 1546

[17] B.F. Abrahams, B.F. Hoskins, D.M. Michail, R. Robson, *Nature* 369 (1994) 727-729

[18] Z.Y. Wu, S.Lee, J.S. Moore, *Journal of the American Chemical society* 114 (1992) 8730-8732

[19] L. Macgillivray, S. Subramanian, M.J. Zaworotko, *JCS Chemical Communications* (1994) 1325-1326

[20] O.M. Yaghi, M. O'Keefe, N.W. Ockwig, H.K. Chae, M. Eddaoudi, J. Kim, *Nature* 423 (2003) 705-714

[21] O.M. Yaghi, M. O'Keeffe *J. Solid. State. Chem* 152 (2000) 1-2

[22] M. Eddaoudi, D.B. Moller, H. Li, B. Chen, T.M. Reineke, M. O'Keeffe, O.M. Yaghi, *Acc. Chem. Res.* 34 (2001) 319-330

[23] O.M. Yaghi, H. Li, C. Davis, D. Richardson, T. L. Groy, *Acc. Chem. Res*. 31 (1998) 474-484

[24] M. O'Keeffe, M. Eddaoudi, H. Li, T.M. Reineke, O.M. Yaghi. *J. Solid. State. Chem*. 152 (2000) 3-20

[25] S.R. Batten, R. Robson, *Angew. Chem. Int. Ed*, 37 (1998) 1460-1494

[26] A.F. Wells, *Three Dimensional Nets and Polyhedra, Wiley Interscience, New York* (1977)

[27] A.F. Wells, *Further studies of three dimensional nets, ACA monograph No 8, American crystallographic association* (1979)

[28] M. O'Keeffe, B.G. Hyde, *Crystal structures I: Patterns and symmetry, Am. Mineral. Assoc, Washington, DC*, (1996).

[29] M. Eddaoudi, J. Kim, N. Rosi, D. Vodak, J. Wachter, M. O'Keeffe, O.M. Yaghi, *Science*, 295 (2002) 469-472

[30] M.J. Bennett, J.V. Smith, *Mater. Res. Bull*, 3 (1968) 633

[31] C. Livage, C. Egger, G. Ferey, *Chemistry of Materials* 13 (2001) 410-414

[32] U. Mueller, M. Schubert, F. Teich, H. Puetter, K. Schierle-Arndt, J. Pastre, *J. Mater. Chem*., 16 (2006) 626

[33] S.S.-Y. Chui, S.M.-F. Los, J.P.H. Charmant, A.G. Open, I.D. Williams, *Science*, 238 (1999) 1148

[34] S.-H. Jhung, J.-H. Lee, J.W. Yoon, J.-S. Hwang, S.-E. Park, J.-S. Chang, *Microporous and Mesoporous Materials* 80 (2005) 147

[35] S.H. Jhung, J.-H. Lee, J.-S. Chang, *Bull. Korean. Chem. Soc*., 26 (2005) 880

[36] S. Mintova, N.H. Olson, J. Senker, T. Bein, *Angew. Chem. Int. Ed*., 41 (2002) 2558

[37] H.K. Chae, D.Y. Siberio-Pérez, J. Kim, YB. Go, M. Eddaoudi, A.J. Matzger, M. O'Keeffe, O.M. Yaghi, *Nature* 427 (2004) 523-527

[38] J.L.C. Rowsell, A.R. Millward, K.S. Park, O. M. Yaghi, *J. Am. Chem. Soc*, 126 (2004) 5666-5667

[39] J.M. Newsam, M.M.J. Treacy, W.T. Koetsier, C.B. de Gruyter, *Proc. R. Soc. London Ser. A* 420 (1988) 375

[40] M.W. Anderson, O. Terasaki, T. Ohsuna, A. Philippou, S.P. MacKay, A. Ferreira, J. Rocha, S. Lidin, *Nature* 367 (1994) 347

[41] C.S. Cundy, P.A. Cox, *Chem. Rev*. 103 (2003) 663

[42] M.J. Zaworotko, B. Moulton, *Chem. Rev.* 101 (2001) 1629

[43] C. Janiac, *Dalton Trans*, (2003) 2781

[44] S.L. James, *Chem. Soc. Rev*. 32 (2003) 276

[45] S. Kitagawa, R. Kitaura, S.-I. Noro, *Angew. Chem. Int. Ed*. 43 (2004) 2334

[46] T. Nakano, Y. Okamoto, *Chem. Rev.* 101 (2001) 4013

[47] E. Yashima, K. Maeda, T. Nishimura, *Chem. Eur. J.* 10 (2004) 42

[48] J.-M. Lehn, A. Rigault, J. Siegel, J. Harrowfield, B. Chevrier, D. Moras, Proc. *Natl. Acad. Sci. USA* 84 (1987) 2565

[49] M. Albrecht, *Chem. Rev*. 101 (2001) 3457

[50] V. Berl, I. Huc, R.G. Khoury, M.J. Krische, J.-M. Lehn, *Nature* 407 (2000) 720

[51] X.-M. Chen, G.-F. Liu, *Chem. Eur. J*. 8 (2002) 4811

[52] M.-L. Tong, X.-M. Chen, B.-H. Ye, S.W. Ng, *Inorg. Chem*. 37 (1998) 5278

[53] E.-Q. Gao, S.-Q. Bai, Z.-M. Wang, C.-H. Yan, *J. Am. Chem. Soc*. 125 (2003) 4984

[54] A.E. Rowan, R.J.M. Nolte, *Angew. Chem. Int. Ed.* 37 (1998) 63

[55] O. Mamula, A. von Zelewsky, T. Bark, G. Bernardinelli, *Angew. Chem. Int. Ed.* 38 (1999) 2945

[56] B.F. Abrahams, P.A. Jackson, R. Robson, *Angew. Chem. Int. Ed*. 37 (1998) 2656

[57] D. Sun, R. Cao, Y. Sun, W. Bi, X. Li, M. Hong, Y. Zhao, Eur. *J. Inorg. Chem*. (2003) 38

[58] F. Tuna, J. Hamblin, G. Clarkson, W. Errington, N.W. Alcock, M.J. Hannon, *Chem. Eur. J*. 8 (2002) 4957

[59] D. Guo, C. He, C.-Y. Duan, C.-Q. Qian, Q.-J. Meng, *New J. Chem.* 26 (2002) 796

[60] C. Kaes, M.W. Hosseini, C.E.F. Richard, B.W. Skelton, A.H. White, Angew. *Chem. Int. Ed.* 37 (1998) 920

[61] Y.-P. Cai, H.-X. Zhang, A.-W. Xu, C.-Y. Su, C.-L. Chen, H.-Q. Liu, L.-Zhang, B.-S. Kang, J. *Chem. Soc., Dalton Trans*. (2001) 2429

[62] C.-L. Chen, C.-Y. Su, Y.-P. Cai, H.-X. Zhang, A.-W. Xu, B.-S. Kang, H.-C. zur Loye, I*norg. Chem*. 42 (2003) 3738

[63] A. Erxleben, I*norg. Chem*. 40 (2001) 412

[64] D.L. Reger, R.F. Semeniuc, M.D. Smith, Eur. *J. Inorg. Chem*. (2002) 543

[65] F.M. Tabellion, S.R. Seidel, A.M. Arif, P.J. Stang, *J. Am. Chem. Soc*. 123, (2001) 7740

[66] X.-H. Bu, W. Chen, M. Du, K. Biradla, W.-Z. Wang, R.-H. Zhang, *Inorg. Chem.* 41 (2002) 437

[67] L. Perez-Garcia, D.B. Amabilino, *Chem. Soc. Rev*. 31 (2002) 342

[68] B. Kesanli, W. Lin, *Coord. Chem. Rev*. 246 (2003) 305

[69] D.N. Dybtsev, A.L. Nuzhdin, H. Chun, K.P. Bryliakov, E.P. Talsi, V.P. Fedin, K. Kim, *Angew. Chem. Int. ed*, 45 (2006) 916-920

[70] B. Kesanli, W. Lin, *Coord. Chem. Rev*. 246 (2003) 305-326

[71] M.E. Davis, *Nature* 417 (2002) 813-821

[72] C.-D. Wu, W. Lin, *Chem. Commun.* (2005) 3673-3675

[73] C.-D. Wu, W. Lin, Angew. *Chem. Int. Ed.* 44 (2005) 1958-1961

[74] Y. Cui, S.J. Lee, W. Lin, *J. Am. Chem. Soc*.125 (2003) 6014-6015

[75] C.J. Kepert, T.J. Prior, M.J. Rosseinsky, *J. Am. Chem. Soc*. 122 (2000) 5158-5168

[76] D.A. Evans, K.A. Woerpel, M.J. Scott, *Angew. Chem., Int. Ed. Engl*. 31 (1992) 430

[77] P.K. Bowyer, K.A. Porter, A.D. Rae, A.C. Wills, S.B. Wild, *Chem. Commun*. (1998) 153

[78] M. Kimura, M. Sano, T. Muto, K. Hanabusa, H. Shirai, N. Kobayashi, *Macromolecules* 32 (1999) 7951

[79] P. L. Caradoc-Davies, L.R. Hanton, *Chem. Commun*. (2001) 1098

[80] F.M. Tabellion, S.R. Seidel, A.M. Arif, P.J. Stang, Angew. *Chem. Int. Ed.* 40 (2001) 1529

[81] Z. Qin, M.C. Jennings, R.J. Puddephatt, *Chem. Eur. J*. 8 (2002) 735

[82] M. Fujita, Y.-J. Kwon, S. Washizu, K. Ogura, *J. Am. Chem. Soc*. 116 (1994) 1151-1152

[83] J.S. Seo, D. Wand, H. Lee, S.I. Jun, J. Oh, Y. Jeon, K. Kim, *Nature* 404 (2000) 982-986

[84] C.-D. Wu, A. Hu, L. Zhang, W. Lin, *J. Am. Chem. Soc*. 127 (2005) 8940-8941

[85] O.R. Evans, H.L. Ngo, W. Lin, *J. Am. Chem. Soc.* 123 (2001) 10395-10396

[86] T. Dewa, T. Saiki, Y. Aoyama, *J. Am. Chem. Soc*. 123 (2001) 502-503

[87] O. Ohmori, M. Fujita, *Chem. Commun.* (2004) 1586-1587

[88] W. Mori, S. Takamisawa, C.N. Kato, T. Ohmura, T. Sato, *Microporous Mesoporous Mater*, 73 (2004) 31-46

[89] P.M. Forster, A.K. Cheetham, *Top. Catal*, 24 (2003) 79

[90] W. Lin, *J. Solid. State. Chem*, 178 (2005) 2486

[91] S. Kitagawa, S.-I. Noro, T. Nakamura, *Chem. Commun*., (2006) 701-707

[92] R. Kitaura, G. Onoyama, H. Sakamoto, R. Matsuda, S.-I. Noro, S. Kitagawa, *Angew. Chem. Int. Ed*., 43 (2004)2684

[93] H.Li, C.E. Davis, T.L. Groy, D.G. Kelley, O.M. Yaghi, *J. Am. Chem. Soc*. 120 (1998) 2186

[94] B.L. Chen, M. Eddaoudi, T.M. Reineke, J.W. Kampf, M. O'Keeffe, O.M. Yaghi, *J. Am. Chem. Soc.* 122 (2000) 11559

[95] T.M. Reineke, M. Eddaoudi, M. Fehr, D. Kelley, O.M. Yaghi, *J. Am. Chem. Soc.* 121 (1999) 1651

[96] L.-G. Qiu, A.-J. Xie, L.-D. Zhang, *Angew. Chem. Int. Ed*., 43 (2004) 2684-2687

[97] S. Hermes, M.-K. Schroter, R. Schmid, L. Jhodeir, M. Muhler, A. Tissler, R.W. Fischer, R.A. Fischer, *Angew. Chem. Int. Ed*., 44 (2005) 6237

[98] H. Byrd, A. Clearfield, D. Poojary, K.P. Reis, M.E. Thompson, *Chem. Mater*., 8 (1996) 2239

[99] A. Dokoutchaev, V.V. Krishnan, M.E. Thompson, *J. Mol. Struct.*, 470 (1998) 191

[100] K.P. Reis , V.K. Joshi, M.E. Thompson, *J. Catal*., 161 (1996) 62

[101] O.R. Evans, H.L. Ngo, W. Lin, *J. Am. Chem .Soc*., 123 (2001) 10395-10396

[102] T. Sawaki, Y. Aoyama, *J. Am. Chem. Soc*., 121 (1999) 4793-4798

[103] B. Gomez-Lor, E. Gutierrez-Puebla, M. Iglesias, M.A. Monge, C. Ruiz-Valero, N. Snejko, *Inorg. Chem*., 41 (2002) 2429-2432

[104] P.M. Forster, N. Stock, A.K. Cheetham, *Angew. Chem. Int. Ed*., 44 (2005) 7608-7611

[105] Q. Zou, H. Sakurai, Q. Xu, Angew. *Chem. Int. Ed*., 45 (2006) 2542-2546

[106] D.A. Bruce, A.P. Wilkinson, M.G. White, J.A. Bertrand, *J. Chem. Soc. Chem. Commun*. (1995) 2059

[107] D.A. Bruce, A.P. Wilkinson, M.G. White, J.A. Bertrand, *J. Solid. State. Chem*.125 (1996) 228

[108] S.M. Stalder, A.P. Wilkinson, *Chem. Matter*. 9 (1997) 2168

[109] M.J. Gray, J.D. Jasper, A.P. Wilkinson, J.C. Hanson, *Chem. Mater*, 9 (1997) 976

[110] J.M. Newsam, M.M.J. Treacy, W.T. Koetsier, C.B. de Gruyter, *Proc. R. Soc. London. Ser. A* 420 (1988) 375

[111] M.W. Anderson, O. Terasaki, T. Ohsuna, A. Philippou, S.P. MacKay, A. Ferriera, J. Rocha, S. Lindin, *Nature* 367 (1994) 347

[112] M.E. Davis, *Nature* 417 (2002) 813-821

[113] J.S. Seo, D. Whang, H. Lee, S.I. Jun, J. Oh, Y.J. Jeon, K. Kim, *Nature* 404 (2000) 982-986

[114] B. Kesanli, W. Lin, *Coord. Chem. Rev*., 246 (2003) 305-326

[115] D.-D. Wu, A. Hu, L. Zhang, W. Lin, *J. Am. Chem. Soc*., 127 (2005) 8940-8941

[116] D.N. Dybtsev, A.L. Nuzhdin, H. Chun, K.P. Bryliakov, E.P. Talsi, V.P. Fedin, K. Kim, *Angew. Chem. Int. Ed*., 45 (2006) 916-920

[117] J. Soo Seo, D. Whang, H. Lee, S.I. Jun, J. Oh, Y.J. Jeon, K. Kim, *Nature* 404 (2000) 982

[118] S. Kitagawa, M. Kondo, *Angew. Chem. Int. Ed. Engl.,* 36 (1997) 1725

[119] M. Eddaoudi, J. Kim, N. Rosi, D. Vodac, J. Wachter, M.O' Keeffe, O.M. Yaghi, *Science* 295 (2002) 469

[120] K. Seki, S. Takamizawa, W. Mori, *Chem. Lett*. (2001) 332

[121] K. Seki, W. Mori, *J. Phys. Chem. B* 106 (2002) 1380

[122] N.L. Rosi, J. Eckert, M. Eddaoudi, D.T. Vodac, J. Kim, M. O'Keeffe, O.M. Yaghi, *Science* 300 (2003) 1127

[123] G. Ferey, M. Latroche, C. Serre, F. Millange, T. Loiseau, A. Percheron-Guegan, *Chem. Commun.* (2003) 2976

[124] P.M. Forster, J. Eckert, J.S. Chang, S.E. Park, G. Ferey, A.K. Cheetham, *J. Am. Chem. Soc*., 125 (2003) 1309-1312

[125] P. Krawiec, M. Kramer, M. Sabo, R. Lunschke, H. Frode, S. Kaskel, *Adv. Eng. Mater*., 8 (2006) 293

[126] B. Panella, M. Hirscher, S. Roth, *Carbon*, 109 (2005) 13094

[127] P. Bernard, R. Chahine, *Langmuir*, 17 (2001) 1950

[128] C. Mellot-Draznieks, J. Dutour, G. Ferey, *Angew. Chem. Int. Ed*, 43 (2004) 6290-6296

[129] L. Sarkisov, T. Duren, R.Q. Snurr, *Mol. Phys*. 102 (2004) 211-221

[130] T. Duren, L. Sarkisov, O.M. Yaghi, R.Q. Snurr, *Langmuir* 20 (2004) 2683-2689

[131] A.Vishnyakov, P.I. Ravikovitch, A.V. Neimark, M. Bulow, Q.M. Wang, *Nano Lett*, 3 (2003) 713-718

[132] A. Rappe, C.J. Casewit, K.S. Colwell, W.A. Goddard III, W.M. Skiff, *J. Am. Chem. Soc*. 114 (1992) 10024

[133] A.I. Skoulidas, *J. Am. Chem. Soc*, 126 (2004) 1356-1357.

[134] A.G. Bezus, A.V. Kiselev, A.A. Lopatkin, P.Q.J. Du. *J. Chem. Soc. Faraday Trans. II,* 74 (1978) 367

[135] A.H. Fuchs, A.K. Cheetham. *J. Phys. Chem. B*, 105 (2001) 7375

[136] M.G. Martin, J.I. Siepmann. *J. Phys. Chem. B*., 102 (1998) 2569

[137] M.G. Martin, J.I. Siepmann. *J. Phys. Chem. B.*, 103 (1999) 4508

[138] G. Garberoglio, A.I. Skoulidas, J.K. Johnson. *J. Phys. Chem. B*, 109 (2005) 13094-13103

[139] S. Mayo, B. Olafson, W.A. Goddard III, *J. Phys. Chem*. 94 (1990) 8897

[140] F. Dakrim, D. Levesque, *J. Chem. Phys*. 109 (1998) 4981-4984

[141] Q. Wang, D.M. Shen, M. Bulow, M.L. Lau, S.G. Deng, F.R. Fitch, N.O. Lemcoff, J. Semanscin, *Microporous Mesoporous Mater*. 55 (2002) 217-230

[142] D.N. Dybtsev, H. Chun, S.H. Yoon, D. Kim, K. Kim, *J. Am. Chem. Soc*. 126 (2004) 32-33

[143] A.I. Skoulidas, D.S. Sholl, *J. Phy. Chem. B*, 109 (2005) 15760-15768

[144] T. Duren, L. Sarkisov, O.M. Yaghi, R.Q. Snurr, *Langmuir* 20 (2004) 2683-2689

[145] L. Sarkisov, T. Duren, R.Q. Snurr, *Mol. Phys*. 102 (2004) 211-221

[146] M.G. Martin, J.I. Siepmann, *J. Am. Chem. Soc* 119 (1997) 8921

[147] J.A. Greathouse, M.D. Allendorf. *J. Am. Chem. Soc., 128* (2006) 10678

[148] P. Dauber-Osguthorpe, V.A. Roberts, D.J. Osguthorpe, J. Wolff, M. Genest, A.T. Hagler. *Proteins: Struct., Funct., Genet*. 4 (1988) 31-47

[149] L.M. Huang, H.T. Wang, J.X. Chen, Z.B. Wang, J.Y. Sun, D.Y. Zhao, Y.S. Yan, *Microporous Mesoporous Mater*. 58 (2003) 105-114

[150] D. Dubbeldam, K.S. Walton, D.E. Ellis, R.Q. Snurr, *Angew. Chem. Int. Ed.* 46 (2007) 4496-4499

2 Simulation Techniques

2.1 Statistical mechanics

Computer simulations give us information about microscopic properties, like atomic positions and velocities. Such information, unlike macroscopic thermodynamic properties such as temperature, pressure, internal energy , entropy and enthalpy, cannot be deduced from direct macroscopic observations (without using sophisticated tools enabling observations at the atomic level such as a x-ray diffractometer or a synchrotron). The concepts used to transform microscopic properties obtained from computer simulations to macroscopic properties obtained from experiments come from statistical mechanics.

If we consider a system of N particles, the positions and momenta of the particles in this system can be considered as coordinates in a multidimensional space called the phase space. Such a phase space would have $6N$ dimensions (each atom having 3 components x, y, z for the position and 3 components p_x, p_y, p_z for the momenta). If we take Γ, a particular point in the phase space, and A the instantaneous value of some specific property, we can then write A as a function of Γ: $A(\Gamma)$.

If the system evolves with time, $A(\Gamma)$ can be averaged over time to give the value of the observable macroscopic property A_{obs}:

$$A_{\text{obs}} = \langle A \rangle_{\text{time}} = \langle A(\Gamma(t)) \rangle_{\text{time}} = \lim_{t_{obs} \to \infty} \frac{1}{t_{obs}} \int_0^{t_{obs}} A(\Gamma(t))\, dt$$

Equation 2-1

The equation governing this time evolution in the classical system is Newton's equation of motion. In Molecular Dynamics (MD) this equation is not integrated in continuous time, instead the time t_{obs} is divided into a large finite number of time steps, N_{obs}, of length $\delta t = t_{obs}/N_{obs}$. In this case the equation becomes:

$$A_{\text{obs}} = \langle A \rangle_{\text{time}} = \frac{1}{N_{obs}} \sum_{N=1}^{N_{obs}} A(\Gamma(N))$$

Equation 2-2

Because of the fact that the evolution of thermodynamic properties with time is difficult to compute for a system with a large number of atoms, Gibbs suggested to replace time averages by ensemble averages. Indeed, for a macroscopic number of particles (order of 10^{23}) it is not even possible to determine an initial configuration of the system, let alone integrate the equation of motion. An ensemble is a collection of points Γ in phase space. These points are distributed according to a probability density $\rho(\Gamma)$. Each point represents a system at any particular instant of time. If the simulation time is long enough to reach equilibrium we can consider that the time average is equal to the ensemble average.

$$A_{obs} = \sum_{\Gamma} A(\Gamma) \rho_{ens}(\Gamma)$$

Equation 2-3

This is the "ergodic hypothesis".

There are five commonly-used ensembles in statistical mechanics. Their names and the fixed macroscopic variables that define them are :

- microcanonical; fixed N, V, E
- canonical; fixed N, V, T
- isothermal-isobaric; fixed N, P, T
- grand canonical; fixed μ, V, T
- constant stress; fixed N, S, T

Where N is the number of particles (or molecules) present in the system, V is the volume of the system, E is the energy of the system, P is the pressure of the system, T is the temperature of the

system, μ is the chemical potential of the system and S is the stress exerted on the system.

The partition function Q_{ens} ("sum over states") is a function of the microscopic properties defining the ensemble and acts as a normalizing factor for the corresponding density, ρ :

$$Q_{ens} = \sum_{\Gamma_i} \rho(\Gamma_i)$$

Equation 2-4

$$\langle A \rangle_{\text{ens}} = \frac{1}{Q_{obs}} \sum_{\Gamma_i} A(\Gamma_i)\rho(\Gamma_i)$$

Equation 2-5

Some thermodynamic properties, like the internal energy or the enthalpy, can be calculated from the partition function alone. For the canonical ensemble:

Helmholtz free energy: $A = -kT \ln Q$

Equation 2-6

Internal energy: $U = k_B \frac{T^2}{Q} \left(\frac{\partial Q}{\partial T}\right)_V = k_B T^2 \left(\frac{\partial \ln Q}{\partial T}\right)_V$

Equation 2-7

Enthalpy: $H = k_B T^2 \left(\frac{\partial \ln Q}{\partial T}\right)_V + k_B TV \left(\frac{\partial \ln Q}{\partial V}\right)_T$

Equation 2-8

2.2 Molecular Dynamics

Molecular dynamics is a way to integrate Newton's second law, also called Newton's equation of motion. This integration leads to a trajectory that describes how the positions and velocities of the atoms in the system vary with time. The average values of the properties of the system are then determined from the trajectory using the ergodic hypothesis, as explained in section 2.1.

$$\vec{\boldsymbol{F}}_i = m_i \vec{\boldsymbol{a}}_i = m_i \frac{d^2 \vec{\boldsymbol{r}}_i}{dt^2}$$

Equation 2-9

Where $\boldsymbol{F}_i$ is the force acting on the particle i, m_i is the mass of the particle i, $\boldsymbol{a}_i$ its acceleration and $\boldsymbol{r}_i = (x_i, y_i, z_i)$ its position.

The force can also be expressed as the gradient of the potential energy:

$$\boldsymbol{F} = -\frac{d\boldsymbol{U}}{dr_i}$$

Equation 2-10

If we combine these two equations we obtain:

$$-\frac{d\boldsymbol{U}}{dr_i} = m \frac{d^2 \boldsymbol{r}_i}{dt^2}$$

Equation 2-11

Where *U* is the potential energy of the system. Newton's second law therefore relates the derivative of the potential energy to the changes in position as a function of time. Thus, from the atomic positions, one gets the potential energy of the system, then from the potential energy, the forces on each atom are computed. Then from these forces the acceleration of each atom is obtained and finally from the accelerations the new atomic positions are determined.

A molecular dynamics program presents three main phases. The first is **initialization**. During the initialization period, position and velocities are assigned to each atom of the system. Positions are chosen in such a way as to replicate the system we want to study. Care as to be taken so that two atoms never overlap. Initial velocities are typically determined from a random distribution (Maxwell-Boltzmann or Gaussian distribution) and are adjusted so that the total momentum is equal to zero.

$$\vec{\boldsymbol{p}} = \sum_{i=1}^{N} m_i \vec{\boldsymbol{v}}_i = 0$$

Equation 2-12

Where $\boldsymbol{p}$ is the total momentum.

The velocities are also scaled to adjust the temperature to the desired value. We can calculate the temperature from the velocities using equation 2-13:

$$T = \frac{1}{3N} \sum_{i=1}^{N} \frac{p_i}{2 m_i}$$

Equation 2-13

Where *N* is the number of atoms in the system, if particles are not constrained.
Once we have the initial positions and velocities of the atoms we can then proceed to the second

phase which is the **calculation of the forces** in the system. This is the most computationally expensive part of all molecular dynamics simulations. Finally, from the positions, velocities and forces the trajectory can be determined from the **integration of Newton's equation of motion**.

For interactions described by soft potentials (also called continuous potentials), as opposed to hard potentials (hard sphere or square well potentials), the motion of the atoms in the system are coupled together in a very complex manner. If the position of an atom changes or the positions of the atoms situated nearby that atom changes, the overall force exerted on that atom will also change. That coupled effect leads to a many-body problem that cannot be solved analytically. Under such conditions, a numerical method, namely a finite difference method has, to be used to integrate the equations of motion.

2.2.1 Finite difference methods

With this method, the integration of the equation of motion is divided into small steps. Each step being separated in time by a time interval δt. The time interval δt needs to be much shorter than the period of the highest frequency motion. In the finite difference method, the positions, velocities and other dynamical informations at time $t + \delta t$ can be determined from the current values of these quantities using Taylor series expansions[1]:

$$r(t+\delta t)=r(t)+v(t)\delta t+\frac{1}{2}a(t)\delta t^2+\frac{1}{6}b(t)\delta t^3+\frac{1}{24}c(t)\delta t^4+\ldots$$

Equation 2-14

$$v(t+\delta t)=v(t)+a(t)\delta t+\frac{1}{2}b(t)\delta t^2+\frac{1}{6}c(t)\delta t^3+\ldots$$

Equation 2-15

$$a(t+\delta t)=a(t)+b(t)\delta t+\frac{1}{2}c(t)\delta t^2+\ldots$$

Equation 2-16

$$b(t+\delta t)=b(t)+c(t)\delta t+\ldots$$

Equation 2-17

where v is the velocity (the first derivative of the position with respect to time), a is the acceleration (the second derivative of the position with respect to time), b is the third derivative of the position with respect to time, and so on.

The acceleration of each particle is calculated from the total force acting on each particle (according to equation 2-8). Then, as shown in the equations above, accelerations, velocities and positions are combined to calculate the same quantities at time $t + \delta t$. This process is then repeated iteratively (new positions, velocities etc., at time $t + \delta t$ are used to determine the same quantities at time $t + 2\ \delta t$) until the trajectory of the atoms is computed over the desired simulation time.

There are many algorithms available for integrating the equations of motion using the finite difference method. The simplest and most broadly used of these integration algorithms, in molecular dynamics simulations, is the Verlet algorithm[2]. The Verlet algorithm uses the positions and accelerations at time t, and the positions from the previous step, $r(t - \delta t)$, to calculate the new positions, $r(t + \delta t)$, at time $t + \delta t$:

$$r(t+\delta t)=r(t)+v(t)\delta t+\frac{1}{2}a(t)\delta t^2+\frac{1}{6}b(t)\delta t^3+\ldots$$

Equation 2-18

$$r(t-\delta t)=r(t)-v(t)\delta t+\frac{1}{2}a(t)\delta t^2-\frac{1}{6}b(t)\delta t^3+\ldots$$

Equation 2-19

Combining these two equations gives:

$$r(t+\delta t)=2r(t)-r(t-\delta t)+a(t)\delta t^2$$

Equation 2-20

Velocities do not explicitly appear in the Verlet integration algorithm. But they can be calculated in different ways, one of which is:

$$v(t)=\frac{[r(t+\delta t)-r(t-\delta t)]}{2\delta t}$$

Equation 2-21

The advantages of the Verlet algorithm is that it is straightforward and symplectic, and hence robust and accurate. The inconveniences are the lack of explicit velocities and that it is of moderate precision. This loss of precision comes from the fact that a small term $a(t)\delta t^2$ is added to the difference of two much larger terms $2r(t)$ and $r(t-\delta t)$.
Because of these drawbacks, variants of the Verlet algorithm have been developed, including: the Verlet Leap-frog algorithm, the velocity Verlet algorithm and Beeman's algorithm.

The following criteria should be considered when choosing an integration algorithm:

- The algorithm should conserve energy and momentum
- It should be computationally efficient
- It should permit a long time step for integration.

In this work we have used DLPOLY2[3] to perform all molecular dynamics simulations. DLPOLY2[3] incorporates both the Leap-frog and the Velocity Verlet algorithms. For this project we have used the Leap-frog algorithm:

$$r(t+\delta t)=r(t)+\delta t\, v(t+\frac{1}{2}\delta t)$$

Equation 2-22

$$v(t+\frac{1}{2}\delta t)=v(t-\frac{1}{2}\delta t)+a(t)\delta t$$

Equation 2-23

From the velocities at time $t-\frac{1}{2}\delta t$ and the acceleration at time *t* we calculate the velocities at time $t+\frac{1}{2}\delta t$, $v(t+\frac{1}{2}\delta t)$. The positions *r(t + δt)* are then deduced from the velocities at time $t+\frac{1}{2}\delta t$ and the positions at time *t*, *r(t).* The velocities at time *t* are calculated the following way:

$$v(t)=\frac{1}{2}[v(t+\frac{1}{2}\delta t)+v(t-\frac{1}{2}\delta t)]$$

Equation 2-24

The positions therefore 'Leap-frog' over the velocities because the positions at time $t + \delta t$ are deduced from the velocities at time $t+\frac{1}{2}\delta t$.

The advantages of this algorithm over the standard Verlet algorithm are the facts that in the Leap-frog algorithm, velocities are explicitly calculated, and it does not require the calculation of the differences of large numbers. The drawback is that positions and velocities are not calculated at the same time.

2.3 Periodic boundary conditions

In a simulation cell, due to the fact that they are mainly surrounded by surface, atoms close to the boundaries of the cell would be surrounded by less atoms than atoms in the center of the cell. To avoid this surface effect, and have a system that replicates bulk systems, periodic boundary conditions are often introduced. Periodic boundary conditions allow simulations of a relatively small number of atoms to be performed in such a way that all atoms experience interactions as though they were in bulk solution.

In periodic boundary conditions, atoms at the edge of the box do not only interact with the other atoms in this box but also with the translational image of these atoms in nearby boxes. Therefore interactions occur through box boundaries, thus eliminating surface effects.

During a simulation, images of atoms in different cells move in the same way. Therefore, if an atom leaves the central cell at one side with a certain velocity, an image of this atom in an adjacent cell will enter the central cell from the opposite side with the same velocity. Thus the cell always contains the same number of atoms in the central cell. This is illustrated in two dimensions in figure 2-1

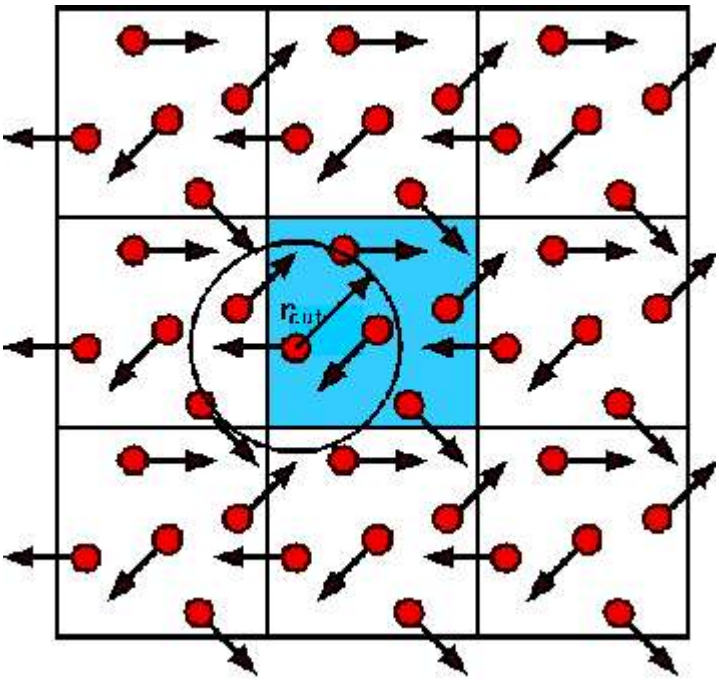

Figure 2-1 Application of periodic boundary conditions in two dimensions

The minimum image convention is generally used in concordance with periodic boundary conditions. It requires that a spherical cut off distance must be used for non bonded interactions. This cut off distance must be inferior or equal to half the length of the simulation cell. In the figure r_{cut} represents the cut off distance. As we can see an atom in the central cell can interact with an atom in an adjacent cell (this atom being the image of an atom in the central cell) if this atom is within its cut off distance. It will not interact with atoms outside the cut off distance, even if they are in the same simulation cell. Thus the interactions will only take place with the closest images of the surrounding atoms.

In theory any cell shape may be used as long as it fills all space by translation of the central simulation cell in three dimensions (thus, a simulation cell with a spherical or elliptical shape cannot be used). The shape of the simulation cell is chosen in such a way that it reflects the underlying symmetry of the studied system.

Eight options are generally available for periodic boundary conditions:

1) no periodic boundary conditions

2) cubic boundary conditions
3) orthorhombic boundary conditions
4) parallelepipeded boundary conditions
5) truncated octahedral boundary conditions
6) rhombic dodecahedral boundary conditions
7) x-y parallelogram boundary conditions with no periodicity in the z direction
8) hexagonal prism boundary conditions

The net electrostatic charge of the simulation cell must be equal to zero when using periodic boundary conditions in order to avoid infinite summing of this charge.

In this work, cubic boundary conditions which is the simplest periodic system for visualization and implementation has been used.

2.4 Force Field

A force field describes the total force on each atom for any configuration of all the atoms. It , in turn, is described by specifying a set of functional forms and associated parameters. The interactions described comprise both bonded terms for atoms within the same molecule and non bonded terms. Force field functional forms and parameters can either be derived empirically from experimental results or theoretically from quantum mechanical calculations.
Most force fields consist of separate terms describing bond stretches, bond angle bends, torsional rotations, inversion angles and non bonded interactions. In some force fields cross terms are also included to describe couplings between different distortions (eg: Bond-Angle or Torsion-Angle).

In DLPOLY2, the configuration energy of a system of particles is calculated using the following formula:

$$U_{total} = (U_{bond} + U_{angle} + U_{dihedral} + U_{inv}) + (U_{2\text{-}body} + U_{3\text{-}body} + U_{4\text{-}body}) + U_{ext}$$

Equation 2-25

U_{bond}, U_{angle}, $U_{dihedral}$ and U_{inv} are intra-molecular potentials representing respectively bond stretches, bond angle bends, torsional rotations and inversion angles. $U_{2\text{-}body}$, $U_{3\text{-}body}$, $U_{4\text{-}body}$ are inter-molecular potentials representing respectively pair-body, three-body and four-body interactions. U_{ext} represents the potential energy exerted by an external field. In this work, inversion angle, three body, four body and external field terms have not been used.

The force field initially used in this work is CHARMM22, but adapted to include appropriate Ni^{2+}– organic interactions.

We can distinguish different types of force fields

- Diagonal force field: In these force fields, there is no energy cross terms like Bond-Angle, Angle-Torsion-Angle, Angle-Angle, Torsion-Bond, Bond-Bond, Torsion-Angle, Torsion-Torsion, Torsion-Planar, Planar-Torsion-Planar and Planar-Planar terms. CHARMM[4] and AMBER[5] are such force fields.
- Matrix force field: These force fields use energy cross terms. MM4[6] and CFF[7] are such force fields.
- Class 2 force fields: These force fields use parameters derived from quantum mechanical calculations. ESFF[8] is such a force field.
- Fast force field: These force fields use only torsion and non-bonded terms. YETI[9] is such a force field.

The different contributions to equation 2-24 are as follows:

2.4a Intra-molecular potentials

Bond potentials

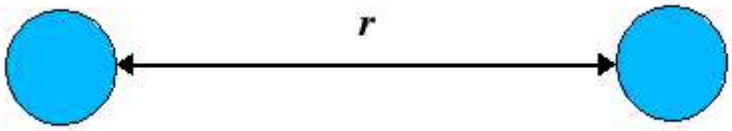

Figure 2-6 Schematic representation of the bond potential

Bond potentials are only functions of interatomic distances. The functional form used to calculate bond potentials is the harmonic bond form:

$$U(r)=\frac{1}{2}k(r-r_0)^2$$

Equation 2-26

r_0 is the equilibrium bond length and k is the force constant associated with the bond r .

Bond angle bending

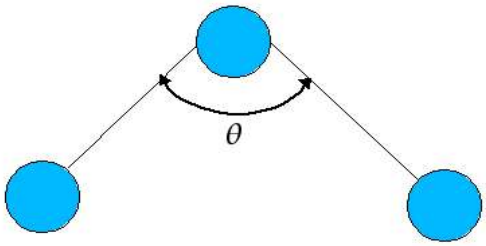

Figure 2-7 Schematic representation of the valence angle potential

The functional form used to calculate bond angle bending terms is the harmonic angle bending potential:

$$U(\theta_{ijk}) = \frac{k}{2}(\theta_{ijk} - \theta_0)^2$$

Equation 2-27

θ_0 is the equilibrium bond angle and k is the force constant associated with the angle θ_{ijk}.

Dihedral angle potentials

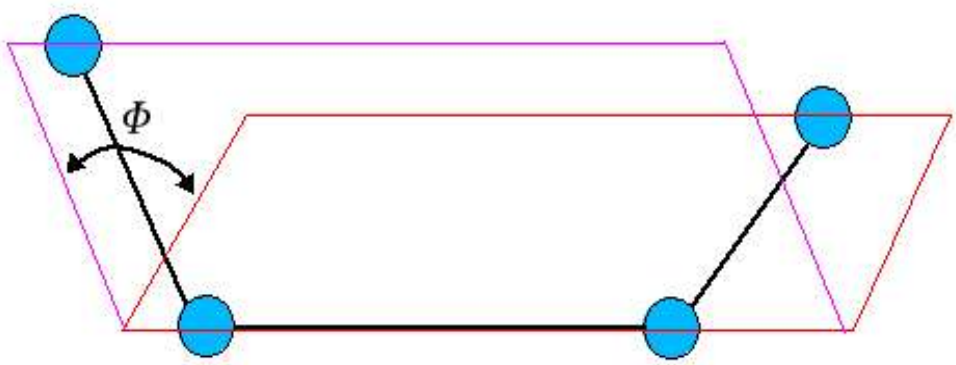

Figure 2-8 Schematic representation of the dihedral angle potential

If we consider four atoms h, i, j, k bound to each other linearly, the dihedral angle Φ_{hijk} represents the angle between the plane formed by atoms hij and the plane formed by atoms ijk.

The functional forms used for the calculation of the dihedral angle bends are the cosine form represented in equation 2-28 and the harmonic form represented in equation 2-29.

$$U(\phi_{hijk}) = A[1 + \cos(m\phi_{hijk} - \delta)]$$

Equation 2-28

Where *m* is the periodicity of the potential, *A* the rotational barrier and δ the phase factor. The cosine function is appropriate because of the periodicity of the angle Φ that repeats itself every 360^0 or more depending on the structure of the molecule.

$$U(\phi_{hijk}) = \frac{1}{2} k (\phi_{hijk} - \phi_0)^2$$

Equation 2-29

Where ϕ_0 is the equilibrium dihedral angle and k is the force constant associated with the dihedral angle ϕ_{hijk}.

2.4b Model potentials

In molecular simulation we can generally distinguish different types of model potentials for short to intermediate ranged potentials. The simplest of these models is the hard sphere model. In this model, molecules are considered to be spheres with a certain radius r_0. If the distance between two hard spheres is inferior or equal to zero, the potential energy tends to infinity and if this distance is greater than r_0 then the potential energy is equal to zero. This kind of potential is called excluded volume or hard wall potential. The mathematical expression for the hard wall potential can be summarized in the following formula:

$U(r) = \{\infty, r \leq r_0 ; 0, r > r_0\}$

Spheres can be replaced by ellipsoids and spherocylinders. This is often the case for simulations of liquid crystals for example. The hard sphere model was used in the first molecular dynamics simulation of a condensed phase system, it was performed by Alder and Wainwright in 1957[10]. Figure 2-2 shows a schematic representation of this hard-sphere potential.

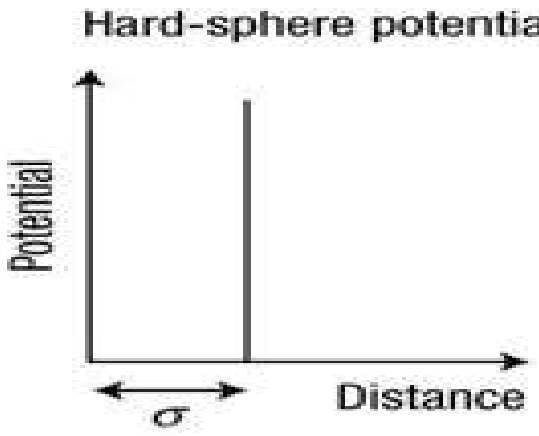

Figure 2-2 Representation of the hard-sphere potential

A more sophisticated model potential is the soft model potential. There is a variety of functional forms for soft model potentials also called van der Waals potentials. In these models, the force on each particle will change whenever its position or the positions of the particles interacting with it change. The first person to use soft potentials was Rahman in 1964[11], to simulate interactions between argon atoms.

The van der Waals potential formula expresses the interaction between two non bonded atoms as a function of the distance between these two atoms. In a molecular system, every atom or molecule experiences forces exerted by the surrounding atoms in the system. These forces can be classified in two categories, attractive forces and repulsive forces. Attractive forces are typically exerted when atoms are at long distances apart from each other and repulsive forces are exerted when atoms are at short distances apart from each other. The attractive forces are also known as dispersion forces. The repulsive forces result from the Pauli repulsion behavior which itself results from the Pauli exclusion principle which states that two fermions (particles with half integer spins, typically electrons, neutrons and protons) cannot occupy the same position at the same time.

The van der Waals potential energy interaction can be expressed by the following formula:

$$U(r)=Ae^{-\alpha r}-\frac{C_6}{r^6}$$

Equation 2-30

$Ae^{-\alpha r}$ expresses the repulsive part of the potential energy and $\frac{C_6}{r^6}$ expresses its attractive part. The repulsive part of the potential energy is often approximated by a different form: $\frac{C_{12}}{r^{12}}$. Thus the potential energy equation becomes:

$$U(r)=\frac{C_{12}}{r^{12}}-\frac{C_6}{r^6}$$

Equation 2-31

The general equation for the interaction between two non bonded chargeless atoms can be stated in the following approximation:

$$U(r)=\frac{C_n}{r^n}-\frac{C_m}{r^m}$$

Equation 2-32

In this expression *n* and *m* are integers, C_n and C_m are constants. The values of C_n and C_m determine the well depth of the potential energy curve and the equilibrium distance between the two atom's nuclei.

Figure 2-3 depicts the shape of a typical van der Waals potential energy curve

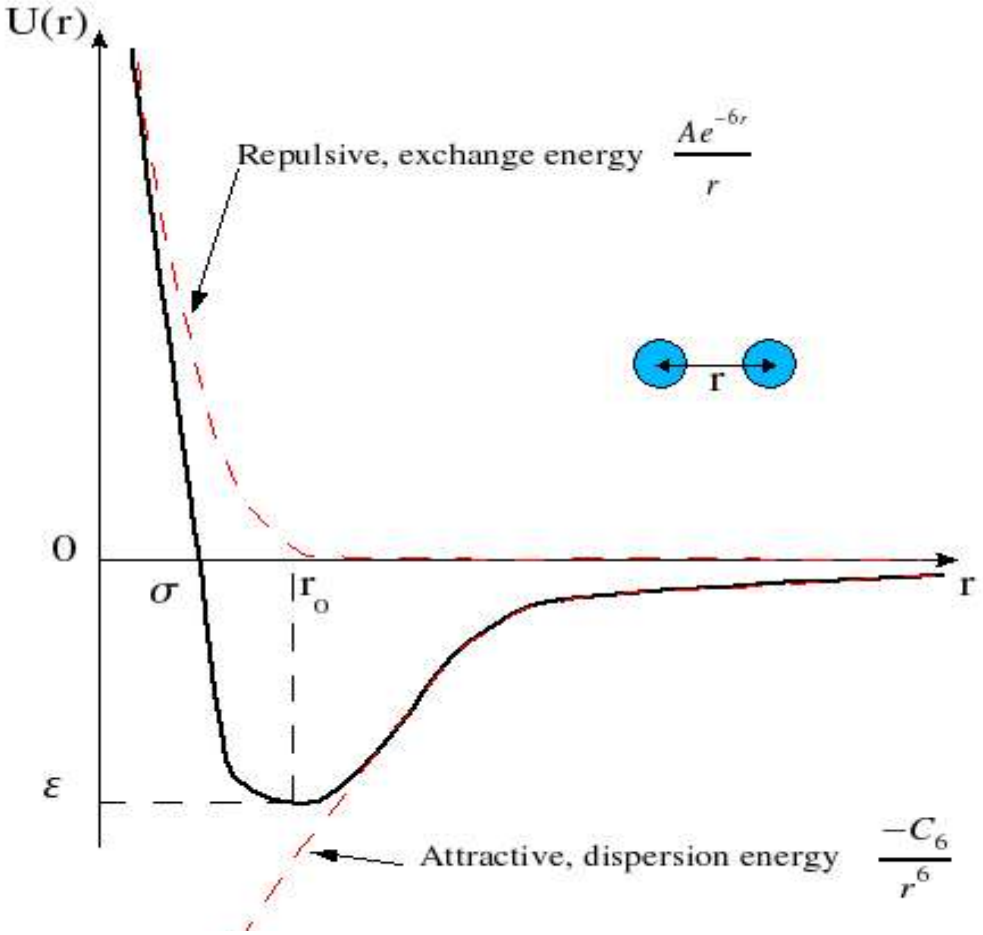

Figure 2-3 Schematic representation of the van der Waals potential

The Lennard-Jones potential is the simplest model for van der Waals potentials. This Lennard-Jones model is the main model that has been used in this study (although Buckingham potentials were also tried). The Lennard-Jones expression represents the van der Waals forces between two instantaneous dipoles. For this expression, *n* and *m* are respectively 12 and 6 which gives the following formula for the Lennard-Jones potential energy interaction:

$$U(r)=4\varepsilon[(\frac{\sigma}{r})^{12}-(\frac{\sigma}{r})^{6}]$$

Equation 2-33

This is called the 12-6 form of the Lennard-Jones potential.

In this formula ε represents the well depth also called dissociation energy of the Lennard-Jones

curve and σ the distance at which the potential energy is equal to zero. When r < σ, the potential energy tends towards infinity. r_0, the equilibrium distance between the two atom's nuclei, and σ are proportional with a proportionality constant equal to $2^{1/6}$. Thus we obtain the following relationship:

$$r_0 = 2^{\frac{1}{6}} \sigma$$

Equation 2-34

The 12-10 form of the Lennard-Jones potential has often been used to model hydrogen bond interactions, though this is more often described as a balance of electrostatic and Lennard-Jones terms these days.

For the interactions between different types of atoms, mixing rules have been used as a first approximation. Mixing rules state that if the dissociation energy between two atoms of type *x* is ε_{xx} and two atoms of type *y* is ε_{yy} then the dissociation energy between an atom of type *x* and an atom of type *y* is

$$\varepsilon_{xy} = \sqrt{(\varepsilon_{xx} \varepsilon_{yy})}$$

Equation 2-35

While the equilibrium distance between the two atom types is

$$r_{0,xy} = \frac{1}{2}(r_{0,xx} + r_{0,yy})$$

Equation 2-36

In the same way:

$$\sigma_{xy} = \frac{1}{2}(\sigma_{xx} + \sigma_{yy})$$

Equation 2-37

2.4c Long ranged electrostatic potentials

The method used in this work to calculate long ranged electrostatic potentials is the Ewald sum.[12,13] This method is considered to be the best method when working on charged periodic systems. The Ewald sum[12,13] was devised to overcome the problem that electrostatic interactions would not decay rapidly with distance (as a function of r^{-1}) when the distance becomes large.

In a system of *N* particles, with periodic boundary conditions that infinitely replicate a central cubic simulation box with a cell parameter *A*, the Coulomb energy can be computed using the formula:

$$U = \frac{1}{2}\sum_{n}{}' \sum_{i=1}^{N}\sum_{j=1}^{N} \frac{q_i q_j}{r_{ij,n}}$$

Equation 2-38

Where q_i, q_j are the charges. For simplicity, factors of $4\pi\epsilon_0$ have been omitted: this corresponds to adopting a non-SI unit of charge. The sum over n is the sum over all simple lattice cubic points, $n = (n_xL, n_yL, n_zL)$ with $n_x, n_y, n_z \in \mathbb{Z}$. The central cell being n (0,0,0) and its images being at nL distances from this central cell. The prime sign in the first sum indicates that terms with i = j are omitted when n = 0.

This sum is conditionally convergent, which means that the result depends on the order in which the terms are summed.

n(-1,1,0)	n(0,1,0)	n(1,1,0)
n(-1,0,0)	n(0,0,0) x y z	n(1,0,0)
n(-1,-1,0)	n(0,-1,0)	n(1,-1,0)

Figure 2-4 A 3×3×1 periodic array built from the central unit cell.

The Ewald sum[12,13] transforms equation 2-32 into a sum of two rapidly convergent series plus a constant.

$$U_{ewald} = U^r + U^m + U^0$$

Equation 2-39

U^r is the real space term of the sum, U^m is the reciprocal term of the sum and U^0 is a constant called the self-term or self energy correction.

In the Ewald sum,[12,13] each charge is considered to be surrounded by a spherical gaussian charge distribution, of the same magnitude but of different sign, centered on that charge. Thus neutralizing those charges. Then a second set of gaussian charge distributions but this time with the same sign and the same magnitude as the initial point charges and centered on these point charges is added in reciprocal space to nullify the addition of the first neutralizing set of gaussian charge distributions. The initial Coulombic interactions between point charges in the system are replaced by interactions between point charges and the neutralizing gaussian charge distributions. These new interactions are now short ranged therefore eliminating the problem of convergence. This forms the real space term of the sum:

$$U^r = \frac{1}{2}\sum_{i,j}^{N'}\sum_{n} q_i q_j \, erfc\frac{(\alpha r_{ij,n})}{r_{ij,n}}$$

Equation 2-40

Where α is an arbitrary parameter determining the width of the distribution.
erfc (x) is the complementary error function given by the formula:

$$erfc(x) = 1 - erf(x) = (\frac{2}{\sqrt{\pi}})\int_{x}^{\infty} \exp(-t^2)\,dt$$

Equation 2-41

erfc (x) decreases monotonically as *x* increases. *erf (x)* is the error function. Thus if α is chosen to be large enough, the only term contributing to the real space term of the sum is that with n = 0. The reciprocal term represents the interaction between the first neutralizing gaussian charge distribution and the second one and hence removes the contribution of the original screening.

$$U^{m}=\frac{1}{2\pi V}\sum_{i,j}^{N} q_i q_j \sum_{m\neq 0} \exp\frac{\left(-\left(\pi\frac{m}{\alpha}\right)^{2}+2\pi i\, m.(r_i-r_j)\right)}{m^{2}}$$

Equation 2-42

Where V is the volume of the simulation box and $m = (l, j, k)$ is a reciprocal space vector. The self term is a correction term which is used to address the fact that each gaussian charge distribution acts on itself.

$$U^{0}=\frac{-\alpha}{\sqrt{\pi}}\sum_{i=1}^{N} q_i^{2}$$

Equation 2-43

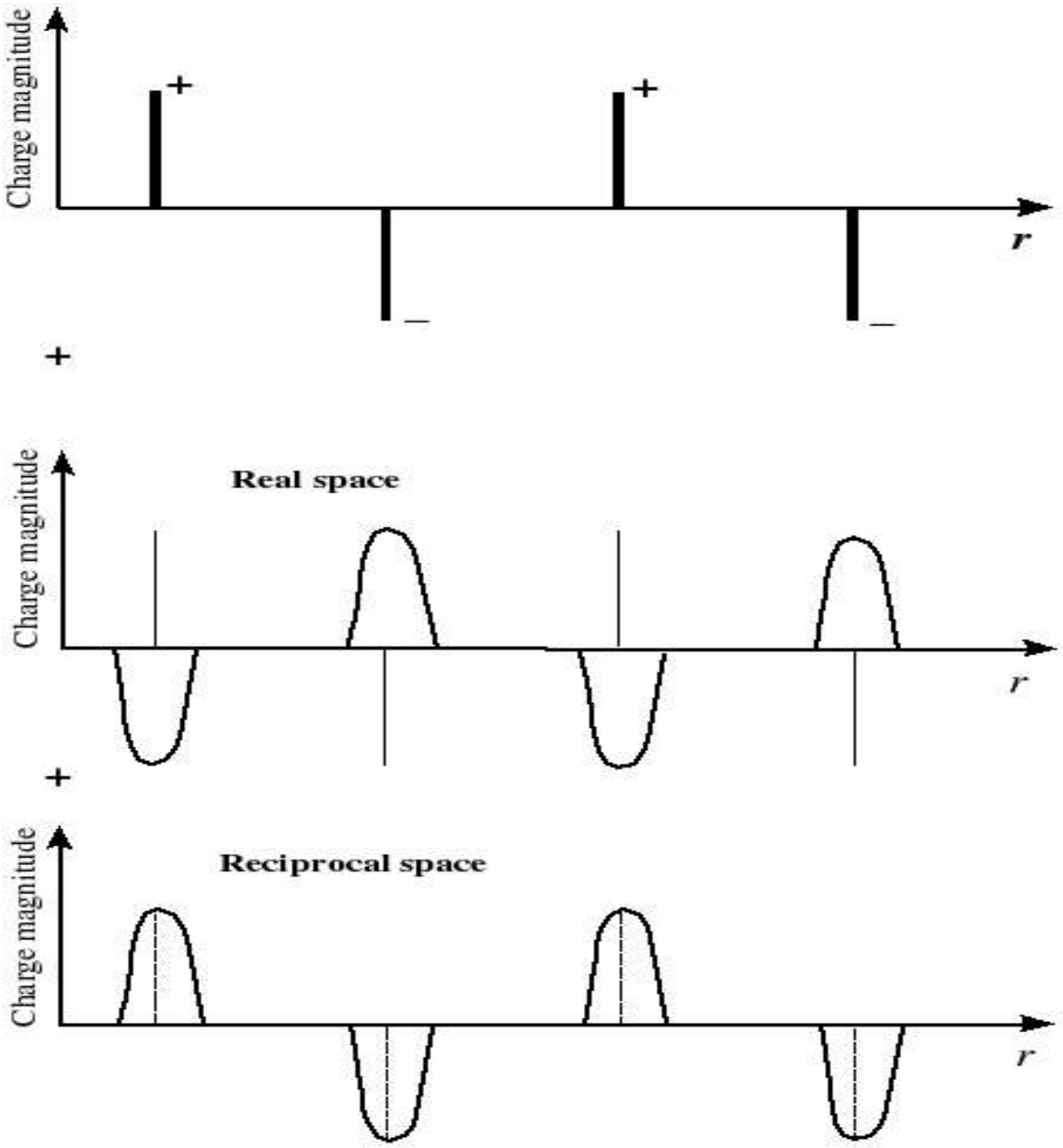

Figure 2-5 Schematic diagram of the charge distribution in the Ewald method. The initial set of charges are surrounded by a Gaussian distribution in real and reciprocal space.

2.5 Quantum mechanics

Quantum mechanics is a mathematical theory that can describe the behavior of microscopic particles (or, at least, of the measuring instruments we use to explore those behaviour). In that capacity, it is a particularly successful theory. It is the essential method for predicting the electronic

and nuclear distribution within a molecular system. It enables one to derive the properties responsible for the physical interactions between molecules: charges, dispersion coefficients etc. There are a number of methods for treating molecular systems in a quantum mechanical way. Some of these methods include Hartree Fock (HF), post Hartree Fock and Density Functional Theory (DFT) methods.

Every quantum particle is characterized by a wave function. Erwin Schrödinger developed the differential equation that describes the evolution of those wave functions. Equation 2-44 represents the time-independant Schrödinger equation.

$$\hat{H}\,\psi = E\,\psi$$

Equation 2-44

Where $\hat{H}$ is the Hamiltonian operator, which gives the observable corresponding to the total energy of the system. This total energy consists of the kinetic energy and the potential energy of the system. The Schrödinger equation can be solved analytically for some one electron systems, such as H-like atoms and H_2^+, but not for more complex systems. For systems with two or more electrons, numerical methods are used.

The variational principle, which states that the energy calculated from an approximation to the true wave function will always be greater than the true energy, can be used to generate approximate solutions of the Schrödinger equation for systems with two or more electrons. The significance of the variational principle is that you can choose a flexible description of the wave function (i.e. a basis set) and choose the best answer within the framework by minimizing the energy.

The HF theory was developed to solve the electronic Schrödinger equation that results from the time independent Schrödinger equation after invoking the Born-Oppenheimer approximation (which states that the motion of the electrons in a molecule can be described separately from the motion of the nuclei; this is based on the fact that the electrons are much lighter than the nuclei and therefore move a lot faster). The HF theory is the basis of molecular orbital theory (MO). In this theory, each electron's motion can be described by a single-particle function (orbital) which does

not depend explicitly on the instantaneous motion of the other electrons. The HF model is a self-consistent model because some initial orbitals have to be guessed and then refined iteratively. There are three main elements of the HF model: each electron moves in a central field equal to the nuclear potential due to the charge densities of the remaining atomic electrons; the Schrödinger equation is solved for each electron in its own central field, this results in wave functions that are self-consistent with the fields from which they are calculated; and the atomic wave function is a product of single-electron orthonormalised wavefunctions.

$$\psi_{HP}(r_1, r_2, \ldots, r_N) = \phi_1(r_1)\phi_2(r_2)\ldots\phi_N(r_N)$$

Equation 2-45

Equation 2-45 is known as the Hartree product.

The Fock operator is an effective one-electron energy operator. It describes the kinetic energy of an electron, the attraction to all the nuclei and the average repulsion from all the other electrons. It is associated with the variation in the total energy. Due to the fact that the variational principle applies to the Hartree-Fock equation, a better approximation to the wave function will always result in a lower energy. The Fock operator depends on all the occupied molecular orbitals (MO). If all the other orbitals are known, iterative methods can be used to determine the specific Fock orbital. Therefore, the HF method is also called the self-consistent field method.

The HF method makes five major approximations:

- The Born-Oppenheimer approximation. The full molecular wave function is a function of the coordinates of each of the nuclei, in addition to those of the electrons.
- Relativistic effects are completely neglected.
- The variational solution is assumed to be a linear combination of a finite number of basis functions, which are usually chosen to be orthogonal.
- Each energy eigenfunction is assumed to be describable by a single Slater determinant, an antisymmetrized product of one-electron wave functions.
- The mean field approximation (which basically consists of replacing all interactions to any one

body with an average or effective interaction) is implied. Effects arising from deviations from this assumption, known as electron correlation, are completely neglected.

Of these five approximations, the mean mean field approximation is typically the most important one. Indeed, neglecting electron correlation can lead to large deviations from experimental results. Therefore a number of methods, collectively called post-Hartree-Fock methods, have been devised to include electron correlation to the multi-electron wave function. The Møller-Plesset perturbation theory (MP) is one of these methods. This method treats correlation as a perturbation of the Fock operator. Since the Møller-Plesset theorem[14] states that the correlation potential does not contribute in first-order to the exact electronic energy, the lowest-order MP correlation energy appears in second order (MP2). Second (MP2), third (MP3), and forth (MP4) order Møller-Plesset are standard levels used in calculating small systems. Fifth order (MP5) Møller-Plesset is also possible but because of its cost, it is rarely used.

An alternative to the HF method is the Density-functional theory method (DFT). This method gives approximate solutions to both exchange and correlation energies. However, it is not a purely *ab initio* method in practice. In the DFT method, the many-body electronic wave function present in HF and post-HF theory is replaced by the electronic density as the basic quantity. A density functional method is uniquely identified by its exchange and correlation functionals. It is common to use calculations that are hybrid to the HF and DFT methods; the B3LYP scheme is one such hybrid density-functional method.

2.5.1 Basis sets

The basis set is the set of mathematical functions used to create the wave function. Generally, in a molecular system, the basis set is composed of a finite number of atomic orbitals, centered at each atomic nucleus within the molecule (a molecular orbital is generally represented as a linear combination of atomic orbitals). Two types of atomic orbitals are commonly used in electronic structure calculations. The first type of atomic orbitals to be used was the Slater Type Orbitals

(STO), which corresponds to a set of functions which decay exponentially with distance from the nuclei. Then S.F. Boys realized that these STOs could in turn be approximated as linear combinations of Gaussian Type Orbitals (GTO). The STOs are more precise but take longer to calculate while the GTOs are quick to evaluate in the electron integrals, but generally more GTOs are needed to achieve as good an approximation as the STO. A minimum basis set is typically composed of the minimum number of basis functions required to represent all of the electrons on each atom. In contrast, the "extended" basis sets are the ones that include additional orbitals that would not be occupied in the isolated atoms, but that would allow a better description of the polarization and bonding effects occurring in the molecule.

One way to extend a minimal basis set is to use the "Split-Valence Basis Sets" method. In this method, valence orbitals are represented by more than one basis function. Basis sets in which there are multiple basis functions corresponding to each valence atomic orbital, are called valence double, triple, or quadruple-zeta basis sets. The term zeta comes from the exponent of the two s-functions. This method allows the electron density to adjust its spatial extent appropriate to the particular molecular environment. Minimum basis sets in contrast are fixed and are unable to adjust to different molecular environments.

A notation for the split-valence basis sets introduced by the group of John Pople[15] is of the form *X-YZg,* where *X* represents the number of primitive Gaussians comprising each core atomic orbital basis function. Those are referred to as Primitive Gaussian Type Orbitals or PGTOs. The *Y* and *Z* indicate that the valence orbitals are composed of two basis functions each, the first one constituted of a linear combination of *Y* primitive Gaussian functions, the other constituted of a linear combination of *Z* primitive Gaussian functions. The presence of two numbers after the hyphens implies that this basis set is a split-valence double-zeta basis set, if it is three then the basis set is a split-valence triple-zeta basis set. The 6-311G basis set (which is a triple split valence basis, where the core orbitals are a contraction of 6 PGTOs and the valence are split into three, represented by 3 PGTOs for the inner part, 1 and 1 for the outer valence PGTOs) is a commonly used split-valence basis set.

Also, some of the most widely used Split-valence basis sets are the correlation consistent basis sets

developed by Dunning and coworkers. These basis sets are labeled cc-pVNZ where cc-p stands for correlation consistent polarized and N = D, T, Q, 5, 6, ... (D = Double, T = Triple, etc.). V indicates that they are valence only basis sets. Examples of these are cc-pVDZ (double-zeta), cc-pVTZ (triple-zeta), cc-pVQZ (quadruple-zeta) basis sets. To all these basis sets, diffuse and polarization functions can be added.

2.6 Analysis

2.6.1 Radial distribution functions

The radial distribution function is generally a pair correlation function (triplet and higher distribution function can also be defined) that gives the probability of finding a particle at a distance *r* from another particle.

Consider a spherical shell of thickness δr at a distance r from a chosen atom:

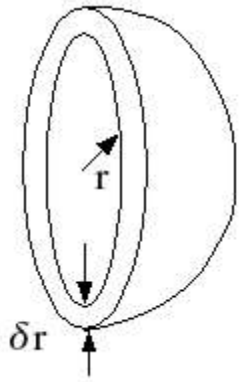

Figure 2-9 Schematic representation of a spherical shell of thickness δr at a distance r from a chosen atom.

The volume of the shell is given by

$$V = \frac{4}{3}\pi (r + \delta r)^3 - \frac{4}{3}\pi r^3$$

Equation 2-46

$$= 4\pi r^2 \delta r + 4\pi r \delta r^2 + \frac{4}{3}\pi \delta r^3$$

Equation 2-47

For very thin shells ($\delta r \rightarrow 0$) the terms δr^2 and δr^3 are negligible, therefore the volume becomes:

$$V = 4\pi r^2 \delta r$$

Equation 2-48

If ρ is the number of particles per unit volume, the total number of particles expected to be found in the shell is $4\pi\rho r^2 \delta r$, and the number of atoms in volume element varies as r^2. This is true for homogeneous systems, however in most cases the distribution of atoms is not homogeneous. In this case, the neighbors around each atoms are sorted into bins of width $\triangle r$, then the number of atoms in each bin is averaged over the entire time of the simulation.

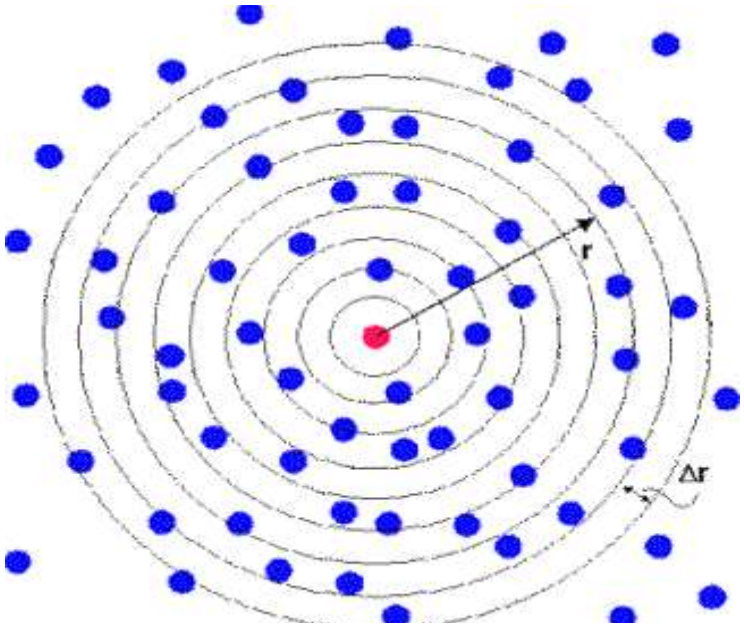

Figure 2-10 Schematic representation of bin distances of width $\triangle r$ in which atoms are stored at each time step for the computation of radial distribution functions

A typical plot of a radial distribution function in liquid is shown in the figure 2-11.

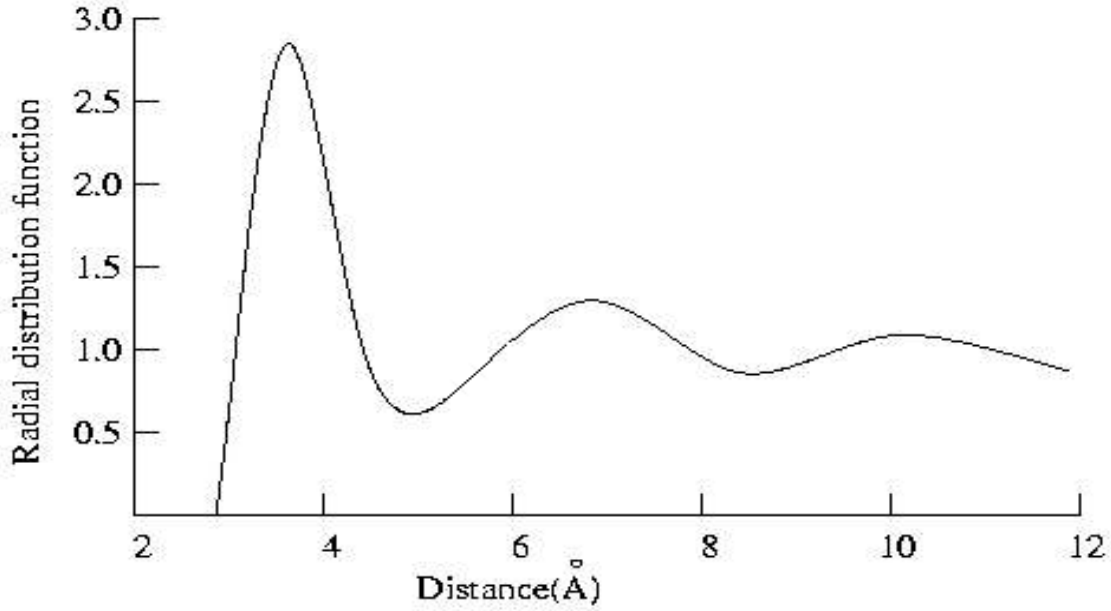

Figure 2-11 Plot of the radial distribution function against distance

At short distances, g(r) = 0. This is due to the strong repulsive forces that occur at short distances which prevents atoms getting too close to each other. At intermediate distances, there are a number of well defined peaks. The amplitude of these peaks define the probability of finding an atom at the given distances. At long distances, g(r) tends to one, this indicates that there is no long range order. Similar features are seen for crystalline solids but the peaks become much narrower and usually resolve into a set of completely resolved peaks at low temperatures.

In this study, RDFs have been extensively used to study how atoms are arranged in the complex framework and how they behave during the course of the simulations. RDFs have also been used to fit short ranged potential energy parameters. They have finally been used to see which solvent enantiomers get closer to the framework.

2.6.2 Mean square displacement

The mean square displacement represents a measure of the square of the vector distance, averaged over all time steps and all identical particles, traveled by a particle over the course of the simulation.

Einstein showed that the mean square displacement of a particle in a liquid grows linearly with time as shown in figure 2-12.

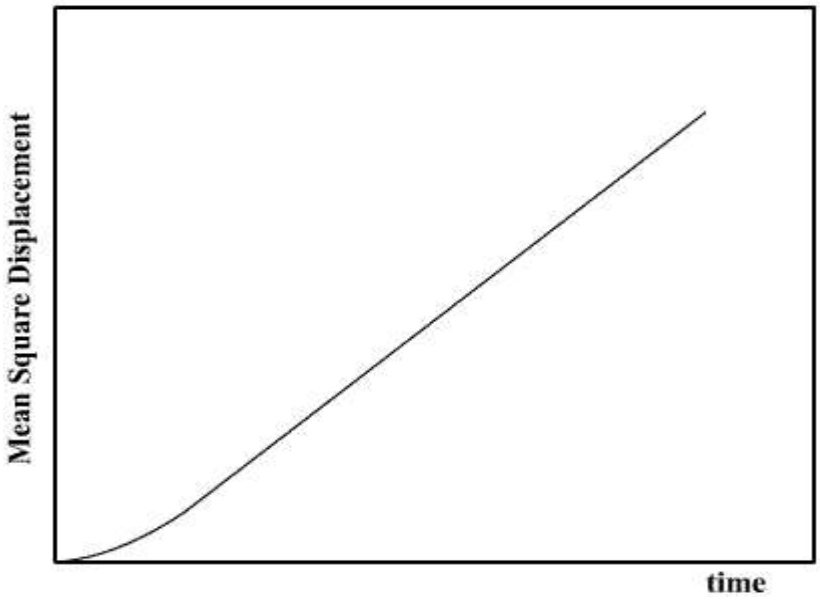

Figure 2-12 Typical plot of the mean square displacement against time in a liquid solution.

For a stable solid this quantity will stay stable over the course of the simulation.

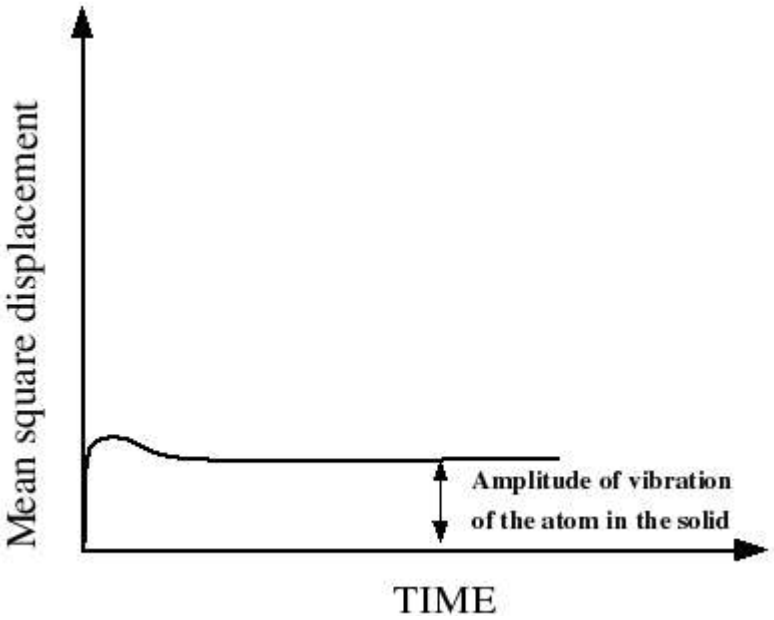

Figure 2-13 Typical plot of the mean square displacement against time in a solid crystal.

Figure 2-13 shows the evolution of the mean square displacement of an atom in a solid crystal. Generally, the amplitude of vibration of an atom in a solid crystal is is small (~ 10^{-1} $Å^2$).

2.6.3 Orientational distribution function

The orientational distribution function is a valuable analysis method since it gives informations about the three-dimensional structure (or composition) of the system studied. The orientational distribution function consists of giving the relative orientation of the molecules or groups of atoms in the system around a central molecule or group of atoms.

The orientational distribution functions in this thesis were obtained using a locally developed program called DL-NEW. This program determines orientational distribution function in the following way:

1. It defines groups of atoms (e.g. aromatic rings or pyridine molecules)
2. It identifies the principal axis, for each of the groups of atoms (or molecules) defined, from the moment of inertia
3. It transforms all other molecule positions to this central molecule fixed axis
4. It evaluates the orientation of the molecules relative to this central molecule
5. it averages the orientational distribution over all molecules

2.7 References

[1] M.P. Allen, D.J. Tildesley, Computer Simulation of Liquids. Oxford, UK: Oxford. Univ. Press, 25, 1987

[2] L. Verlet, *Phys. Rev*., 159, 1967, 98

[3] W. Smith, T.R. Forester, *J. Mol. Graphics*, 14, 1996, 136

[4] B. R. Brooks, R. E. Bruccoleri, B. D. Olafson, D. J. States, S. Swaminathan, M. Karplus, *CHARMM: A Program for Macromolecular Energy, Minimization, and Dynamics Calculations, J. Comp. Chem*. 4, 187-217 (1983); F. A. Momany, R. Rone, J. Comp. Chem. 13, (1992) 888; A. D. MacKerell, Jr., D. Bashford, M. Bellott, R. L. Dunbrack, Jr. J. D. Evanseck,M. J. Field, S. Fischer, J. Gao, H. Guo, S. Ha, D. Joseph-McCarthy, L. Kuchnir, K. Kuczera, F. T. K. Lau, C. Mattos, S.

Michnick, T. Ngo, D. T. Nguyen, B. Prodhom, W. E. Reiher, III, B. Roux, M. Schlenkrich, J.C. Smith, R. Stote, J. Straub, M. Watanabe, J. Wio´rkiewicz-Kuczera, D. Yin, M. Karplus, *J. Phys. Chem B* (1998) 102, 3586

[5] W. D.Cornell, P. Cieplak, C. I. Baily, I. R. Gould, K. M. Merz, Jr., D. C. Ferguson, T. Fox, J. W. Caldwell, and P. A. Kollman, *J. Am. Chem. Soc*. 117 (1995) 5179–5197; A. D.MacKerell, J. Wiorkiewicz-Kuczera, and M. Karplus. *J. Am. Chem. Soc*. 117 (1995) 11946–11975.

[6] N. L. Allinger, K. Chen, J.-H Lii, *J. Comput. Chem* 1996, 17, 642; N.Nevins,K, Chen, N. L. Allinger, *J. Comput. Chem* 1996,17, 669.

[7] J. R. Maple, M.-J. Hwang, K. J. Jalkanen, T. P. Stockfisch, A. T. Hagler. *J. Comput. Chem,* 19 (1998) 430-458; J. R. Maple, M.-J. Hwang, T. P. Stockfisch, U. Dinur, M. Waldman, C. S. Ewig, and A. T. Hagler, *J. Comput. Chem*,15 (1994) 162; M.-J. Hwang, T. P. Stockfisch, and A. T. Hagler, *J. Am. Chem. Soc*., 116 (1994) 2515

[8] S. Shi, L. Yan, Y. Yang, J. Fisher-Shaulsky, T. Thacher. *J. Comput. Chem*, 24 (No. 9) (2003) 1059

[9] A. Vedani, D. W. Huhta, *J. Am. Chem. Soc., 112 (1990) 4759-4767*

[10] B.J. Alder, T. E. Wainwright, *J. Chem. Phys*, 27, (1957), 1208-1209

[11] A. Rahman, *Correlations in the motion of atoms in liquid argon*, 136 (2A), (1964), A405-A411

[12] P. Ewald. *Ann. Phys*., 64, 1921, 25

[13] A. Y. Toukmaji, J. A. Board Jr, *Comp. Phys. Com* 95 (1996) 73-92

[14] C. Møller, M.S. Plesset, *Phys. Rev*, (1934) 46, 618-622

[15] J.S. Binkley, J.A. Pople and W.J. Hehre, *J. Am. Chem. Soc*., 102 (1980) 939; M.S. Gordon, J.S. Binkley, J.A. Pople, W.J. Pietro and W.J. Hehre, *J. Am. Chem. Soc*., 104 (1982) 2797; M.J. Frisch, J.A. Pople and J.S. Binkley, *J. Chem. Phys*. 80 (1984) 3265

3 Force field development and study of the helical metal-organic framework with 4,5-octanediol as its alcohol ligand.

Metal-organic framework materials (MOFs) are constituted by metal centres bridged by organic ligands to form 1D, 2D and 3D networks. In the metal-organic frameworks studied in this work the bridging ligands are carboxylated ligands, more specifically the 1,3,5-benzenetricarboxylate (BTC), also called trimesic acid. The first paper on metal-organic frameworks using BTC as bridging ligand was by Omar Yaghi et al.[1] In this chapter, simulations of a specific helical chiral metal-organic framework[2] consisting of octahedral Ni^{2+} metal centers bridged by BTC molecules have been performed.

This metal-organic framework consists of two interpenetrating three-dimensional three-connected (10,3)-a nets. The way to define the topology of the structure of this MOF is by specifying the three-dimensional nets on which this topology is based.[3] Nets are always described in terms of the number of members in their spheres or polygonal circuits[3] (see the simple example explained in figure 1-1 in chapter 1). For the metal-organic framework studied in this work, each of these polygonal circuits is consists of 10 members (points). Figure 3-1 shows a three connected net were a 10 membered polygonal circuit is outlined.

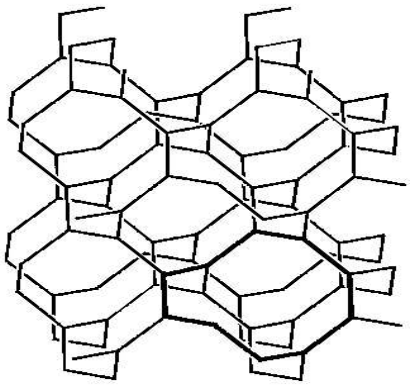

Figure 3-1 A three connected net where a 10-membered ring is outlined.[4]

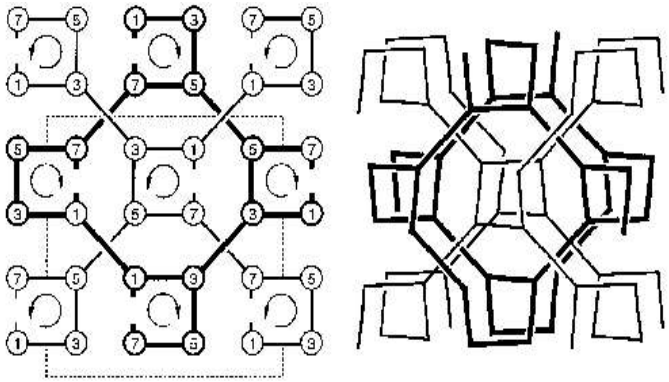

Figure 3-2 Left: intergrowth of two three connected nets of opposite hand. Right: the same in clinographic projection.[4]

The other features from which these nets are described is their level of connectedness. In this case the nets are three-connected (each point is connected to three other points). Since two of these nets interpenetrate to form the framework, the overall structure is describe as two interpenetrating (10,3)-nets. There are thirty known examples of uniform three-dimensional, three connected nets: one (12,3) net, seven (10,3) nets, three (9,3) nets, fifteen (8,3) nets and four (7,3) nets. The seven (10,3)-nets are differentiated using letters going from a to g.

This specific metal-organic framework studied in this work was selected because of its chirality resulting from the handedness of its helical structure. This material is also interesting because of its large void volume. This is of particular interest since one part of this research project involves the investigation of possible enantioselective properties that such a chiral framework can exert, an issue that is of particular interest for the pharmaceutical industry where there is a need to discriminate, select and store specific enantiomers. This is due to the fact that, often in biological systems, especially for reaction catalysis, only one enantiomeric form of a specific molecule is active[5]. It can also be the case that both enantiomeric forms are biologically active but that they have different effects (phthalidomide is the classical example of this). The reason why only the two interpenetrating (10,3)-a nets are studied and not the 4 interpenetrating ones (even though structures consisting of 4 interpenetrating nets are thermally more stable than structures consisting on two interpenetrating ones) is due to the fact that no chiral diols were stabilized bound to the metal in the four interpenetrating network, removing the possibility of chirally templating this more stable phase. Furthermore, the four interpenetrating network has a smaller void volume than the two interpenetrating one.

Molecular modeling could provide a great deal of useful information to aid in addressing these issues, but as explained in chapter 1, at present there is no suitable force field available to model the frameworks with even adequate realism. In this chapter we report the development of just such a force field. We begin (in chapter 3.4) by characterizing an existing force field (CHARMM22, extended to include Ni^{2+} using standard combining rules) and show that this is inadequate. We then proceed to describe the extensions to this force field that are needed to obtain a reasonable

description of the MOF structural properties. Since the benchmark for "adequacy" is the structure of the MOF, we begin in chapter 3.1 with a detailed description of that structure as revealed in crystal structures.

3.1 Description of the crystal structure of the helical MOF

The secondary building unit (SBU) of the metal-organic framework studied consists of an octahedral complex formed by the assembly of two BTC molecules (1,3,5-benzenetricarboxylate), two cis pyridine molecules and a 4,5-octanediol molecule coordinated to a nickel center. These SBUs are assembled together through nickel-oxygen bonds (one out of two oxygen of each carboxylic group of the BTC molecules is bound to a nickel atom) to form a 3-D structure. A representation of that SBU is shown in figure 3-3:

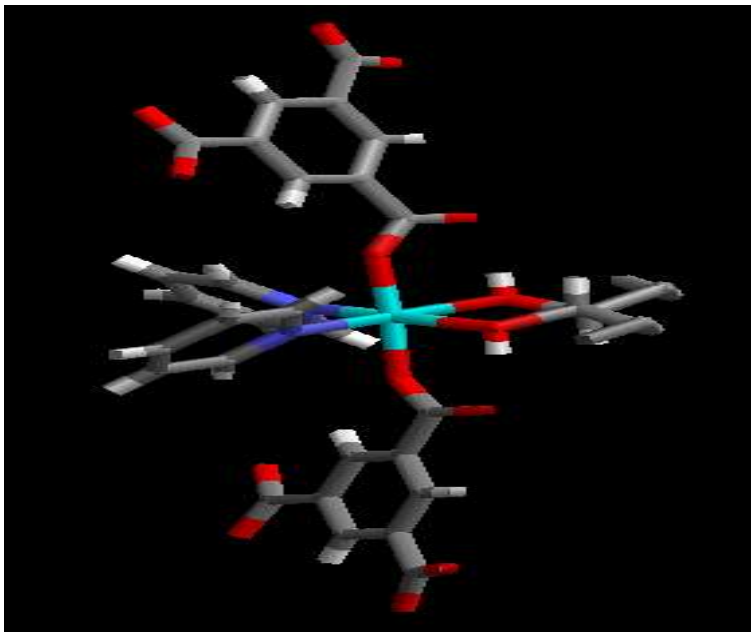

Figure 3-3 Representation of the secondary building unit of the MOF studied (green represents nickel atoms, red represents oxygen atoms, blue represents nitrogen atoms, white represents hydrogen atoms and grey represents carbon atoms).

The MOF resulting from the assembly of these secondary building units forms a 3-D network

constituted of 2 interpenetrating helices with a large proportion of void space (60%). This structure can be considered as 2 interpenetrated (10,3)-a networks. Figure 3-4 reveals the three-dimensional structure of the metal-organic framework studied.

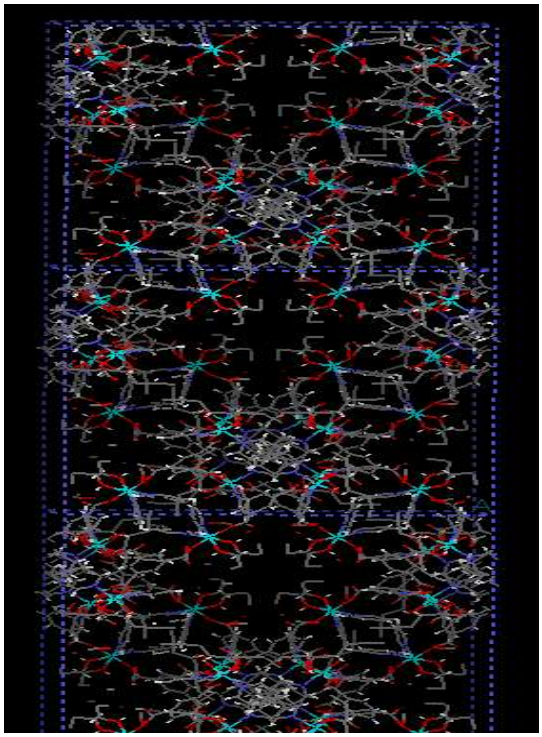

Figure 3-4 representation of the framework (see figure 3-3 for the colour-atom correspondence)

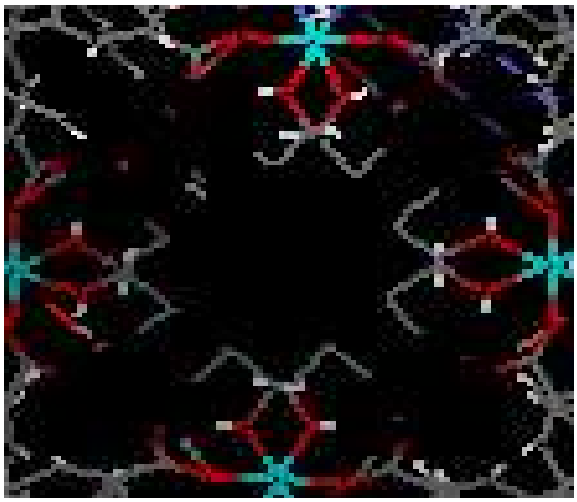

Figure 3-5 representation of a pore (see figure 3-3 for the colour-atom correspondence)

Showing an array of 1×1× 3 unit cells depicted in figure 3-4 it is observable that the framework has a helical structure. Indeed, this framework forms left handed helices (with the S version of the diol ligand bound to nickel centers). Between the two left handed helices represented in figure 3-4 there is a void volume which can be represented by square pores (as shown in figure 3-5) in which 4 alcohol molecules (distinguishable by the long carbon chains represented in gray) are observable. These pores are interconnected to each other to form three-dimensional channels. A visual impression of these channels is given in figures 3-6 and 3-7. In these figures, the structure of these channels are represented in blue. These figures have been obtained by using the free volume calculation tool available within the Cerius^2 software. This free volume calculation tool applies the

Connolly method[6] to calculate for example the 'accessible volume' of a system (V_{acc}, defined as the volume that a probe molecule of a given radius delineates as it is 'rolled over' the van der Waals surface of the framework atoms, and which can be reached from the outside of the crystal). This metal-organic framework has a void volume of 60% which is accessible upon careful removal of the pore solvent.

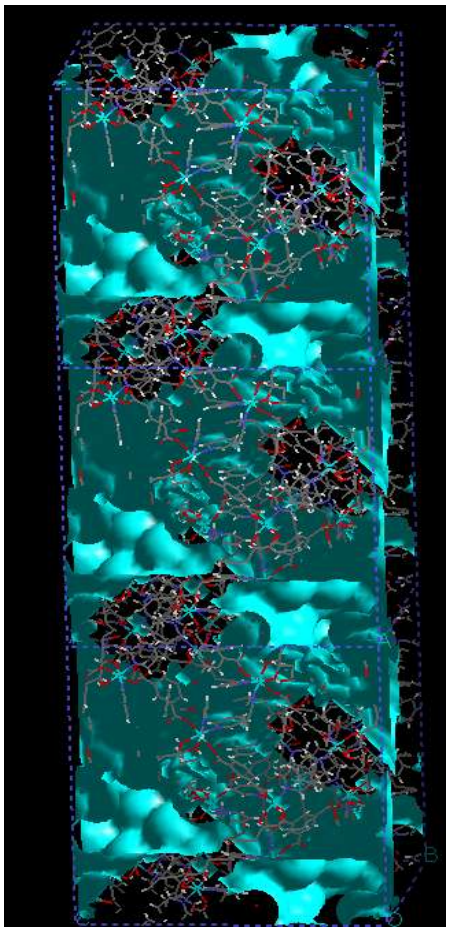

Figure 3-6 view along the y axis

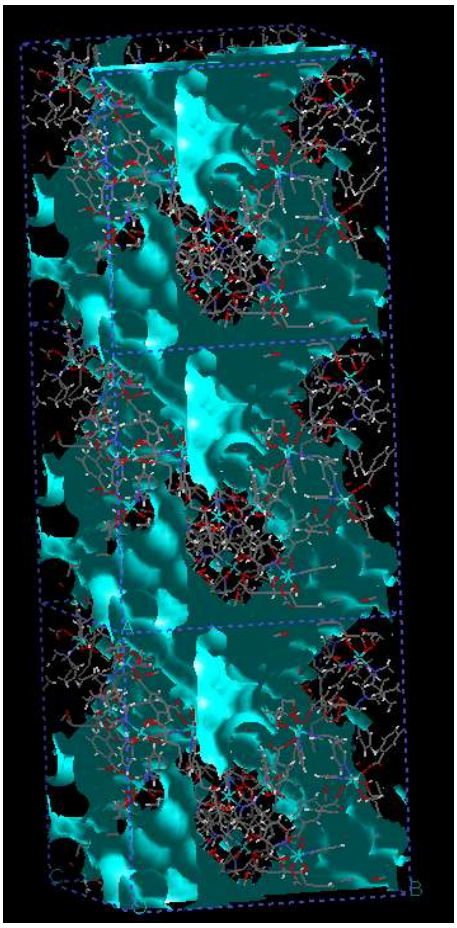

Figure 3-7 simultaneous view of 100 and 010 faces

The figures 3-6 and 3-7 show that the structures of the channels form a helical structure. Indeed it seems that the helices that constitute the framework are wrapped around the voids which also forms some kind of helical structure. It is therefore possible to say that both the MOF and the channels have 3-dimensional helical structures. It has been determined experimentally that, for this family of MOFs, the void volume is occupied by solvent molecules and that the framework collapses upon desolvation of the framework.

Each helix of this MOF consists of 2 strands. In each strand BTC molecules are arranged by pair with the plans of their rings being parallel and gauche to each other as shown in figure 3-8.

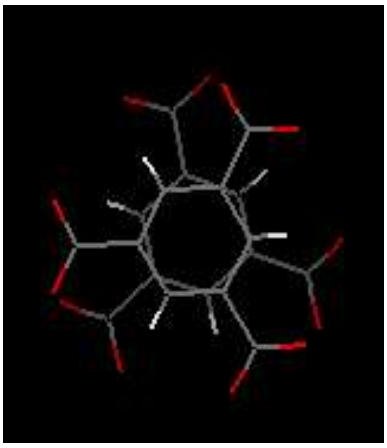

Figure 3-8 two BTC molecules, of two different helices, parallel to each other (see figure 3-3 for the colour-atom correspondence)

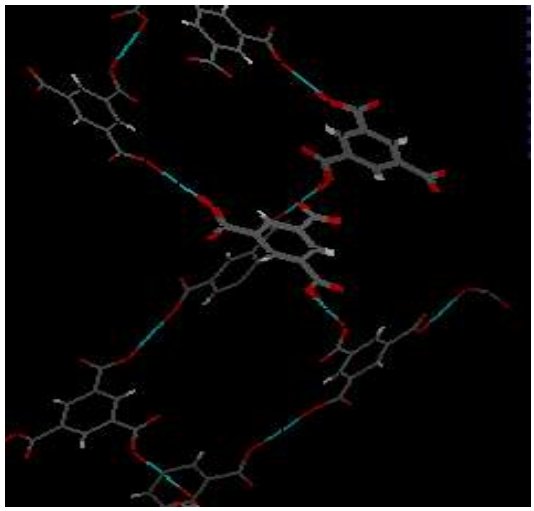

Figure 3-9 representation of the helices of a channel. Two parallel BTC rings are represented shaded (see figure 3-3 for the colour-atom correspondence)

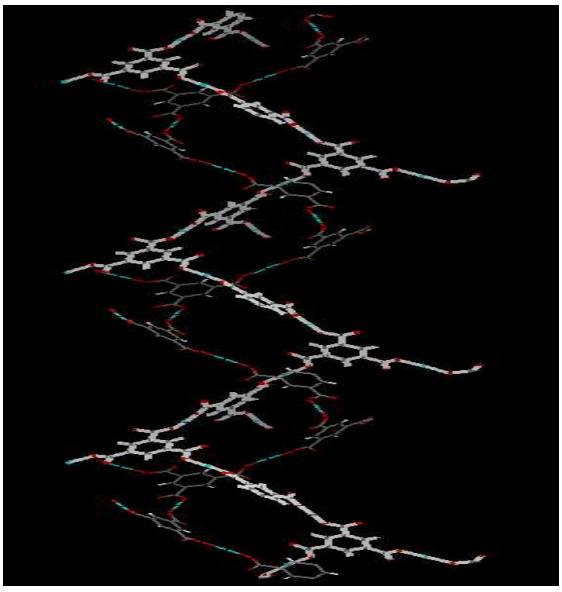

Figure 3-10 representation of the two interpenetratimg helices forming a DNA like structure (see figure 3-3 for the colour-atom correspondence)

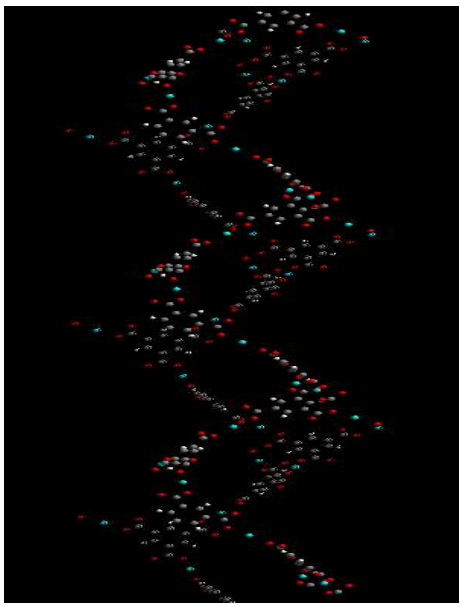

Figure 3-11 Polyhedra representation of the two interpenetrating helices

Figure 3-8 presents the two BTC molecules, of a helix, parallel to each other presented in figure 3-9

(as shaded BTC molecules). In figure 3-8 the view is taken through an axis going through the center of the aromatic BTC rings. The distance between the 2 parallel BTC molecules of a helix, presented in figure 3-8 is 7.9 Å. This means that the helix is about 7.9 Å wide (diameter of the helix). The BTC is not completely planar, with the angle between the aromatic ring and the carboxylic groups being about 10º (9.9º).

Figure 3-10, and especially figure 3-11, show the helical structure of this metal-organic framework. To better see the 3D structure of these helices, one should combine figure 3-10 and 3-11 with figures 3-6 and 3-7.

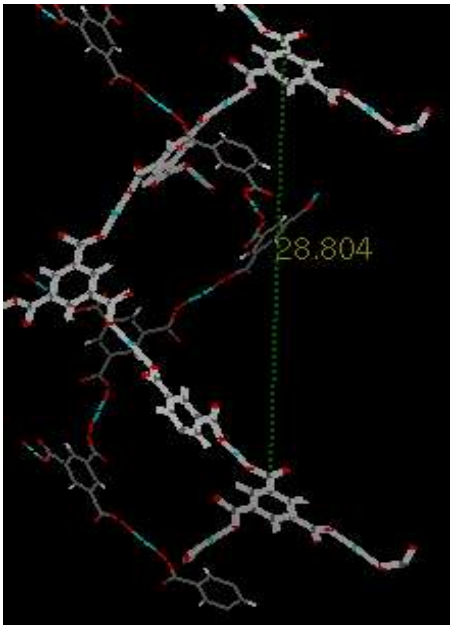

Figure 3-12 Representation of one helical turn (see figure 3-3 for the colour-atom correspondence)

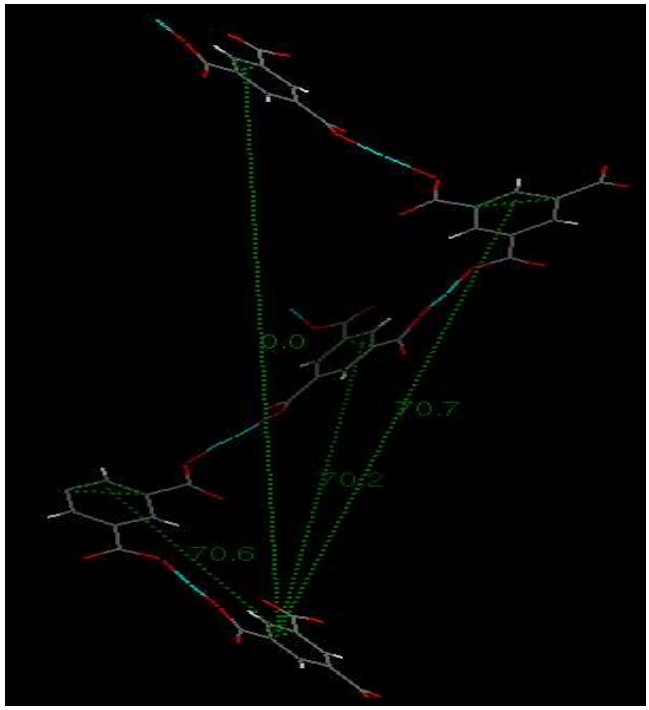

Figure 3-13 Representation of the angles between the ring plans of BTC molecules (see figure 3-3 for the colour-atom correspondence)

Figure 3-12 represents the helical turn of this metal-organic framework. This helical turn is composed of 5 BTC molecules and 4 nickel atoms. Therefore each helical turn is constituted of 4 secondary building units. The height of the helical turn is 28.804 Å. Figure 3-13 shows the angles between the aromatic benzene rings of the BTC molecules in one helical turn. This shows how the BTC molecules "rotate" through a single helical turn. It is observable that the angle between two adjacent BTC rings is roughly equal to 70º.

Because of the fact that BTC molecules are the organic linker molecules that link the metal centers to form the backbone of the three-dimensional structure of the MOF (in this case a helical structure), the orientation of these BTC molecules relative to each other is a key structure determining factor which will be monitored by the determination of the orientational distribution function during this study. The structure and configuration of these organic linker molecules are, together with the electronic structure of the metal center, the main factors that will determine the overall three-dimensional structure of the resulting framework.

Figure 3-14 represents the three connected 10-membered polygonal circuit that forms a (10,3)-a net. Figure 3-15 shows the extended structure of the MOF studied, using different presentation styles for each net.

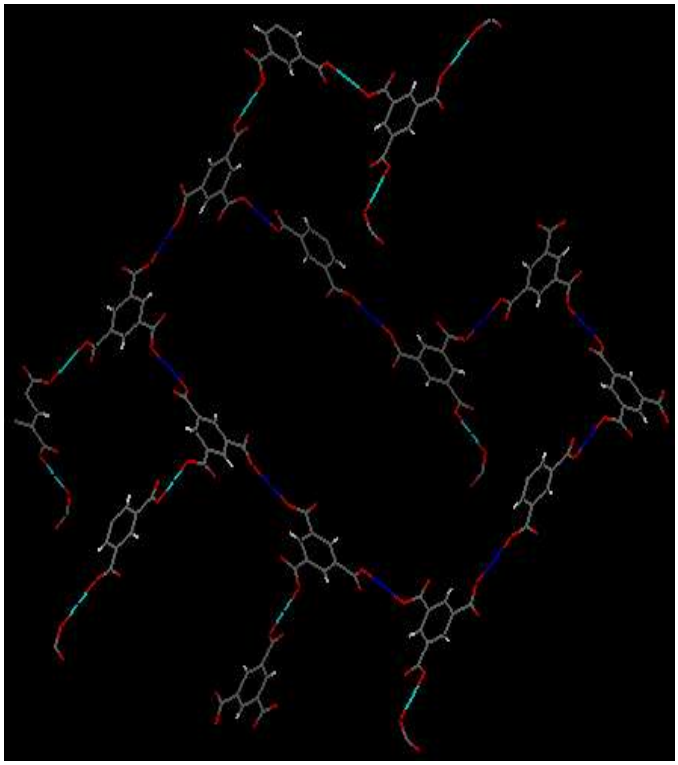

Figure 3-14 Representation of the 1×(10,3)-a nets of the MOF studied. In the 10-membered ring, nickel atoms are displayed in blue to make the polygonal circuit more obvious. Only nickel metal centers and BTC organic linkers are represented (see figure 3-3 for the colour-atom correspondence)

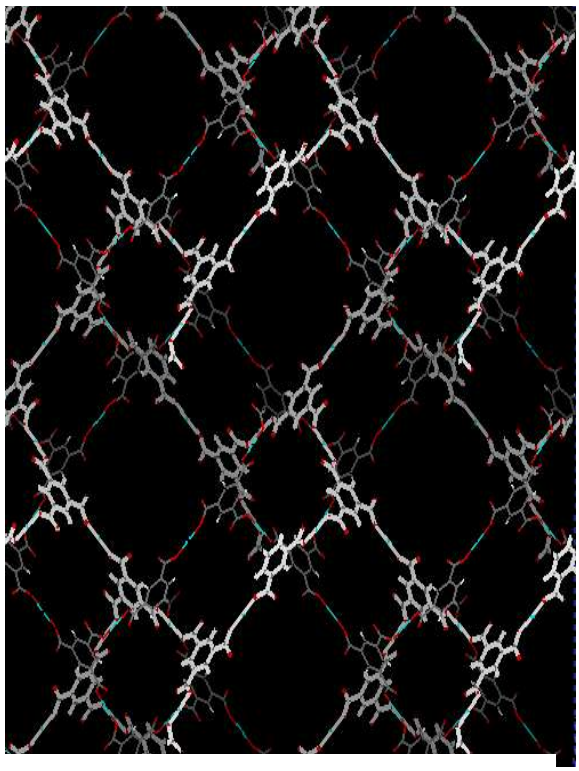

Figure 3-15 Representation of the two (10,3)-a nets of the MOF studied. Only the nickel metal centers and BTC organic linkers are represented. In one of the nets the bonds are represented by sticks while in the other net they are represented by ellipsoids (see figure 3-3 for the colour-atom correspondence)

3.2 Overview

The crystallographic structure in figure 3-4 determined using synchrotron crystallography was obtained from the analysis of a material which was synthesized using 1,2,6-hexanetriol as the alcohol ligand. Experimentally, it was not possible to determine the side 4-hydroxybutyl group using synchrotron crystallography because of the fact that this group is highly mobile. It was not possible to determine in particular the hydroxyl group of this 4-hydroxybutyl chain. Also, it was not possible to determine at which side of the diol group (bound to the nickel atom) this 4-hydroxybutyl chain was placed. Because of all these issues the experimentalists decided to consider, instead of this unobservable 4-hydroxybutyl chain, two well determined propyl groups at each side of the diol group bound to the nickel atom.

This modification is not expected to be of major importance since, as we have described in chapter 1, the main structure determining factors for metal-organic frameworks are the electronic structure of the metal atoms and the nature and configuration of the organic linker which is in this case a BTC molecule. As for the alcohol molecule, the most important group is the diol group, which binds to nickel ions. This group is really the main structural feature of the alcohol ligand. However, the length of the carbon chain have an effect on the degree of interpenetrability of the (10,3)-a nets in the sense that the length of this carbon chain will determine if the resulting metal-organic framework will consist of four or two interpenetrating (10,3)-a nets. Indeed, metal-organic frameworks with alcohol ligands consisting of diol molecules with a carbon chain of three or less carbon atoms have a structure consisting of the interpenetration of four (10,3)-a nets. This is the case when the alcohol ligands are 1,2-propanediol and ethylene glycol molecules. However, when this carbon chain is longer, the resulting metal-organic framework will consist of only two interpenetrating (10,3)-a nets, resulting in higher void volume. This is true, however, only for diol molecules for which the hydroxyl groups are adjacent leading to a OH-CH_2-CH_2-OH group. For diol molecules in which the hydroxyl groups are not adjacent, the binding to the nickel will be monodentate rather than bidentate. This is well exemplified by the metal-organic framework with

1,4-butanediol as its alcohol ligands since these ligands bind in a monodentate rather that bidentate way to the nickel atoms.

Structures consisting of the assembly of nickel atoms, pyridine molecules, BTC molecules and alcohol molecules with two adjacent hydroxyl groups (bound to two adjacent carbon atoms) and a carbon chain greater than three carbon atoms will lead to similar metal-organic frameworks consisting of the interpenetration of two (10,3)-a nets. This has been verified by looking at, and comparing the available structures of metal-organic frameworks that we found in the Cambridge Structural Database (this has been performed by comparing their cell parameters and by superposing these structures on top of each other to see if the structure and atomic positions of these frameworks coincided). This is well shown by Figure 3-16 which presents a visual superposition of two metal-organic frameworks. One of these metal-organic frameworks was synthesized using 1,2,6-hexanetriol and the other was synthesized using 2,3-butanediol as alcohol component. It is very clear from figure 3-16 that even though these two frameworks have different alcohol ligands their three-dimensional framework structure are very similar. Atomic positions of the two frameworks are nearly identical and the two structures are barely distinguishable from each other. Even the cell parameters of the two cubic cells are similar: 28.804 Å for the hexanetriol compared with 28.4 Å for the 2,3-butanediol MOF, a difference of only 1.5 percent.

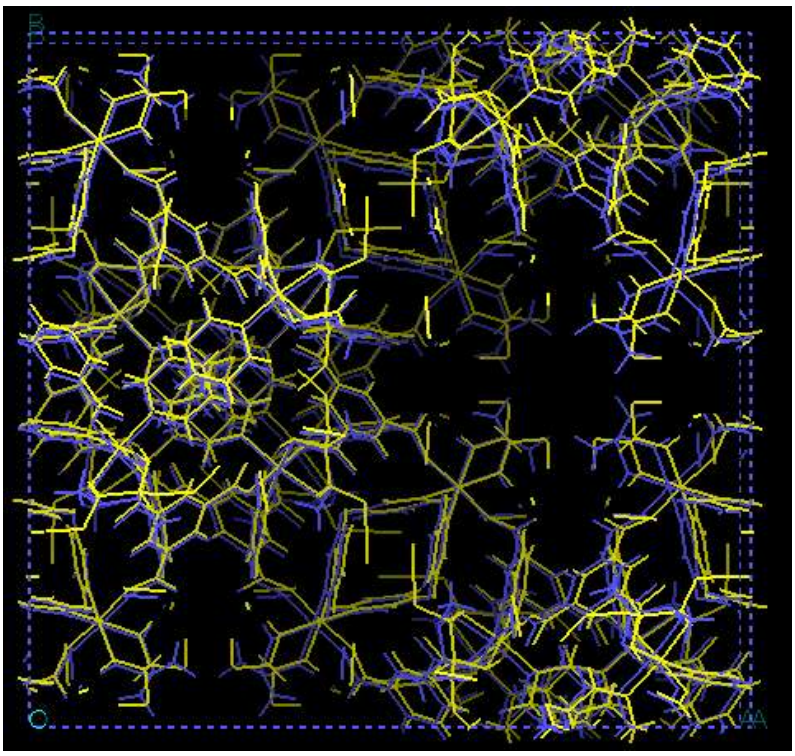

Figure 3-16 Representation of the superposition of two metal-organic frameworks, one containing 4,5-octanediol as its alcohol ligand (represented in yellow) and the other containing 2,3-butanediol as its alcohol ligand (represented in blue).

Therefore, we consider that we can work with 4,5-octanediol to remove uncertainty of disorder (with 1,2,6-hexanetriol, the alcohol binds to the Ni^{2+} via the 1,2-diol but there is two-fold disorder in the attachment site for the rest of the alcohol) and not expect major structural changes to result.

The main purpose of this chapter is to describe the development of a force-field that is capable of describing the structural and dynamical properties of helical MOFs. A hierarchy of force fields, ranging from the CHARMM22 force field which was used as a benchmark and improved force fields through fitting of the van der Waals parameters and quantum mechanical calculations to determine the partial charges on the atoms of the framework were used. The validity of each force field was assessed empirically by comparing cell parameters, cell volume, and bond lengths within the framework, after simulations with similar data obtained experimentally. There is no report of an experimental determination of the solvent content of this material. Therefore solvent content has been determined within this study theoretically. This has been done by running a number of

simulations differing from each other only by the number of solvent molecules inserted in the system. The appropriate solvation content as been determined as the minimum number of solvent molecules that would lead to a stable framework with volume comparable to experiment at low temperature (200 K). A series of simulations at different temperatures has then been performed. This temperature effect study has been done at different solvent contents of the material and for each solvent content the temperature at which the framework degrades has been determined. From the stable CHARMM22 force field empirical fitting of van der Waals parameters have been performed by systematically comparing cell volume, cell parameters and radial distribution functions with experimental data. Indeed, the CHARMM22 force field does not have very accurate parameters for metal-organic interactions. This force field has been developed to deal with purely organic systems, mainly biological systems and is not really well suited for systems containing transition metals. Therefore emphasis was placed on fitting Ni-X parameters (X = oxygen or nitrogen atoms). Then quantum mechanical calculations using different methods, functionals and basis sets were performed on each organic ligand to determine atomic partial charges that better reproduce experimental data. Quantum mechanical calculations were attempted on a secondary building unit to include polarization effects in the determination of partial charges, but unfortunately it was not possible to obtain convergence of SCF cycles, and therefore partial charges, in this case. The fact that quantum mechanical calculations have been performed on ligands rather than on the secondary building unit (which is described in figure 3-3) implies that polarization effects are not taken into consideration in the force fields developed in this work. Therefore, this study also gives an indication of how well pair potentials can reproduce experimental data for MOFs.

3.3 Simulation details.

Molecular Dynamic simulations were performed on a single unit cell with periodic boundary conditions invoked to mimic the infinite crystal. A typical simulation cell was a 28.804 Å cube and

contained 1456 atoms (for the system containing 20 solvent molecules). The atomic coordinates, determined by synchrotron crystallography[2], of this structure has been taken from the Cambridge structural Database (CSD). The Metal-Organic framework was initially modeled using the CHARMM22 all atom force field. The Molecular Dynamics simulation package used to perform these simulations is DLPOLY2. The conversion from CHARMM to DLPOLY force field formats was achieved using a purpose built program which converted the CHARMM psf, prm and crd files into a DLPOLY readable FIELD and CONFIG files (details are given in the appendix). The .crd files specify atomic coordinates while .psf files specify the atom names, types, bonds and partial charges. The .prm files however, provided a mapping between bonded and non bonded interactions involving the various combinations of atom types found in the .psf files; they also provided specific spring constants and similar parameters for all the bond, angle, dihedral, improper and van der Waals terms. Nickel ions were assigned a charge of +2*e*. For the first benchmark force field, the partial charges on the other atoms of the MOF were assigned according to the CHARMM22 force field. To ensure overall neutrality, the positive charges of nickel atoms were compensated by negatively charged BTC molecules. The +2*e* charge of each nickel atom was balanced by a -3*e* charge on each BTC molecule thus making the overall system neutral (In the unit cell, the 24 nickel atoms, each with a +2*e* charge, are neutralized by the 16 BTC molecules each with a -3*e* charge). The partial charges on pyridine and alcohol molecules were smoothed to give an overall charge of zero for each of these molecules. Simulations were performed in both *NPT* and *NST* ensembles using the Hoover thermostat and barostat.

For some force fields, the initial system had a very high configurational energy and so a relaxation stage was introduced which used very small time steps (varying from 10^{-3}fs to 1 fs) prior to the production phase. Successive equilibration phases with the time step increased after each phase were performed. The length of these equilibration phases depended on the time it took for the configurational energy of the system to stabilize. For the solvated systems, a locally developed program called SOLVADD was used for the inclusion of solvent molecules in the framework. In this program a tolerance parameter had to be chosen for σ parameters between the atoms of the

solvent molecules and the atoms of the framework. Because of the fact that the solvent molecules are long octanediol molecules, it was necessary to use small tolerances for σ parameters ($\sigma < 1$) to get a significant number of solvent molecules inside the framework. This results in significant overlap of solvent and solute atoms and so can give high configurational energies for the initial system. This was rectified using small time steps initially (10^{-3}–1 fs) and freezing the framework while the solvent relaxed.

After the equilibration phases a time step of 1 fs was used for the production phase. The EWALD summation method was used for the calculation of long ranged electrostatic interactions. The mass of the hydrogen atoms were set to 2 *u* instead of 1 *u*. This has been done in order to decrease the frequency of the hydrogen bond vibrations and thereby get a better energy conservation with a larger time step. United atom models were used to describe the methyl and ethyl groups of the diol ligand. A Van der Waals cut off distance of 10 Å was used. Simulations were performed at a pressure of 0.1 kbar. To increase the probability that the structure was in its most stable configuration, 1.5 ns simulations at a temperature of 10 K and a pressure of 0.1 kbar were performed before studying the temperature effects on the structure.

3.4 Results of simulations.

3.4.1 Simulations performed using the benchmark **CHARMM22** *force field*

The point of this section is to see if the benchmark CHARMM22 force field is good enough. We present results of a series of simulations of our MOF using the CHARMM22 force-field. This is an established force field for organics and is expected to give a good description of the BTC, pyridine and alcohols, but has not been developed with metallic ions in mind. It is therefore of interest to know how well such a force-field can describe the intimate mixture organic-inorganic interactions found in this MOF even for a relatively simple transition metal ions like Ni(II). To test this we have

performed a series of simulations at temperatures ranging from 10 K- 600 K. Variations in solvent content were also considered by inserting *n* solvent molecules (4,5-octanediol) into the framework pore space, with *n* varying from 6 to 52.

Results have been analyzed by calculating various radial distribution functions, mean square displacements, configurational energy and orientational correlations to supplement the crystal unit cell properties.

3.4.1.1 Study of the influence of temperature on the framework stability

Figure 3-16 presents the evolution of the cell volume with time for a system containing 28 solvent molecules. These simulations were performed for 500 ps in the *NPT* ensemble at 0.1 kbar and at respectively 10 K and 600 K. We have chosen to present data for the solvent content of 28 solvent molecules because this solvent content proved to stabilize the framework at temperatures above or equal to 250 K (see chapter 3.4.1.1). Indeed, as it will be shown subsequently in this study, a certain number of solvent molecules needs to be inserted into the system to efficiently stabilize the framework at temperatures above or equal to 250 K.

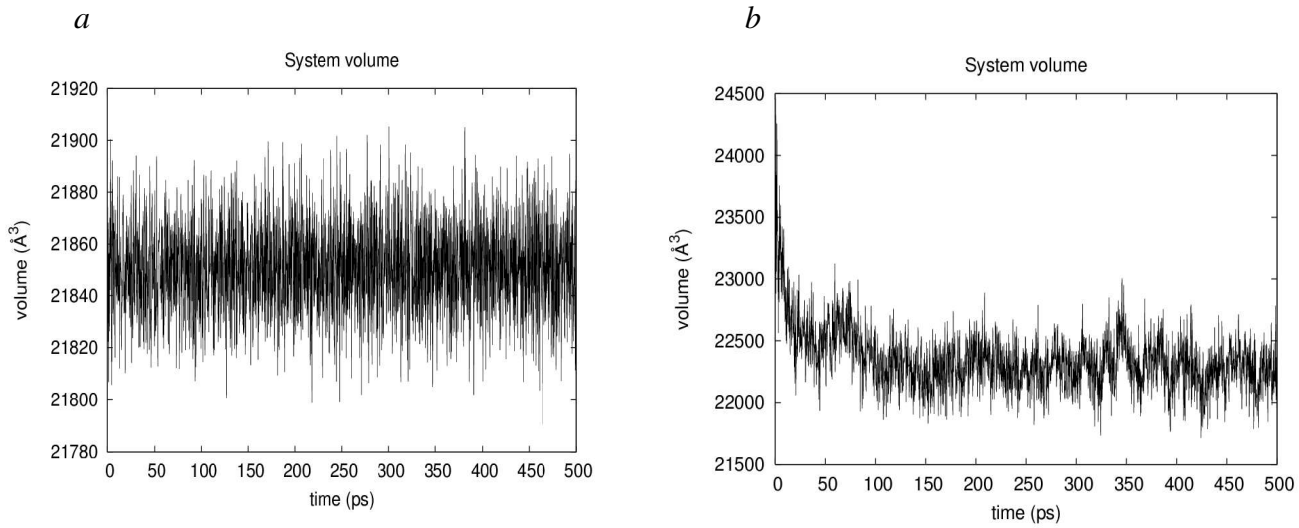

Figure 3-17 Evolution of the cell volume with time for a system containing 28 solvent molecules in the *NPT* ensemble at 0.1 Kbar and a) 10 K (left graph) and b) 600 K (right graph)

It is clear from figure 3-17 that at both temperatures, the 500 ps simulation is long enough to reach an equilibrium state with constant volume. In the figure Figure 3-17b, during the first 0.4 ps of simulation, the cell volume goes from 21860 $Å^3$ to 24463 $Å^3$. Then the cell volume goes from 24463 $Å^3$ after 0.4 ps of simulation to 22306 $Å^3$ after 100 ps of simulation where it stabilizes. Another observation that can be made from figure 3-17 is that the average cell volume of 21850 $Å^3$ obtained at 10 K is significantly lower than the average cell volume obtained at 600 K which is 22352 $Å^3$. This is consistent with thermal expansion. It has also been observed in this study that the cell parameter of the MOF stays stable and has values approaching the value of the cell parameter of the original crystal structure (structure before simulation) for all temperatures ranging from 10 K to 600 K. Indeed, the highest difference between the simulated cell parameters and the cell parameter of the original crystal structure has been found to be around 4 %. This suggests that at this range of temperatures, the framework stays stable and does not experience any phase change during the course of the simulations.

To verify this suggestion, radial distribution functions (RDFs) for key atom pairs have been calculated. The framework contains 12 different atom types, which gives a total of 78 different pairs of atoms. It is not practicable to study all of these, and indeed it is not even desirable: not all of

them are important probes of the MOF structure. We have therefore focussed on the ones that include the nickel ions, the different types of oxygen atoms and the nitrogen atoms. Those RDFs are MNI-MNI, MNI-OC, MNI-N6R, MNI-OT, N6R-OC and OC-OT (MNI = Nickel ions, OC = Oxygen atoms of BTC molecules, OT = Oxygen atoms of alcohol molecules and N6R = Nitrogen atoms of pyridine molecules).

These radial distribution functions have been studied for a system containing 28 solvent molecules at different temperatures. A selected functions are plotted in figure 3-18. Using these radial distribution functions, attempt has been made to understand what are the interactions that stabilize this framework.

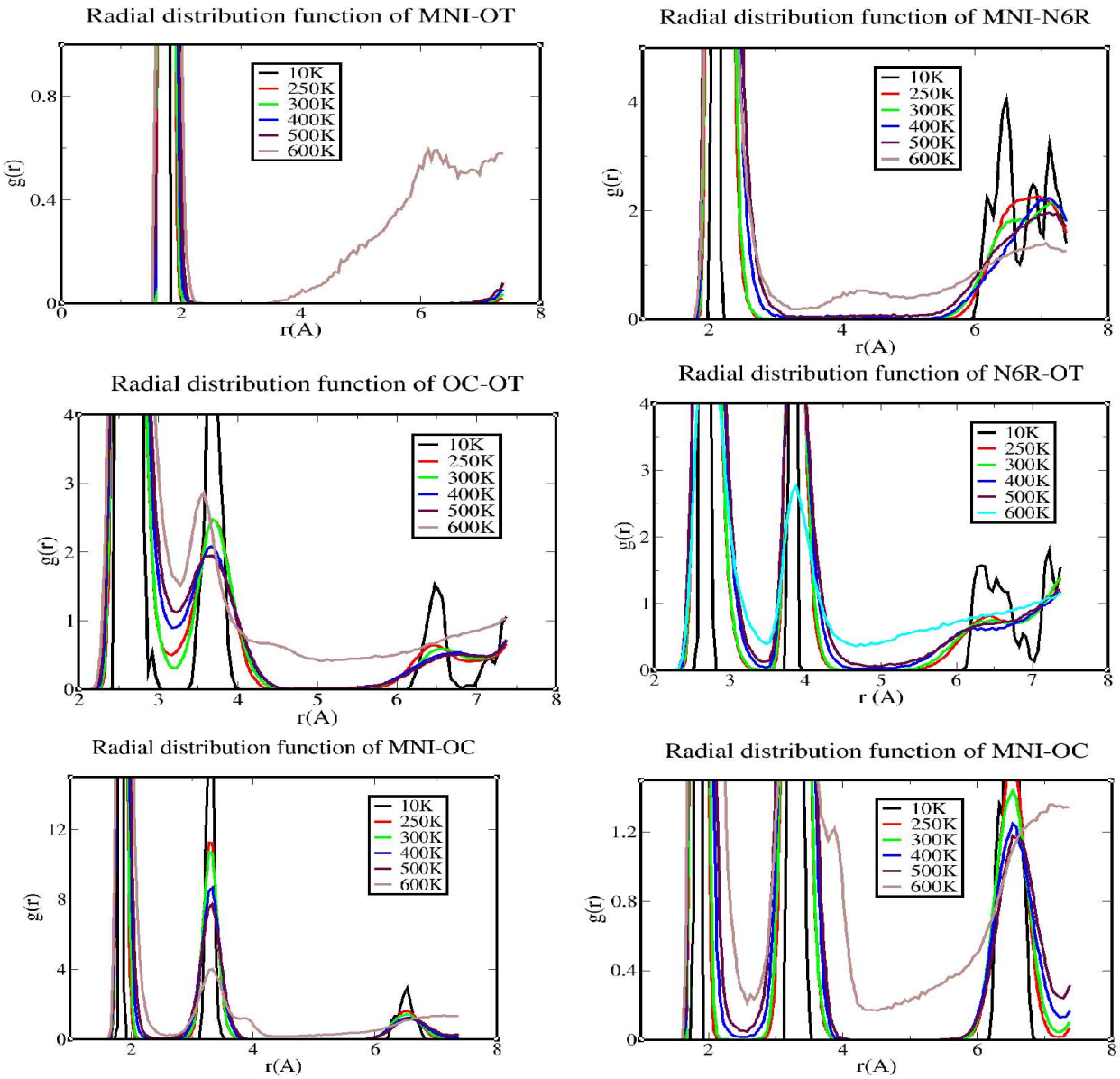

Figure 3-18 Radial distribution functions obtained after 500 ps of simulation in the NPT ensemble for a system containing 28 solvent molecules at different temperatures using the CHARMM22 force field.

It is observable from figure 3-18 that nickel-oxygen and nickel-nitrogen bonds remain unbroken at temperatures ranging from 10 K to 500 K. Indeed, it is observable from the Ni-OC, Ni-OT and Ni-N RDFs that the first peak of these RDFs is still present and well defined at this range of temperatures. This means that between 10 K and 500 K, the $NiBTC_2pyr_2alc$ secondary building units retain their integrity and that the nickel metal center stays bound to the BTC, pyridine and alcohol molecules. This is corroborated by the N-OT and OC-OT RDFs which represent RDFs between atoms of different ligand molecules in the Ni^{2+} coordination shell. Indeed, in these RDFs it

is observable that the first two peaks of each RDF is still present at all temperatures up to 500 K, confirms that the secondary building unit does not fragment at these temperatures. However, for the 600 K RDF, in the case of Ni-N and Ni-OC it is observable from figure 3-18 that the void between the first and second peaks vanishes, so that the value of g(r) is always higher than zero in this region. This shows that the range of Ni-OC and Ni-N distances varies continuously during the course of the simulation. This suggests that the Ni-OC and Ni-N bonds break at this highest temperature. It is also observable from figure 3-18 that for longer range RDFs, the 600 K RDFs show significantly different trends than the RDFs obtained at lower temperatures. For example, in the case of Ni-OT, for temperatures up to 500 K, only one peak is observable while at 600 K a very large second peak appears at 6.2 Å with the non-zero density starting at 3.8 Å. This shows a significant change in the long range distribution of Ni-OT distances. This significant change at long distances is also observable in the case of Ni-N RDFs: while no peak is observable between around 3 Å and 5.8 Å and that the values of g(r) in this range are roughly equal to zero for temperatures up to 500 K, at 600 K the RDF shows a peak centered at around 4.2 Å and the value of g(r) after the first peak always stays higher than zero. Similar observations and conclusions can be made from the Ni-OC, N-OT and OC-OT RDFs. In these RDFs, while for the temperatures up to 500 K, three peaks are observable, at 600 K the RDF shows only two peaks at short distances and a very different structure at longer distances. This difference in long ranged interatomic distances suggests an alteration in the three-dimensional structure of the MOF. Indeed, the main conclusion that is suggested by these RDFs is that the MOF containing 28 solvent molecules stays stable at temperatures up to 500 K but undergoes some sort of structural change at 600 K. It can also be observed from the Ni-N RDF that at 400 K and 500 K there does seem to be some bond breaking events (seen in $g(r) \neq 0$ for r between 2–6 Å) although this seems to be very limited and does not lead to structural change of the framework.

Another important observation that can be made from these RDFs is that the peaks are very broad, indicating that the amplitude of Ni-X bond vibrations is close to 1 Å. This is clearly too large and is one of the incentives for the refinement of this CHARMM22 force field described in section 3.4.2.

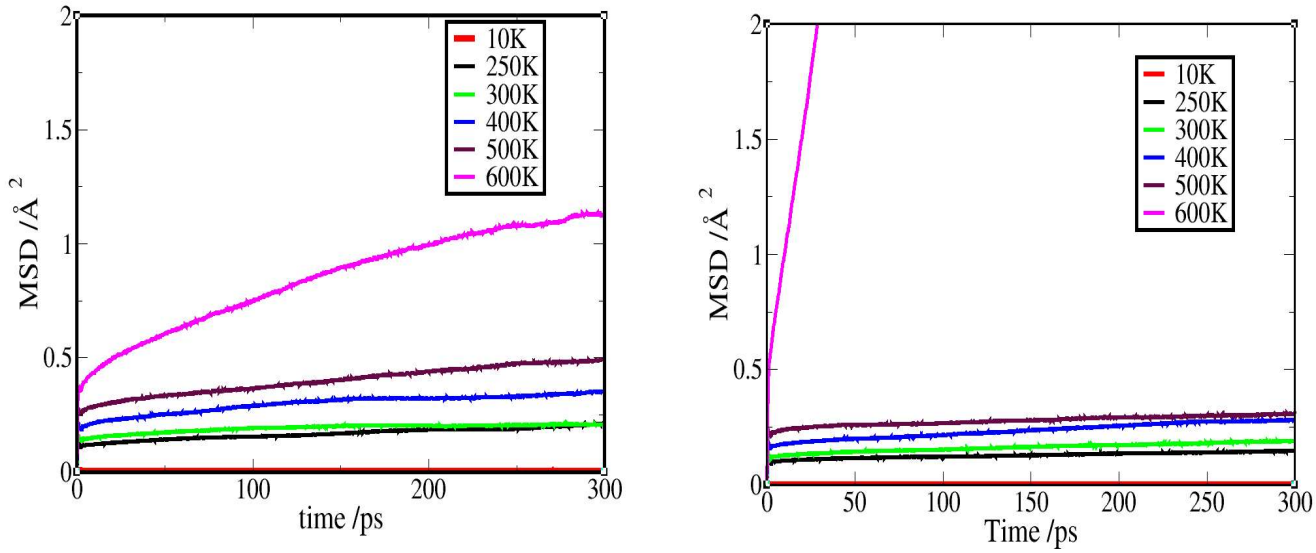

Figure 3-19 Evolution of the mean square displacement of nickel atoms with time at different temperatures for a system containing 28 solvent molecules (left) and 38 solvent molecules (right)

Figure 3-19 presents the evolution of the mean square displacement of the nickel atoms with time at different temperatures. It is observable from figure 3-19 that for temperatures up to 500 K, the value of the root mean square displacement of nickel atoms attains the horizontal long time limit curves that is characteristic of solids. The fact that the value of the root mean square displacement of nickel atoms at 10 K is lower than the root mean square displacement at 500 K is because vibrational amplitudes are greater at higher temperatures. In all cases this value is lower than 0.5 $Å^2$ for temperatures up to 500 K, which is much less than the diameter of a nickel atom (around 1.4 Å) suggesting that at these temperatures nickel atoms do not experience significant motions and therefore that the MOF has a stable structure. For the 600 K simulation however, it is clear that the curve of the evolution of the root mean square displacement with time is not horizontal anymore. Indeed, it is clear that this curve has a significant slope. This behavior may be characteristic of atoms in a liquid solution although a significant curvature is apparent and linear behavior would be expected for the liquid. It is possible that at 600 K, the MOF has experienced a phase change leading to extensive movements of the atoms initially constituting this framework.

For the the non solvated system and for systems with very low degrees of solvation, the framework is not very stable and experiences phase change rapidly upon increase of temperature.
Figure 3-20 presents the evolution of the cell volume with time for the unsolvated system at respectively 150 K and 200 K in the *NPT* ensemble.

a *b*

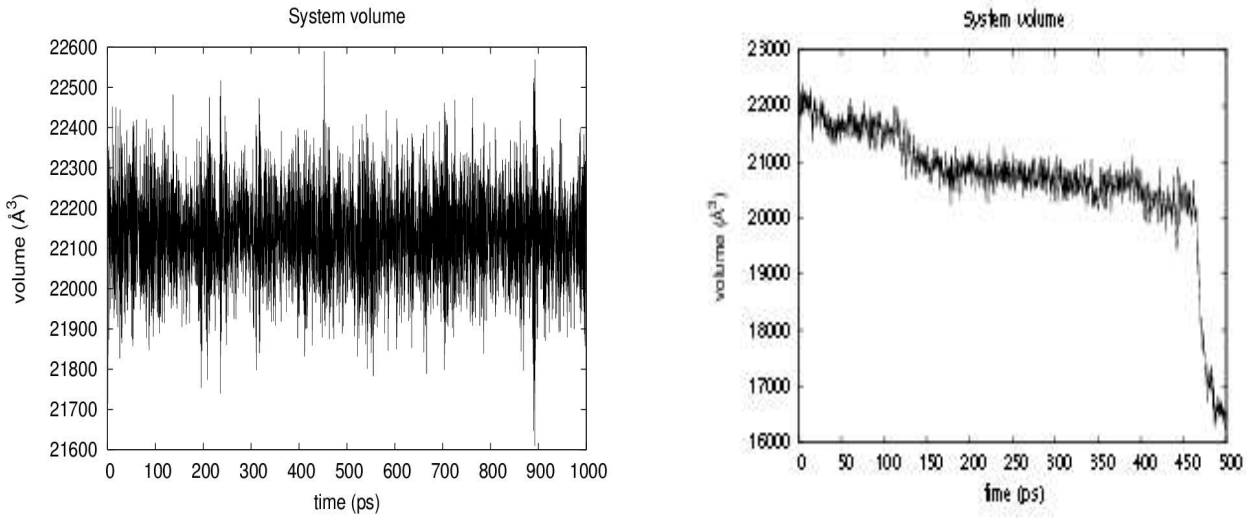

Figure 3-20 Evolution of the cell volume with time for a system containing no solvent moleules at a) 150 K (left) and b) 200 K (right).

It is clear from figure 3-20a that during the course of the1 ns simulation, the cell volume stayed stable for the unsolvated framework at 150 K. For the unsolvated framework at 200 K however, it is clear that the system experienced a large drop in cell volume after 460 ps of simulation. This large drop in cell volume suggests that the temperature of phase change for the unsolvated system is around 200 K.

Figure 3-20 presents key radial distribution functions averaged over 500 ps of simulation in the *NPT* ensemble at different temperatures for a system containing no solvent molecules.

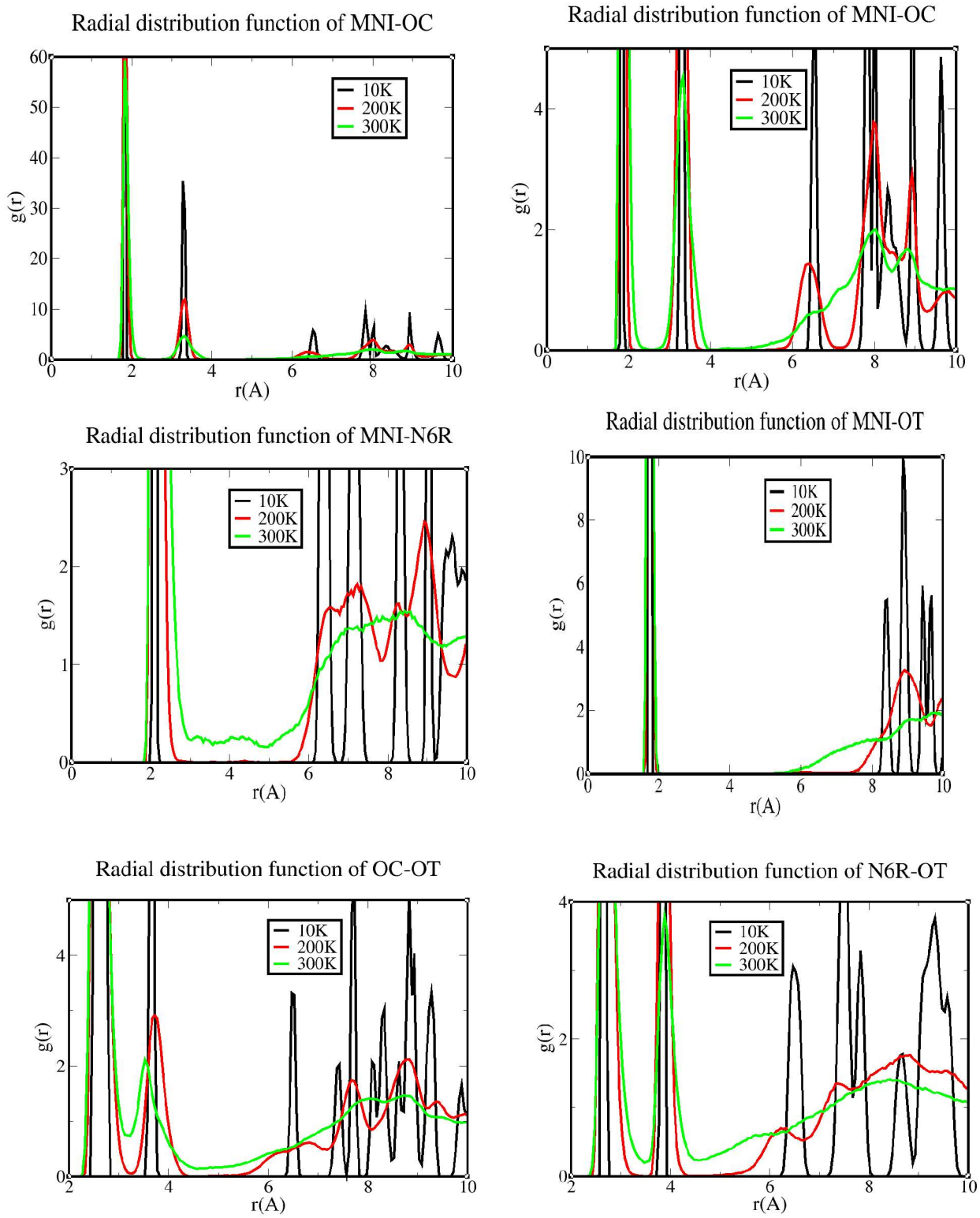

Figure 3-21 Radial distribution functions obtained after 500 ps of simulation in the NPT ensemble for a system containing no solvent molecules at different temperatures using the CHARMM22 force field.

It is observable from figure 3-21 that, as was the case for the system containing 28 solvent molecules, for all three temperatures of simulation (10 K, 200 K and 300 K) the peaks at short

distances representing bond distances between nickel atoms and oxygen atoms on one hand and nickel atoms and nitrogen atoms on the other hand, even though they are well defined, they are very broad for a chemical bond. Indeed, at 200 K and 300 K the width of the first peak of the Ni-N RDF again suggests bond vibrations with an amplitude of about 1 Å. This shows that CHARMM22 does not reproduce very accurately the interactions between nickel atoms and oxygen atoms on one hand and nickel atoms and nitrogen atoms on the other hand. Section 3.4.2 of this thesis will focus on refining this CHARMM22 force field to better reproduce these nickel-oxygen and nickel-nitrogen interactions.

It is observable from these RDFs that at long range distances, the peaks obtained at 10 K are very well defined suggesting stability of the MOF. Most of these peaks are still noticeable at 200 K, but have disappeared at 300 K. This is particularly clear in the cases of the Ni-OC, Ni-N and OC-OT RDFs. For example, the Ni-N RDFs at 200 K show four peaks between 6 Å and 10 Å whose positions match well the positions of the four peaks obtained at 10 K. At 300 K, however, only one very broad peak is observable at this range of Ni-N distances. It is also observable from the Ni-N RDFs that, while for the 200 K simulations g(r) = 0 between 3 Å and 5.6 Å, at 300 K the range of observed nickel-nitrogen distances varies continuously from 3 Å to 10 Å (i.e. g(r) is significantly higher than zero), indicating significant change in the arrangement of the atoms of the framework compared to the original structure. This also suggests that, at 300 K, some nickel-nitrogen bonds have been broken leading to this continuous variation of nickel-nitrogen interatomic distances at short distances. This non-zero g(r) range is not observed in the case of Ni-OC and Ni-OT RDFs, showing that even at 300 K no bond breaking behavior takes place between nickel and oxygen atoms. Structural changes are still seen, however the four well defined peaks between 4 Å and 10 Å for Ni-OC at 200 K and 10 K become just two small peaks by 300 K. Similarly for OC-OT and N-OT, the four peaks at long distances at 200 K and 10 K collapse to a single broad peak at 300 K. The void between 4.4–5.5 Å (i.e. where g(r) = 0) at low temperatures again is not present at 300 K, suggesting that the arrangement of the atoms in the framework has changed compared to the original structure. A conclusion that could be drawn from these RDFs is that at 200 K, the framework stays stable while at 300 K it experiences phase change. However, the study of the

evolution of the cell volume with time, the evolution of the root mean square displacement with time and the snapshot of the framework after 500 ps of simulation suggested that the unsolvated framework experiences a phase change at 200 K. The fact that these RDFs suggest that the framework stays stable at 200 K can be explained by the fact that these RDFs are averaged over the 500 ps of simulation and that indeed, during most of the simulation the framework stays stable. The study of the evolution of the cell volume with time showed that the framework stayed stable during most of the 500 ps simulation but experienced a phase change at the end of it (after around 460 ps). The framework remaining stable for 460 ps and experiencing a phase change during only the 40 ps remaining for the simulation it is understandable that these RDFs are characteristic of an ordered crystal rather than of an amorphous structure (this will also be observed with the study of the orientational distribution which is also averaged over the simulation period, this study will be developed in section 3.4.1.4).

This study therefore showed that the unsolvated MOF stays stable up to a temperature of 200 K where it experiences a phase change.

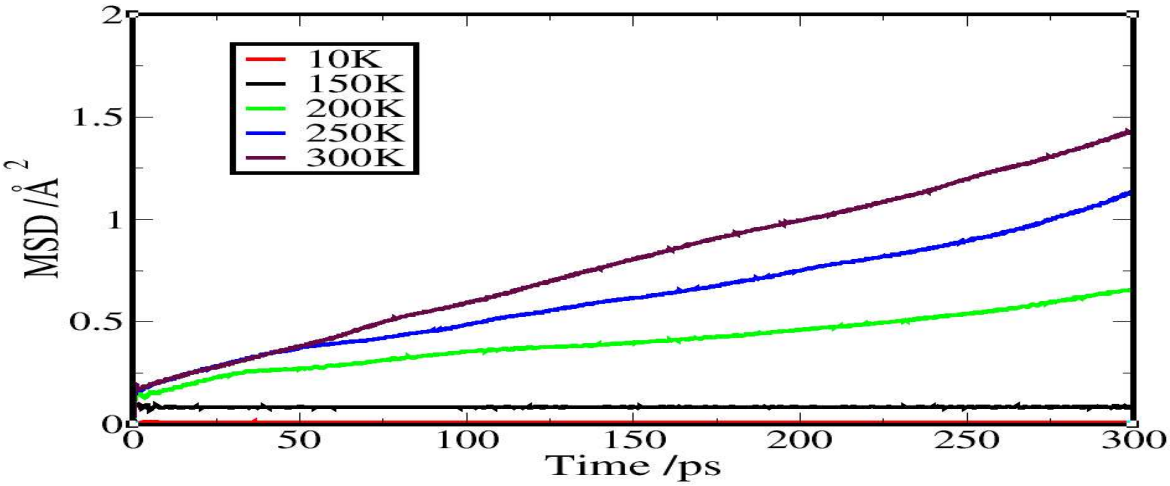

Figure 3-22 Evolution of the mean square displacement of nickel atoms with time at different temperatures for a system containing no solvent molecules in the *NPT* ensemble.

Figure 3-22 presents the time evolution of the mean square displacement of nickel atoms at different temperatures for a system containing no solvent molecules. It is clear from figure 3-22 that the system is already unstable at 200 K. Indeed for all the temperatures above 150 K we can see that the curves display a liquid like behavior. This means that for temperatures equal or higher than

200 K the nickel ions diffuse through the framework in the CHARMM22 model: the non solvated framework becomes unstable. Therefore, the temperature of phase change for the non solvated framework is around 200 K. This prediction of the CHARMM22 model still needs to be tested experimentally.

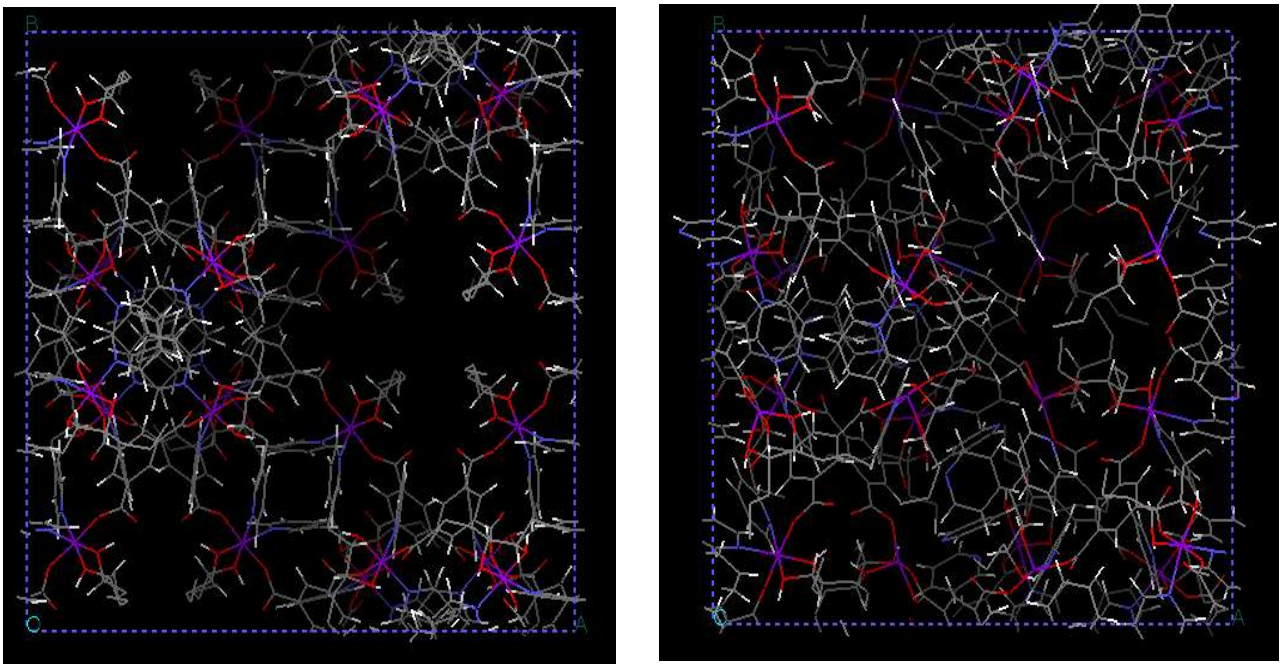

Figure 3-23 Structure of the MOF after 1.5 ns of simulation at 10 K (left); Structure of the MOF after 500 ps of simulation at 200 K(right).

Figures 3-23 presents snapshots of the unsolvated MOF after undergoing simulations at, respectively, 10 K and 200 K.

It is clear that after 500 ps of simulation at 200 K the framework structure has begun to change. Indeed, in contrast with what is observed in figure 3-20a, figure 3-20b shows that the three-dimensional structure appears to have disordered. This, once again, corroborates the conclusion that the unsolvated MOF experiences phase change at around 200 K.

From the results obtained in this study, one observation that can be made is that the systems containing 28, 38 and also 52 solvent molecules stay stable to much higher temperatures than the unsolvated system. Indeed, these solvated frameworks stay stable up to a temperature of 500 K and

experience phase change only between 500 K and 600 K while the unsolvated framework begins to experience phase change at 200 K.

Efforts have therefore been made to understand why solvated frameworks stay stable at much higher temperatures than unsolvated frameworks. To do that, the RDFs between the oxygen atoms of the solvent molecules (labeled OTX) and various framework atoms have been calculated.

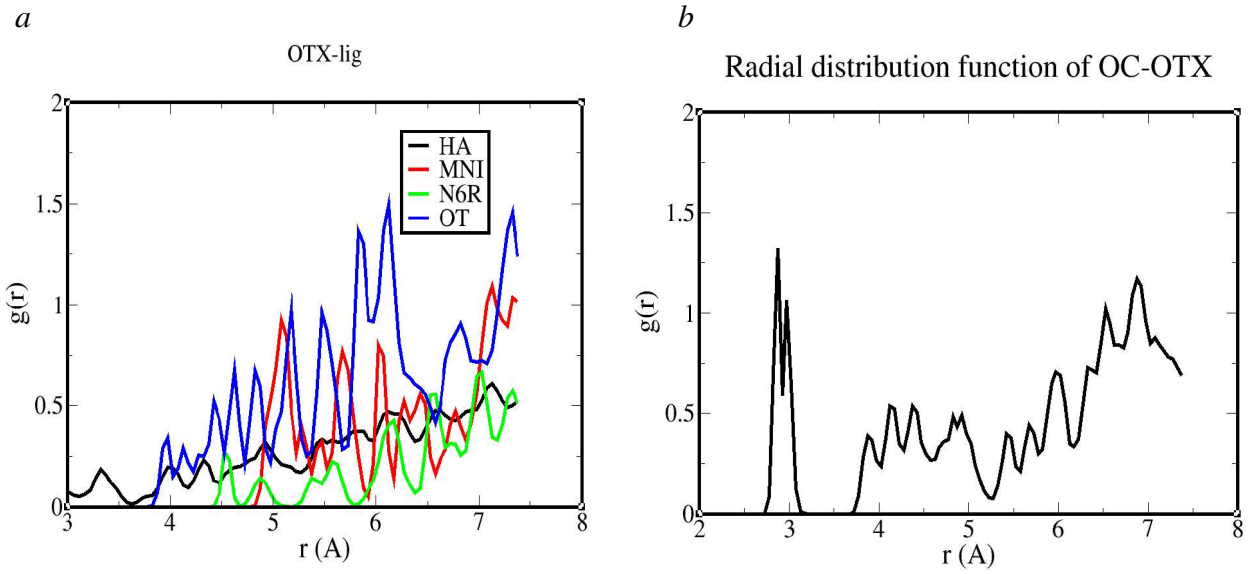

Figure 3-24 a) Radial distribution functions of a series of atoms around OTX (left); b) Radial distribution function of OTX around OC (right).
MNI = Nickel atoms, OC = Oxygen atoms of BTC molecules, OT = Oxygen atoms of alcohol molecules, N6R = Nitrogen atoms of pyridine molecules and HA = Hydrogen atoms on aromatic BTC rings.

Figure 3-24a shows that the oxygen atoms of the solvent molecules do not get very close to any of the atoms of the framework. Indeed, the closest nitrogen atoms of the pyridine molecules are 4.5 Å aways from the solvent oxygens and the alcohol oxygens of the framework are around 3.8 Å away from the solvent oxygens. The graph presented in figure 3-24b shows that the solvent oxygens do get relatively close to the oxygen atoms of BTC molecules. Indeed, the closest solvent oxygen atoms to the BTC oxygens are at around 2.7 Å. This is closer than any of the distances between the oxygen atoms of the solvent molecules and the atoms described in figure 3-24a. Also, 2.7 Å is

typical of the distance between two oxygen atoms interacting through a hydrogen bond. The RDF presented in figure 3-25 also shows that there is formation of a hydrogen bond between the hydroxyl hydrogen atoms of the solvent molecules and the oxygen atoms of the BTC molecules.

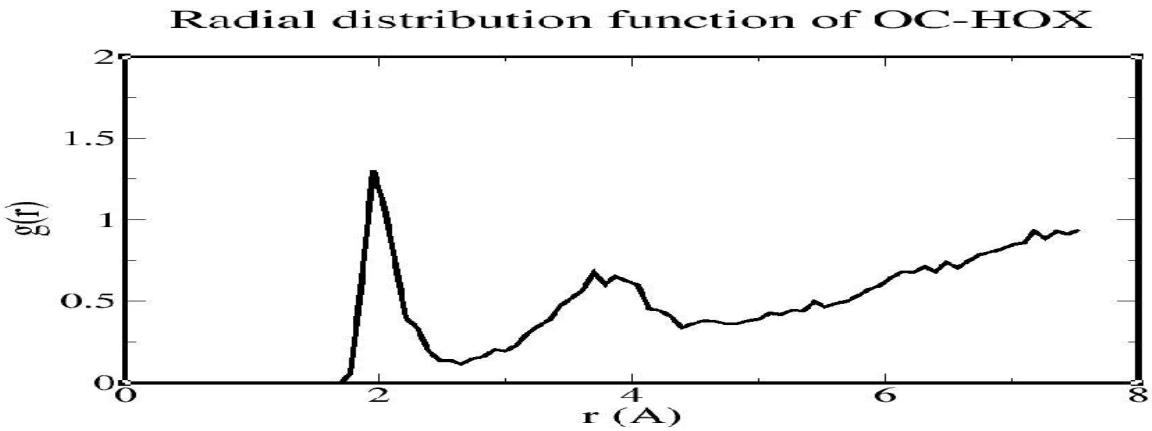

Figure 3-25 Radial distribution function of HOX (hydroxyl hydrogen atoms of the solvent molecules) around OC.

Figure 3-25 shows that the hydroxyl hydrogen of the solvent molecules get very close (2 Å) to the oxygen atoms of BTC molecules. A distance of around two angstroms between an oxygen atom and a hydrogen atom is typical of a hydrogen bond interaction. The conclusion drawn from these RDFs is that these hydrogen bond interactions are likely to be the factor that leads to higher stability of the framework when it is solvated. They are likely to be the reason why the fully solvated framework does not experience phase change until 500 K to 600 K while the unsolvated one experiences phase change at only 200 K.

Another observation that we have made is that even at a very low temperature, 10 K, the RDFs representing Ni-X distances after simulations with the CHARMM22 force field do not exactly match the RDFs representing these same distances on the crystal structure. This is explained by the fact that the CHARMM22 force field does not reproduce accurately the interactions between transition metals and organic molecules. The purpose of section 3.4.2.1 of this thesis will be to try to fit van der Waals parameters to the crystallographic RDFs, which represent experimental bond lengths within the framework, to ensure that the force field does reproduce the experimental

structure for the SBU. This fitting process will also be performed to better reproduce crystallographic cell parameters.

3.4.1.2 Study of the influence of the degree of solvation on the framework stabilty

The Figure 3-26 presents the evolution of the mean square displacement of nickel atoms with time at 250 K and five different degrees of solvation.

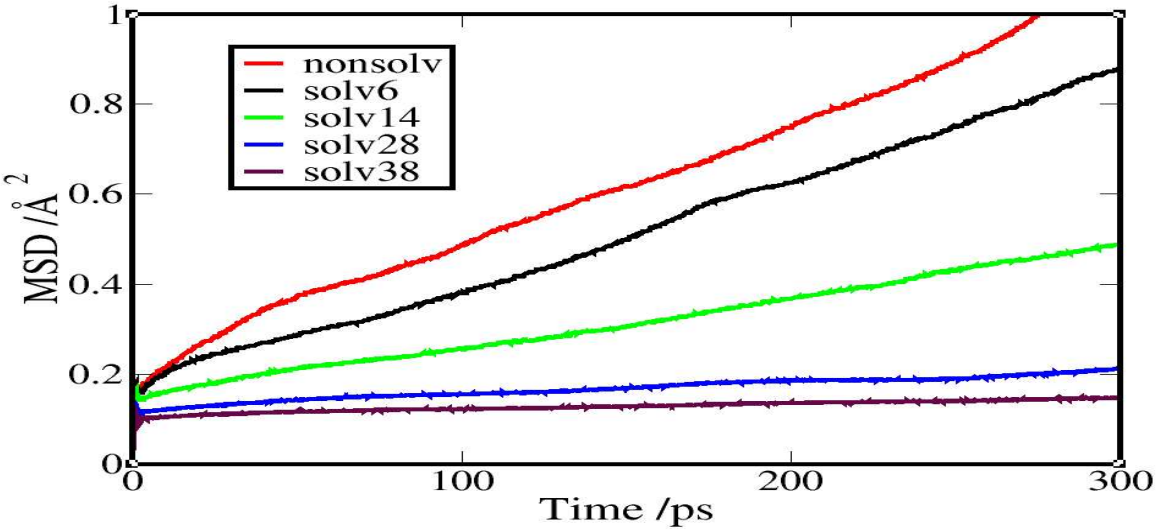

Figure 3-26 Evolution of the mean square displacement of nickel atoms with time at different degrees of solvation for a system at 250 K in the NPT ensemble.

Figure 3-26 clearly shows that the more solvated the system the lower the mean square displacement of nickel atoms. These graphs also show that the only stable systems at 250 K are the frameworks containing 28 and 38 solvent molecules. The curves for the systems containing 28 and 38 solvent molecules are roughly horizontal with values of mean square displacement not exceeding 0.2 $Å^2$. This suggests that for these solvated frameworks, the position of nickel atoms is fixed and that the framework is stable. For the systems containing 14, 6 or no solvent molecules, the evolution of the mean square displacement of nickel atoms with time is more like diffusion. This shows that at 250 K the position of nickel atoms for systems containing 14, 6 and no solvent molecules are not fixed, and the structure of the framework changes.

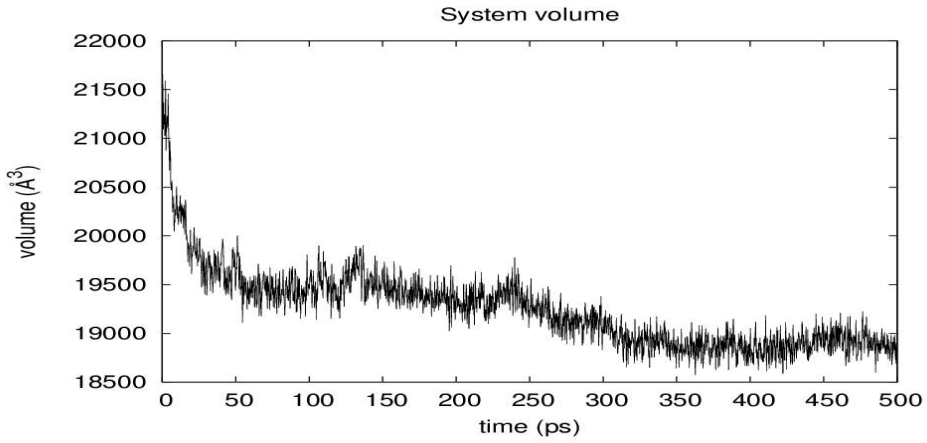

Figure 3-27 Evolution of the cell volume with time for a system containing 14 solvent moleules at 250 K in the NPT ensemble.

Figure 3-27 presents the evolution of the cell volume with time for a system containing 14 solvent molecules at 250 K. There is a significant decrease in cell volume at 250 K that continues throughout the first 400 ps of simulation. This decrease in volume corroborates the suggestion above that for a system containing only 14 solvent molecules the initial framework structure is unstable at relatively low temperatures. It is also clear from the study of the evolution of the mean square displacement with time and of the evolution of the cell volume with time that the system containing 14 solvent molecules is much less stable that the systems containing 28 or 38 solvent molecules. This means that to stabilize the framework, a solvation level higher than 14 solvent molecules is needed. These 14 solvent molecules are apparently not enough to stabilize the framework.

All the analyses on the system containing only 14 solvent molecules (mean square displacement, the cell volume, snapshots of the resulting structure and also the orientational distribution of the molecules inside the framework) have clearly demonstrated that, unlike what is observed for higher solvation degrees (solvation degrees higher or equal to 20 solvent molecules), at this solvation degree, the framework experiences a phase change very rapidly upon increase of temperature. These results clearly demonstrate that a higher degree of solvation than 14 solvent molecules is needed to stabilize this framework.

That is exactly what was expected, solvent molecules have a stabilizing effect on the system. However, a minimum number of solvent molecules needs to be present in the system to effectively stabilize the framework.

3.4.1.3 Configurational energy as a function of solvation degree and temperature.

Figure 3-28 shows simultaneously how the configurational energy of the system, evolves with temperature and solvent content.

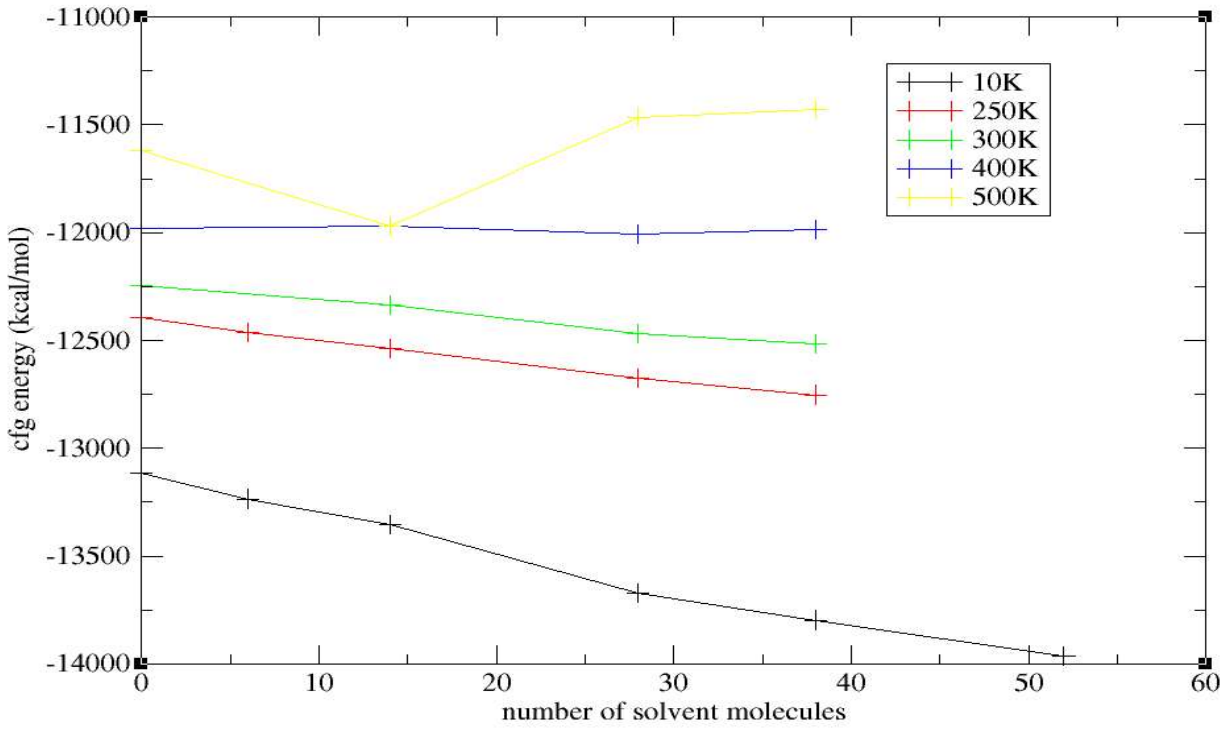

Figure 3-28 Evolution of the configurational energy of the system with temperature and solvation (these configurational energies were averaged over 500 ps of simulation in the *NPT* ensemble).

It is observable from figure 3-28 that as the temperature increases, the slope of the curve decreases, becoming zero at 400 K. That can be explained by the fact that at higher temperatures, the less solvated frameworks have experienced phase change. Therefore increasing the degree of solvation does not necessarily stabilize the system. Also, when the system is already in a high degree of

solvation, increasing the number of solvent molecules will not lead to a big decrease in the energy (because the system is already stable). The data contained in figure 3-28 corroborate well the results obtained from the RDF, orientational distribution function and root mean square displacement studies which have been presented in this work.

3.4.1.4 Orientational distribution study of this chiral Metal-organic framework.

In this section, an attempt will be made to understand the results described previously by looking at the orientational distribution of the molecules constituting the framework. This framework has a well defined structure. Molecules in the framework are arranged in a certain way, at well defined distances from each other and with well defined relative orientations. Significant changes in these distances and relative orientations would indicate changes in the framework structure and potentially a phase change. This close link between orientational distribution of molecules in the framework and the stability of this framework explains why it is so useful to calculate the orientational distribution functions described in chapter 2.6.3.

The orientational distribution of molecules within the metal-organic framework were examined at a set of different temperatures and solvent content. The orientational distribution has been determined using a locally developed program (see chapter 2.6.3). Then the analysis of the orientational distribution has been done using the iris explorer software.
From the BTC molecules, two groups have been considered, the aromatic ring and the carboxylic groups. This has been done to study how the angle between the aromatic ring and the carboxylic groups bound to it evolve with temperature and solvation. Doing that will also help to show if the hydrogen bonds between the carboxylic oxygen atoms of BTC molecules and the hydroxyl hydrogen atoms of alcohol molecules are critical for the stability of the framework. Indeed, if randomness in the angle between the aromatic ring and the carboxylic groups matches the moment

when the network experiences a phase change then it will be possible to deduce that the phase change is likely to be caused (at least in part) by the breaking of these hydrogen bonds.

These simulations have all been performed in the *NPT* ensemble. During these simulations, configurations have been saved every 0.2 ps. The total length of each simulation has been set to 500 ps. The total number of configurations obtained is therefore 2500. The orientational distribution function was then averaged over these 2500 configurations.

3.4.1.4.1 Study of the original crystal structure.

For comparison, the orientational distributions of molecules inside the framework will first be studied for the original crystal structure (before simulations were performed).

Figure 3-29 presents the orientational distribution (see section 2.6.3 for description and see below for the meaning of the three axes) of aromatic BTC rings around a central aromatic BTC ring.

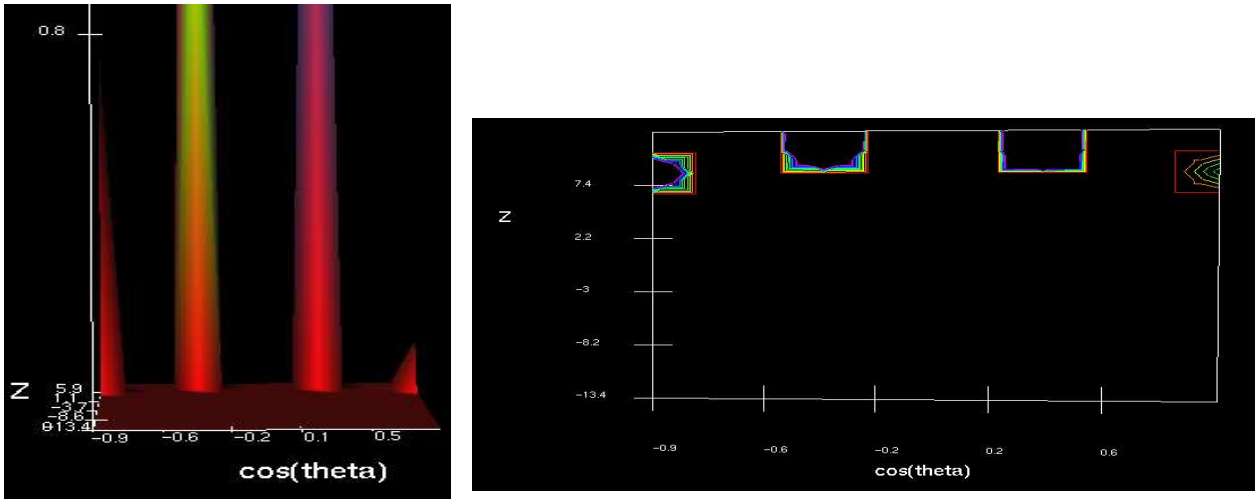

Figure 3-29 ring-ring orientational distribution

In figure 3-29, cos(theta) represents the angles between the plane of a central BTC ring and the planes of BTC rings around it (the axes of reference to evaluate these angles are the z axis of each BTC ring (or COO group in the case of ring-COO orientational distribution) compared to the z axis

of a central BTC ring), z represents the distance from the central molecule and the third axis in the left represents the frequency (which represents the probability of finding a specific orientation at a specific z distance from the central molecule).

In Figure 3-29 four peaks are clearly distinguishable. The cosine function being a symmetric function, the two peaks in the left of the graph represent the same angles as the two peaks in the right. The peak at $|\cos(\theta)| \approx 1$ represents the aromatic ring of BTC parallel to the central BTC ring as described in figure 3-8. The peak at $|\cos(\theta)| \approx 0.34$ represents the aromatic BTC ring just bellow or above the central BTC ring (θ=70°) as described in figure 3-13.
Figure 3-30 presents a snapshot of the BTC molecules where the angle between the COO group and the BTC ring is described. This angle is equal to 9.9°.

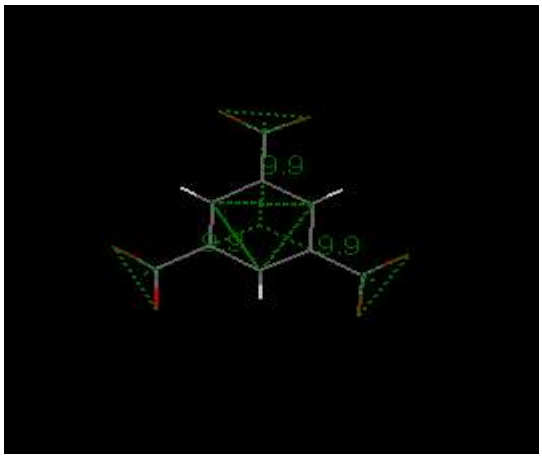

Figure 3-30 Facial view of BTC

Figure 3-31 presents the orientation distribution of carboxylic groups around a BTC ring.

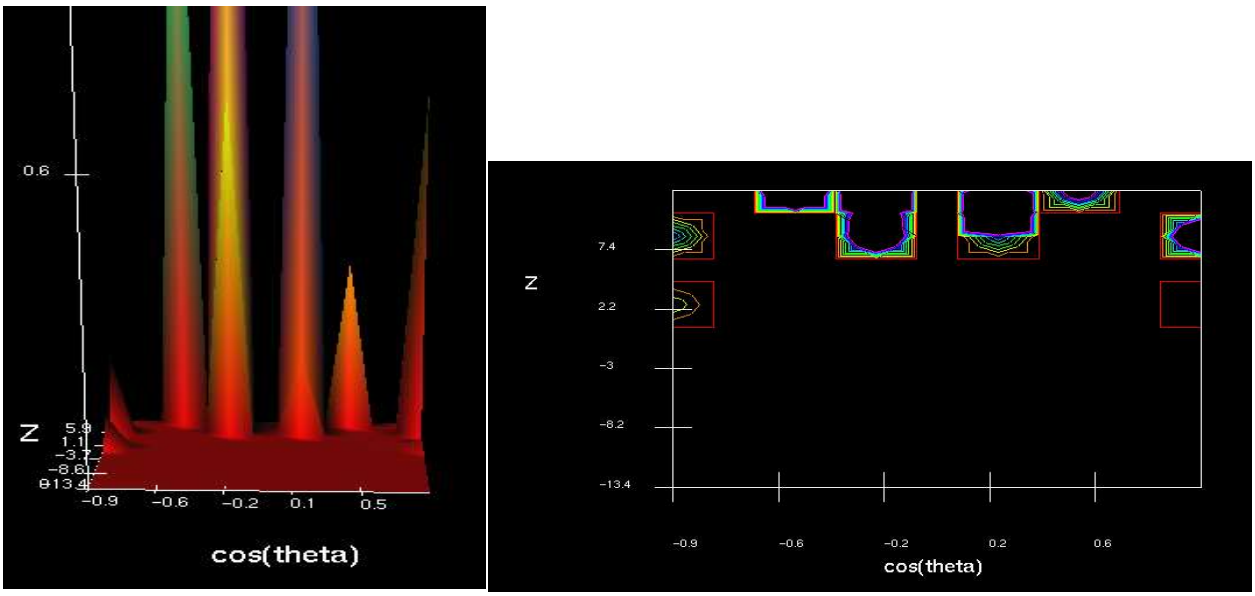

Figure 3-31 ring-COO orientational disribution

In figure 3-31, the peaks at $|\cos(\theta)| \approx 0.98$ represent the angle between the ring and the carboxylic group directly attached to it. Indeed, cos (9.9) = 0.98. The other peaks represent the angles between a central aromatic BTC ring and the carboxylic groups of the BTC molecules below and above this central ring.

3.4.1.4.2 Study of the unsolvated system

Figure 3-20 which presented the evolution of the cell volume with time at 200 K showed that at 200 K, the unsolvated framework experiences phase change after 450 ps of simulation.
The fact that the orientational distribution has been averaged over 2500 configurations (configurations have been saved every 0.2 ps) and the fact that the phase change occurs at the end of the simulation makes us expect that the total average will be showing structural stability.

Figure 3-32 presents the orientational distribution of aromatic BTC rings around a central aromatic BTC ring for the unsolvated system at 200 K.

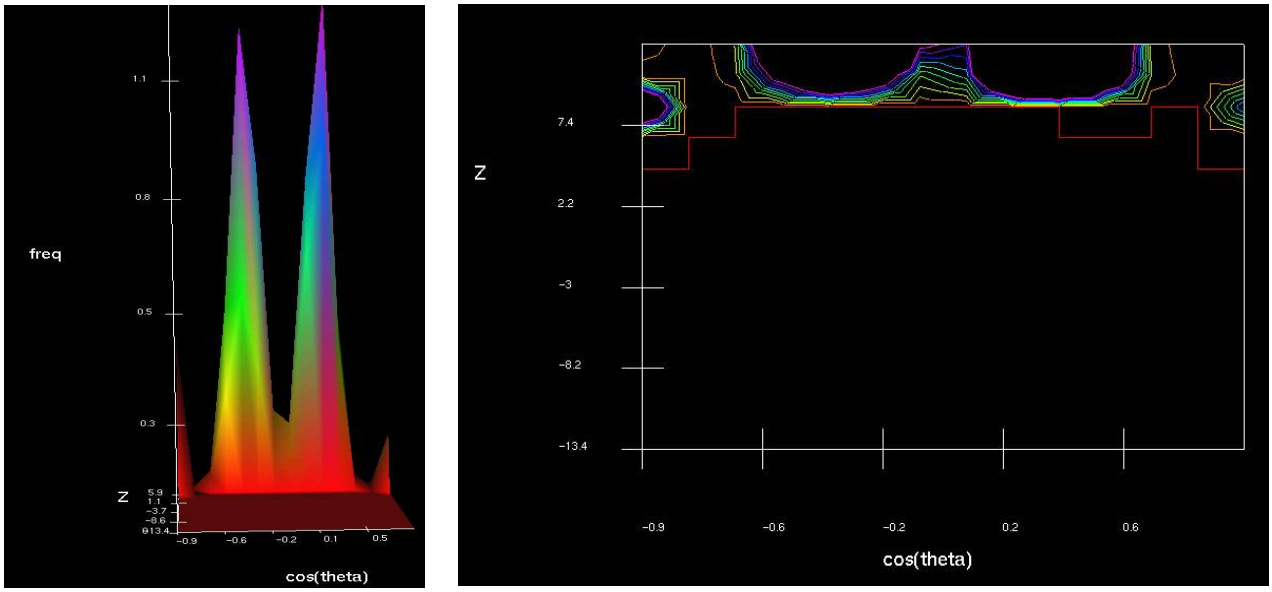

Figure 3-32 ring-ring orientational distribution at 200 K.

Figure 3-32 shows that the peaks representing parallel BTC rings (represented by the peaks at $|\cos(\theta)| \approx 1$) are still very well defined. The peaks representing BTC rings of the same strand are broader but still quiet well defined and centered at $|\cos(\theta)| \approx 0.34$.

Figure 3-33 presents the orientational distribution of COO groups around a central aromatic BTC ring for the unsolvated system at 200 K.

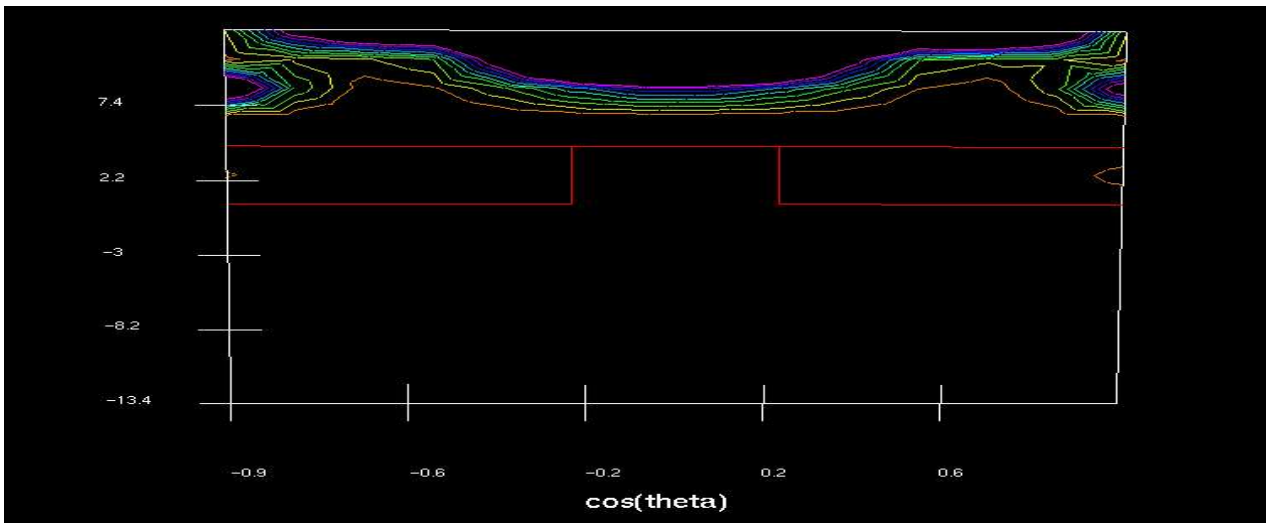

Figure 3-33 ring-COO orientational distribution at 200 K.

It is observable from figure 3-33 that the peaks at $|\cos(\theta)| \approx 0.98$ are still present.

It is also observable from figure 3-33 that there is now randomness in the orientational distribution between BTC rings and the COO groups that are not attached to these BTC rings, so that all orientations are now observed.

It is possible to make a link between the two graphs above (ring-ring and ring-COO orientational distributions). Indeed, it is possible to suggest that the fact that, the angle between a BTC ring and the COO groups attached to it is well defined, explains the fact that the angles between the BTC rings are well defined. Indeed, it is likely that the hydrogen bond formed between the COO groups and the alcohol ligands impede any significant rotation of these COO groups and as a result hinder rotations of the BTC rings.

These graphs show that the unsovated framework stays stable up to a temperature of 200 K.

As it has been shown by the evolution of the system volume with time described in figure 3-20, for the unsovated system the framework stays stable during the first 450 ps of simulation and then it experiences a phase change. The fact that the orientational distribution function shows well defined peaks is due to the fact that those are calculated as an average over the time of the simulation.

Figure 3-34 presents the orientational distribution of aromatic BTC rings around a central aromatic BTC ring obtained for the unsolvated system at 300 K.

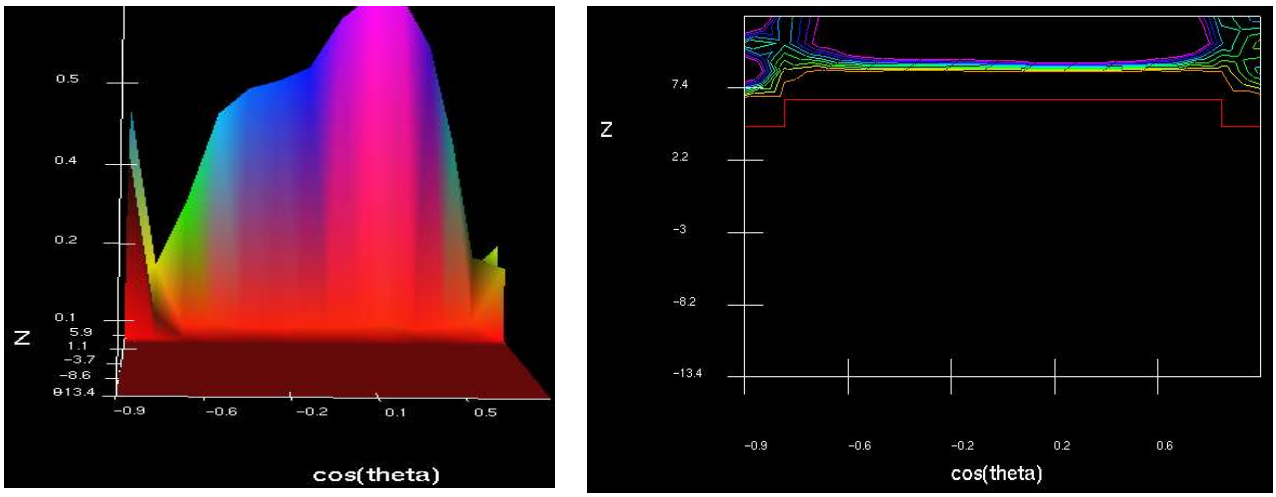

Figure 3-34 ring-ring orientational distribution at 300 K.

It is clear from figure 3-34 that the orientational distribution of BTC rings around a BTC ring becomes very random at 300 K. This randomness shows that the structure has changed.

Figure 3-35 presents the orientational distribution of COO groups around an aromatic BTC ring obtained for the unsolvated system at 300 K.

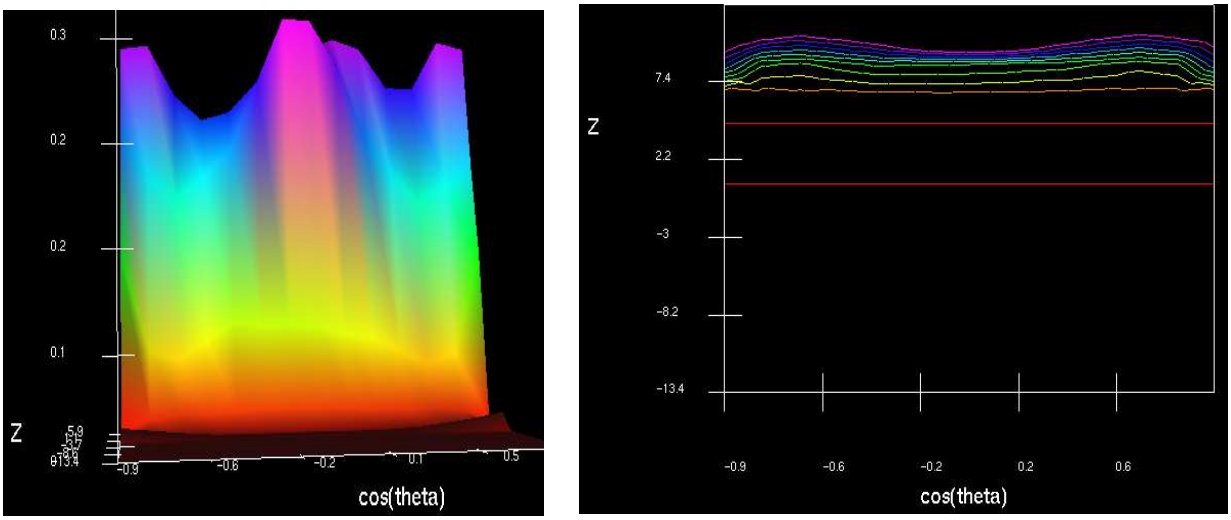

Figure 3-35 ring-COO orientational distribution at 300 K.

Figure 3-35 shows a complete randomness in the orientational distribution of COO groups around BTC rings. As was done for the 200 K results, it is possible to suggest that at 300 K, the randomness in ring-COO angular distribution explains the randomness in ring-ring angular distribution.

These graphs clearly demonstrate that at 300 K, the structure of the unsolvated framework has experienced a phase change and therefore they corroborate the other types of results obtained previously in this chapter (thermodynamic, radial distribution function, root mean square displacement).

3.4.1.4.3 Study of a solvated system.

In this section, the analysis of the orientational distributions at different temperatures for a system containing 28 solvent molecules will be presented.

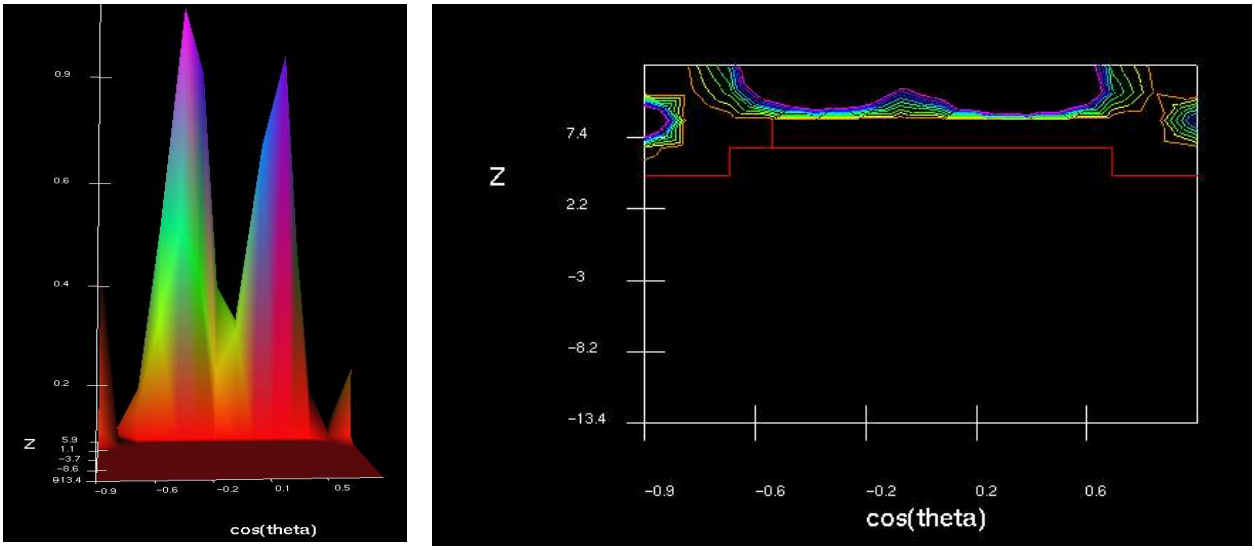

Figure 3-36 ring-ring orientational distribution at 500 K (solvated system).

Figure 3-36 presents the orientational distribution of BTC rings around a central BTC ring for a system containing 28 solvent molecules at 500 K. The parallel BTC rings (represented by the peaks at $|\cos(\theta)| \approx 1$) are still well defined at 500 K. Figure 3-36 also shows that the two broad peaks centered at $|\cos(\theta)| \approx 0.34$ are still well defined even though they are broad. This shows that the overall framework structure is still stable at this temperature. However, the fact that the peaks at $|\cos(\theta)| \approx 0.34$ are broad shows that there are fluctuations in the angles between BTC molecules of a same strand and therefore it shows that at this temperature the framework begins to experience some thermal fluctuations that eventually (at higher temperatures) will lead to instability.

This orientational distribution study also corroborates the conclusion drawn from analyses presented earlier in this chapter, that the framework stays stable at up to 500 K at this solvent content.

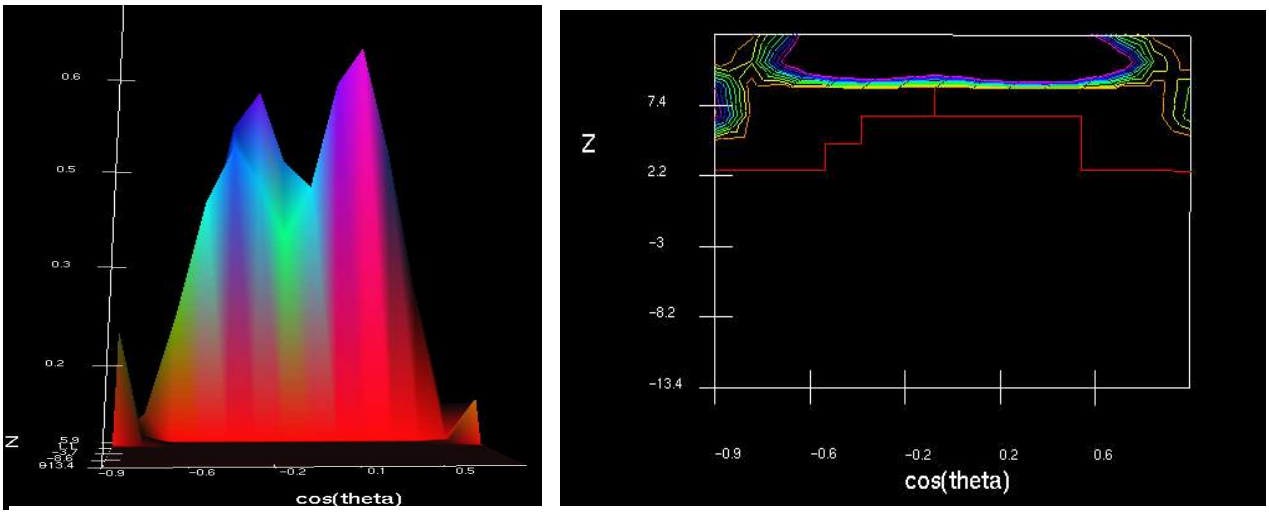

Figure 3-37 ring-ring orientational distribution at 600 K (solvated system).

Figure 3-37 presents the orientational distribution of BTC rings around a central BTC ring for a system containing 28 solvent molecules at 600 K. These graphs are very different from those at the lower temperatures. The two central peaks have essentially merged, so that no ring orientations are now favored.

Figure 3-38 presents the orientational distribution of COO groups around a central BTC ring for a system containing 28 solvent molecules at 600 K.

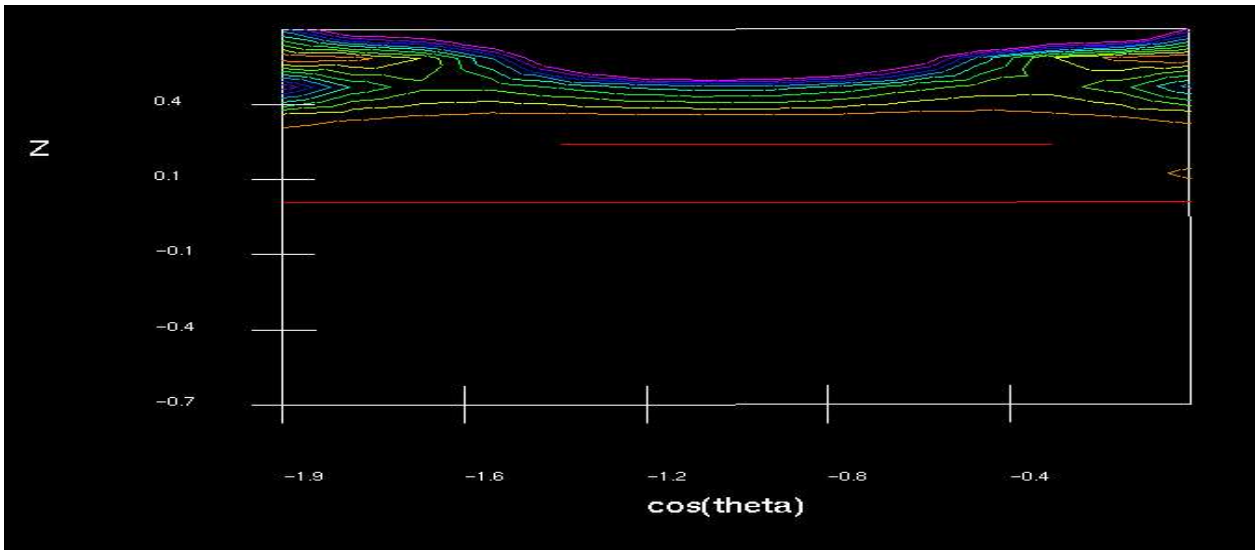

Figure 3-38 ring-COO orientational distribution at 600 K (solvated system).

Figure 3-38 shows that the orientational distribution is completely random. This figure does not show any distinct peak what so ever. The distribution of the angles between the COO group and the benzene ring spread through all the possible values of cosine ranging from -1 to 1.
This might be explained by the fact that the hydrogen bond (between an oxygen of the COO groups and a hydroxyl hydrogen of the alcohol molecules) which partially constrained the COO-BTC_ring angle has been broken due to the increase in the internal energy of the system.
These graphs show that at 600 K, the structure has experienced phase change.

This orientational distribution study corroborates the thermodynamic properties, the radial distribution functions and the mean square displacement results that were obtained at the range of solvation degrees and temperatures studied. This study shows that the unsolvated system stays stable up to a temperature of 200 K and over a time of 1.5 ns of simulation. The system containing 28 solvent molecules stays stable up to a temperature of 600 K. This study also suggests that the hydrogen bond between the oxygens of the BTC molecules and the hydroxyl hydrogens of the alcohol molecules are critical to the stability of the system.

Conclusion

This work has demonstrated so far that systems with a high degree of solvation (systems containing 28 and 38 solvent molecules) stay stable up to a temperature of 500 K and experience phase change between 500 K and 600 K. This work also demonstrated that this metal-organic framework begins to experience phase change at 200 K when it is not solvated. However, for both the solvated and the unsolvated systems, the study of the RDFs showed that the nickel-oxygen and nickel-nitrogen bonds have an amplitude of vibration close to 1 Å for temperatures higher that 10 K. This is too much an amplitude for nickel-oxygen and nickel-nitrogen bond vibrations. Further, the results show the Ni-OT bond to be more stable than Ni-OC, which is not as expected from experiment. These observations show that CHARMM22 force field does not reproduce very accurately the

nickel-oxygen and nickel-nitrogen interactions. Therefore this CHARMM22 force field will be refined in the next section of this thesis to better model these interactions.

The radial distribution function studies showed that the phase change of this MOF at high temperatures is not due to nickel-oxygen bonds being broken. Indeed, for the unsovated system, the temperature of phase change of the framework is 200 K. However the peaks in the RDFs representing the distances between nickel atoms and the oxygen atoms that are directly bound to these nickel atoms are still present and well defined even at 300 K. This corroborates the assumption that the phase change of the framework is not due to the breaking of nickel-oxygen bonds. The difference between the temperatures of phase change between the highly solvated and the non solvated MOF is likely to be explained by the fact that, for the highly solvated framework, solvent molecules form hydrogen bonds with BTC molecules. Indeed, it is likely that these hydrogen bonds strongly stabilize the framework and that it is these hydrogen bonds which allow the solvated framework to stay stable up to a temperature of 500 K while the unsolvated framework experiences phase change at 200 K. Indeed, it was shown by the study of the RDFs that the oxygen atoms of the solvent molecules get closer to the oxygen atoms of the BTC molecules than to any other atoms of the framework. The study of the orientational distributions of groups or molecules inside the framework showed that for the system containing 28 solvent molecules the orientational distribution between COO groups and the benzene ring they are bound to becomes random ($\cos(\theta)$ ranging from -1 to 1) at 600 K. It has also been observed that for the unsolvated system, the orientational distribution between COO groups and the benzene ring they are bound to becomes random ($\cos(\theta)$ ranging from -1 to 1) at 200 K therefore coinciding with the temperature of phase change of the framework. One conclusion that could be drawn from these coincidences between the phase change of the framework and the randomness of the orientational distribution of COO groups relatively to the benzene rings they are bound to is that the orientation of these COO groups play an important role in the stabilization of the framework. The randomness of the orientational distribution of COO groups relatively to the benzene rings they are bound to indicates that COO groups rotate freely around these benzene rings at sufficiently high temperatures. In the stable framework, one oxygen of each COO group is bound to a nickel atom while the other forms a

hydrogen bond with the hydroxyl group of the alcohol molecule of the same secondary building unit. Our hypothesis is that at high temperatures, this hydrogen bond is broken and the oxygen atom of the COO group that initially formed this hydrogen bond rotates freely around the Ni-O-C axis (O = oxygen atom of the COO group that is bound to nickel and C = carbon atom of the COO group). It is likely that this hydrogen bond breaking is also responsible for torsions and rotations of the diol molecules and this is also a factor of instability for the framework. Indeed, each hydroxyl group of a diol molecule forms a hydrogen bond with one of the two BTC molecules of the secondary building units. These diol molecules therefore form two hydrogen bonds with BTC molecules that stabilizes these diol molecules and the entire framework. However, since diol molecules are bound in a bidentate way to nickel atoms, the rotation of these diol molecules is restricted and therefore it is our believe that the diol molecules are not primarily responsible for the phase change of the structure at high temperature. It seems more likely that the phase change of the framework at high temperature results from the free rotation of COO groups around Ni-O-C axes (caused by the breaking of the hydrogen bond just described) which subsequently leads to rotations of BTC rings relatively to each other.

3.4.2 A refined flexible force field for MOFs

3.4.2.1 Improved van der Waals parameters.

It has been seen from the study of the radial distribution functions that the force field used so far, the CHARMM22 force field, has not been able to reproduced accurately nickel-oxygen (Ni-OC, Ni-OT) and nickel-nitrogen (Ni-N) bond distances.

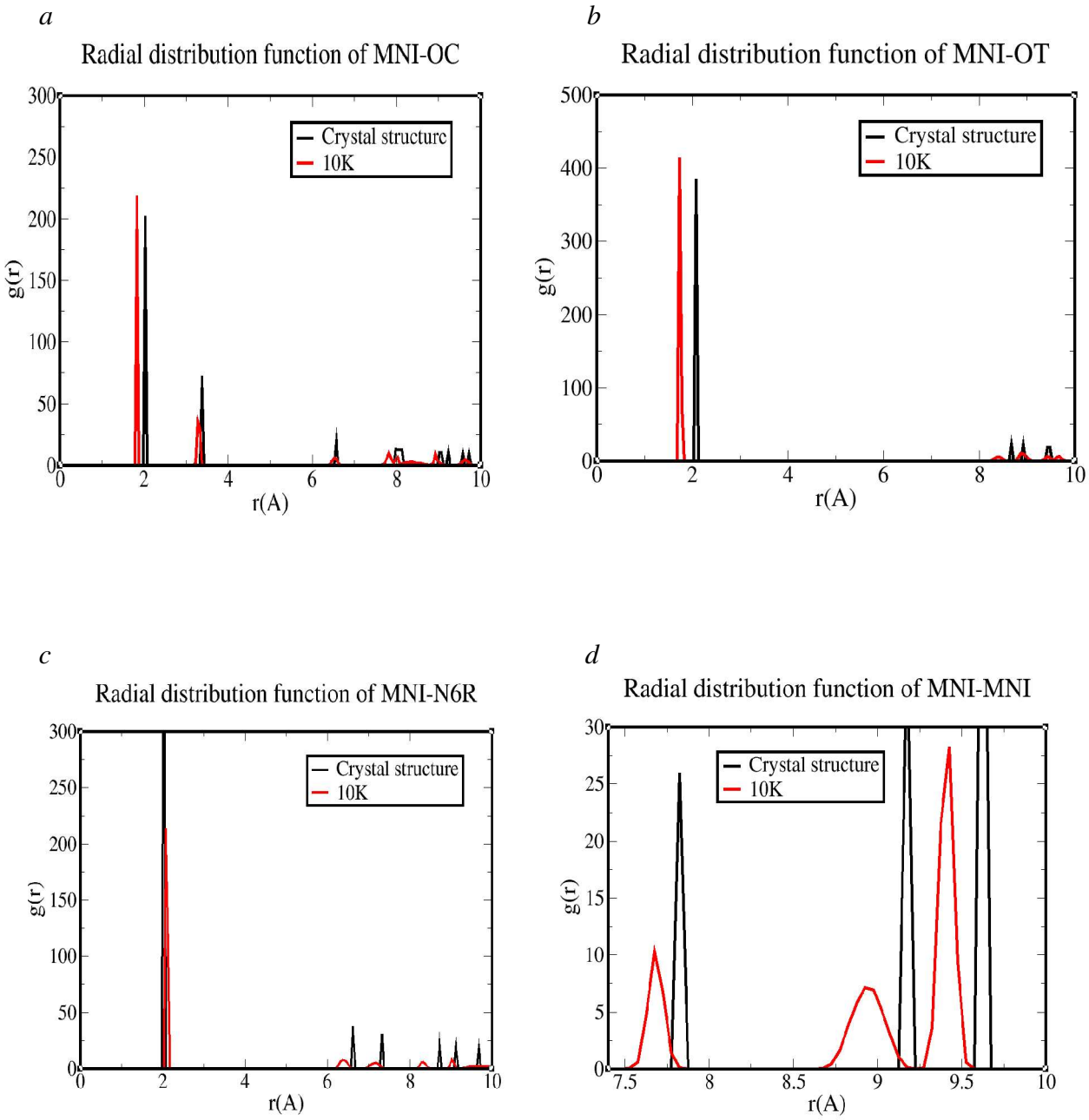

Figure 3-39 Radial distribution functions of the original (black) and the simulated (red) structure for a) MNI-OC (top left); b) MNI-OT (top right); c) MNI-N6R (bottom left) and d) MNI-MNI (bottom right). The red curves represent the structure after 1.5 ns of simulation at 10 K in the NPT ensemble. These simulated RDFs have been averaged over the last 500 ps of the simulation.

Figure 3-39 presents various radial distribution functions associated with the Ni^{2+} ion obtained from both the original crystal structure and from simulations at 10 K with the CHARMM22 force field. In the case of Ni-OC (the BTC oxygen), figure 3-39a, the first peak arises from the two OC atoms directly bound to the nickel center. The positions of this first peak is 2.042 Å for the original crystal

structure and 1.632 Å for the simulated one. Thus the CHARMM22 force-field underestimates this bond length by 0.41 Å. Similarly, for the Ni-OT (alcohol oxygen), see Figure 3-39b, the position of the first peak is 2.09 Å for the original and 1.632 Å for the simulated system. Therefore, this potential leads to the nickel-oxygen bond length contracting by 0.458 Å during the simulation. In contrast, the third complex bond, Ni-N, increases by 0.234 Å in the simulation (figure 3-39c). Figure 3-39d presents the relative positions of nickel atoms around other nickel atoms. It is clear from this graph that after the simulation, the nickel atoms are closer to each other. The third peak of this RDF is particularly interesting since it represents the distance between nickel atoms of the same helix. The shortening of the distance between these two atoms indicates that the helix to which these atoms belong has contracted. Associated with this, the volume decreases from 28.804 Å (original) to 28.055 Å (simulated). This is a 2.6 % decrease in cell parameter.

It is likely that the fact that the nickel atoms got closer to each other led to the contraction of the framework which resulted in a smaller cell volume. This is unexpected at such a low temperature and again represents a short coming of CHARMM22. Therefore, as shown in detail in the last section, it is possible to conclude that there is a problem with the accuracy of the CHARMM22 force field for MOFs.

Since the linker molecules are BTC molecules, it is likely that the shortening of the Ni-OC bond length is a significant factor leading to the contraction of the framework. As described in the introduction, the BTC linker molecules together with metal coordination geometry are the key factors in determining the structure of the framework.

The point of these RDFs is that the CHARMM22 force field has not been able to reproduce accurately the metal-organic interactions. Indeed, the CHARMM22 force field has been developed mainly to deal with biological systems especially proteins and DNA molecules. This force field is well suited for purely organic systems, but does not reproduce accurately the interaction between transition metal atoms and organic molecules. The first stage of our refinement of the force-field is therefore targeted at improving the metal-ligand interactions.

Single point electronic structure calculations were performed on the, $NiBTC_2Pyr_2alc$ SBU, in an attempt to calculate theoretically the key interatomic distances. The package used was the Gaussian 03 package. Density functional theory (DFT) and MP2 methods were used for these calculations. B3LYP, BPW91 functionals were used along with a series of basis sets including 6-31G, 6-311G, cc-pTDZ, cc-pVDZ. For Nickel atoms, effective core potentials, including LANL2DZ and SDD potentials, were used to improve the probability that the SCF (Self Consistent Field) cycles would converge. Despite all these efforts, the SCF cycles did not converge and so single point calculations on $NiBTC_2Pyr_2alc$ units proved not to be possible without prohibitive computational expense.

Therefore, it was decided instead to try to fit nickel-oxygen and nickel-nitrogen parameters in an empirical way. As a result, attempts to improve the force field focused on empirical refinement of the metal-ligand distances within the SBUs, varying the Lennard-Jones σ and ε parameters to reproduce the bond lengths seen in the crystal structure. Once this bond distances fitting was performed, simulations were performed with each set of parameters so obtained to see if the resulting cell parameters and framework was stable and accurate.

One difficulty with this procedures is that the MOF solvent content has not been determined experimentally and yet, as described in the previous section, it can have a large impact on the stability of the framework. Within the timescale of this project, it was impractical to implement an iterative cycle of determining the equilibrium solvent content, then refining the potential, then re-determining the solvent content etc. As a result, we have been guided by the systematic study of the CHARMM22 force-field, and adopted 20 solvent molecules per unit cell as the benchmark concentration. This was the minimum level of solvation that was shown to lead to a stable framework at 250 K.

Since the temperature used to determine the crystallographic structure of this metal-organic framework was 150 K, the same temperature was used for the van der Waals parameters refinement.

The refinement process was firstly performed in a speculative way: σ parameters were rescaled by a

series of different values, then simulations performed to compare the predicted bond lengths to experiment. An attempt was made to adjust simultaneously Ni-OC, Ni-OT and Ni-N parameters by a first method which consisted of adding the difference between the crystal and the simulated bond lengths to the σ value in the force filed. The sigma parameters described in the third row of table 3-1 were obtained. Then an attempt was performed to adjust Ni-OC, Ni-OT and Ni-N parameters by multiplying the σ value in the force field by the fraction $\sigma_{exp} / \sigma_{sim}$ (where σ_{exp} represents the σ value obtained by multiplying the equilibrium distance in the original crystal structure by $2^{1/6}$ and σ_{sim} represents the σ value obtained from the equilibrium distance between the atom pair after simulation). The σ values obtained using this second method are given in the forth row of table 3-1. However, the refinement process that led to the best fitting of the first peak positions of the RDFs for the simulated structure resulted from a combination of the parameters obtained using both methods. The sigma parameters described in the fifth row of Table 3-1 led to Ni-O and Ni-N bond distances after simulation that matched accurately the equivalent bond distances in the original crystal structure. The reason why the values of sigma parameters in the fifth row are different from sigma values in the third and forth row is due to the fact that the refinement process for the fifth row parameters was done in a progressive way. First $\sigma_{Ni\text{-}OC}$ value was refined by multiplying the σ value in the force field by the fraction $\sigma_{exp} / \sigma_{sim}$. Then from the RDFs obtained after this simulation, $\sigma_{Ni\text{-}OT}$ value was refined and in a third and final stage $\sigma_{Ni\text{-}N}$, $\sigma_{OC\text{-}OT}$ and $\sigma_{N\text{-}OT}$ were all refined. In the third and forth row, all the σ parameters have been refined simultaneously. Therefore, the most effective strategy was to optimize individual σ parameters in an iterative cycle.

Only the analysis of simulations done using the refined parameters obtained using the last refinement method (fifth row parameters) will be considered here. This choice is due to the observation that the short range RDFs resulting from these simulations agreed best with the short range RDFs of the original crystal structure.

Atom pairs	*MNI-OC*	*MNI-N6R*	*MNI-OT*	*OT-OC*	*N6R-OT*
σ parameter obtained from the CHARMM22 force field /Å	2.3698	2.5212	2.2718	2.8598	3.0112
σ parameters obtained after fitting using the first method /Å	2.5698	2.4712	2.6218	2.8598	3.0112
σ parameters obtained after fitting using the second method /Å	2.6295	2.4607	2.7327	2.8598	3.0112
σ parameters obtained after refinement using the third method (FFR-1) /Å	2.6295	2.5850	2.6865	2.9598	3.4127

Table 3-1 Representation of the σ values obtained using the different refinement methods compared to the σ values obtained from the CHARMM22 force field

Another deficiency in the CHARMM22 force field was that it underestimated the O-C-O angle in BTC. The reason for this appeared to be the strong attraction of the negatively charged O for the Ni^{2+} sites, which attracted both O atoms to the Ni^{2+} and so squeezed the O-C-O angle. Thus some strengthening of the BTC bond-angle energy term was required. Adjustments to both the ideal angle and the force constant for this bond angle vibration were considered, and it was found that increasing the "ideal" bond angle for BTC was the most effective cure. The value of this angle had to be increased from 123^{o} in the CHARMM22 force field to 143^{o} to accurately reproduce the experimental O-C-O angle after simulation. We note that this procedure is appropriate for BTC bound to Ni^{2+}, but would need to be adjusted if labile BTC-Ni complex bonds were expected within a given simulation.

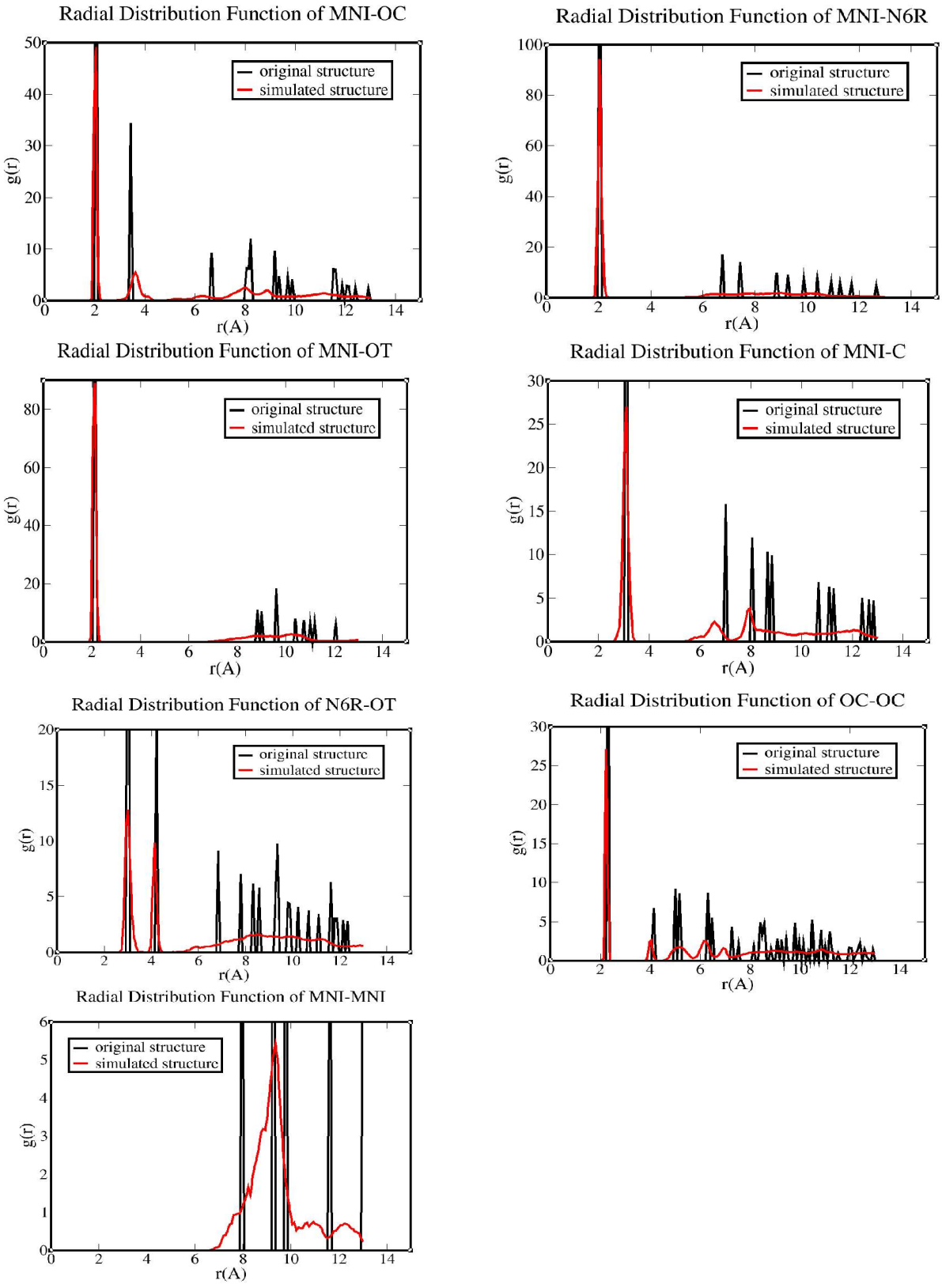

Figure 3-40 Radial distribution functions averaged over 30 ps of simulation at 0.1 kbar and 10 K in the NPT ensemble using the CHARMM22 force field with the modified parameters described in the fifth row of table 3-1 (FFR-1).

Figure 3-40 presents key RDFs obtained after 30 ps of simulation in the *NPT* ensemble using this refined force field. It is obvious from these RDFs that the aim of getting a good match between simulation and experiment for interatomic distances within the octahedral secondary building unit has been achieved with great accuracy. Indeed, it is observable from Ni-OC, Ni-N, Ni-OT, Ni-C, N-OT and OC-OC RDFs that the position of the first peak of the simulated structure matches the position of the first peak of the original structure to within the resolution of the plots. This means that both, the Ni-X bond distances and the distances between the heteroatoms in the Ni coordination shell, are equivalent in the original and the simulated structures. Thus the refinements do give a good description of the SBU.

However, when it comes to longer range distances and distances between atoms that do not belong to the same SBU, this good match between RDF peaks in the original and simulated structure is not observable anymore. Indeed, it is observable from Ni-N and Ni-OT RDFs that for the simulated structure there is only one obvious peak, the first peak which represents the distance between the nickel atom and the nitrogen and alcohol-oxygen atoms directly bound to it. Since the first peak represents the two and only two nitrogen and alcohol-oxygen atoms belonging to a single SBU, the fact that the other peaks have disappeared (even at a temperature as low as 150 K) suggests that the three-dimensional structure of the framework has been substantially altered. Indeed, these other peaks representing distances between a nickel atom and nitrogen and alcohol-oxygen atoms of different SBUs tell us more about the overall framework structure, since the framework is constituted of an assembly of these SBUs. A similar observation holds for the N-OT RDF (although in this case the SBU contains two N and two OT atoms, and so gives rise to two peaks from within the SBU). It is again noticeable from this RDF that, in the case of the simulated structure, there are no noticeable peaks other than those arising from within the SBU. This again suggests a substantial alteration of the three-dimensional structure of the framework during the course of the simulation.

The fact that for Ni-OC, Ni-C and OC-OC RDFs there is more than one observable peak is explained by the fact that there is three C atoms and six OC atoms for each BTC molecule. In the Ni-C RDF, the three different distances between these two atoms in a single octahedral unit are clearly represented by three different peaks. No other peaks are evident. The fact that there are even

more peaks for RDFs involving OC atoms is explained by the relatively large number of OC atoms in a single octahedral unit.

The Ni-Ni RDF is another good indicator of the stability of the framework. Indeed, the Ni-Ni RDF contains only long range structure since there is only one nickel ion per SBU. Therefore the position of nickel ions relative to other nickel ions gives useful information about whether or not the three-dimensional arrangement of SBUs into the framework has been significantly altered by the force field. It is observable from this RDF that in the simulated structure, the first peak (of the original structure) has disappeared and has merged with the second and third peak resulting in a wide peak centered at 9.2 Å. The second and third peak of this RDF are also very wide and of small height. It is also observable from this RDF that after around 6.4 Å, g(r) is always significantly higher than zero. This again suggests that during the course of the simulation, the positions of nickel ions have still not been fixed at the framework nodes. Thus this first refined potential still leaves instability in the framework that leads to relative motion of these nickel ions and results in these wide and not ill-defined peaks. The fact that this is observed at a temperature as low as 150 K suggests that there is some disorder in the lattice.

A good way to verify if whether or not these nickel atoms experienced significant motion during the course of the simulation is to study the evolution of their mean square displacement with time. This is shown in figure 3-41.

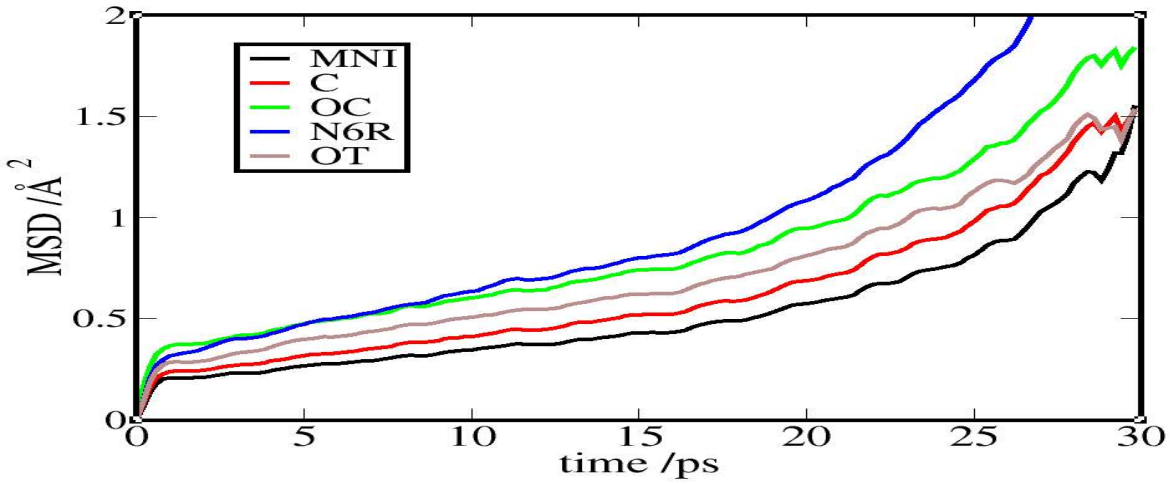

Figure 3-41 Mean square displacement of nickel and heteroatoms of the system using the force field with the refined parameters of the fifth row of table 3-1

It is obvious that the framework was unstable during the course of the simulation. None of the mean square displacements in figure 3-41 displays solid-like behavior: these curves are not horizontal at long times. This corroborates the interpretation made from the study of the key RDFs of the system, that the framework had lost its original three-dimensional structure.

Another important structural analysis is to examine the orientational distribution functions. Since the orientation of molecules in the original structure are very well defined (as described in section 3.4.1.5), the study of these orientations will be very informative when inquiring on the three-dimensional structure of the system obtained after simulation.

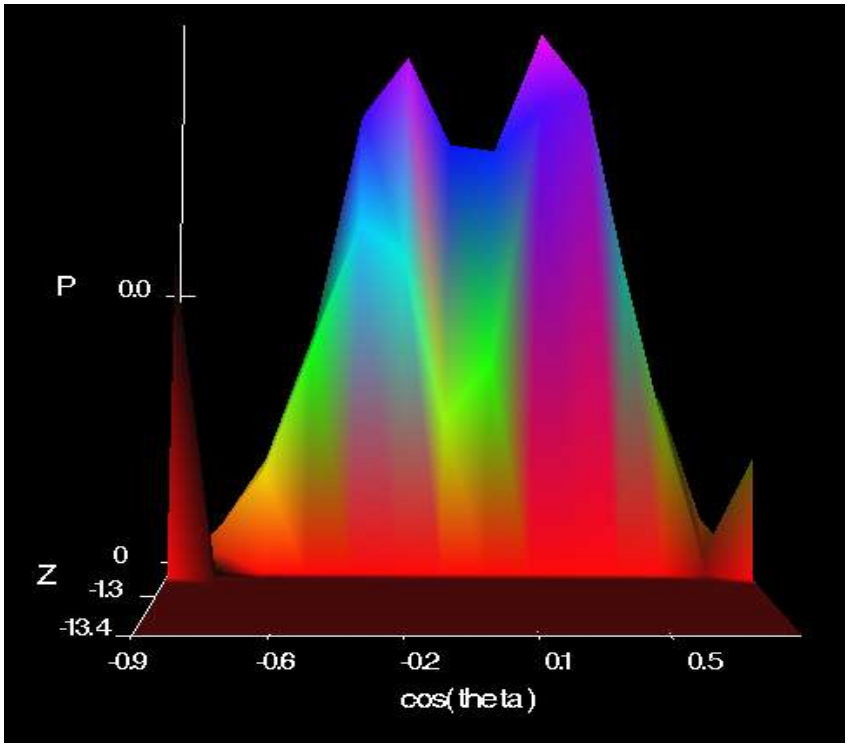

Figure 3-42 ring-ring orientational distribution when using the force field with the refined parameters of the fifth row of table 3-1. Simulations were averaged over 30 ps of simulation at 150 K and 0.1 kbar in the NPT ensemble.

Figure 3-42 shows the orientation of BTC rings relative to each other. There is a very broad distribution ranging from $\cos(\theta) = -1$ to $\cos(\theta) = 1$ and no sign of the two well resolved peaks seen in the crystal structure (see figure 3-29).

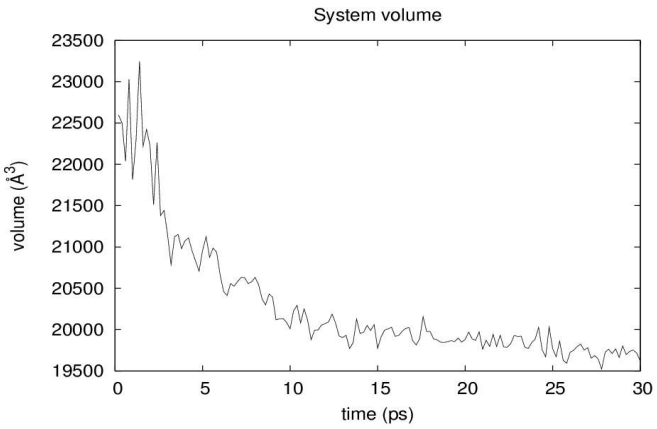

Figure 3-43 Evolution of the system volume with time using the force field with the refined parameters of the fifth row of table 3-1

Figure 3-43 shows the evolution of the cell volume with time when this potential is used. The system volume decreases by 8.3 % during the 30 ps of the simulation. This volume loss is another indication of the instability of the framework during the simulation.

From all these analyses we conclude that while the first refinement of the potential has been able to give a good description of the SBU, it has failed to reproduce the manner in which these SBUs are assembled into the MOF. Further refinement of the potential is therefore needed.

Additional refinement was therefore undertaken by adjusting the metal-organic ε parameters.
In the first instance a series of trials were made by multiplying the epsilon parameters of nickel-oxygen and nickel-nitrogen pair potentials, Ni-OC, Ni-OT and Ni-N by 1.5, 2, 3 and 4. The acceptability of the refinement was tested by looking at the resulting cell parameter averaged over 30 ps of simulations in the *NPT* ensemble. Table 3-2 lists the average cell parameters obtained from each potential.

Multiplying factor for $\varepsilon_{Ni\text{-}X}$ parameters	***1***	***1.5***	***2***	***3***	***4***	***5***	***original cell parameter***
Resulting cell parameter /Å	27.936	28.127	27.822	28.098	27.859	27.495	28.804

Table 3-2 Cell parameters obtained after multiplying the ε value of MNI-OC, MNI-OT and MNI-N6R pair potentials by different factors

Table 3-2 shows that the multiplying factors that led to simulated cell parameters after 30 ps of simulation in the *NPT* ensemble that better reproduced the experimental cell parameter than the CHARMM22 force field (multiplying factor equal to 1) are 1.5 and 3. However, after 200 ps of simulation, the system for which the $\varepsilon_{Ni\text{-}X}$ parameters were multiplied by 3 underwent a sudden reduction in cell volume while the cell parameter for the system for which $\varepsilon_{Ni\text{-}X}$ parameters were multiplied by 1.5 roughly maintained the same volume throughout the 200 ps of simulation. Therefore, the force field with these new $\varepsilon_{Ni\text{-}X}$ parameters was used as a benchmark for subsequent improvements.

Then, in an iterative way, the σ parameters of the atom pairs for which the RDF obtained after simulation did not match the RDF of the original crystal structure were refined. The differences in Lennard-Jones parameters between this refined force field and the CHARMM22 force filed are summarized in table 3-3 for the σ parameters and 3-4 for the ε parameters.

	MNI-N6R	***MNI-C***	***N6R-OC***	***OC-OT***	***N6R-OT***
CHARMM22 σ value /Å	2.5212	2.5569	3.1092	2.8598	3.0112
refined σ value /Å	2.3234	2.6310	3.2092	3.0598	3.2980

Table 3-3 Values of CHARMM22 and refined σ parameters

	MNI-OC	***MNI-OT***	***MNI-N6R***
CHARMM22 ϵ value /kcal.mol^{-1}	0.89191E-01	0.87207E-01	0.67082E-01
refined ϵ value /kcal.mol^{-1}	0.13378	0.13081	0.10062

Table 3-4 Values of CHARMM22 and refined ϵ parameters

Table 3-5 shows a comparison between the cell parameters averaged over 500 ps of simulation in the *NPT* ensemble when using the CHARMM22 and the refined force field.

	CHARMM22 force field	***refined force field***	***original structure***
Cell parameter /Å	27.696 +/- 0.110	28.048 +/- 0.113	28.804

Table 3-5 Cell parameters averaged over 500 ps of simulation at 150 K and 0.1 kbar in the NPT ensemble using the CHARMM22 force field and the refined force field.

Table 3-5 shows that there is an improvement in the cell parameter when using the new refined force field. Indeed, the refined force field leads to a simulated cell parameter that differs by 2.63 % from the cell parameter of the original structure while when it is the CHARMM22 force field that is used this difference becomes 3.85 %.

Figure 3-44 shows the RDFs obtained after 500 ps of simulation in the *NPT* ensemble using the refined force field and the CHARMM22 force field compared to the equivalent RDFs obtained from the original crystal structure.

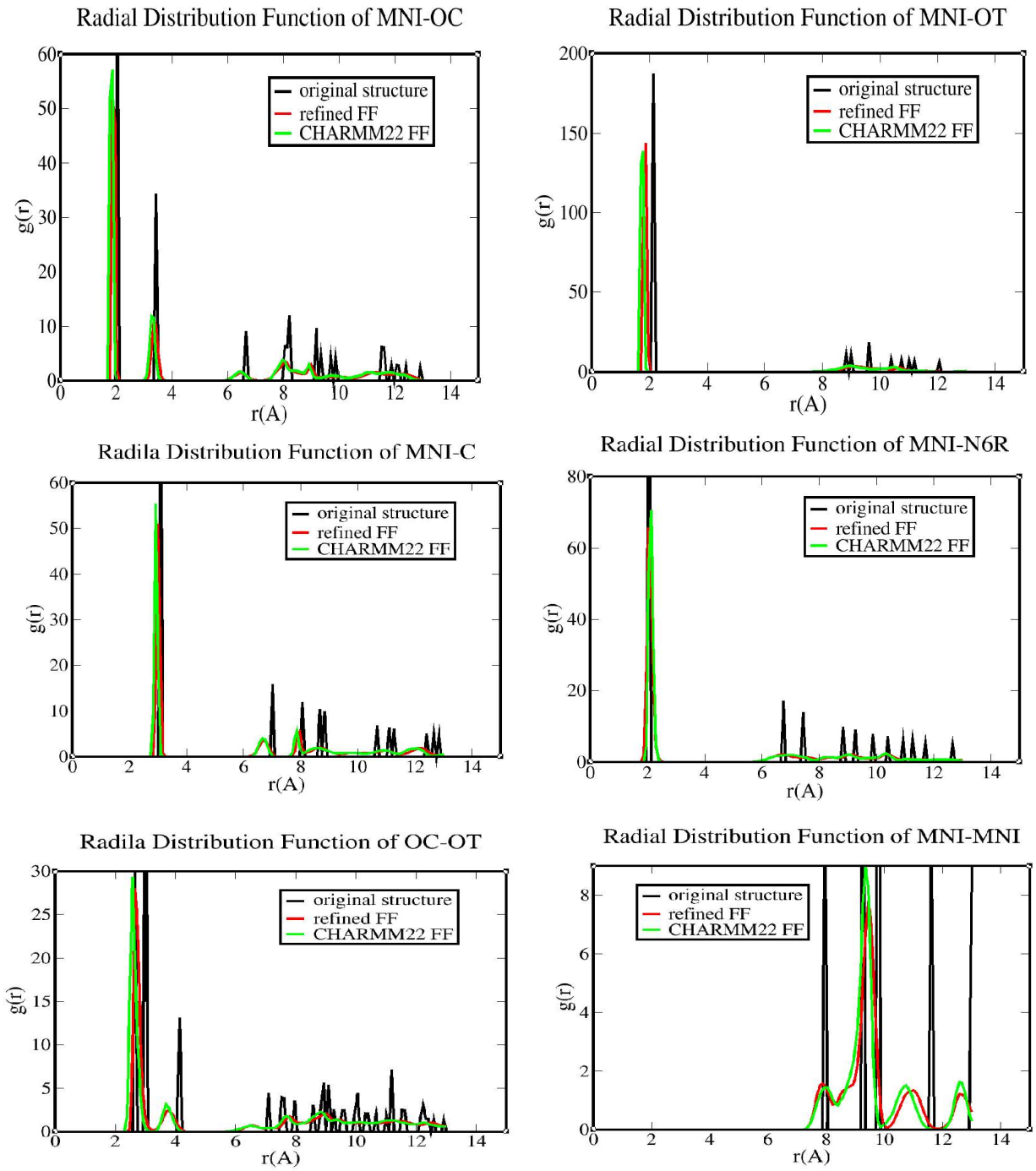

Figure 3-44 Radial distribution functions averaged over 500 ps of simulation in the NPT ensemble using the refined force field and the CHARMM22 force field compared to the original structure

Figure 3-44 shows that there is a slight improvement in the matching of RDFs with the RDFs of the original crystal structure when using the force field with the refined Lennard-Jones parameters that when using the CHARMM22 force field. Indeed, it is noticeable from figure 3-44 that for all the RDFs the position of the first peak obtained using the refined force field matches slightly better the

position of the first peak of the original structure than the peak obtained using the CHARMM22 force field. However this improvement is limited and both RDFs resulting from simulations using the refined Lennard-Jones parameters and CHARMM22 parameters are very similar to each other. Even for the long ranged RDFs best exemplified by the Ni-Ni RDFs it is clear that the two RDF plots resulting from the refined force field and the CHARMM22 force field are very similar, even though the RDF resulting from the refined force filed match slightly better the positions of the peaks of the original structure.

Many other attempts were made to fit the simulated RDFs to the original RDF. However most of these refinements led to unstable MOFs. This is especially true for the Ni-OT potential, where the difference between simulated and original RDF is the greatest. But any further modification of the parameters of the pair potential led to framework instability.

Simulations using Buckingham potentials with parameters obtained from GULP have also been performed to obtain Ni-OT bond distances after simulations that matched the Ni-OT bond distance of the original crystal structure. However, the study of the evolution of the cell volume with time showed that this attempt did not lead to a better force field since the volume obtained after simulation was even lower than the volume obtained using all Lennard-Jones potentials.

Quantum mechanical calculations were therefore needed since, as seen from the RDFs described in figure 3-44, fitting of van der Waals parameters alone has not proved enough to get data that matched very accurately experimental data. Indeed, it is noticeable from these RDFs that the Ni-OC and especially (in a much more pronounced way) Ni-OT parameters do not exactly reproduce the RDFs of the original crystal structure. Any attempt to further improve this matching by refining either ε or σ parameters has led to the instability and eventually phase change of the three-dimensional structure of the framework.

3.4.2.2 Refinement of electrostatic interactions.

After this van der Waals parameters refinement process, quantum mechanical calculations on the ligand molecules that surround the nickel ions have been performed. Due to the reasons described previously, quantum mechanical calculations on a $Ni(BTC)_2pyr_2alc$ unit was not possible. Therefore electronic structure calculations for the determination of partial charges were performed on the isolated ligand molecules. These calculations, therefore did not include charge transfer from ligands to metal, but they are consistent with our aim of producing a potential that is simple and transferable by design.

In a molecule, partial charges on each atom cannot be determined exactly, there is always an uncertainty coupled with these determinations whichever method is used. This is due to the fact that atomic charges are not a measurable property of a molecule. Indeed, when doing quantum calculations, molecules are not constituted by well localized atoms but by nuclei and electrons.

To determine to which nuclei some electrons belong to can be difficult. Indeed, if we consider the equation of the electron density of a molecular orbital (which determines the number of electrons belonging to the molecular orbital), we can observe a part of the equation which represents the overlap population. The difficulty to determine the partial charge on each nuclei comes from the fact that there is no unique way to determine to which nuclei each electron of the overlap population belongs to. Different methods for the calculation of partial charges will lead to different values. Sometimes the differences between these values can be very significant. In this work, the charge on nickel atoms was chosen to be +2*e* for all systems. Then a series of electronic structure calculations using different methods and basis sets were tried to determine what is the force field that best describes the system. The methods used were the unrestricted density functional theory (UDFT)[7-10] and the UMP2[11] method. The functional used for the UDFT calculations was the hybrid UB3LYP[7-10] functional. The basis sets used were 6-311G, 6-311G** and cc-pVTZ basis sets. The population analysis method used for the calculation of the partial charges was the ESP (electrostatic potential) population analysis method[12-17] which belongs to the class of MEP methods (molecular electrostatic potential).[18, 19] The ESP method has been chosen because of the fact that it has proved to be highly

accurate in simulation of condensed-phase properties, and to handle well inter-molecular properties. More importantly, it is designed to reproduce the forces between molecules optimally, and so is the appropriate method for use with MD.

As described previously, several force fields were generated by using different methods and basis sets for the calculation of the partial charges on the different ligand molecules of the octahedral unit. Tables 3-6 and 3-7 show the partial charges obtained on the equatorial ligands of the octahedral unit, respectively pyridine and 4,5-octanediol molecules, using the UMP2 method and the 6-311G basis set. Charges from the CHARMM22 force field were retained on the BTC molecules since BTC molecules with these charges led to cell parameters that better coincided with the experimental cell parameters.

	q / e	***q / e***
	CHARMM22	***UMP2/6-311G/ESP***
C6R	0.22800	0.49977
HA	0.10800	0.04688
C6R	-0.15200	-0.55803
HA	0.10800	0.21003
C6R	-0.15200	0.23853
HA	0.10800	0.10376
C6R	-0.15200	-0.54746
HA	0.10800	0.20795
C6R	0.22800	0.48119
HA	0.10800	0.05302
N6R	-0.54000	-0.73564

Table 3-6 Partial charges on the pyridine molecules obtained from the CHARMM22 force field and quantum mechanical calculations using the uMP2 method and the 6-311G basis set.

	q / e	***q / e***
	CHARMM22	***UMP2/6-311G/ESP***
CT	-0.04000	0.48727
HC	0.11000	0.13252
CH2E	0.06000	-0.55483
CH2E	0.06000	0.53002
CH3E	0.06000	-0.32348
OT	-0.65000	-0.76667
HO	0.40000	0.48085
CT	-0.04000	0.58186
HC	0.11000	0.11073
CH2E	0.06000	-0.59783
CH2E	0.06000	0.54672
CH3E	0.06000	-0.32486
OT	-0.65000	-0.77981
HO	0.40000	0.47751

Table 3-7 Partial charges on the 4,5-octanediol molecules obtained from the CHARMM22 force field and quantum mechanical calculations using the uMP2 method and the 6-311G basis set.

It is noticeable from tables 3-6 and 3-7 that quantum mechanical calculations using the unrestricted MP2 method and the 6-311G basis set gave higher negative values of the partial charges of the electronegative O and N atoms of alcohol and pyridine molecules than the values of the partial

charges obtained from the CHARMM22 force field. Since these electronegative oxygen and nitrogen atoms are bound to the positively charged metal center, more electronegative ligand donors lead to stronger bonds between nickel-oxygen and nickel-nitrogen atoms. It is likely that this increase in bond strength will lead to higher stability of the octahedral building units and of the overall framework.

Another significant difference between the two charge sets is that, after quantum mechanical calculations, a higher negative charge on the oxygen atoms of the alcohol molecules and a higher positive charge on the hydrogen atoms bound to these oxygen atoms have been obtained, therefore leading to hydroxyl groups with higher dipole moments. Since these hydroxyl groups are involved in hydrogen bond formation with the carboxylic groups of the BTC molecules, higher dipole moments of the hydroxyl groups generate stronger hydrogen bonds between the equatorial alcohol molecules and the axial BTC molecules. These stronger hydrogen bonds play a key role in stabilizing the three-dimensional structure. Indeed, as we have described in chapter one, the main structure-determining factors of metal-organic frameworks are the electronic structure of the metal atoms and the configuration of the organic linkers between these metal centers. In the metal-organic framework studied in this thesis the organic linker is the BTC molecule. Therefore the configuration of the BTC molecules and the way they are oriented comparatively to each other are of critical importance for the three-dimensional configuration of the whole framework. Since the hydrogen bonds between alcohol and BTC molecules impede rotation of the BTC molecules, the fact that this hydrogen bond has been strengthened is probably the reason why the framework got more stable and that the cell parameters obtained after simulations using the force field with these new partial charges better matched the cell parameters of the original crystal structure. Indeed, a 1ns simulation in the *NPT* ensemble at 150 K using these partial charges obtained from quantum mechanical calculations using the unrestricted MP2 method and the 6-311G basis set led to an average cell parameter of 28.343 Å. The cell parameter of the original crystal structure is 28.804 Å therefore a difference of only 1.6 % has been obtained with the cell parameter of the original structure. This is very good agreement considering the complexity of the system studied here. Simulations in the *NST* ensemble (using the last configuration obtained from the 1 ns simulation in the *NPT* ensemble as the

starting configuration) led to the average cell parameters described in table 3-8 after 500 ps of simulation at 150 K and 0.1 kbar. The force field used is the FF-1 force field consisting of the refined van der Waals parameters of tables 3-3 and 3-4 and the partial charges of tables 3-6 and 3-7 obtained from quantum mechanical calculations (see appendix for details of this force field).

a/Å	***b/Å***	***c/Å***	***α***	***β***	***γ***
28.25 +/- 0.11	28.54 +/- 0.11	28.38 +/- 0.11	90.29 +/- 0.36	91.70 +/- 0.36	89.94 +/- 0.36

Table 3-8 Cell parameters averaged over 500 ps of simulation in the NST ensemble using the partial charges in tables 3-6 and 3-7

Table 3-8 shows that even in the *NST* ensemble, simulations using the force field with partial charges on alcohol and pyridine molecules calculated from quantum mechanical calculations with the unrestricted MP2 method and the 6-311G basis set resulted in cell parameters that match very well the cell parameters of the original crystal structure. It is particularly noteworthy that the cubic symmetry is maintained for this highly porous material even in constant stress simulations. The overall volume is also very close to that of the target structure. This strongly suggests that this new force field reproduces well interactions within the framework and therefore is a good model to use for subsequent studies.

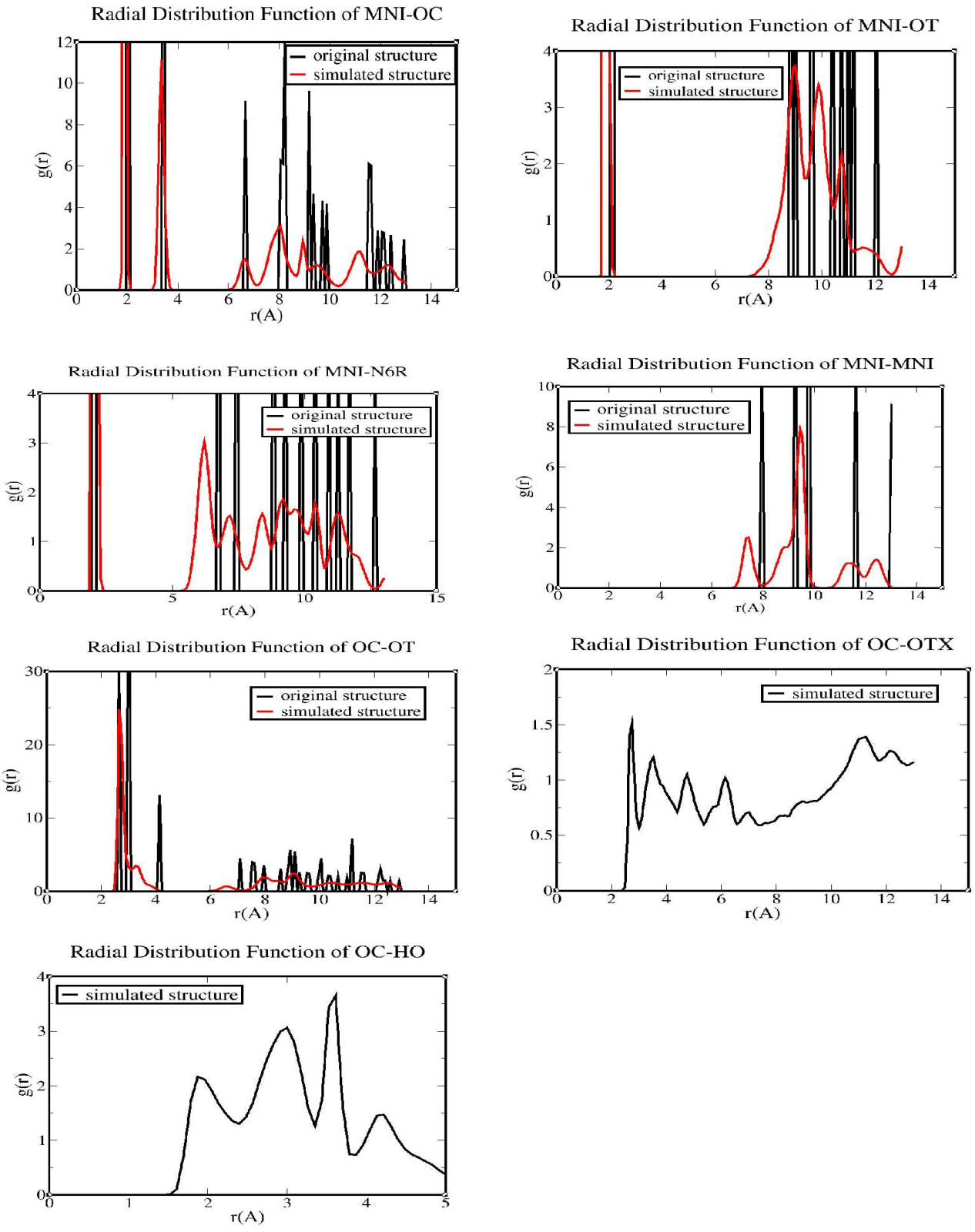

Figure 3-45 Radial distribution functions obtained after 500 ps of simulation in the NST ensemble using the force field with the partial charges in tables 3-6 and 3-7. OC = oxygen atoms of BTC molecules, OT = oxygen atoms of alcohol ligand molecules, OTX = oxygen atoms of alcohol solvent molecules, MNI = nickel atoms, N6R = nitrogen atoms and HO = hydrogen atoms of hydroxyl groups of alcohol molecules.

Figure 3-45 presents key RDFs of the system. These RDFs show that there still is a difference between the nickel-oxygen bond lengths of the original crystal structure and the simulated one. This difference is moderate for the Ni-OC bond, with the simulated bond length being (2.045 – 1.87) Å = 0.17 Å smaller (compared with 0.41 Å when the CHARMM22 force field was used). The difference between the Ni-OT bond distances is more pronounced, giving d_{exp} – dsim = (2.13 – 1.87) Å = 0.26 Å (compared with 0.458 Å for CHARMM22). Therefore, it is noticeable from these RDFs that a considerable improvement in the reproduction of the nickel-oxygen bond distances of the original crystal structure has been achieved using this refined force field compared to the CHARMM22 force field. In contrast the Ni-N bond length is reproduced to within the resolution of the RDF (compared to a difference of 0.234 Å when the CHARMM22 force field is used): in both cases the position of the first peak is 2.045 Å.

As discussed in the last section, the structure in the RDF at r > 5 Å is very interesting, since this region gives information about the arrangement of the SBUs, and so is crucial for judging the stability of the framework. Figure 3-45 shows that there is generally good agreement for this longer range structure between the original crystal structure and the simulated structure. Thus despite some inadequacy in the description of the SBU, the overall framework is well reproduced. The quality of the agreement is best for the Ni-OC, Ni-OT and Ni-N RDFs, where the peaks of the simulated structure are very well defined and their positions match particularly well to the equivalent peak positions in the original crystal structure. Thus this latest refinement (we will refer to this refined force field as FF-1) gives a good basis for describing the two interpenetrating (10,3)-a nets that make up this MOF structure.

Although a good basis, the structure prediction is not perfect. The Ni-Ni RDF shows qualitative agreement, but the peaks shift to shorter distances in the simulation (e.g 7.9 Å to 7.5 Å for the first peak) and the doublet at about 10 Å becomes strongly asymmetric in the simulation. The inward shift of the peaks is also seen in Ni-N, though is not obvious in the Ni-O RDFs.

The OC-OT, OC-OTX and OC-HO RDFs show that there is hydrogen bond formation between the oxygen atoms of the BTC molecules and the hydrogen atoms of both structural and solvent alcohol molecules. It is observable from these RDFs that the closest distance (first peak) between on one

hand, OC and OT atoms, and on the other hand, OC and OTX atoms, are virtually the same: this distance is 2.7 Å. The peak at 1.9 Å in the OC-HO RDF reveals the hydrogen bond interaction between BTC molecules and alcohol molecules. This hydrogen bond interaction occurs with both structural and solvent alcohol molecules. As described in table 3-7, quantum mechanical calculations have led to hydroxyl groups with a higher dipole moment. That led to strengthening of the hydrogen bonds between BTC and alcohol molecules. This is likely to be the critical factor that led to the fact that cell parameters and interatomic distances within the system after simulation correspond well with those of the original crystal structure.

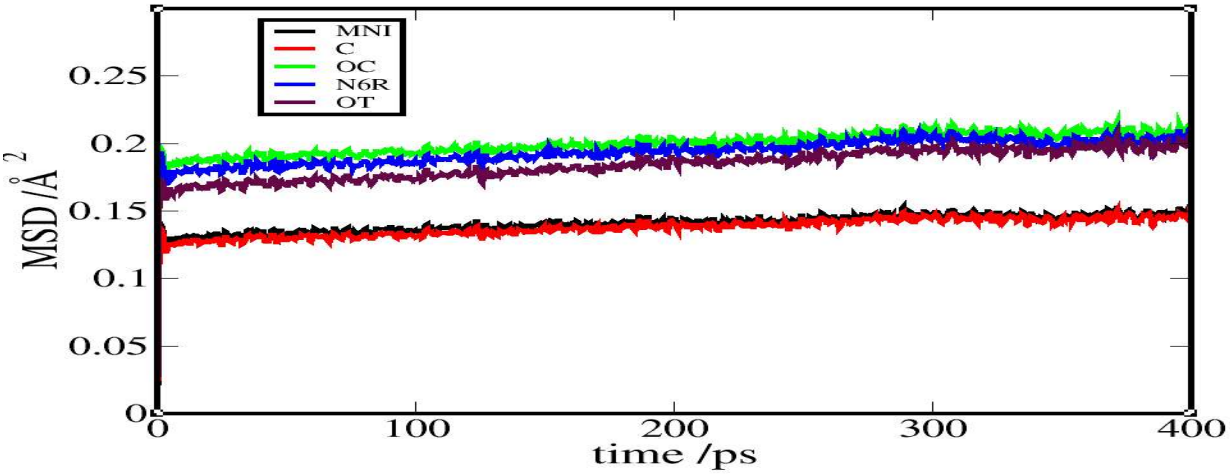

Figure 3-46 Mean square displacement of nickel atoms and heteroatoms of the system using the partial charges in tables 3-6 and 3-7

Figure 3-46 presents the mean square displacement of the nickel, oxygen and nitrogen atoms of the system, calculated from the final 500 ps on an *NST* simulation at 150 K and 0.1 kbar. It is clear that the nickel, oxygen and nitrogen atoms remained confined to their lattice sites during the course of the simulation: no diffusion is evident. This reinforces the earlier conclusion that the structure stayed stable during the simulation with this force field (FF-1).

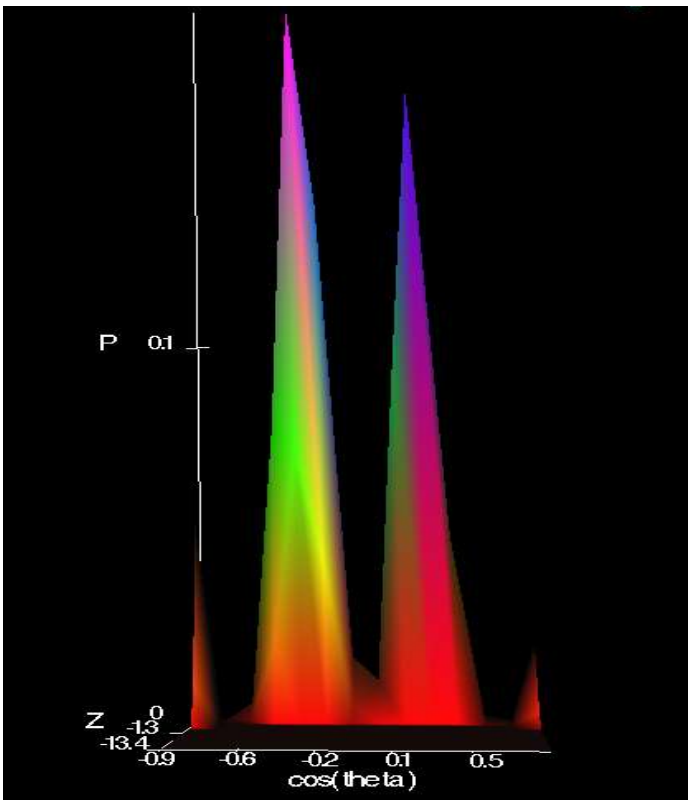

Figure 3-47 ring-ring orientational distribution at150 K

Figure 3-47 presents the orientational distribution of BTC rings around a central BTC ring averaged over 500 ps of simulation in the *NST* ensemble at 150 K and 0.1 kbar. All four peaks are well resolved, again consistent with a stable framework.

Figure 3-48 shows a snapshot of the framework structure after the 500 ps simulation in the *NST* ensemble. This snapshot shows, in accordance with what has been described so far, that the framework has retained the three-dimensional structure of the original crystal structure.

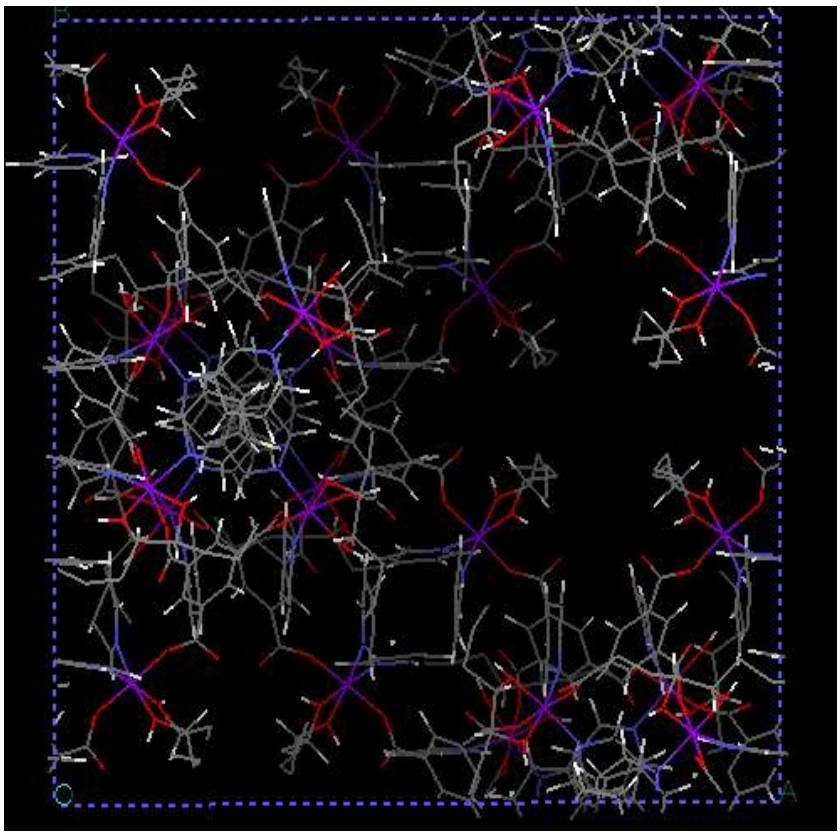

Figure 3-48 Snapshot of the unit cell after 500 ps of simulation at 150 K in the NST ensemble using partial charges in tables 3-6 and 3-7 (solvent molecules were removed for clarity)

A series of force fields with partial charges on alcohol and pyridine molecules obtained from quantum mechanical calculations using other methods, and basis sets were tried on this metal-organic framework.

Study of other force fields

A number of force fields have been developed to try to get the best possible reproduction of experimental data. Table 3-9 shows the cell parameters obtained using a series of force fields that did not lead to a significant reduction in the cell volume during the course of the simulation. These simulations were performed on a system containing 20 solvent molecules at 150 K and 0.1 kbar in the *NST* ensemble.

	α* / °** ***+/- 0.36	***β* / °** ***+/- 0.36***	***γ* / °** ***+/- 0.36***	***a* /Å** ***+/- 0.11***	***b* /Å** ***+/- 0.11***	***c* /Å** ***+/- 0.11***	***Volume /Å^3*** ***+/- 80***
CHARMM22	89.26	90.53	89.82	26.154	28.683	28.024	21020
UMP2 refined: FF-1	88.93	91.72	91.97	28.067	28.828	28.147	22760
UMP2 CHARMM22 : FF-2	90.72	88.83	89.17	28.069	28.281	28.073	22280
UMP2 refined2*: FF-3	87.60	90.77	90.37	27.658	28.980	28.688	22938
UMP2/cc-pVTZ refined	92.36	88.74	91.81	27.84	28.22	27.50	21597
UMP2/cc-pVTZ CHARMM22	90.97	89.62	90.50	27.55	28.67	27.97	22091
UB3LYP refined	90.51	89.59	91.52	28.770	27.751	25.990	20740
UB3LYP CHARMM22	90.12	91.01	88.80	27.922	28.518	27.827	22151
original structure	90.00	90.00	90.00	28.804	28.804	28.804	23898

* Force field modified to get stronger H-bonds between alcohol and BTC molecules

Table 3-9 Cell parameters obtained using a series of force fields at 150 K in the NST ensemble for a metal organic framework containing 20 solvent molecules.

In table 3-9, CHARMM22 means that the force field used is the CHARMM22 force field when it is specified alone. When it is specified along with UMP2 or UB3LYP it means that the van der Waals

parameters were obtained from the CHARMM22 force field but the partial charges on the pyridine and alcohol molecules were obtained from quantum mechanical calculations. When the term refined is used, it means that the refined van der Waals parameters described in tables 3-3 and 3-4 have been used. The UMP2 refined2* force field (FF-3) is similar to the UMP2 refined force field (FF-1) but with $\varepsilon_{OC\text{-}HO}$ multiplied by 5 to strengthen this hydrogen bond and $\sigma_{OC\text{-}HO}$ further refined (from 1.735 Å in FF-1 to 1.485 Å in FF-3) to enable the corresponding H-bond distance to match that in the crystal structure. For simplification, the UMP2 refined force field will be referred to as FF-1, the UMP2 CHARMM22 force field will be referred to as FF-2 and the UMP2 refined2* force field will be referred to as FF-3.

When it is not notified in table 3-9, the basis set used for quantum mechanical calculations is the 6-311G basis set. These electronic structure calculations have been performed only on the pyridine and alcohol molecules of the metal-organic framework, which are the equatorial ligands of the metal-organic framework. Simulations with partial charges on all three ligand molecules (pyridine, alcohol and BTC molecules) obtained from quantum mechanical calculation have also been performed: but these simulations led to cell parameters that did not match the original cell parameters as well as when these calculations were only performed on the equatorial ligands (pyridine and alcohol).

For the rest of this chapter, only the outcomes of the simulations using the force fields labeled as FF-2 and FF-3 will be analyzed. This choice is motivated by the fact that, in the case of the FF-3 force field, this force field led to a simulated cell volume that matches best the cell volume of the original crystal structure. Indeed, there is a difference of only 4 % between the cell volume obtained after 2 ns of simulation using the FF-3 force field and the original cell volume.

In the case of the FF-2 force field, this choice is motivated by the fact that this force field is the only force field that has been successfully transferred to metal-organic frameworks with other alcohol ligands than 4,5-octanediol, as will be extensively described in chapter 4. Indeed, in chapter 4, a temperature and solvation study on the metal-organic frameworks with 2,3-butanediol and 1,2,6-hexanetriol as alcohol ligands will be presented using the FF-2 force field. It is also noticeable from

table 3-9 that, after the FF-3 and the FF-1 force fields, this force field leads to a simulated cell volume that matches best the cell volume of the original crystal structure.

Figure 3-49 shows key radial distribution functions obtained using the FF-3 force field, compared with the radial distribution functions obtained from the original structure (obtained after 1fs of simulation) and the radial distribution functions obtained using the FF-1 force field. This latter comparison between the RDFs obtained using the FF-3 force field and the FF-1 force field gives interesting informations about the impact of strengthening the hydrogen bond between the BTC molecules and the alcohol molecules on the resulting three-dimensional structure of the framework.

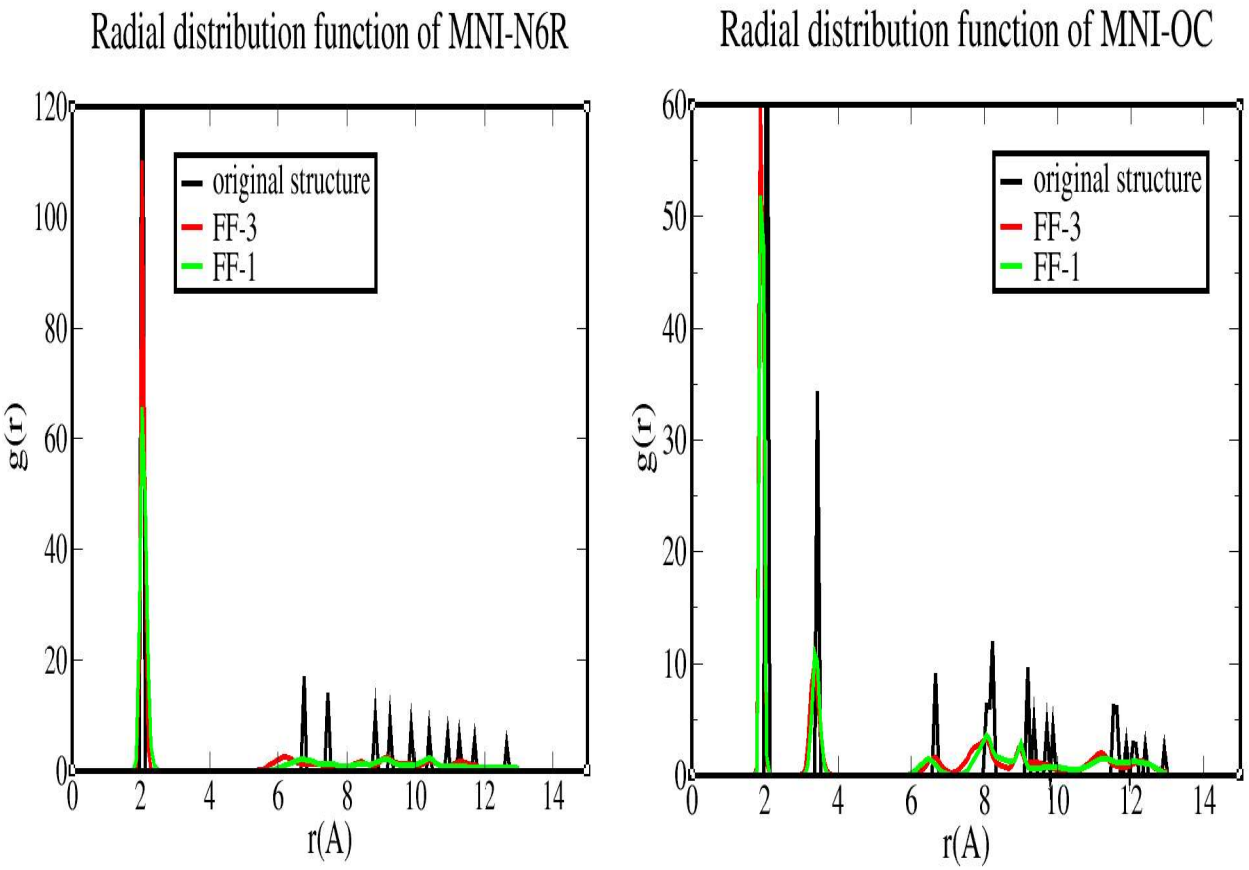

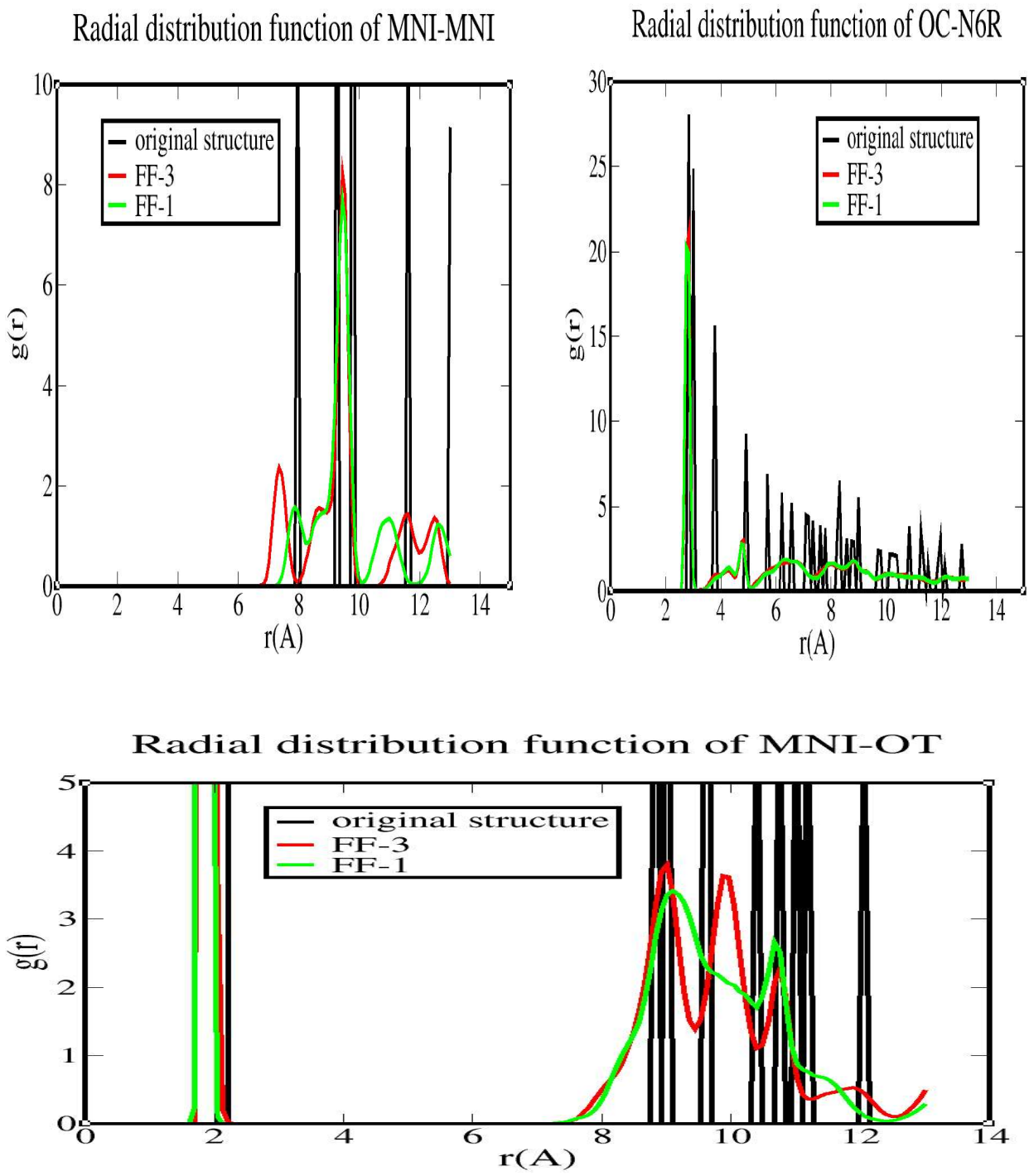

Figure 3-49 Radial distribution functions obtained after 500 ps of simulation in the NST ensemble using the FF-3 force field compared with the RDFs obtained from the original crystal structure and the RDFs obtained from the FF-1 force field.

Figure 3-49 shows that the RDFs obtained using the FF-3 force field are generally similar to the RDFs obtained using the FF-1 force field. Indeed, this is especially evident in the case of Ni-OC and OC-N RDFs where the curve representing the RDFs obtained using the two force fields

practically overlap each other over the range of the RDF. This is also observed for the Ni-N RDFs even though the first peak obtained using the FF-3 force field is sharper than the first peak resulting from the FF-1 force field. This difference in sharpness suggests that the FF-3 force field leads to a simulated framework with the positions of the nitrogen atoms better defined (the amplitude of the Ni-N bond vibration is smaller when the FF-3 force field is used). The main difference between these two force fields is observed in the Ni-OT RDF. Indeed, it is clear from the Ni-OT RDF that the peaks obtained for the FF-3 force field are better defined than the peaks obtained from the FF-1 force field. In the case of FF-3 force field 4 peaks are observable at distances superior to 7 Å while for the FF-1 force field only two peaks are apparent. This Ni-OT RDF therefore suggests that the simulated framework obtained using the FF-3 force field matches slightly better the configuration of the original crystal structure than the simulated framework obtained using the FF-1 force field. This shows that strengthening the hydrogen bond between the BTC molecules and the alcohol molecules leads to a better reproduction of the experimental structure. This points out the importance of this hydrogen bond in stabilizing the framework.

To verify the fact that the atomic positions stayed fixed during the course of the simulation, and therefore that the framework stayed stable, the mean square displacement of some atoms of the framework with time have been calculated and these are presented in figure 3-50 for the FF-3 force field. The simulation was performed at 150 K and 0.1 kbar in the *NST* ensemble for a system containing 20 solvent molecules in the unit cell. The simulation was performed for 800 ps.

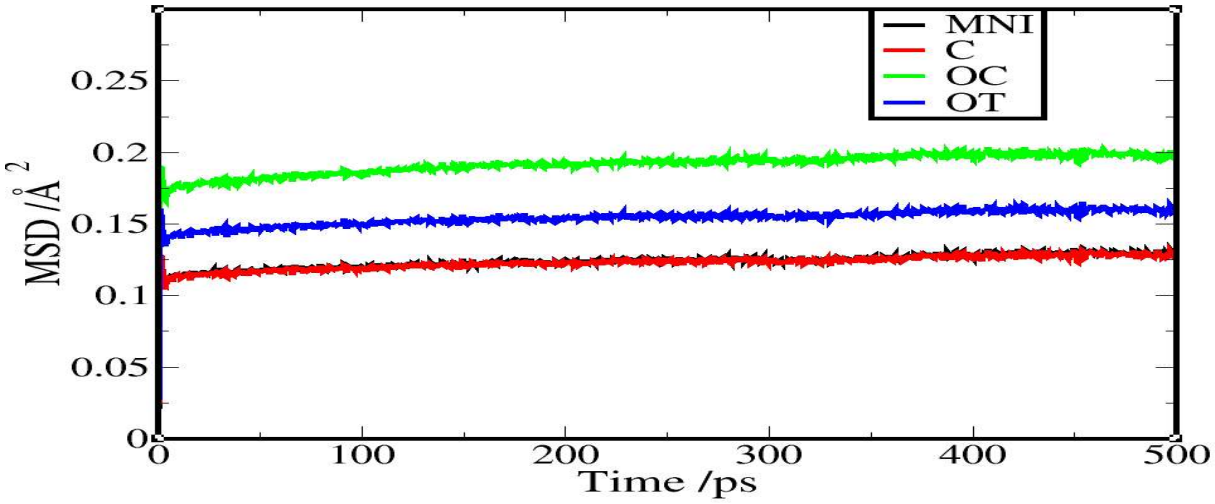

Figure 3-53 Evolution of the mean square of some atoms of the framework with time when the FF-3 force field is used.

Figure 3-50 shows that the atoms constituting the framework do not display any significant diffusion. The evolution of the mean square displacement of these atoms with time is characteristic of a solid: the long-time behavior is a straight line of zero slope. This confirms the stability of the framework during the course of the simulation.

To look more closely at the arrangement of molecules and the order within the framework when using the FF-3 force field a study of the orientational distribution of some groups and molecules constituting the framework has been performed. Figure 3-51 shows the orientational distribution of the benzene rings of the BTC molecules around a central benzene ring. The angular distribution of these benzene rings has been average over 800 ps of simulation at 150 K and 0.1 kbar in the *NST* ensemble.

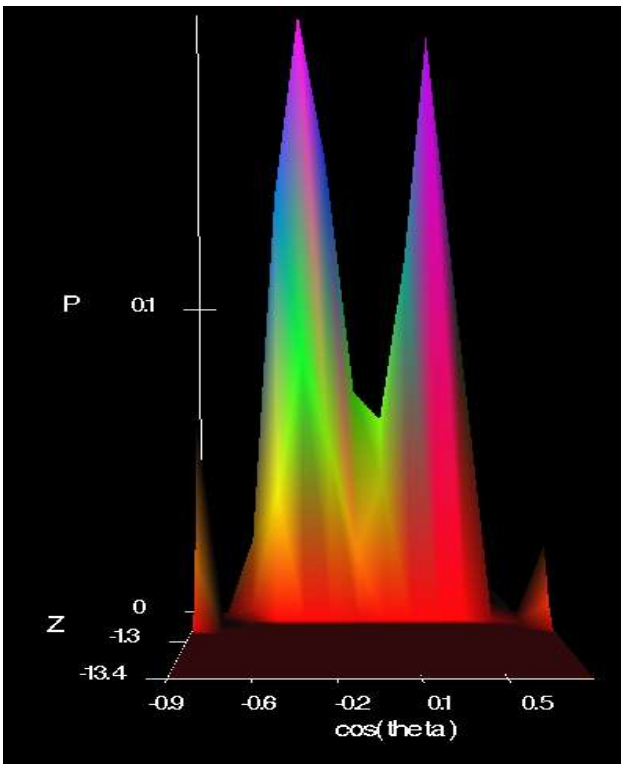

Figure 3-51 ring-ring orientational distribution when using the FF-3 force field.

Although the 4 peaks are present and well resolved, the two central peaks are not perfectly resolved. Thus there must be some enhanced vibrational motion or rotational disorder in this rings with FF-3. This was unexpected since the study of the RDF and the study of the evolution of the cell volume with time suggested that this force field led to the framework that was expected to experience the less deviation from the reference structure. However, even though figure 3-51 shows that there is some limited rotation of the benzene rings of BTC molecules, the framework stayed stable during the course of the simulation and retained its original three-dimensional structure.

figure 3-52 shows a snapshot of this framework obtained after 2 ns of simulation.

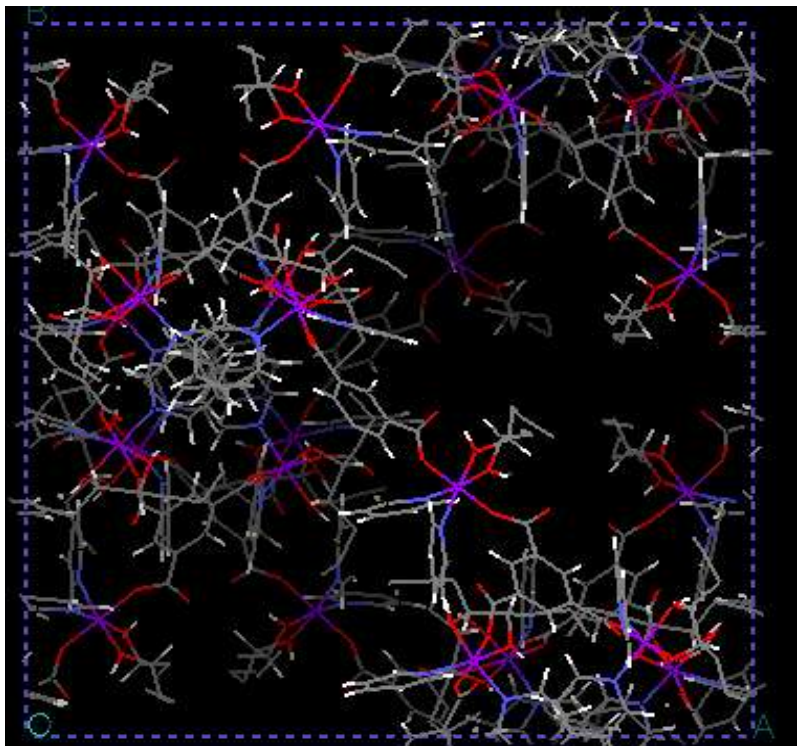

Figure 3-52 Snapshot obtained after 2 ns of simulation in the NST ensemble the FF-3 force field.

It is clear from figure 3-52 that the framework stayed stable over the course of the 2 ns simulation. Indeed, the framework has retained its three-dimensional structure consisting of the two interpenetrating (10,3)-a nets.

The conclusion drawn from these analyzes is that the FF-3 force field leads to a stable framework that gave a cell volume and RDFs that best matched those of the original structure. The study of the evolution of the root mean square displacement of a number of the atoms of the framework with time showed that these atoms did not experience significant motions and hence that the structure remained stable. The snapshot of the framework after 2 ns of simulation also showed that this framework stayed stable and retained its original three-dimensional structure. The only motion that has been deduced from these analyzes is that of the benzene rings of the BTC molecules which have experienced some limited rotation during the simulation. The main conclusion to draw from this study is that, as shown by the simulated cell volume and by the study of the RDFs, increasing the strength of the hydrogen bond between BTC molecules and alcohol molecules has led to a very stable framework and the force field provides a reasonable, flexible, model of the real MOF, though not yet a definitive model.

Since the only force field that has successfully been transferred to other metal-organic frameworks is the FF-2 force field (see chapter 4), it is also important to analyze the structural data obtained from simulations using this force field. This force field consists of van der Waals parameters and partial charges on BTC molecules obtained from the CHARMM22 force field and partial charges on alcohol and pyridine molecules obtained from quantum mechanical calculations using the UMP2 method and the 6-311G basis set. As shown in table 3-9 this force field led to simulated cell parameters that reproduced well the cell parameters of the original crystal structure.

Figure 3-53 presents the evolution of the root mean square displacement of some atoms of the framework with time for a simulation performed at 150 K and 0.1 kbar in the *NST* ensemble when the FF-2 force field is used. The simulation was performed during 500 ps.

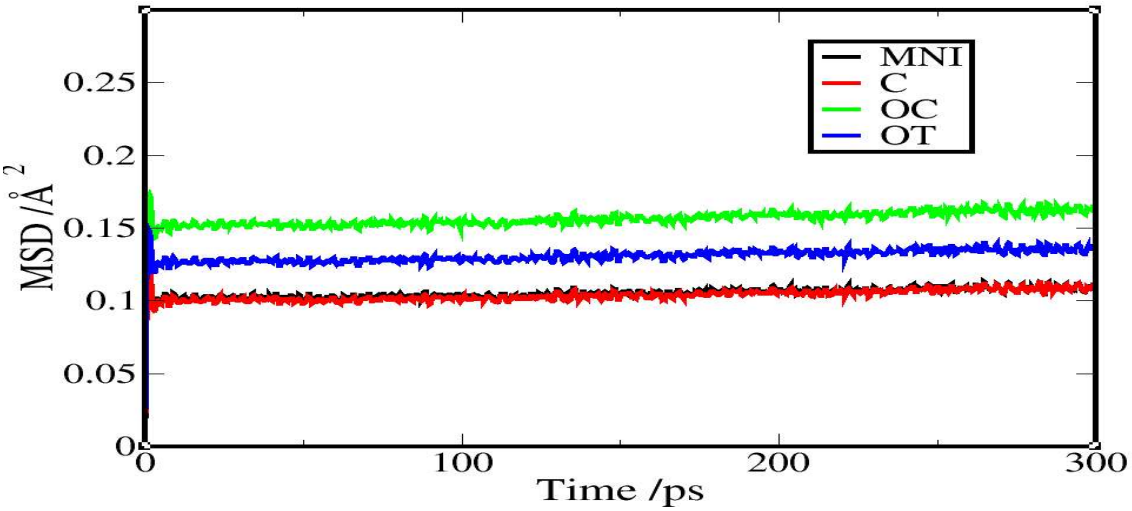

Figure 3-53 Evolution of the mean square displacement of some atoms of the framework with time when the FF-2 force field is used.
Simulations were performed at 150 K and 0.1 kbar in the NST ensemble.

It is clear from figure 3-53 that the positions of the atoms of the framework remained bounded in the neighbourhood of their lattice sites during the course of the simulation, indicating a stable framework model under these conditions.

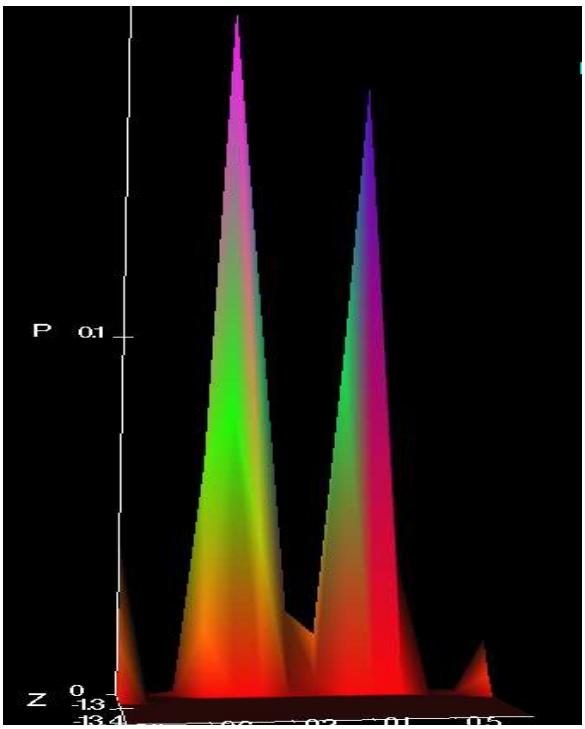

Figure 3-54 ring-ring orientational distribution when using the FF-2 force field. Simulations were performed at 150 K and 0.1 kbar in the NST ensemble.

The orientational distribution of the benzene rings of BTC molecules around a central benzene ring corroborates this (see figure 3-54), with the four peaks being much better resolved than for FF-3 . This indicates that the framework has conserved its original three-dimensional structure with a high degree of fidelity during the course of the simulation. This is also seen in the snapshot of the structure at the end of the simulation (figure 3-55). We conclude that this force field is an appropriate force field to model this metal-organic framework.

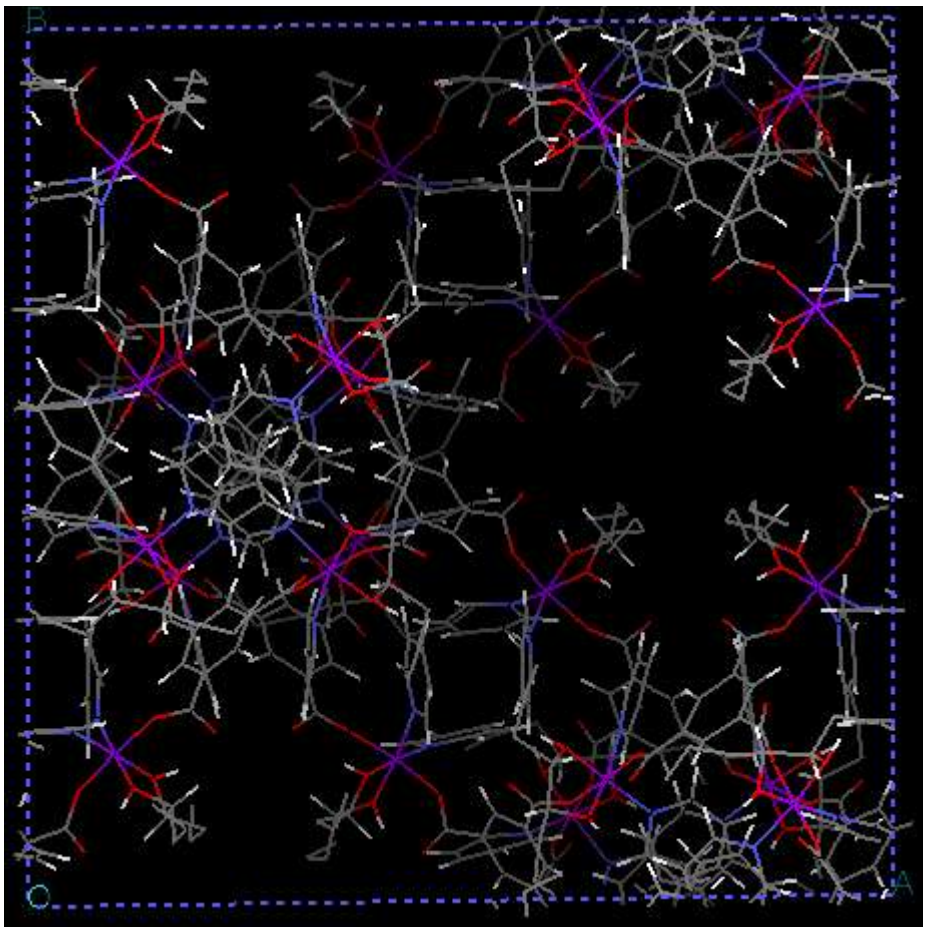

Figure 3-55 Snapshot of the framework obtained after 1 ns of simulation at 150 K and 0.1 kbar in the NST ensemble using the FF-2 force field.

Conclusion

In this work, the Lennard-Jones parameters of the system were successfully fitted to lead to bond distances after simulation that reproduced exactly the bond distances observed in the original crystal structure. Indeed, the study of the RDFs showed that the positions of the first peaks of the RDFs obtained after simulation matched exactly the positions of the first peaks of the RDFs obtained for the original crystal structure. However this RDF study showed that at long distances this match between the peaks of the RDFs obtained after simulation and those of the original crystal structure was not observable anymore. Furthermore, the study of the evolution of the cell volume with time, the evolution of the mean square displacement of nickel atoms with time and the study of the

orientational distribution showed that even though this refined force field led to short ranged interatomic distances, especially Ni-O and Ni-N bond distances, that were in good agreement with those found in the original structure, the overall three-dimensional structure of the framework obtained using this refined force field has experienced phase change during the simulations. The fact that the RDFs obtained after simulations using this force field matched exactly the RDFs of the original crystal structure showed that the $NiBTC_2pyr_2alc$ secondary building units retained their integrity during the course of the simulation and therefore that the Ni-O and Ni-N bonds were not broken. Indeed, this study shows that the phase change of the framework is not due to bonds breaking within a secondary building unit but it rather suggests that the phase change of the framework is due to significant modifications in the way these secondary building units are arranged relatively to each other. This refined force field therefore managed to reproduce accurately the geometry of each secondary building unit but it failed to reproduce accurately the longer range interactions taking place between the different secondary building units that form the framework by assembly. This leading to ligand molecules, although still bound to nickel metal centers, arranged differently relatively to each other and therefore leading to a three-dimensional structure and cell parameters significantly different from the three-dimensional structure and cell parameters of the original crystal structure. This therefore showed that this force field, since it led to a phase change of the framework after few picoseconds of simulation in the *NPT* ensemble at 150 K and 0.1 kbar for a system containing 20 solvent molecules, did not reproduce accurately long range interactions within the framework and therefore that it is not an appropriate force field to use to model this MOF. Faced with this failed attempt to create a force field that reproduces accurately experimental data, a second attempt which met with more success was tried. Indeed, a more careful refinement of Lennard-Jones parameters led to cell parameters and interatomic distances obtained after simulation that matched better the values of the cell parameters and bond distances of the original crystal structure than those obtained when the benchmark CHARMM22 force field is used. Indeed, this refined force field led to a simulated cell parameter that differed from the original cell parameter by 2.63 % while when it is the CHARMM22 force field that is used this difference is 3.85 %. However, this study showed that even though this refined force field reproduced more accurately

experimental data that the benchmark CHARMM22 force field, the extend of this improvement was limited and the refined force field did not reproduce exactly experimental data (RDFs obtained using this refined force field and the CHARMM22 force field were very similar showing little improvement in the reproduction of the original interatomic distances when the refined force field is used compared to the CHARMM22 force field). Indeed, this study showed that electronic structure calculations to determine partial charges on the atoms of the equatorial ligand molecules, namely alcohol and pyridine molecules had to be performed to get force fields that accurately reproduce experimental data. The use of the UMP2 method and the 6-311G basis set for the calculation of the partial charges on pyridine and alcohol molecules proved particularly efficient in improving the force field and getting simulated cell parameters and bond distances that matched accurately the cell parameters and bond distances of the original crystal structure. One of these force fields, the FF-1 force field (see table 3-9), led to simulated cell parameters that differed from the original ones by only 1.6 % when simulations were performed in the *NPT* ensemble and 1.44 % when they were performed in the *NST* ensemble. The FF-1 force field also led to simulated bond lengths that reproduced the original bond lengths much better than the CHARMM22 force field. Indeed, the FF-1 force field led to a simulated Ni-N bond distance that reproduced exactly the Ni-N bond distance of the original structure (compared to a difference of 0.234 Å when the CHARMM22 force field is used), to a Ni-OC (OC = Oxygen atoms of BTC molecules) bond distance that differed from the original Ni-OC bond distance by 0.17 Å (compared to 0.41 Å when the CHARMM22 force field is used) and a Ni-OT (OT = Oxygen atoms of alcohol molecules) bond distance that differed from the original Ni-OT bond distance by 0.26 Å (compared to 0.46 Å when the CHARMM22 force field is used). This study also showed that this match between simulated and experimental data is further improved when the hydrogen bond between BTC molecules and alcohol molecules is strengthened therefore further pointing out the importance of this hydrogen bond in stabilizing the three-dimensional structure of the framework.

3.5 references

[1] O.M. Yaghi, H. Li, T. L. Groy, *J. Am. Chem. Soc*, 1996, 118, 9096-9101.

[2] T.J. Prior, M.J. Rosseinsky, *Inorg. Chem*. 2003, 42, 1564-1575

[3] M. O'Keeffe, M. Eddaoudi, Hailian Li, T. Reineke, O.M.Yaghi, *J. solid. state. chem*, 152,3-20 (2000).

[4] A. F. Wells, *the Geometrical basis of Crystal chemistry. XII. Review of structures based on three-Dimensional 3-Connected Nets*, *Acta Cryst*. (1976). B32, 2619-2626

[5] I. W. Wainer, D. E. Drayer, Drug Strereochemistry, New York 1988, 209-226

[6] M. L. Connolly, *J. Am. Chem. Soc*, 1985, 107, 1118-1124

[7] R. G. Parr and W. Yang, *Density Functional Theory of Atoms and Molecules* (Oxford, New York, 1989).

[8] R. M. Dreizler and E. K. U. Gross, *Density Functional Theory* (Springer-Verlag, New York, 1990).

[9] *Density Functional Methods in Chemistry and Materials Science*, ed. M. Springborg (Wiley, New York, 1997).

[10] A. Szabo and N. S. Ostlund, *Modern Quantum Chemistry* (McGraw-Hill, New York, 1989).

[11] Assessment of the MP2 Method, along with Several Basis Sets, for the Computation of Interaction Energies of Biologically Relevant Hydrogen Bonded and Dispersion Bound Complexes

[12] U. C. Singh, P. A. Kollman. *J. Comput. Chem*. (1984) 5:129–145

[13] C. I. Bayly, P. Cieplak, W. D. Cornell, P. A. Kollman. *J. Phys. Chem*. (1993) 97, 10269–10280

[14] W. D. Cornell, P. Cieplak, C. I. Bayly, P. A. Kollman. *J. Am. Chem. Soc.* (1993) 115, 9620–9631

[15] P. Cieplak, W. D. Cornell, C. Bayly, P. A. Kollman. *J. Comput. Chem*. (1995) 16, 1357–1377

[16] R. J. Woods, R. Chappelle. *J. Mol. Struct.* (2000) 527:149–156

[17] V. M. Anisimov, G. Lamoureux, I. V. Vorobyov, N. Huang, B. Roux, A. D. Jr. MacKerell. *J. Chem. Theory and Comput.* (2005) 1, 153–168

[18] D. E. Williams. *Net atomic charge and multipole models for the ab initio molecular electric*

potential. In: Reviews in Computational Chemistry—Lipkowitz KB, Boyd DB, eds. (1991) 2. New York: Wiley VCH. 219–271

[19] M. M. Francl, L. E. Chirlian. *The pluses and minuses of mapping atomic charges to electrostatic potentials. In: Reviews in Computational Chemistry*—K. B. Lipkowitz, B. D. Boyd, eds. (2000) 14. New York: Wiley VCH. 1–31

4 Transferability of the force fields to similar metal-organic frameworks

4.1 Overview

A detailed study of a metal-organic framework with 4,5-octanediol as its alcohol ligand has been described in chapter 3. In that study we showed that an "off-the-shelf" force field (CHARMM22) was incapable of accurately describing the MOF. The failure stemmed from both the electrostatic model of the organic species and the organic-inorganic interaction terms. Therefore, a refinement process aimed at fitting nickel-oxygen bond distances, nickel-nitrogen bond distances and the cell parameters of the simulated system to experimental data was performed. This refinement process is described in detail in section 3.4.2 of this thesis. In this chapter, some of the force fields used successfully on the MOF with 4,5-octanediol as its alcohol ligand, will be tested on MOFs with different alcohol ligands. Simulations with two different MOFs, designed to test the transferability of the refined force fields developed in chapter 3, are reported. The first included 2,3-butanediol, and the second 1,2,6-hexanetriol, at the equatorial sites in the secondary building unit (SBU). Crystal structures for both have been taken from the Cambridge Structural Database. For 1,2,6-hexanetriol the crystal structure contains some disorder. The alcohol binds to the Ni^{2+} via the 1,2-diol but there is two-fold disorder in the attachment site for the rest of the alcohol. Further, the ends of the diol are too mobile to be resolved, and so the crystal structure actually reports a 4,5-octanediol ligand. To initialise our simulations, one propylene group was removed (random choise) from each octanediol and replaced by a hydrogen; the terminal methyl group on each remaining propyl chain was then replaced by a CH_2CH_2OH group, hence resulting in 1,2,6-hexanetriol.

The purpose of this chapter is to investigate the transferability of the force fields developed in section 3.4.2 by using them to simulate the MOFs based on both 2,3-butanediol and 1,2,6-hexanetriol. Simulations will first be performed at a temperature of 10 K using the best force fields identified in section 3.4.2. Then, for the force field where the transferability was judged to be most successful at 10 K, a solvation and temperature study will be performed.

4.2 Simulation details

To investigate the transferability of our force fields, MD simulations were performed on MOFs containing 2,3-butanediol and 1,2,6-hexanetriol molecules as bidentate ligands bound equatorially to the metal centers. Like all other simulations performed for this thesis, the simulation package used for this chapter was DLPOY2. Simulations were performed both in the *NPT* and *NST* ensembles. Unless otherwise noted, the time step used was 1 fs. Simulations were performed for a minimum of 500 ps before analysis. When solvent molecules were first added to the system, time steps of 0.1 fs were used during an initial relaxation phase. This was because inserting enough solvent to obtain the higher solvent contents was achieved only by allowing significant framework/solvent overlap in the initial configuration, and the resulting large forces required very short time steps to avoid catastrophic numerical integration errors occurring during the relaxation. The EWALD summation was used to calculate electrostatic interactions. All simulations were performed using the Hoover thermostat and barostat, with a relaxation time constant of 0.5 ps for the thermostat and a relaxation time constant of 1 ps for the barostat.

Partial charges of the atoms of metal-organic frameworks containing 2,3-butanediol and 1,2,6-hexanetriol molecules as their equatorial alcohol molecules were determined by quantum mechanical calculation. These were performed using the Gaussian 03 software package and using the methods, functionals and basis sets described in section 3.4.2.2. Partial charges were only required for the alcohols, since charge models for all the other constituents of the metal-organic frameworks had already been identified in section 3.4.2.2.

4.3 Result of simulations

In this section, a detailed MD simulation study of the MOF with 2,3-butanediol as its alcohol ligands will be described.

4.3.1 Molecular Dynamics simulations on a metal-organic framework with 2,3-butanediol as its alcohol ligands.

In a first instance, MD simulations were performed on the unsolvated MOF. In this study the effect of temperature on this unsolvated MOF and the sensitivity of the force field used was investigated. The effect of temperature on the solvated MOF was conducted as a second study.

4.3.1.1 Simulations on the unsolvated system

FF-2 force field

In this section and for most of this chapter, the force field used for simulations is the FF-2 force field (see table 3-9 and appendix). As described in chapter 3, this force field led to simulated 3D structure and cell dimensions of the 4,5-octanediol as alcohol ligand MOF that matched well the reference crystal structure (see table 3-9).
Table 4-1 shows the average cell parameters (averaged over the last 500 ps of simulation) and the cell parameters of the final configuration of the metal-organic framework, obtained after 1 ns of simulation in the *NPT* ensemble, at three different temperatures

	10 K	***100K***	***150K***	***original cell***
Average cell parameter/ Å	27.88 +/- 0.11	27.88 +/- 0.11	25.81 +/- 0.21	28.40
Cell parameter of the final configuration/ Å	27.88	27.91	25.40	28.40

Table 4-1 Cell parameters obtained after simulations in the NPT ensemble at three different temperatures and 0.1 kbar. (for the 150 K temperature the simulation was ran for only 500 ps).

An interesting observation which can be made from table 4-1 is that at 10 K and 100 K, the average cell parameters and the cell parameters of the final configuration of the system are similar to the cell parameter of the original crystal structure, differing by less than 2%. However, at 150 K the simulated cell actually contracts, leading to a substantial discrepancy (10 %) from the experimental crystal structure. This suggests that at 10 K and 100 K the framework stayed stable during the course of the simulation while at 150 K the framework underwent some sort of structural change. Thus the framework force field does provide mechanical stability for the correct structure, but some degree of thermal instability is apparent in the absence of solvent. We note that structural changes on desolvation are observed in experiments, but on a much longer time scale.

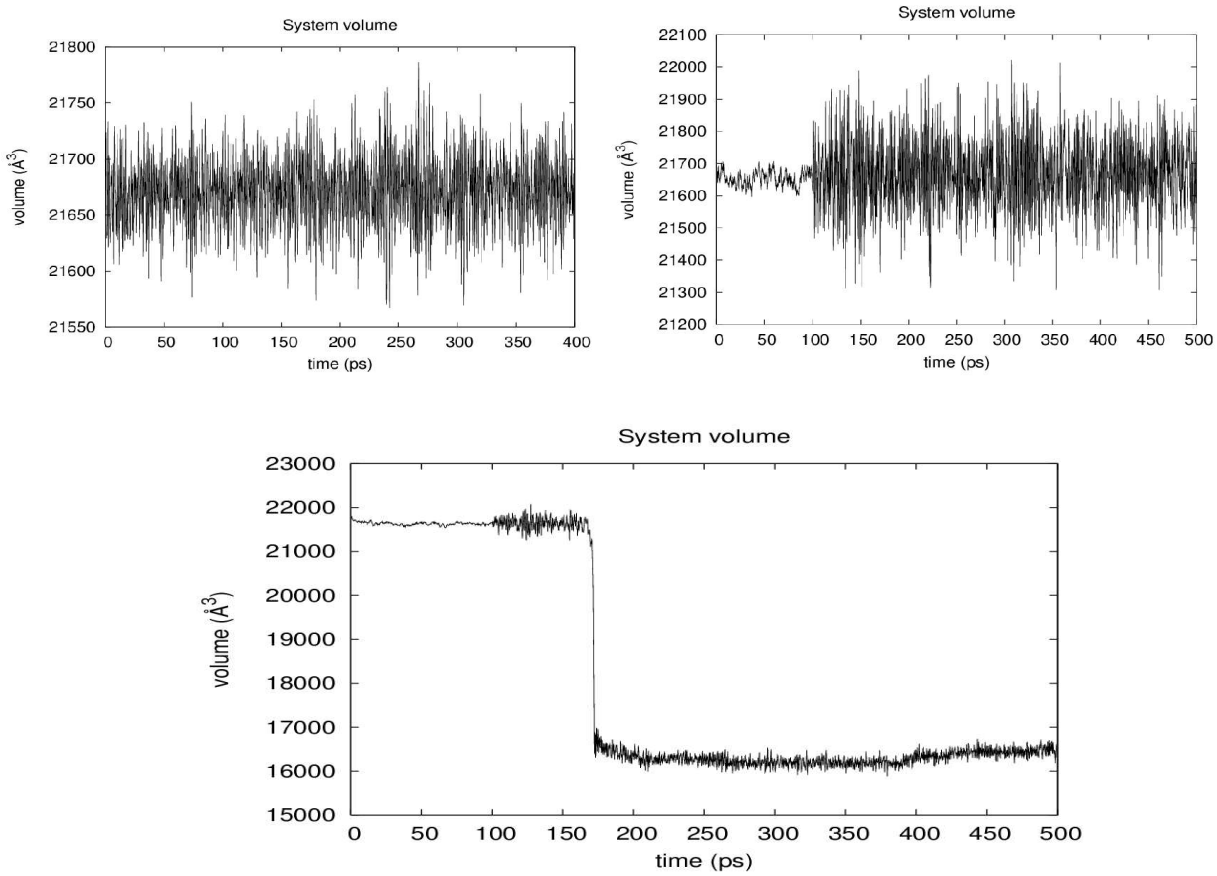

Figure 4-1 Evolution of the system volume with time at a) 10 K (top left), b) 100 K (top right) and c) 150 K (bottom). Temperature rescaling was used during an initial 100 ps equilibration period for simulations at 100 K and 150 K.

The reason for this is readily explained by examining the cell volume as a function of time in these simulations (see figure 4-1). The volume is, indeed, stable at the lower temperatures, but at 150 K there is a sudden and substantial drop in the volume of the system after around 170 ps of simulation. Indeed, the rapidity of the change suggests that a first order phase change has occurred 1/m with this force field and for the unsolvated material. Further, the transition temperature of around 150 K would be consistent with the temperature of 200 K at which the framework structure was observed to change in chapter 3. The fact that at 150 K, the volume stayed stable for relatively a long period of time would suggest that this temperature is an upper bound to the transition temperature.
A study of the evolution of the mean square displacement with time, for key atoms within the framework has been performed to examine the nature of the phase change in more depth.

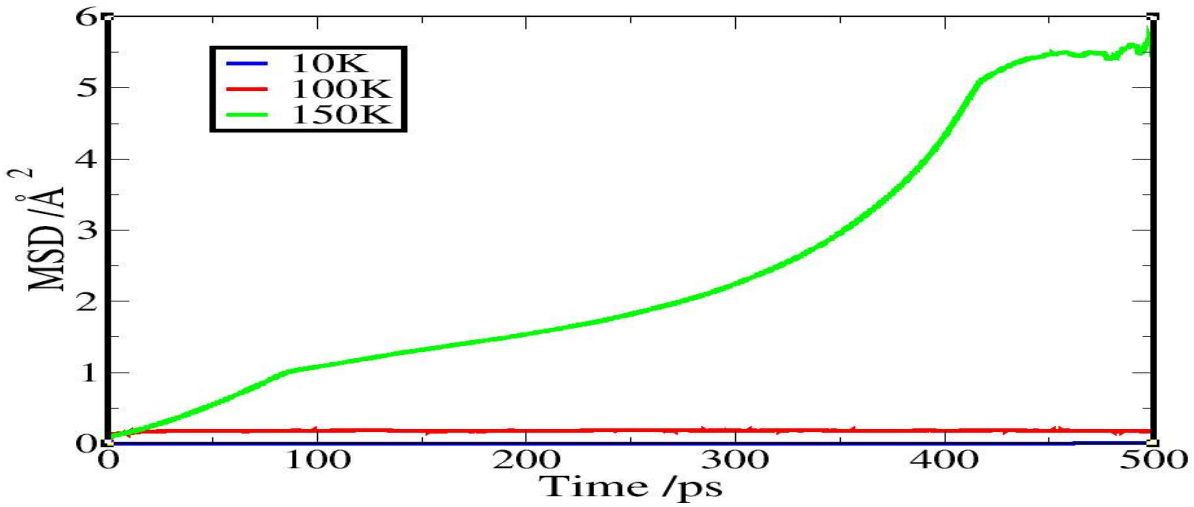

Figure 4-2 Evolution of the mean square displacement of the nickel atoms of the system with time at 10 K, 100 K and 150 K.

Figure 4-2 presents the evolution of the mean square displacement of the nickel atoms of the framework at 10 K, 100 K and 150 K. The data corroborates the conclusions given above, with relatively rapid motion of Ni^{2+} ions being observed only at 150 K. At tower temperatures the mean square displacement is characteristic of a stable solid (the mean square displacements of OC and OT show the same trend: no mobility at 10 K and 100 K but significant mobility at 150 K).

a b

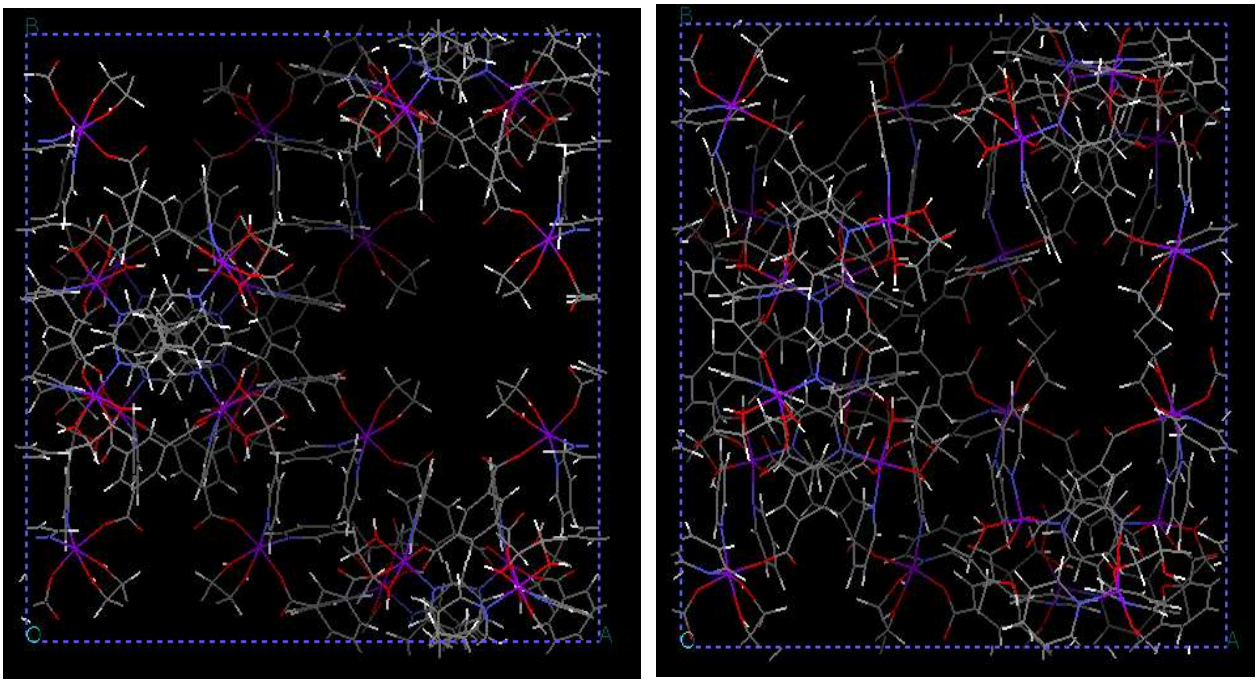

Figure 4-3 a) Structure of the framework obtained after 1ns of simulation at 100 K (left) and b) structure of the framework obtained after 500 ps of simulation at 150 K (right).

Snapshots of the structure at the end of the simulations are shown in figure 4-3. The three-dimensional structure of the framework has remained intact during the course of the 100 K simulation,with large well defined pores (squares delimited by four O-Ni-O segments as described in figure 3-5) being retained. At 150 K, however, significant distortion of the framework is evident. It has not, however, completely collapsed. Figure 4-3b shows that even though this framework is distorted, its three-dimensional structure is still present and the original bonds have not been broken. Furthermore the pores are still visible, albeit somewhat distorted. We note that the volume change occurred very suddenly, and then remained constant for the remaining 330 ps, so this should not be seen as a gradual decomposition, but may rather be a new stable (or metastable) phase.

	***a* /Å**	***b* /Å**	***c* /Å**	***α* / °**	***β* / °**	***γ* / °**	***Volume***
10K	27.800 +/- 0.11	27.966 +/- 0.11	27.860 +/- 0.11	91.10 +/- 0.36	89.96 +/- 0.36	89.97 +/- 0.36	21659 +/- 80
100K	27.825 +/- 0.11	27.976 +/- 0.11	27.826 +/- 0.11	90.97 +/- 0.36	90.03 +/- 0.36	89.93 +/- 0.36	21658 +/- 80
150K*	25.234	25.532	25.481	90.01	90.53	89.96	16415
original cell	28.4	28.4	28.4	90.00	90.00	90.00	22906

Table 4-2 Cell parameters obtained after 500 ps of simulation in the NST ensemble for simulations at 10 K, 100 K, 150 K.

Studies in the *NST* ensemble led to very similar results. Table 4-2 shows the cell parameters averaged over 500 ps of simulation in the *NST* ensemble at three different temperatures and 0.1 kbar. At 10 K and 100 K, the unit cell retains its size and shape, with the cell length being within 2 % of experiment. For the simulation performed at 150 K, the simulation cell has kept its shape (α, β and γ practically equal to 90º and a ≈ b ≈ c), but shrinks by more than 10 % (linear measure). The retention of cubic shape during this process does suggest that the new phase is crystalline rather than amorphous. Indeed, the configuration of the unit cell at the end of the *NST* simulation (figure 4-4) shows no obvious signs of amorphisation.

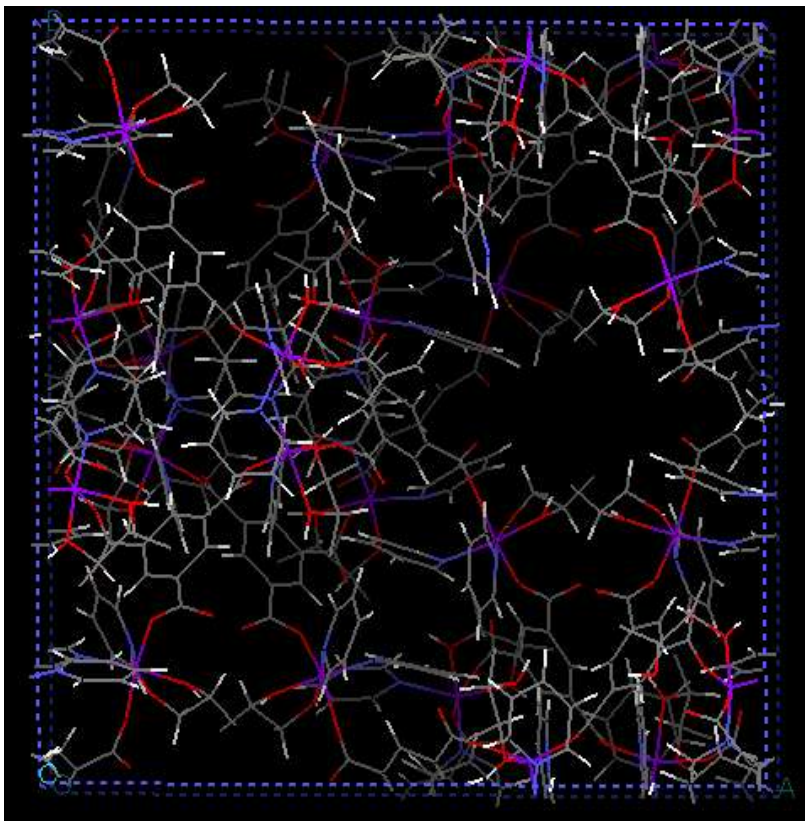

Figure 4-4 unit cell after 1ns of simulation at 150 K in the NST ensemble.

Radial distribution functions have been calculated from these simulations (*NST)* and are presented in figure 4-5. At 10 K and 100 K the RDFs were averaged over the whole 500 ps of the simulation, only the last 300 ps (i.e. after the phase change) were used at 150 K.

Radial distribution function of MNI-C

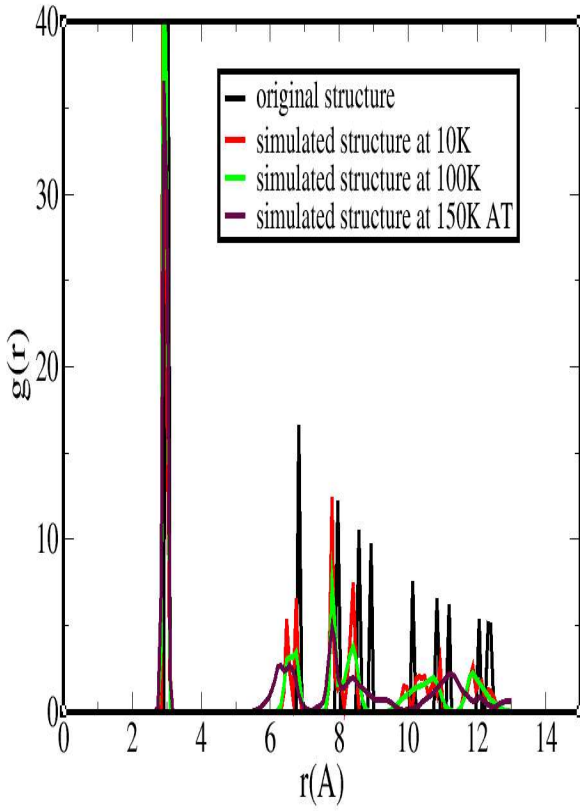

Radial distribution function of MNI-OT

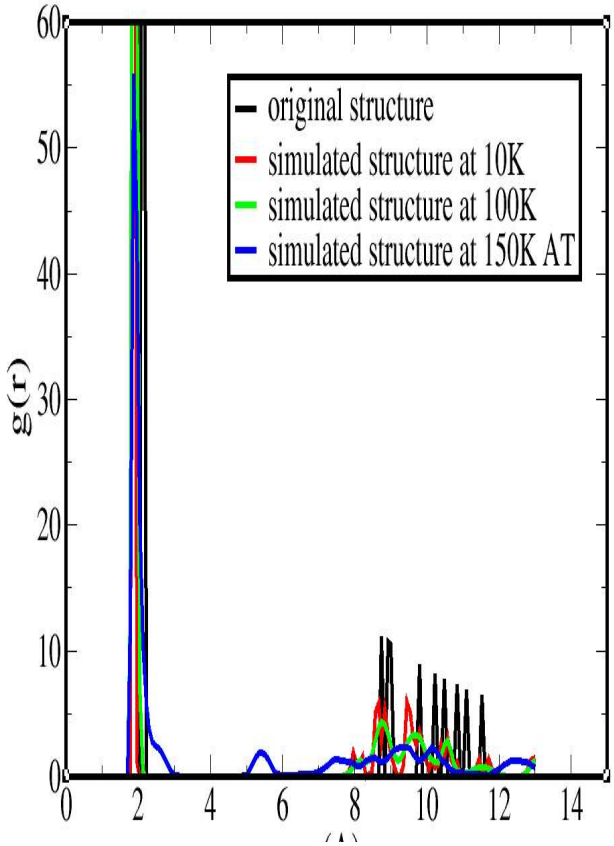

Radial distribution function of MNI-HO

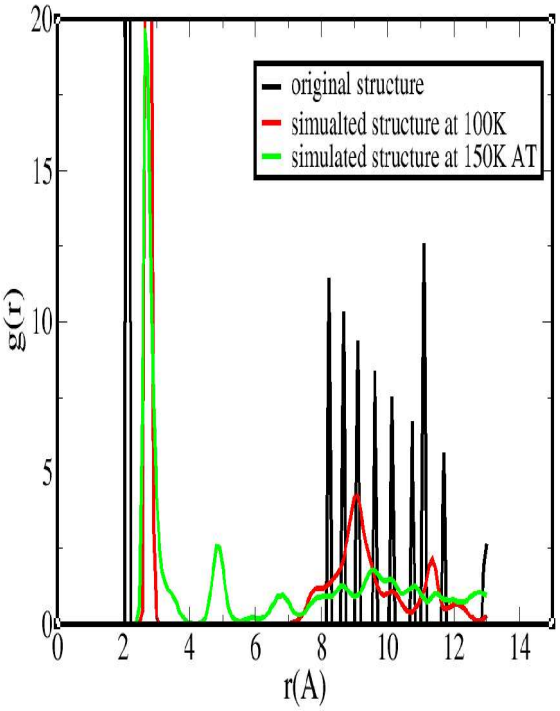

Radial distribution function of OC-OT

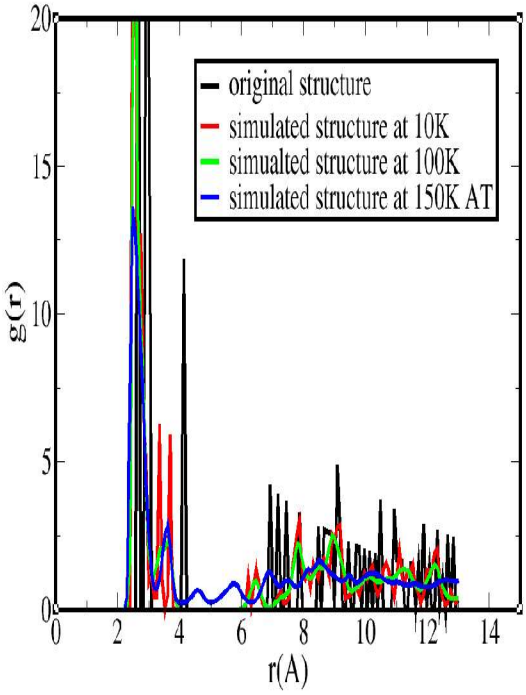

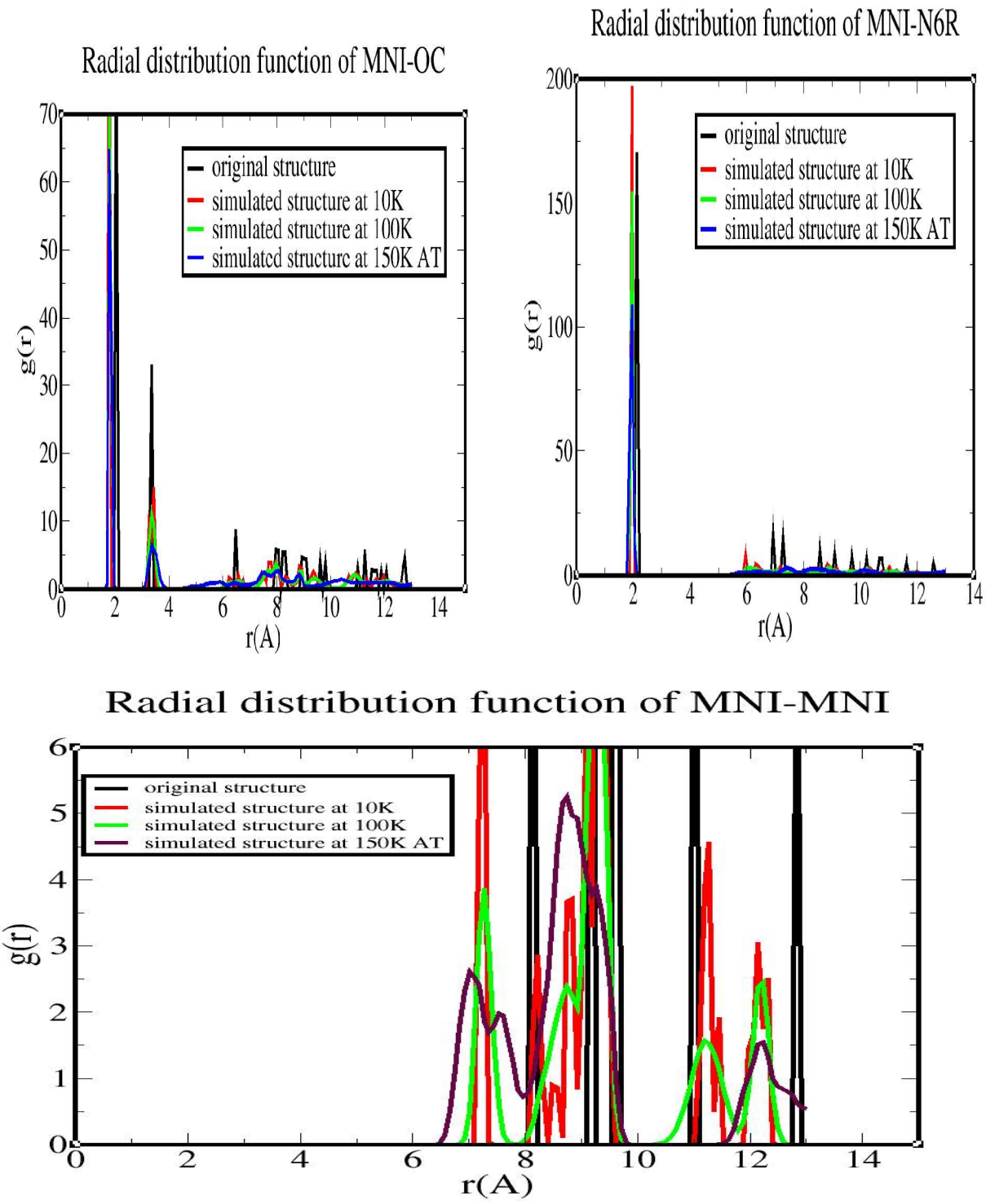

Figure 4-5 Radial distribution functions obtained after 500 ps of simulation in the NST ensemble for the unsolvated framework at 10 K, 100 K, and 150 K compared to the original crystal structure.

In general there is good agreement between the three temperatures for the peaks associated with the SBU (i.e. r < 6 Å). It is noticeable that, the simulated Ni-O and Ni-N bond distances underestimate the experimental values, but the discrepancy is entirely in line with that observed in chapter 3.

The longer range RDFs exemplified by Ni-Ni, OC-OT and Ni-HO show that a considerably different structure emerges at 150 K compared to that seen at 10 K or 100 K. The peaks in this region of the RDFs at 150 K are not as sharp as at lower temperatures, and are located at different positions. The latter point is to be expected given the structural changes already noted. For the Ni-Ni RDF the two very well defined peaks at around 11.05 Å and 12.05 Å for the two lower temperatures are replaced by one peak, albeit with a shoulder, at 12.05 Å at 150 K. For the smaller Ni-Ni distances there is good agreement between RDFs obtained at 10 K, 100 K and 150 K. Similarly, for the OC-OT and Ni-HO RDFs, even though there is good agreements between the first peak obtained at 100 K and 150 K, for the longer distance RDFs, the peaks obtained at 150 K are less well defined than the peaks obtained at 100 K and do not match as well the peak positions of the original crystal structure as the peaks obtained at 100 K. All of this suggests that at 150 K, the framework has experienced some limited distortion but the three-dimensional structure represented by the two interpenetrating (10,3)-a nets is still present as shown from the snapshot displayed in figure 4-4 (also these RDFs show that no bond breaking behavior takes place). Indeed, it is clear than even though the atoms of the framework have experienced some motion (as it is shown by the study of the root mean displacement described in figure 4-2), the framework has not decomposed and the structure obtained at 150 K is similar (although a little distorted) to the original crystal structure.

The study of the Ni-OT RDF is particularly interesting in the sense that it helps us to understand the possible origins of the distortion of the framework. The differences between the RDFs of the structures simulated at 150 K and lower temperatures are particularly apparent in the Ni-OT RDFs. Although the position of the first peak is practically identical for the three temperatures, it is noticeable that the first peak for the 150 K simulation has a shoulder at larger r that is not present at lower temperatures. This shows that the Ni-OT bond has a very large amplitude of vibration at 150 K which might have caused some instability of the framework. Furthermore, the RDF

representing relative atomic positions for the simulation undertaken at 150 K shows a peak at around 5.8 Å which is not visible for the original crystal structure or the simulated structures at 10 K and 100 K. This suggests that the instability of the framework is likely to be due to Ni-OT interactions. Indeed, it is clear from the Ni-OT RDFs, compared to Ni-OC RDF for example, that at long distances, the peaks at 150 K do not match well the peaks at 10 K and 100 K. Since it is this region that describes the arrangement of SBUs, this is indicative of changes in the structure of the framework. It is also observable from figure 4-5 that the RDFs that show the most significant differences when simulated at 10 K (or 100 K) and 150 K are the RDFs involving atoms belonging to the alcohol molecules (OC-OT, Ni-OT or Ni-HO). It is therefore our belief that the fact that the cell parameters obtained after 500 ps of simulation in the *NST* ensemble are significantly smaller for simulations undertaken at 150 K than for simulations undertaken at 10 K or 100 K as shown in figure 4-1 and table 4-2, is due to the instability in the position of the oxygen atoms of the alcohol molecules which is likely to be due to the high amplitude of vibration of Ni-OT bonds. This would need to be verified but we think that it is very likely to be at least one of the reason for the framework instability at 150 K. To increase the stability of the oxygen atoms of the alcohol molecules and the Ni-OT bond distances one could either fit the Lennard-Jones parameters for the Ni-OT pair potential or increase the strength of the hydrogen bond between the OH group of the alcohol molecules and the oxygen atoms of the BTC molecules. However, it is not clear from experimental data if the unsolvated framework would stay stable at 150 K. These experimental data just show that for the solvated system, the framework would definitely be stable at 150 K since it is the temperature at which the crystallographic structures of these metal-organic frameworks have been determined.

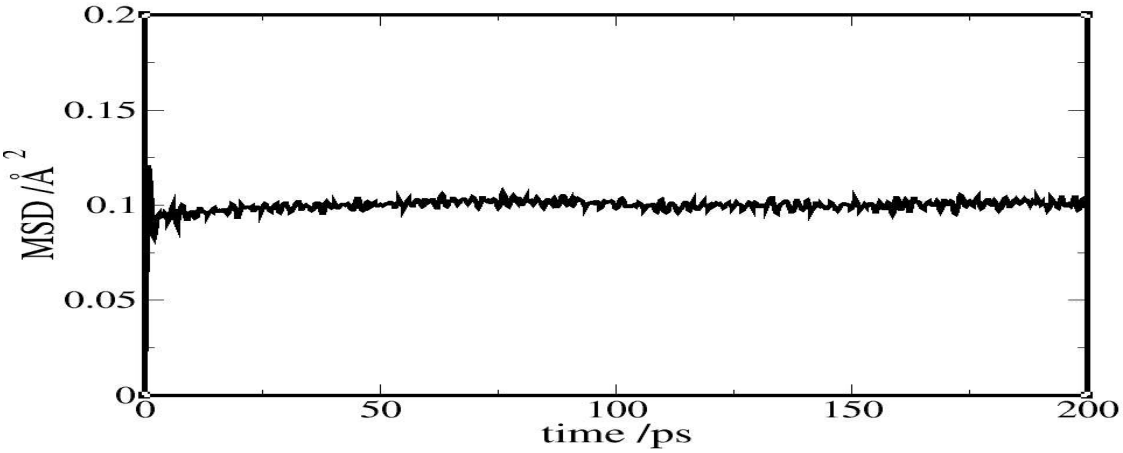

Figure 4-6 Evolution of the mean square displacement of the nickel atoms of the system with time at 150 K after the phase change has occured.

Figure 4-6 presents the evolution of the mean square displacement of nickel atoms calculated over the last 300 ps of the simulation (the first 200 ps were not taken into consideration so as to avoid the time during the phase change). Clearly, the nickel ions are bound to specific sites for this entire period (the mean square displacements of OC and OT show the same trend). This confirms that the motion evident in figure 4-2 is actually confined to the first 200 ps (probably the interval 150-200 ps) after which a mechanically stable solid is formed. This is in good agreement with the conclusions drawn from figures 4-3 to 4-4.

To verify the conclusions that have been drawn from the study of the mean square displacements of the atoms of the framework, the evolution of the cell volume with time and the study of the radial distribution functions, the study of the orientational distribution of molecules constituting the framework have been performed.

Figure 4-7 presents the orientational distribution of the benzene rings of BTC molecules relatively to a central benzene ring for the simulations performed at 10 K, 100 K and 150 K in the *NST* ensemble.

a

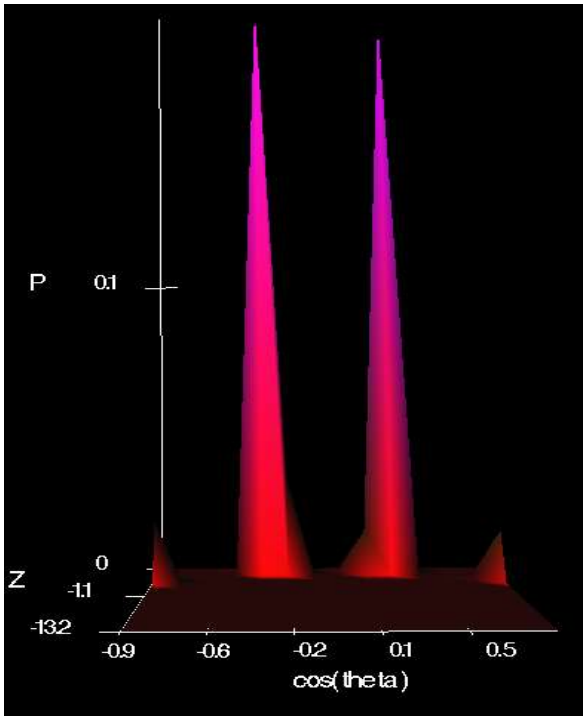

b

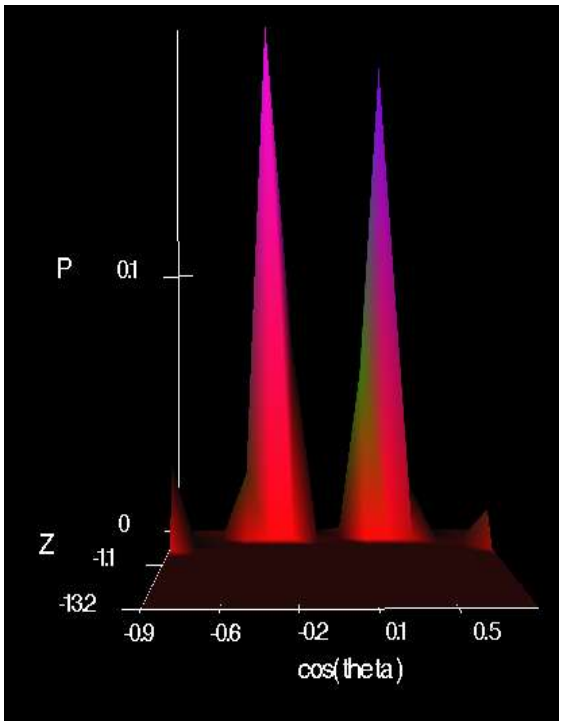

c

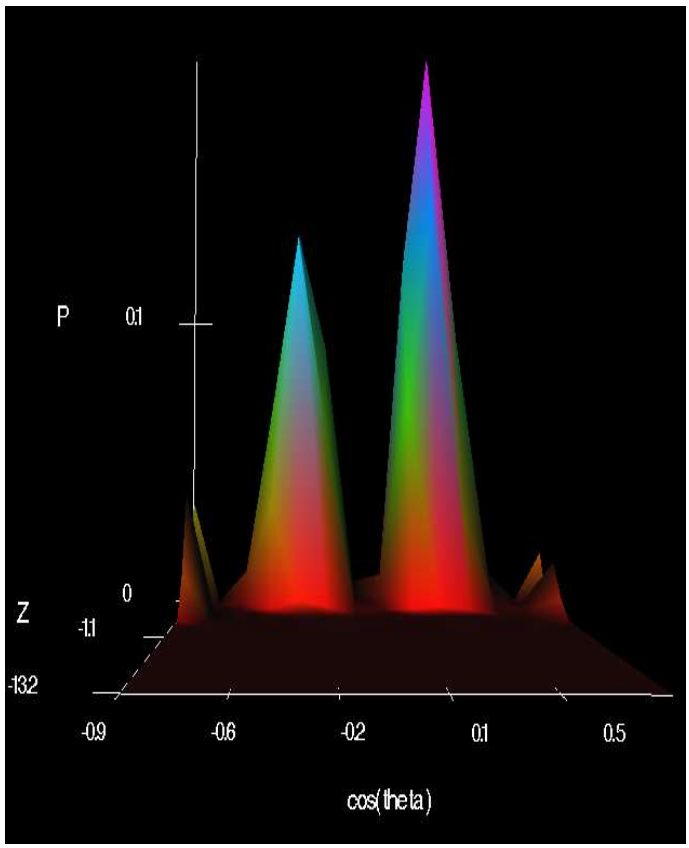

Figure 4-7 ring-ring orientation distribution for the simulation performed in the NST ensemble at a) 10 K (top right) b) 100 K (top left) and c) 150 K (bottom)

Figure 4-7 shows that at 10 K, the relative orientations of the BTC rings are well resolved and match the orientational distribution of the BTC rings in the experimental crystal structure. It is noticeable that the removal of the terminal ethyl groups from the 4,5-octanediols has had little effect on the relative orientation of BTC rings. It is clear from figure 4-7a that the peaks situated at $|\cos(\theta)| \approx 1$ and $|\cos(\theta)| \approx 0.34$ are sharp and well defined suggesting high order in the framework structure and therefore that the framework remains stable at 10 K.

Similarly to what has been observed in figure 4-7a, it is clear from figure 4-7b that the relative orientation of BTC rings are very well defined suggesting that the framework remained stable during the course of the simulation at 100 K. Figure 4-7c shows that at 150 K, the orientational distribution of BTC rings relatively to each other are still relatively well defined. Indeed, even though the peaks at $|\cos(\theta)| \approx 0.34$ are broad, they are still well defined and they have not fusioned to spread through all ranges of angular distribution. This suggests that at 150 K, even though the framework has experienced some motion and instability as it was shown by the radial distribution function study, the framework has not collapsed. Indeed, this indicates that order is still present in the framework as it is shown by the snapshot presented in figure 4-4.

This corroborates the conclusion that 150 K is a temperature of phase change characterized by some distortion of this metal-organic framework structure without however leading to its collapse.

4.3.1.2 Study of the sensitivity of the force field and attempts to improve it

It has been observed from figure 4-5 that the nickel-oxygen and nickel-nitrogen bond distances after simulations underestimated the nickel-oxygen and nickel-nitrogen bond distances observed in the original crystal structure. These differences in bond distances were observed for simulations at temperatures as low as 10 K. Therefore, Attempts have been performed to fit the ε value of the van der Waals parameters of these nickel-oxygen and nickel-nitrogen pair potentials to better reproduce the cell parameters and the bond distances in the original crystal structure. This has been performed by multiplying the ε value of nickel-oxygen and nickel-nitrogen pair potentials (Ni-OC, Ni-OT and

Ni-N) by a number of factors. The resulting cell parameters obtained by using this method are described in table 4-3.

	***a* /Å**	***b* /Å**	***c* /Å**	**α / °**	**β / °**	**γ / °**	***Volume* /Å^3** **+/- 80**
original crystal structure	28.40	28.40	28.40	90.00	90.00	90.00	22906
ε × 1	27.80	27.97	27.86	91.10	89.96	89.97	21659
ε × 1.25	27.90	28.07	27.98	91.13	89.91	90.00	21910
ε × 1.5	27.94	28.12	28.04	91.16	89.86	90.02	22031
ε × 1.75	27.89	28.01	27.86	91.23	89.80	90.06	22154
ε × 2	25.35	25.13	25.27	90.09	90.17	90.18	16094
ε × 3	25.46	28.19	26.24	92.09	88.63	90.74	18831
ε × 5	25.48	25.78	25.74	94.16	86.29	93.64	16863

Table 4-3 Parameters obtained after 500 ps of simulation in the NST ensemble at 10 K using different multilying factors for the nickel-oxygen and nickel-nitrogen parameters

The study described in table 4-3 shows that, similarly to what was found in chapter three, the Lennard-Jones parameters for the interactions between nickel atoms and the heteroatoms of the framework can be fitted to better reproduce the original cell parameters and hence provide an improvement of the force field used. However, due to time constraints, this fitting process will not be undertaken. This study was performed just to show that there is room for improvement in the force field by simply scaling the van der Waals parameters appropriately.

Table 4-3 shows that for multiplying factors lower than 2, the total volume obtained after simulation is closer to the original cell volume than when using parameters obtained from the FF-2

force field (ε × 1). With 1.75 being the best multiplying factor which leads to the highest cell volume with a difference of only 3.3 % with the cell volume of the original crystal structure. It is also noticeable from table 4-3 that if the multiplying factor for the ε value is greater or equal to 2, the resulting simulated cell volume decreases very significantly compared to the original cell volume. Indeed, table 4-3 shows that when the ε value of the nickel-oxygen and nickel-nitrogen pair potentials was multiplied by 2, the resulting cell volume decreased by 25.7 % compared with the cell volume obtained using the FF-2 parameters, and by 29.7 % when compared to the cell volume of the original crystal structure. It is noticeable however that even though the cell volume decreases significantly when the ε value is multiplied by 2, the cell remains cubic which, suggests that some structure has been kept during this simulation. This is not the case when the ε value is multiplied by 3 or more. Indeed, for these multiplying factor the angular parameters for the cell are significantly different from 90^0 suggesting, along with the significant decrease in cell volume, that the framework has experienced phase change in both of these cases.

Figure 4-8 shows the radial distribution functions for the structure for which the ε value of the nickel-oxygen and nickel-nitrogen pair potentials is multiplied by 1.75 compared to the RDFs of the original crystal structure and the simulated structure for which the ε values have not been modified.

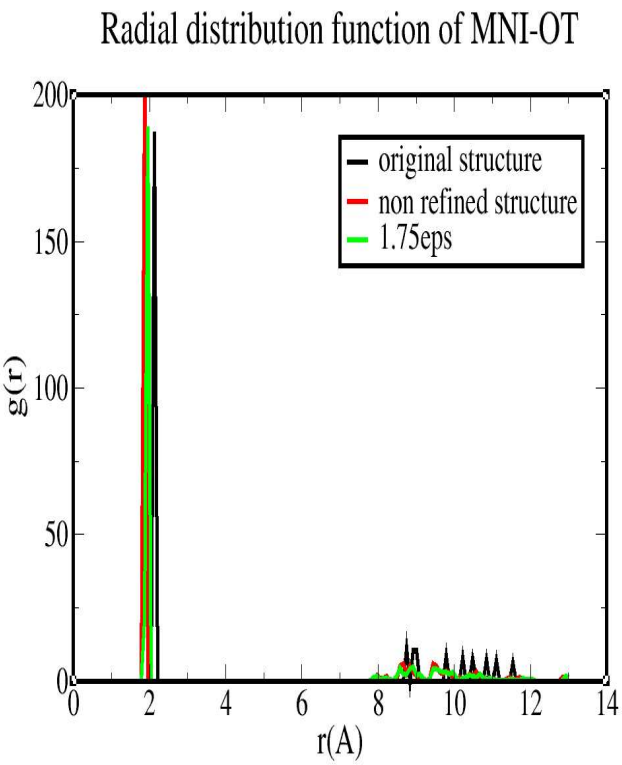
Radial distribution function of MNI-OT
original structure
non refined structure
1.75eps
g(r)
r(A)
0
50
100
150
200
0
2
4
6
8
10
12
14

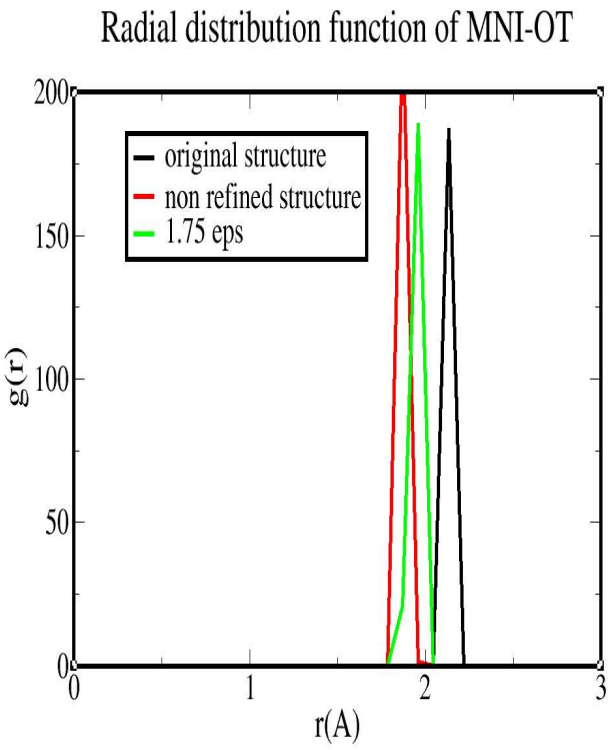
Radial distribution function of MNI-OT
original structure
non refined structure
1.75 eps
g(r)
r(A)
0
50
100
150
200
0
1
2
3

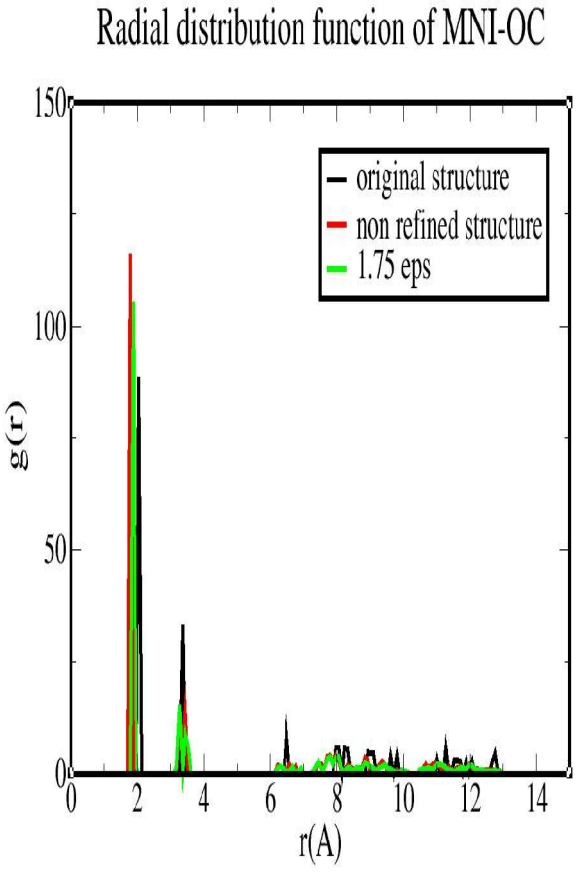
Radial distribution function of MNI-OC
original structure
non refined structure
1.75 eps
g(r)
r(A)
0
50
100
150
0
2
4
6
8
10
12
14

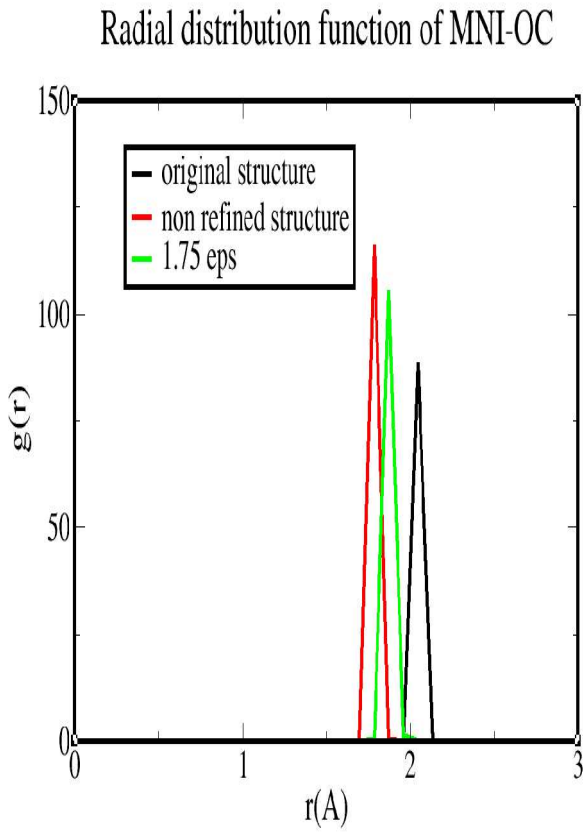
Radial distribution function of MNI-OC
original structure
non refined structure
1.75 eps
g(r)
r(A)
0
50
100
150
0
1
2
3

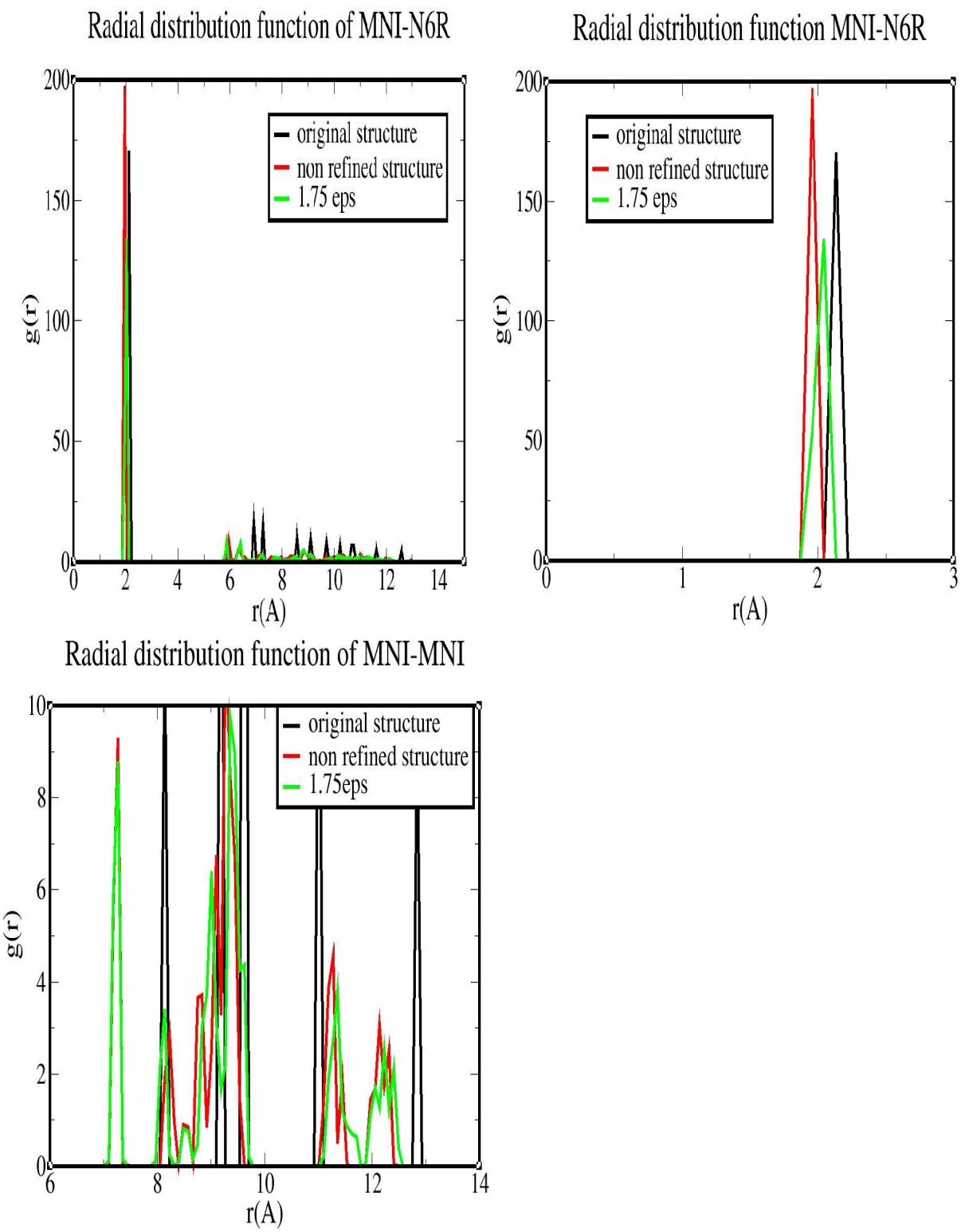

Figure 4-8 Radial distribution functions obtained after 500 ps of simulation in the NST ensemble for the unsolvated framework at 10 K using ε parameters obtained from the FF-2 force field and the force field for which the ε values of the nickel-oxygen and nickel-nitrogen parameters have been multiplied by 1.75.
The graphs in the right represent the same RDFs as the graphs in the left but at different scale of the horizontal axis .

Figure 4-8 shows that multiplying the ε value of the nickel-oxygen and nickel-nitrogen parameters by 1.75 results in RDFs where the bond distances between nickel and the two types of oxygen atoms present in the framework (OC and OT) in one hand, and the nickel and nitrogen (N6R) atoms in the other hand, match better the equivalent bond distances obtained from the original crystal structure. Even though the improvement is small it is still noticeable from the Ni-OT, Ni-OC and Ni-N RDFs. However, it is also noticeable that at long distance, multiplying the value of by 1.75 does not significantly affect the RDFs. This is best shown by the Ni-Ni RDF where the peaks obtained from the two force fields are extremely similar even though the peaks representing the RDFs obtained from the simulation where ε was multiplied by 1.75 seem to a small extent to better match the peaks of the original crystal structure.

4.3.1.3 Trial of other force fields on the unsolvated system

Simulations using other force fields on this unsolvated system have also been performed. Simulations performed using Lennard-Jones parameters and partial charges obtained from the CHARMM22 force field led to a significant rapid drop in the simulation cell volume, suggestive of a first order phase transition, even at temperatures as low as 10 K and in the *NPT* (not even *NST*) ensemble, as shown in figure 4-9. The volume drop is so large (~ 25 %) and rapid (< 5 ps) at 10 K that we must conclude CHARMM22 to be an inadequate force field for this material.

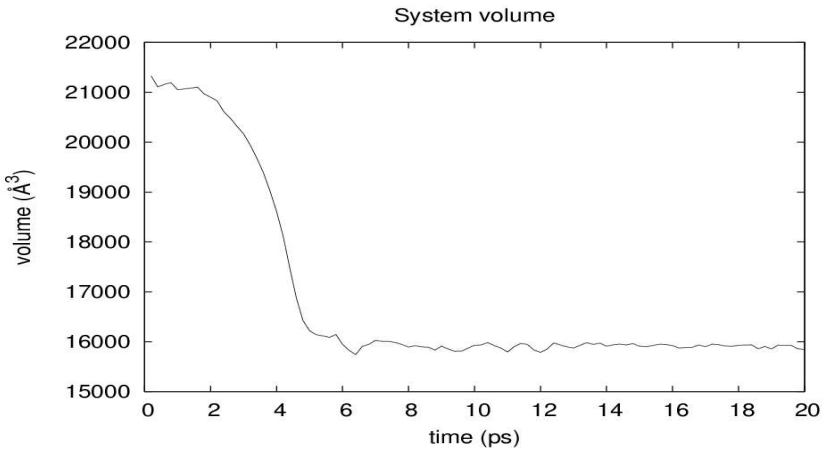

Figure 4-9 Evolution of the cell volume with time for a 20 ps simulation at 10 K in the NPT ensemble using CHARMM22 force field.

An interesting observation which can also be made from comparing this force field with the FF-2 force field is that the only differences between these two force fields is the partial charges on the equatorial ligands of the framework namely pyridine and alcohol molecules. Van der Waals parameters and the partial charges on the BTC molecules are equivalent in these two force fields. Therefore, electrostatic interactions are of primary importance in the stabilization of this metal-organic framework.

However, the van der Waals interactions are of primary importance too in the stabilization of this force field. Indeed, if the FF-1 force field is used instead (which differs from FF-2 in that Lennard-Jones parameters were adjusted to improve the SBU with octanediol, see tables 3-3 and 3-4), a significant drop in volume is still obtained after just 20 ps at 10 K (see figure 4-10). The fact that the volume drop is so large (~ 25 %) and occurred rapidly (~ 20 ps) at such a low temperature (10 K) shows that the FF-1 force field is inadequate to model this material. This also means that it is unlikely that adding solvent would be sufficient to redress this problem.

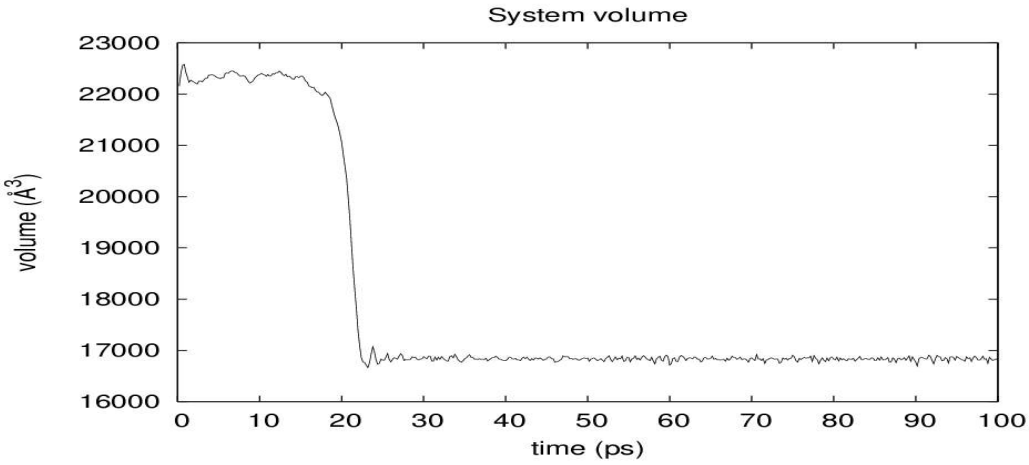

Figure 4-10 Evolution of the unit cell volume with time for a 100 ps simulation at 10 K in the NPT ensemble.

Similar volume drops were obtained when using force fields with partial charges on the equatorial ligands obtained from density functional theory calculations using the B3LYP functional and the 6-311G basis set. In fact, except the FF-2 force field, all the force fields that have been tried on this MOF have led to phase change of the framework even at temperatures as low as 10 K.

4.3.1.4 Simulations on the solvated systems

MD simulations were performed on this metal-organic framework (with 2,3-butanediol as alcohol ligand) with a series of different solvent content. The force field used was the FF-2 force field (see table 3-9). Simulations were performed in both *NPT* and *NST* ensembles. The system was equilibrated for 50 ps before production time.

Table 4-4 presents the cell parameters averaged over 500 ps of simulation in the *NST* ensemble at 10 K and 0.1 kbar for different degrees of solvation.

number of solvent molecules	***a/ Å***	***b/ Å***	***c/Å***	***α/ °***	***β/ °***	***γ/ °***	***Volume/Å^3***
0	27.800 +/- 0.11	27.959 +/- 0.11	27.860 +/- 0.11	91.10 +/- 0.36	89.96 +/- 0.36	89.97 +/- 0.36	21659 +/- 80
56	26.740 +/- 0.11	26.388 +/- 0.11	26.848 +/- 0.11	91.65 +/- 0.36	89.68 +/- 0.36	91.17 +/- 0.36	18939 +/- 80
40	28.054 +/- 0.11	25.767 +/- 0.11	26.355 +/- 0.11	88.16 +/- 0.36	90.49 +/- 0.36	92.17 +/- 0.36	19040 +/- 80
30	26.128 +/- 0.11	27.442 +/- 0.11	26.537 +/- 0.11	88.66 +/- 0.36	91.69 +/- 0.36	91.53 +/- 0.36	19018 +/- 80
20	26.153 +/- 0.11	25.315 +/- 0.11	27.485 +/- 0.11	90.18 +/- 0.36	89.13 +/- 0.36	89.69 +/- 0.36	18198 +/- 80
10	28.578 +/- 0.11	24.218 +/- 0.11	25.253 +/- 0.11	92.63 +/- 0.36	89.67 +/- 0.36	91.17 +/- 0.36	17467 +/- 80

Table 4-4 Cell parameters obtained after 500 ps of simulation in the NST ensemble at 10 K and 0.1 kbar for different degrees of solvation with FF-2.

In these simulations, solvent molecules were added to the simulation cell using a locally developed program called SOLVADD. The way SOLVADD works is described in section 3-4 of this thesis. First 56 solvent molecules were added to the system, then from this solvated system, solvent molecules were removed at random to get the lower solvent contents.

Table 4-4 shows that the unsolvated system has a higher volume than the solvated systems. The fact that smaller cell parameters are obtained for the solvated systems than for the unsolvated one is also observed for simulations performed in the *NPT* ensemble. This shows that even with the cubic constraint of *NPT* simulations, the contraction was observed (see table 4-5).

number of solvent molecules	*cell parameter/Å*
0	27.88 +/- 0.11
56	26.58 +/- 0.11
40	26.56 +/- 0.11
30	26.31 +/- 0.11

Table 4-5 Cell parameters obtained after 500 ps of simulation in the NPT ensemble at 10 K and 0.1 kbar for different degrees of solvation.

Table 4-5 presents the cell parameters averaged over 500 ps of simulation in the *NPT* ensemble at different degrees of solvation.

However for the 10 K simulations in the *NST* ensemble, even though the volume decreased a little the framework seemed to stay stable and the nickel atoms did not display any significant motion.

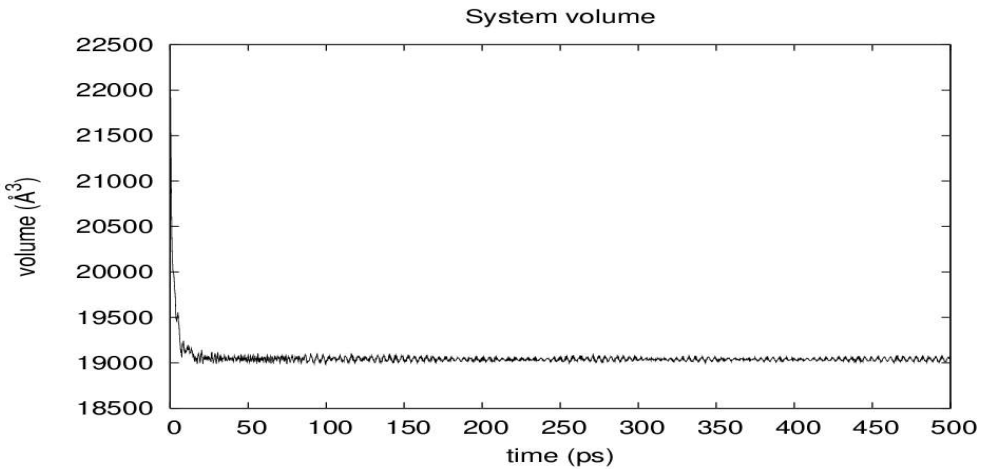

Figure 4-11 Evolution of the unit cell volume with time for a system containing 40 solvent molecules at 10 K in the NST ensemble.

Figure 4-11 shows the evolution of the system volume with time for a system containing 40 solvent molecules at 10 K and 0.1 kbar. It can be seen that the decrease in volume for the system containing 40 solvent molecules occurs at the very beginning of the simulation: within the first 8 ps.

Figure 4-12 shows the evolution of the system volume with time for a system containing 56 solvent molecules at 10 K and 0.1 kbar. The simulation was run for 8 ps. The time step used for this simulation was 0.1 fs.

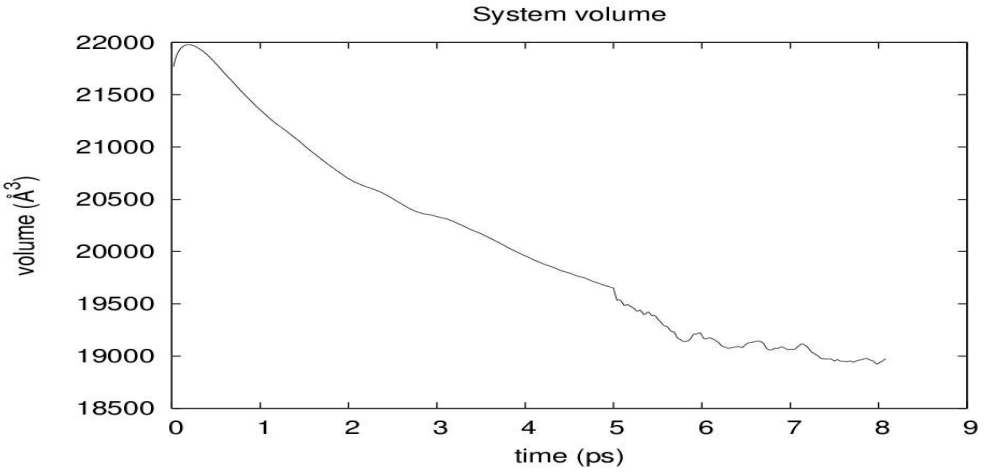

Figure 4-12 Evolution of the unit cell volume with time for a system containing 56 solvent molecules at 10 K and 0.1 kbar in the NST ensemble.

Figure 4-12 shows that the decrease in volume for the system containing 56 solvent molecules occurred gradually during the first 6 ps of the simulation in the *NST* ensemble.

To investigate what are the kind of interactions that led to this decrease in cell volume, the evolution of the configurational energy, the van der Waals energy and the electrostatic energy with time has been studied.

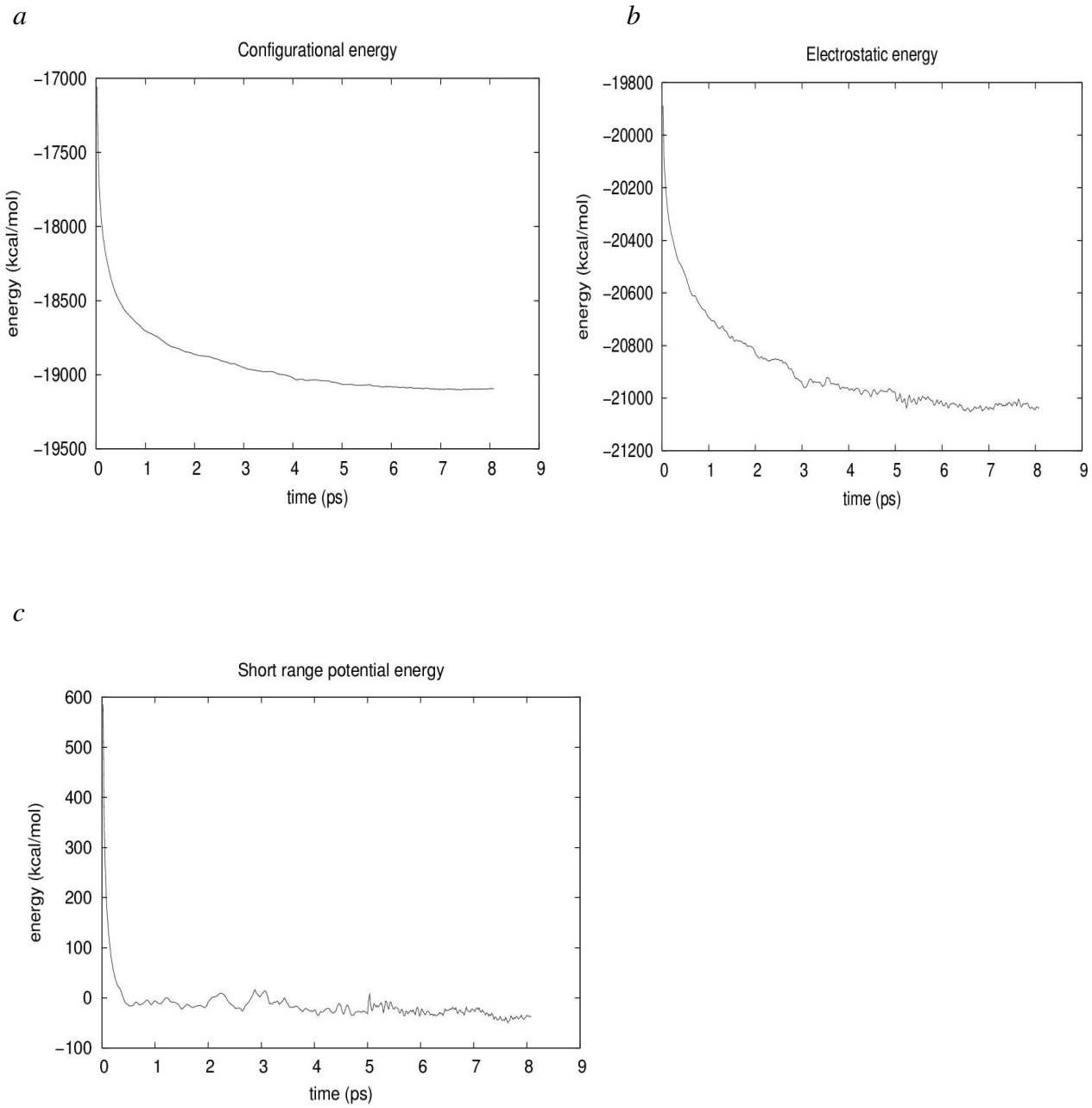

Figure 4-13 Evolution of a) the configurational (top left) b) the ectrostatic (top right) and c) the van der Walls (bottom) energies with time for a system containing 56 solvent molecules at 0.1 kbar and 10 K in the NST ensemble.

The evolution of various energy contributions are shown in figure 4-13. There is a significant decrease in the configurational, electrostatic and van der Waals energies within the first picoseconds of the simulation, i.e. preceding the volume relaxation.

The immediate response of the system is a rapid loss of steric overlap, as revealed in the short-range

energy (figure 4-13c). This is complete within about 0.5 ps. There is then a slower relaxation of the electrostatic energy that occurs on the same timescale as the volume change. It is likely that the initial strain due to solvent-framework interactions initiates a relaxation that then proceeds on a scale of 5-10 ps and is accompanied by subsequent changes in the electrostatic energy.
It is likely that the introduction of solvent molecules inside the system led to this decrease in cell volume without destabilizing the framework and even stabilizing it further. To corroborate this assumption, a study of the evolution of the mean square displacement of atoms constituting the framework with time has been performed.

Figure 4-14 presents the evolution of the mean square displacement of nickel atoms with time for the system containing 40 solvent molecules at different temperatures in the *NST* ensemble.

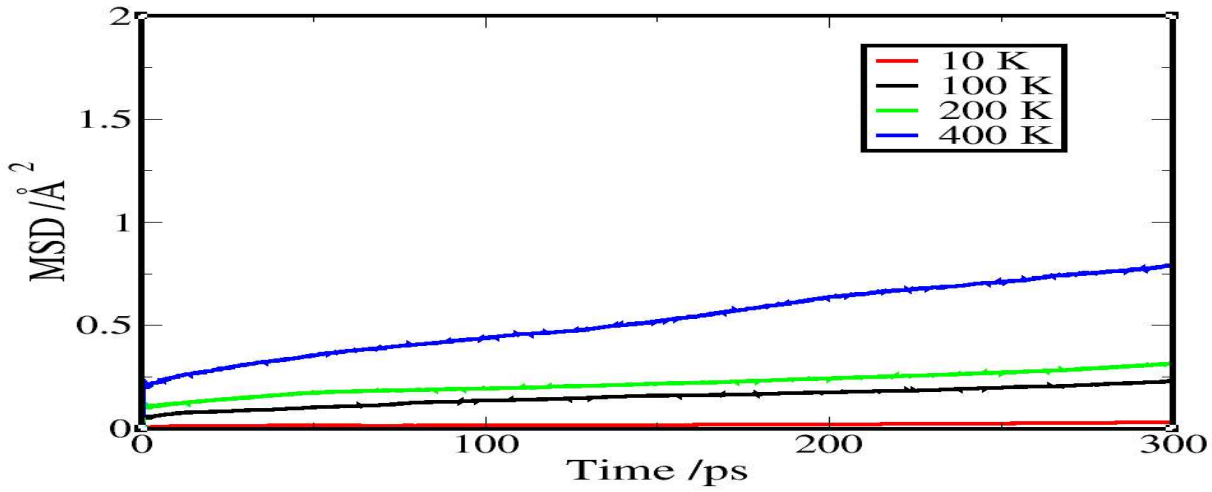

Figure 4-14 Evolution of the mean square displacement of nickel atoms with time for the system containing 40 solvent molecules at different temperatures and 0.1 kbar in the NST ensemble.

Figure 4-14 shows that for low temperatures, 10 K, 100 K, 200 K and even 400 K, the nickel atoms experience no or very little motion. This would suggest that even though the volume of the cell decreased during the simulation when solvent molecules were added to the system, the framework stayed very stable and retained its integrity. Indeed, the decrease in cell volume occurs at temperatures as low as 10 K, however the study of the root mean square displacement of the atoms

of the framework with time shows that at 10 K these atoms are roughly immobile and therefore that the structure of the framework has not changed from the original crystal structure.

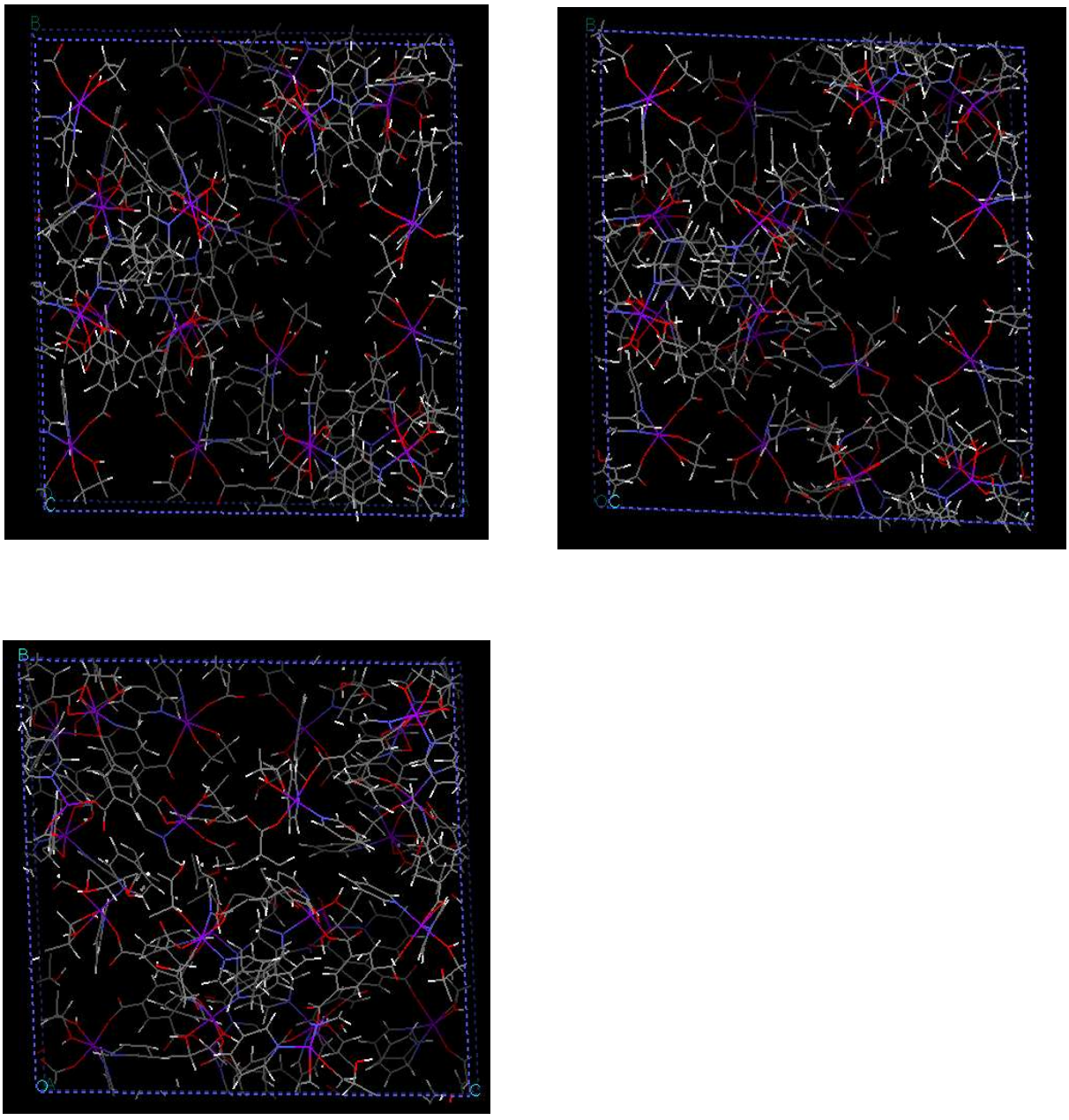

Figure 4-15 snapshots of the framework after 500 ps of simulation at (from top to bottom and left to right) 10 K, 200 K and 400 K in the NST ensemble.

It is observable from figure 4-15 that at 10 K and 200 K, the framework is well defined and therefore has retained its stability and three-dimensional structure during the course of the

simulation. For the simulation at 400 K the framework seemed to have experienced some motion but its three-dimensional structure is still visible. Indeed, the helical structure and the square pores are still visible even though they are not as well defined as the ones obtained from the simulation at 10 K and 200 K. It is possible to suggest from these snapshots that 400 K is probably the temperature of phase change for this solvated system.

To investigate if whether or not the framework stay stable up to a temperature of 400 K and then begins to experience instability, a study of the key radial distribution functions have been performed.

Figure 4-16 shows the key radial distribution functions obtained for systems simulated at 10 K, 100 K and 400 K. This has been performed so that the data obtained from the 400 K simulation for which the system seems to become unstable can be compared to data from which the framework is supposed to stay stable.

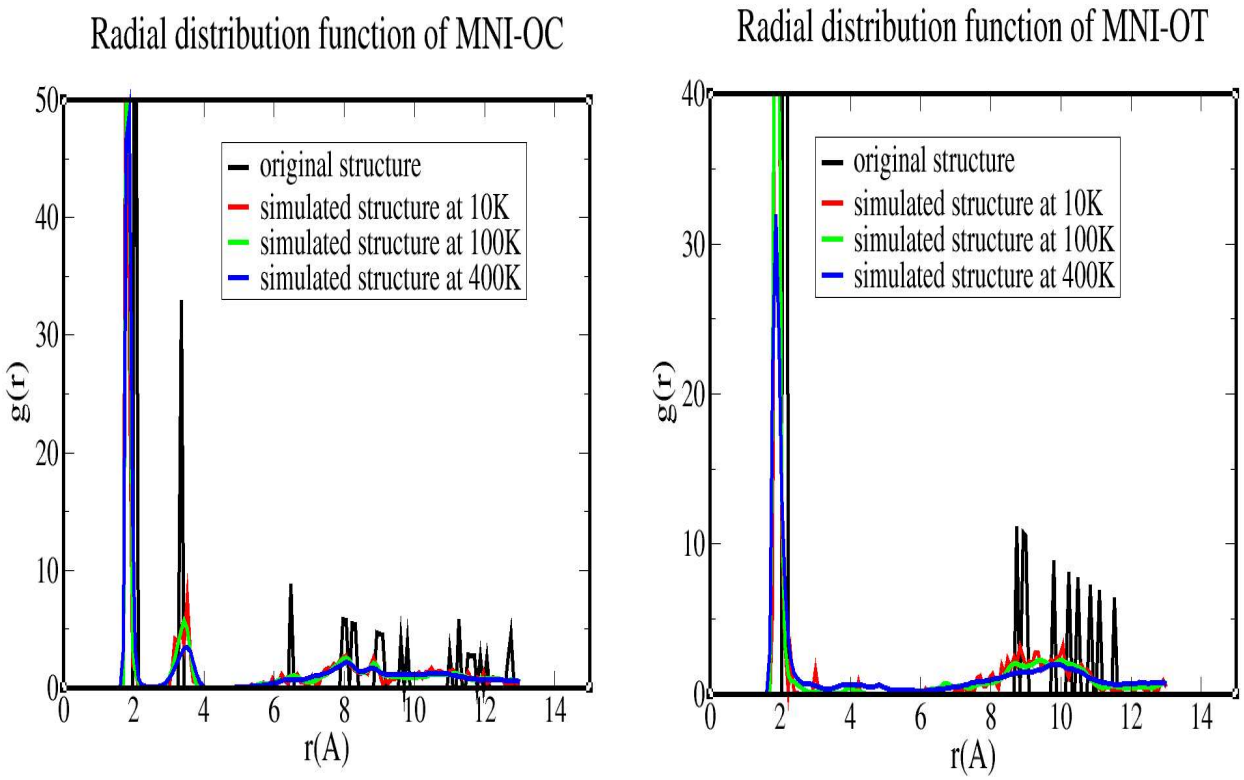

Radial distribution functio of MNI-N6R

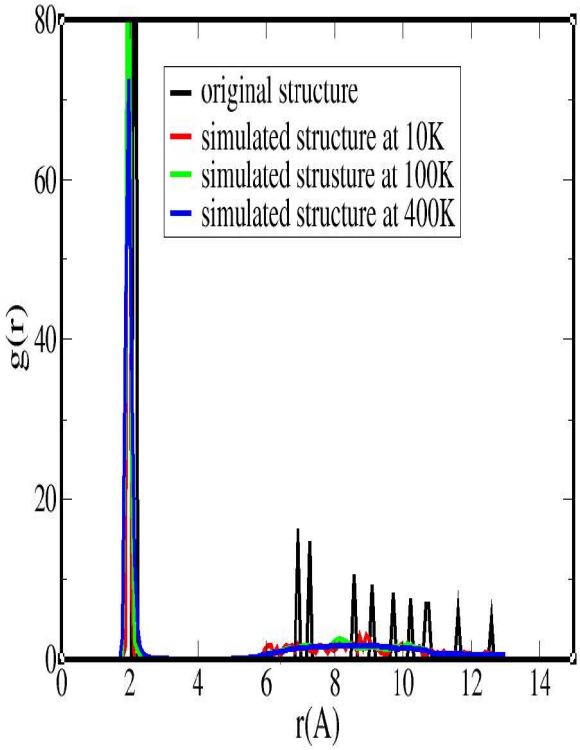

Radial distribution function of MNI-C

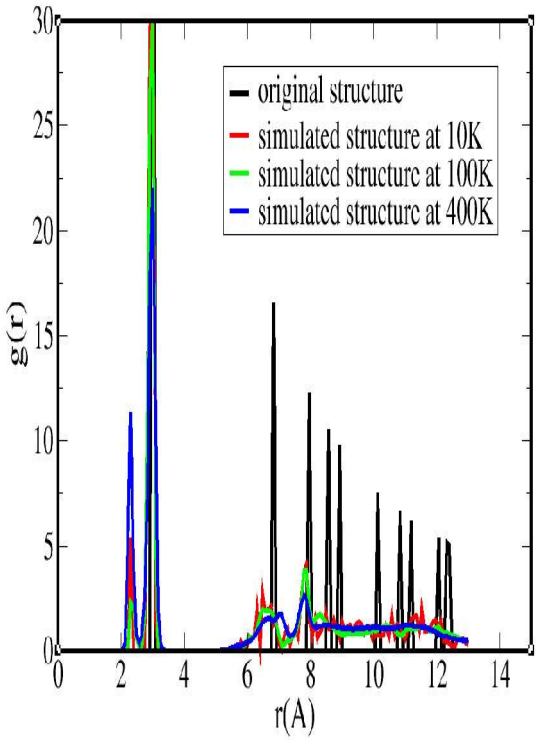

Radial distribution function of MNI-MNI

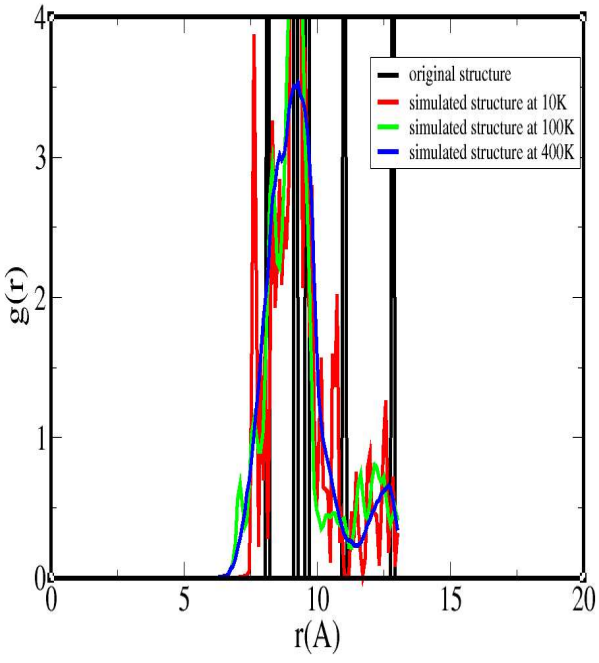

Radial distribution function of OC-OT

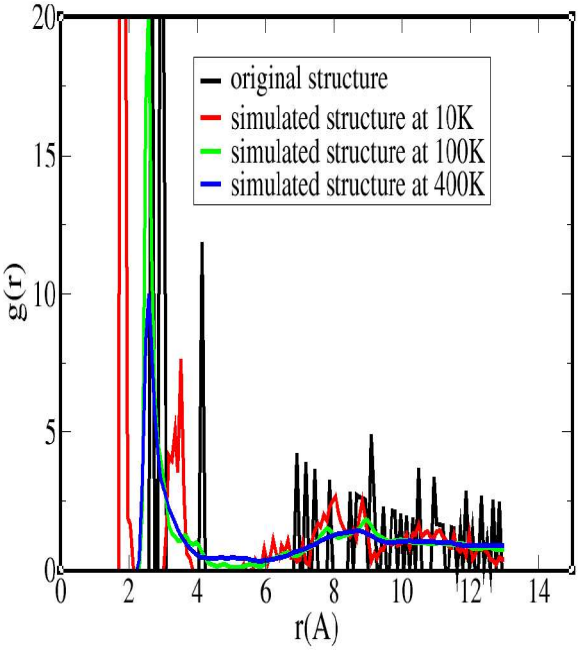

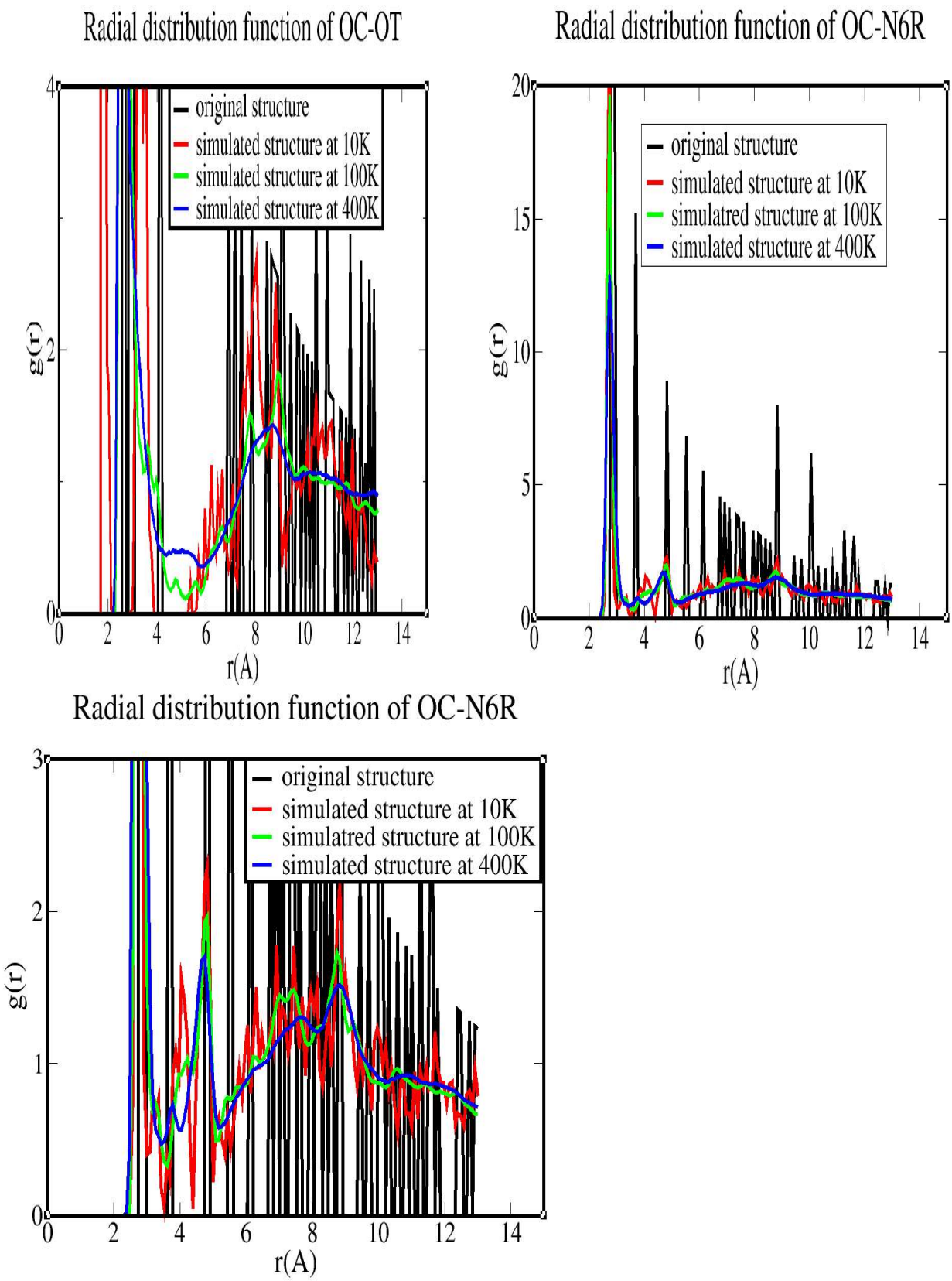

Figure 4-16 Radial distribution functions obtained after 500 ps of simulation in the NST ensemble for a system containing 40 solvent molecules at 10 K, 100 K and 400 K compared to the original crystal structure.

Figure 4-16 shows that generally the radial distribution functions obtained at 400 K match relatively well the RDFs obtained at 10 K or 100 K. This is clear for example for the Ni-OC RDFs where the short distance peaks for each temperature match each other very well. It is also noticeable that at long distances these RDFs display a similar behavior even though the peaks of the RDF of the 400 K simulation are not as well resolved as the peaks obtained from the 10 K and 100 K simulations (this is due to thermal motion). This is particularly visible in the Ni-Ni RDF where the RDF of the 400 K simulation shows only two broad peaks while the RDFs of the 10 K and 100 K simulations show a significantly larger number of peaks. It is also noticeable that the peaks obtained from the 10 K and 100 K simulation in the Ni-Ni RDF are much sharper than the peaks obtained for the 400 K simulation. This Ni-Ni RDF shows more clearly long distance RDFs compared with the other RDFs in figure 4-16 since the peaks, only occur of long distances, are only a few (so no multiplets to confuse things) and most importantly, are the structural links that define the long-range structure. This Ni-Ni RDF shows, since only two broad peaks are visible that the structure has not remained very stable and that nickel atoms have experienced some motion during the course of the simulation. However, the fact that for the other RDFs, the peaks obtained from the 400 K simulation match well the peaks and shape of the RDFs obtained at 10 K and 100 K suggests that the framework has retained its three-dimensional structure, described as the 2 interpenetrating (10,3)-a nets. Our conclusion is therefore that the temperature of phase change of this solvated MOF is around 400 K.

To corroborate this fact, orientational distribution functions have been calculated for study this solvated framework for temperatures of 10 K, 100 K and 400 K in the *NST* ensemble. The results are shown in figure 4-17.

a

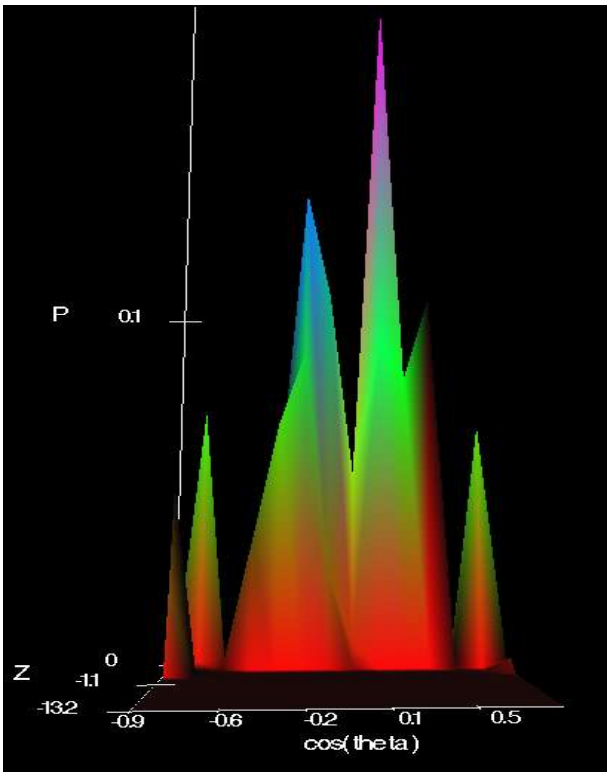

b

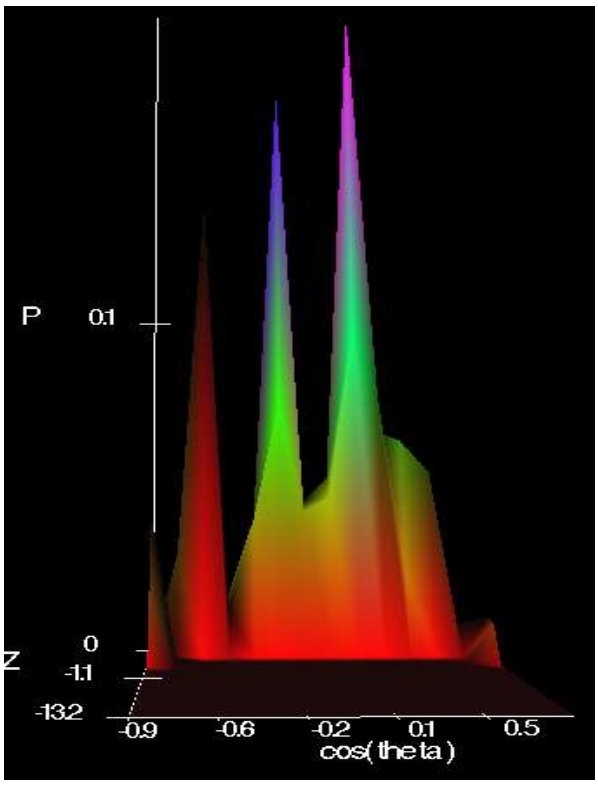

Figure 4-17 ring-ring orientation distribution for the simulation performed in the NST ensemble for the system containing 40 solvent molecules at a) 10 K (left) and b) 100 K (right)

The orientational correlation functions show that even though the peaks at $|\cos(\theta)| \approx 1$ are very well defined, the peaks at $|\cos(\theta)| \approx 0.34$ have merged at their base. This suggests that unlike what has been observed for the unsolvated system, the BTC rings of the framework have experienced some little motions. This suggests that since these motions have not been observed in the case of the unsolvated system (see figure 4-7) the inclusion of the solvent molecules is the parameter responsible for this BTC ring motion. Indeed, as it will be explained later in this section, this motion of BTC rings is likely to be explained by hydrogen bond competition between the alcohol ligand molecules and the alcohol solvent molecules, the alcohol solvent molecules leading to a relative weakening of the hydrogen bonds formed between the alcohol ligand molecules and the BTC molecules therefore allowing for some limited initial rotation of the BTC rings. However, even though the BTC rings seem to have experienced some motion, the four peaks in figure 4-17a are still present and well resolved. This suggests, along with the study of the evolution of the mean square displacements with time, the study of the RDFs, the visualization of the structure after

simulation and the evolution of the system volume with time that the structure stayed stable during the course of the simulation.

The same conclusions can be drawn from figure 4-17b. Indeed, it is also clear from figure 4-17b that even though the peaks at $|\cos(\theta)| \approx 0.34$ have merged at their base, all the peaks are still well defined. This also suggests that the inclusion of solvent molecules led to some motion of the BTC rings without destabilizing the entire three-dimensional structure of the framework.

Figure 4-18 presents the orientational distribution of BTC rings around a central BTC ring for simulations performed at 400 K.

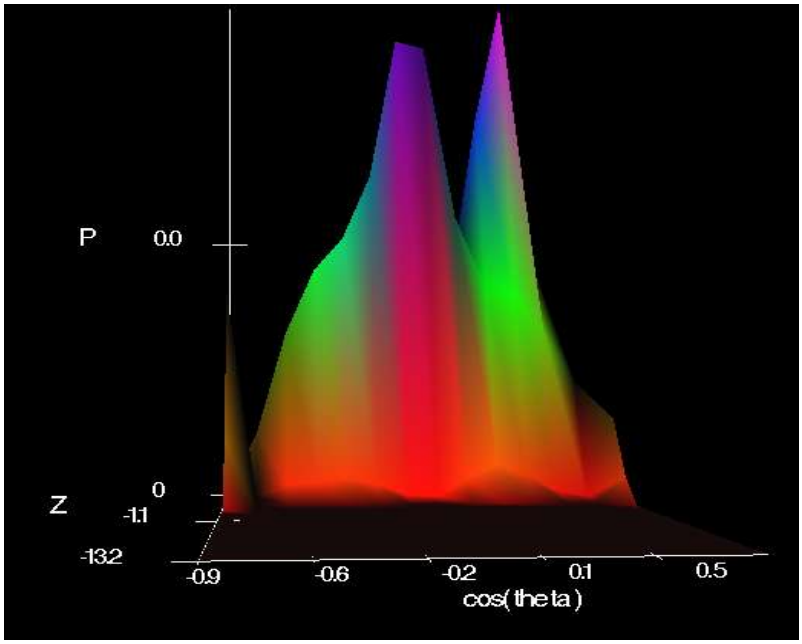

Figure 4-18 ring-ring orientational distribution for the simulation performed at 400 K and 0.1 kbar in the NST ensemble for the system containing 40 solvent molecules.

Figure 4-18 shows that the orientational distribution of the BTC rings at 400 K does not reproduce well the equivalent orientational distribution observed in the original crystal structure. Indeed, it is clear from figure 4-18 that the BTC rings have experienced significant motions during the course of the simulation even though the structure has not completely collapsed (peaks are still visible). This corroborates the fact that 400 K is the temperature of phase change for this solvated MOF.

Figure 4-19 describes radial distribution functions which are aimed at investigating the presence of hydrogen bonds between on one hand, the oxygen atoms of the BTC molecules and the hydrogen

atoms of the alcohol molecules, and on the other hand, the hydrogen bonds between alcohol ligand molecules and alcohol solvent molecules.

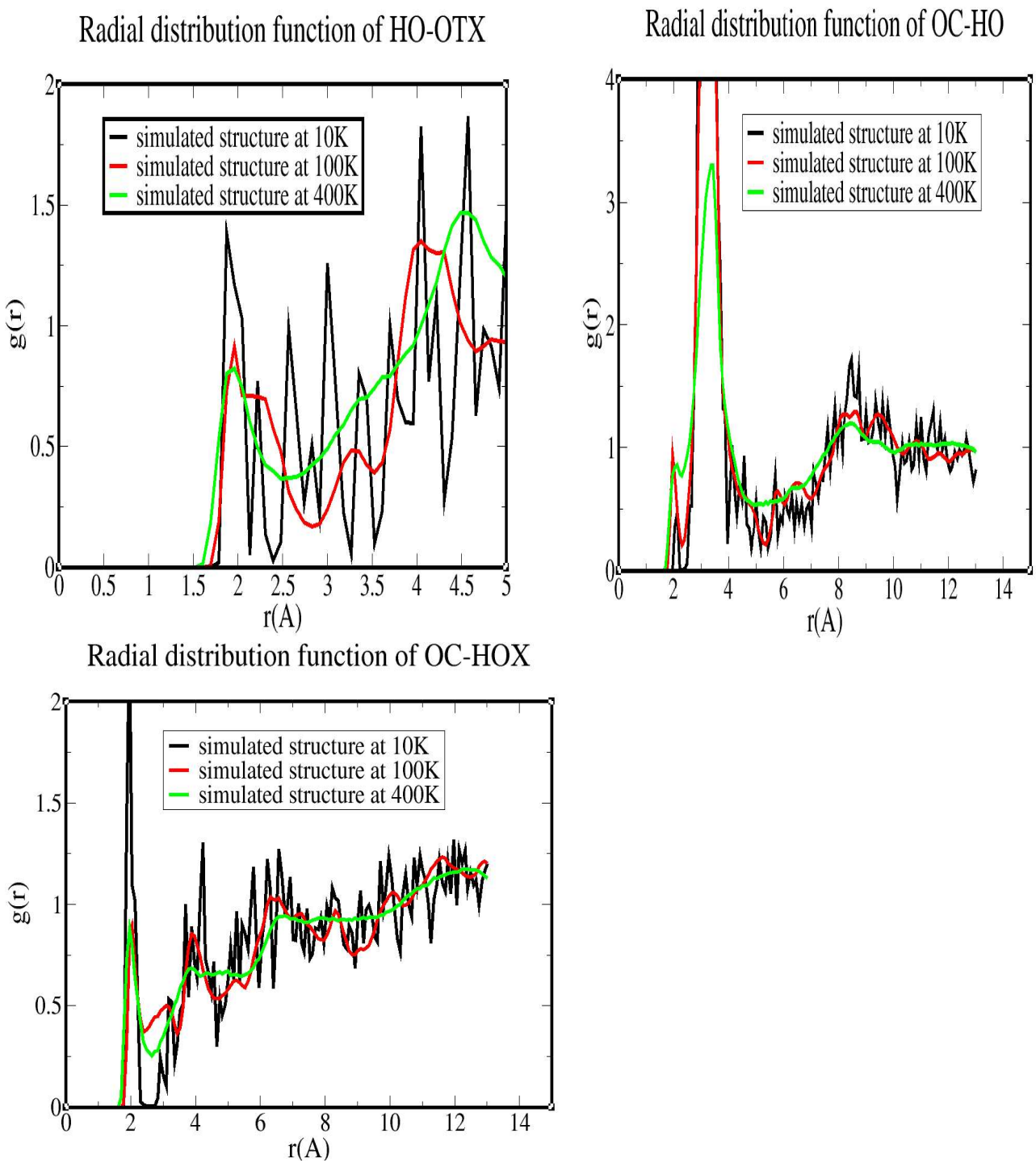

Figure 4-19 Radial distribution functions obtained after 500 ps of simulation in the NST ensemble for a system containing 40 solvent molecules at 10 K, 100 K and 400 K compared to the original crystal structure. ***OC*** *represents oxygen atoms of BTC molecules,* ***OTX*** *represents oxgen atoms of alcohol solvent molecules,* ***HOX*** *represents hydrogen atoms of the hydroxyl groups of solvent molecules and* ***HO*** *represents hydrogen atoms of the hydroxyl groups of the alcohol ligand molecules.*

Figure 4-19 shows that different hydrogen bonds are formed in this system. The HO-OTX RDF shows that at 10 K, 100 K and 400 K the OH groups of the alcohol solvent molecules form a hydrogen bond with the OH group of the alcohol ligand molecules. Indeed, the peak at 2 Å between the hydrogen atom of the hydroxyl group of the ligand molecules (HO), and the oxygen atoms of the alcohol solvent molecules (OTX) is typical of a hydrogen bond. It is noticeable from this RDF that this hydrogen bond remains even at 400 K. The OC-HOX RDF which represents the RDF between the oxygen atoms of the BTC molecules and the hydrogen atoms of the alcohol solvent molecules also shows by the presence of the peaks at 2 Å that a hydrogen bond is formed between these two atoms. It is also noticeable from this RDF that this hydrogen bond forms even at 400 K suggesting that the strength of this bond is high. It is also noticeable that these peaks at 2 Å are relatively sharp and well defined which further suggests that there is strong interaction between the oxygen atoms of the BTC molecules and the hydrogen atoms of the solvent molecules. It is likely that this strong hydrogen bond plays an important role in stabilizing the framework. Indeed, when the solvent is not present, the framework becomes unstable at temperatures higher than 150 K. However when more than 40 solvent molecules are added to the system, this framework does not experience phase change until temperatures higher than 400 K are reached. This hydrogen bond is most likely the factor that stabilizes this framework. The OC-HO RDF which represents the RDF between the oxygen atoms of the BTC molecules and the hydrogen atoms of the alcohol ligand molecules also shows peaks at 2 Å characteristic of a hydrogen bond formation. It is noticeable that at 10 K and 100 K this peak is very well defined and sharp while at 400 K it has become much less well defined. Even though it is noticeable that this peak is still present at 400 K and that the OC-HO hydrogen bonds still form at that temperature, it is clear that the closest distances between OC and HO atoms are not fixed suggesting significant motion of these atoms and thus a weaker hydrogen bond. The fact that the framework becomes unstable at 400 K can be linked to the weakening of this hydrogen bond. Indeed, a direct correlation can be made between the framework instability (demonstrated by a smaller cell volume, higher mean square displacement of nickel atoms, broader peaks in the RDFs) and the breaking of the hydrogen bond between the oxygen atoms of the BTC molecules and the hydrogen atoms of the alcohol ligand molecules. This hydrogen bond is a key

element in stabilizing the entire framework. This hydrogen bond is the main factor that impedes the carboxylic groups of the BTC molecules from twisting and therefore from leading to the destabilization and alteration of the three-dimensional structure of the framework.

A conjecture that can be made from figure 4-19 is that there might be a competition between the hydroxyl groups of the alcohol solvent molecules and alcohol ligand molecules to form a hydrogen bond with the oxygen atoms of the BTC molecules. This would explain why the orientation of the benzene rings of the BTC molecules show more variation for the solvated system than they do for the unsolvated system. Hydrogen bond formation between the alcohol solvent and BTC would lead to fewer hydrogen bonds between the alcohol ligand molecules and BTC molecules, and hence allow more motion in the geometry of the aromatic ring of BTC molecules. At the same time, however, the alcohol solvent molecules will stabilize the framework by forming hydrogen bonds with both the BTC molecules and the alcohol ligand molecules. This is well exemplified by the fact that the removal of these solvent molecules at temperatures higher than 150 K leads to the phase change, and subsequently (at higher temperatures) to the collapse of the framework.

Another observation that can be made from the study of the impact of the degree of solvation in the stability of the framework is that, while for the metal-organic framework with 4,5-octanediol as its alcohol ligands only 20 solvent molecules are required to stabilize the framework, for the metal-organic framework with 2,3-butanediol, however, twice as many solvent molecules are needed to stabilize the framework. Indeed, simulations using a number of solvent molecules lower than 40 for this metal-organic framework led to structures that got unstable and experienced phase change at temperatures as low as 150 K. This difference in degrees of solvation required for stability between the two metal-organic frameworks is explained mainly by the size of the solvent molecules. Indeed, 4,5-octanediol molecules are twice as long as the 2,3-butanediol molecules. It is therefore expected that for the system containing 2,3-butanediol molecules twice as many solvent molecules are needed to stabilize the framework than the number of solvent molecules required for the system containing 4,5-octanediol molecules.

Conclusion

This study showed that for the metal-organic framework containing 2,3-butanediol molecules as its alcohol ligands it was a lot more difficult to find a force field that accurately reproduced the experimental data than it has been for the metal-organic framework studied in chapter 3. Indeed, most of the force fields that gave relatively good agreement between the simulated and the experimental data in chapter 3 led to a significant decrease in cell volume and change of structure for the metal-organic framework with 2,3-butanediol, even at temperatures as low as 10 K. Out of the force fields developed in chapter 3, only one force field has successfully been transferred to the metal-organic framework containing 2,3-butanediol as its alcohol ligands. This force field is the FF-2 force field (see figure 3-9). This force field led to simulation results that agreed very well with the experimental data. Indeed, the average cell parameter obtained over 500 ps of simulation using this force field when simulating the framework in the *NPT* matched at 98.2 % the cell parameter of the original crystal structure. The fact that it has been easier to obtain force fields that do not lead systematically to phase change of the framework at 10 K for the system containing 4,5-octanediol than it has been for the system containing 2,3-butanediol might be explained by the length of the carbon chain of the alcohol ligands. One explanation for the difficulty to transfer these force fields would be that in the case of the metal-organic framework with 4,5-octanediol, the carbon chain of the alcohol molecules act as a sort of shield protecting the framework (especially metal-centers). Indeed, it is probable that the octanediol ligand molecules provide some steric protection to the framework by not allowing solvent molecules to access it. It is also possible that the carbon chain of the alcohol molecules form stabilizing interactions with the rest of the framework. These stabilizing interactions would most likely occur with the BTC molecules since these molecules are the closest to the methyl groups of the side carbon chains of the alcohol molecules. The fact that these interactions are diminished in the case of the framework with 2,3-butanediol might explain the difficulty to transfer these force fields. Another explanation for the difficulty to get force fields that led to stable metal-organic frameworks which accurately reproduced experimental data after

simulation can reside in the fact that polarization effects were not taken into consideration for the calculation of the partial charges of the atoms of the metal-organic frameworks. This lack of polarization effect might for example be the reason for the difficulty to model particularly the interaction between the nickel atoms and the hydroxyl oxygen atoms. Indeed, RDFs showed that out of all the atoms bound to nickel, the one for which the equilibrium bond distance after simulation differed the most from the equilibrium distance in the original crystal structure is the hydroxyl oxygen atom. This difference is observed for both the metal-organic framework with 4,5-octanediol and the one with 2,3-butanediol as alcohol ligand.

This study also showed that the unsolvated framework containing 2,3-butanediol stays stable up to a temperature of 150 K where it experiences a phase change. The solvated framework however stays stable up to a temperature of 400 K. For the solvated system, to stabilize the framework a minimum of 40 solvent molecules need to be added to the system. This is twice as many as the number of solvent molecules needed to stabilize the metal-organic framework with 4,5-octanediol as its alcohol ligand. This is explained by the difference in size between the two alcohol molecules. The 2,3-butanediol molecules are half the size of the 4,5-octanediol molecules, therefore twice the number of these molecules are needed to stabilize the framework. This study also showed the hydrogen bond formation between, respectively, the alcohol ligand molecules and the BTC molecules, the alcohol solvent molecules and the BTC molecules and the alcohol solvent molecules and alcohol ligand molecules. All these hydrogen bonds participate in stabilizing the three-dimensional structure of the framework. However, one of the suggestion drawn from this study is that there might be a competition between the alcohol ligand molecules and the alcohol solvent molecules to form hydrogen bonds with BTC molecules leading to some little rotation of the benzene rings of the BTC molecules without however destabilizing the framework. In this case, it would have been interesting to see what what are the polarization effects on the alcohol molecules, and especially on the hydroxyl group of the alcohol molecules, since they are bound to nickel atoms. Indeed, if polarization effects were taken into consideration for the calculation of partial charges, the framework alcohol molecules would have a different set of partial charges to the partial charges of the solvent alcohol molecules. This would affect the hydrogen bond competition between

on one side, the alcohol ligand molecules and the BTC molecules, and on the other side, the alcohol solvent molecules and the BTC molecules.

It is difficult to assess why it has been so difficult to find transferable force fields. This force field transferability problem is likely to be due to the complexity of the structure and the variety of atom types thus resulting in a large variety of pair potentials. We effectively get a set of 78 pair potentials which is a considerable number. Coupled with the complexity of the electrostatic interactions caused by the large number of atom types this effectively results in a very complex set of interactions and any modification of that set of interactions can dramatically change the resulting behavior of the 3 dimensional structure during the simulation.

4.3.2 Molecular Dynamics simulations on a metal-organic framework with 1,2,6-hexanetriol as its alcohol ligand.

Molecular dynamic simulations on the metal-organic framework with 1,2,6-hexanetriol as its alcohol ligand have been performed to investigate if the force field used for the two previous metal-organic frameworks, the one with 4,5-octanediol as its alcohol ligand and the one with 2,3-butanediol as its alcohol ligand, can also be transferred to this metal-organic framework. Due to the fact that, as described in section 4-1, CH_2CH_2OH groups have randomly been added to the sides of each diol groups in the crystal structure obtained with 4,5-octanediol molecules (but experimentally performed with 1,2,6-hexanetriol molecules in the reaction mixture for the synthesis of the metal-organic framework) it was expected that high starting configurational energies will be observed during the simulation. This high configuration energy results from the fact that atoms of the added CH_2CH_2OH groups, and especially the hydroxyl group of these CH_2CH_2OH groups gets very close to other atoms of the framework resulting in very high van der Waals energy and hence very high configurational energy. This high starting configurational energy led to either, a premature stopping of the simulation or, when very small time steps were used, to instability and then phase change of the framework. Therefore to run simulations successfully, a very small time step, typically in the

order of a hundredth of a femtosecond, had to be used in order to get a running simulation (otherwise the program crashes due to the resulting very high repulsion forces). Together with the use of a very small time step, to minimize this very high starting configurational energy the atomic positions of all the atoms of the framework, except the end butanol chains of the 1,2,6-hexanetriol molecules, had to be fixed for the first sets of simulations. Only after the configurational energy had dropped to stable values, these constrains on the atomic positions have been removed and the framework allowed to move freely if the force field dictated it.

Simulations on this MOF were first performed in the *NVT* ensemble at low temperature (10 K) and using a very small simulation time step. The use of larger time steps invariably led to the crashing of the molecular dynamics program. The very small time step was therefore used as an equilibration method, and this time step was increased at every successive simulation. To relax the system the 0.01 fs time step was used for the first 200 000 steps with an equilibration period of 100 000 steps. For this first simulation period the positions of all the atoms of the system except from the terminal oxygen atoms, the carbon atoms and the hydrogen atoms of the 1,2,6-hexanetriols were kept fixed. This process was done so that the butanol chain of the trialcohol finds more stable configurations and thus to remove the excess energy resulting from the steric hindrance between these butanol chains and other atoms of the framework.

In this section it will be demonstrated that the distance between the nickel atoms and the alcohol oxygen atoms which are bound to these nickel atoms in the initial configuration have to be constrained during the course of the simulation to get simulation results that accurately reproduce experimental data (the constrained Ni-O distance that was chosen is the Ni-O distance observed in the original crystal structure). Indeed, as it will be shown in this study, without this constrained, one of the oxygen atoms of the triol systematically gets away from the nickel atom it was initially bound to. This Ni-O bond breaking behavior destabilizes the framework and this constrained helps to stabilize it. There might be several reasons for that bond breaking behavior. Firstly it might be caused by the competition between one of the initially bound oxygen to the nickel center and the terminal oxygen of the same triol to bind to the same nickel by the folding of the carbon chain of

this alcohol. It might also result from the binding competition of one of the oxygen initially bound to the nickel with a terminal oxygen atom from an adjacent alcohol. Finally this Ni-O bond breaking behavior might result from the fact that the terminal hydroxyl group of the triol gets strongly attracted by some sites in its neighboring environment (most likely by creating a hydrogen bonding interaction with a neighboring carboxylic group of a BTC molecule).

Figure 4-20 shows snapshots of the unsolvated framework before and after the first 500 ps of simulation at 10 K and 0.1 kbar in the *NVT* ensemble.

a *b*

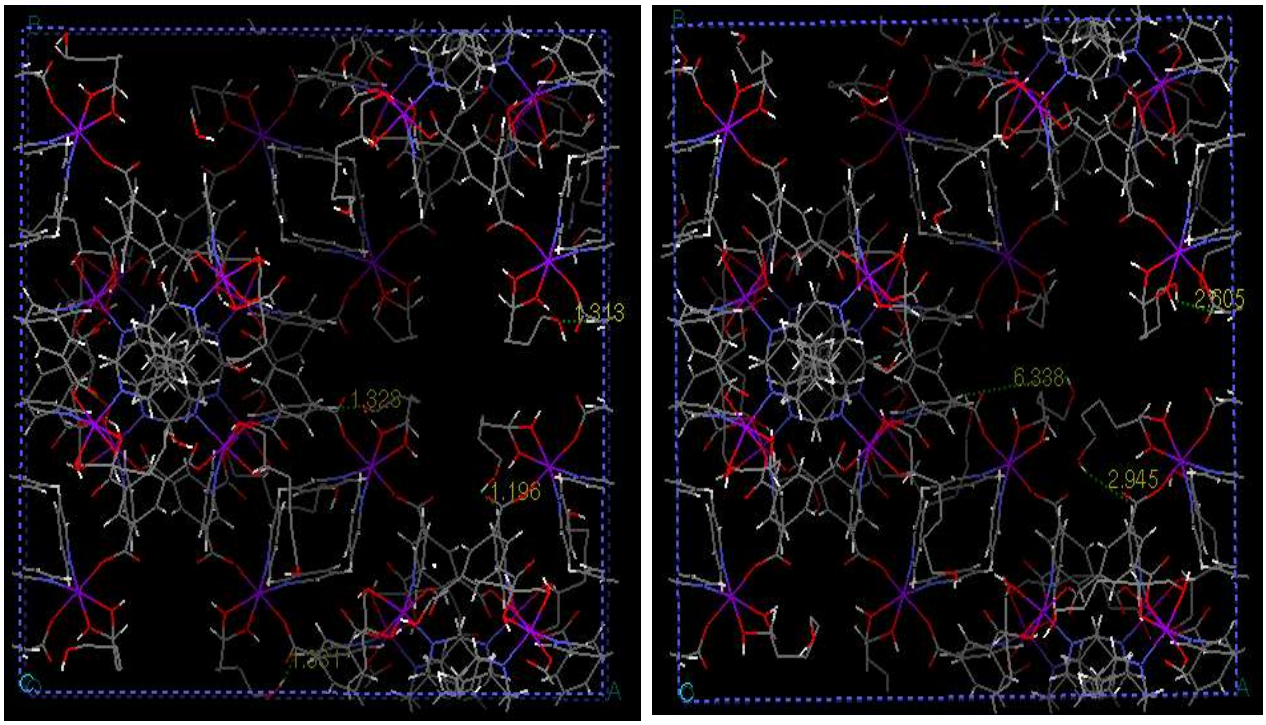

Figure 4-20 Snapshots of the framework a) before (left) and b) after (right) simulations in the NVT ensemble. Except for the side chain of the triol molecules, all the atoms of the framework were held fixed during the course of the simulation.

It is noticeable from figure 4-20a which presents the configuration of the framework before simulation that for all the triol molecules, the terminal hydroxyl groups gets close to the the BTC and pyridine molecules. However, in the snapshot represented in figure 4-20b, which presents the

relaxed framework, it is noticeable that the terminal hydroxyl groups of the triol molecules got away from the framework, that the alcohol molecules unfolded and that their terminal hydroxyl groups point towards the pores. The evolution of the root mean square displacement with time and the RDFs showed that the very high configurational energy resulted from the close contact between the terminal hydroxyl group of the alcohol molecules and the hydrogen atoms of the aromatic pyridine and benzene rings. Indeed, in the initial structure the minimum distance between HA (aromatic hydrogen of BTC and pyridine molecules) and HO is 1.5 Å while the sigma parameter between these two atoms is 1.8620 Å. Similarly, the minimum distance between HA and OT (oxygen atoms of the alcohol molecules) in the original structure is 1.7 Å while the sigma parameter between these two atoms is 2.5658 Å. The sigma parameter representing the minimum distance between two atoms from which the van der Waals energy begins to tend to infinity, it is therefore obvious that this very high initial configurational energy results from the very close contact between the terminal hydroxyl groups of the alcohol molecules and the hydrogen atoms of the BTC rings. Once the system has relaxed, simulations were performed in both the *NPT* and *NST* ensembles.

Once the configurational energy of the system stabilized and the structure relaxed, some simulations were performed with all the atoms of the framework being allowed to move freely depending on the interactions they experienced. From those simulations, it has been observed that one of the hydroxyl group which was formerly bound to the nickel atom has moved away from nickel and that this Nickel-Oxygen bond has been broken. We observe that phenomenon for all alcohol molecules and whatever force filed we use. We also observe that behavior at different solvation degrees. The fact that this Nickel-Oxygen bond breaking happens at 10 K and after a very short simulation time, typically few picoseconds, shows that there are strong interactions leading to that increase in Nickel-Oxygen distance.

The fact that this bond breaking behavior was not observed when we used diols as equatorial ligands of the framework suggests that the terminal hydroxyl group of these triol molecules is the cause of these Nickel-Oxygen bond breaking and that there are behaviors and interactions involving

that terminal hydroxyl group that lead at least partially to this Nickel-Oxygen bond breaking and thus to the destabilization of the 3D structure of the framework.

Figure 4-21 shows a snapshot of the metal-organic framework obtained at 100 K and 0.1 kbar in the *NPT* ensemble after 200 ps of simulation when all atoms of the framework are allowed to move freely. Prior to these 200 ps of simulation, simulations were performed with all the atoms of the framework (except the atoms of the side chains of the triol molecules) fixed to allow the system to relax.

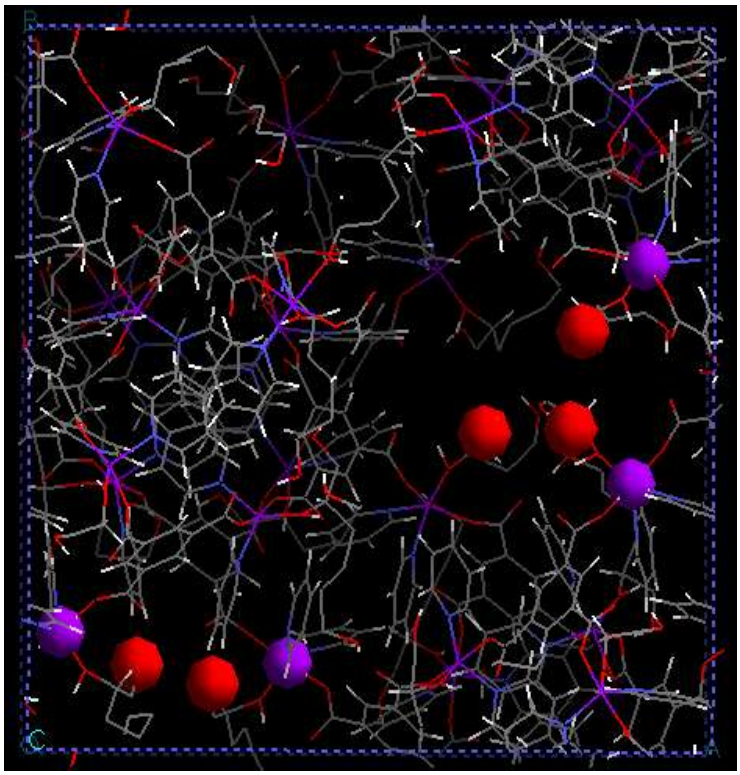

Figure 4-21 Snapshot of the completely flexible framework when simulated at 100 K in the NPT ensemble for 200 ps. The red balls represent the terminal oxygen atoms of the triol molecules while the violet balls represent nickel atoms.

It is clear from figure 4-21 that for each alcohol molecule, one of the oxygen atoms of the diol group of the triol molecule gets detached from the nickel atoms. Indeed, it is clear from figure 4-21 that the triol molecules are bound in a monodentate way to the nickel atoms rather than in a bidentate way. Out of the two oxygen atoms of the diol group that was bound initially in a bidentate

way to the nickel center, the nickel-oxygen bond breaking always occurs with the oxygen atom that is closest to the side chain of the triol molecule. One mechanism for this bond breaking behavior would be that the terminal hydroxyl group of the triol molecules pulls one of the oxygen atoms of the diol group away from the nickel centers, hence leading to the breaking of the nickel-oxygen bond.

This breaking of the nickel-oxygen bond led to destabilization of the framework and a smaller cell parameter than what was expected. Indeed, the simulation in the *NPT* ensemble led to a cell parameter equal to 26.7 Å. Compared to the 28.804 Å of the original cell, it is noticeable that the cell has experience a significant volume reduction during the course of the simulation. The difference between the original cell parameter and the simulated cell parameter is therefore 7.3 %. This a lot more than what was obtained for the metal-organic frameworks with 4,5-octanediol or 2,3-butanediol as alcohol ligand where the differences between the original and simulated cell parameters were in the order of 2 %. This failure of the force field to accurately reproduce the experimental cell parameter is likely to be caused by the nickel-oxygen bond breaking. This bond breaking is likely to be caused by the motion of the terminal oxygen of the alcohol molecule.

Figure 4-22 shows the evolution of the mean square displacement of some atoms of the framework, for simulations performed at100 K and 0.1 kbar in the *NPT* ensemble.

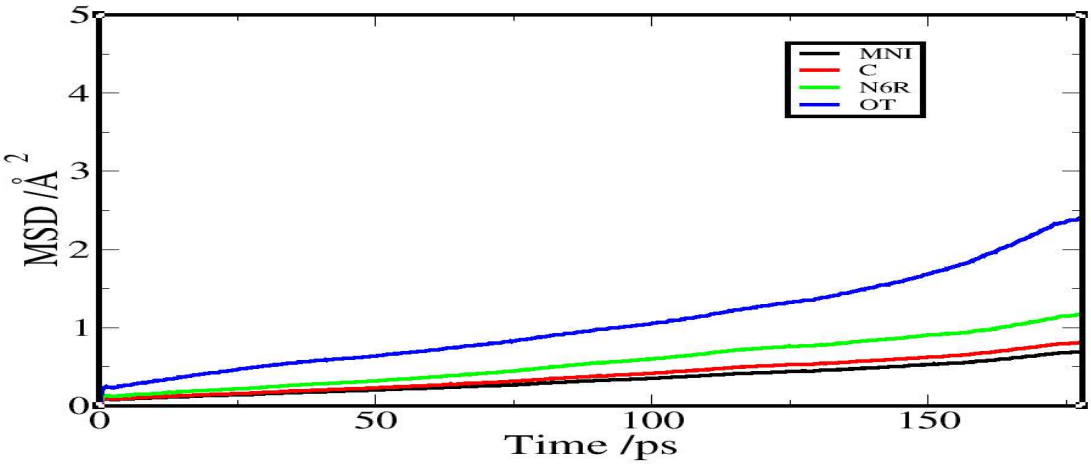

Figure 4-22 Evolution of the mean square displacement of some atoms of the framework with time at 100 K in the NPT ensemble.
MNI represents nickel atoms, C represents the carbon atoms of the carboxylic groups of BTC molecules, N6R represents nitrosen atoms and OT represents the oxygen atoms of the alcohol molecules.

It is clear from figure 4-22 that OT atoms have a much higher mean square displacement than the other atoms of the framework. This corroborates what has been seen in the snapshot represented in figure 4-21. Indeed, this higher mean square displacement of OT atoms can be partly explained by the fact that one of the OT atoms of the diol group got away from the nickel it was bound to. This motion hence led to the breaking of this bond.

It is also noticeable from figure 4-22 that the other atoms of the framework also experienced some motion even though they do not show a liquid like behavior which would have suggested that the framework has collapsed. Indeed, the root mean square displacement of these atoms is still small.

The principal conclusion which can be drawn from figure 4-22 is that the extensive motion of oxygen atoms, and the breaking of the nickel-oxygen bond led to the destabilization of the entire framework (even though it has not collapsed) resulting in a significantly smaller cell parameter than the cell parameter of the original crystal structure.

To overcome this problem of nickel-oxygen bond breaking, simulations were performed with the Ni-OT bond distances constrained. The value of the constrained bond distance was taken from the original crystal structure. Figure 4-23 shows the radial distribution function of OT atoms around a central nickel atom for both the frameworks without constraint and the framework for which the Ni-

OT bond distance was constrained. These simulations were performed for 200 ps at 100 K and 0.1 kbar in the *NPT* ensemble.

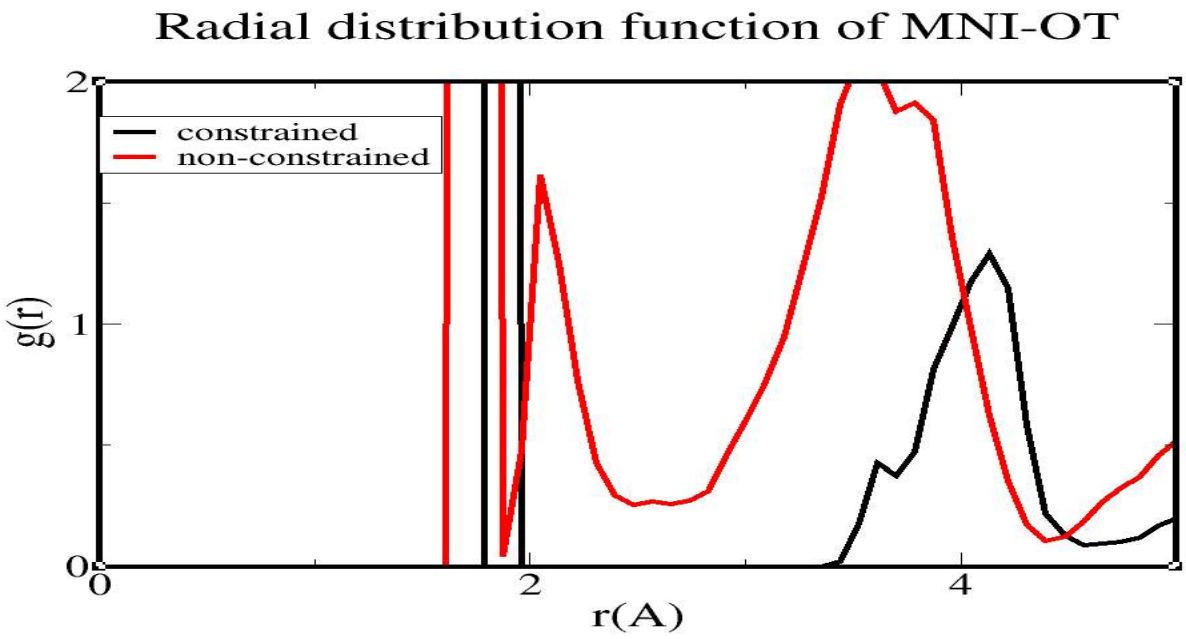

Figure 4-23 Radial distribution function of MNI-OT for the framework without constraint and the framework for which MN-OT bond distance was constrained.

With the constraints present there is one sharp peak at around 1.87 Å, and then nothing between 2 Å and 3.5 Å. This peak at 1.9 Å represents the distance between the nickel atoms and the two hydroxyl oxygen atoms that are bound to these nickel centers due to the constraint. The situation is very different for the RDF of the non constrained framework (red curve). In this RDF there is still a well defined peak at around 1.7 Å which represents the distance between a nickel atom and the one hydroxyl oxygen atom that stays bound to it. Then from 1.9 Å to the rest of the range of the RDF, the nickel-oxygen bond distances vary without discontinuity (g(r) always higher than zero). This is explained by the fact that the second hydroxyl oxygen atoms that were initially bound to the metal-centers moved away from these metal-centers leading to the breaking of this nickel-oxygen bong. It is clear from figure 4-23 that constraining this nickel-oxygen bond distance impedes the nickel-oxygen bond from being broken therefore resulting in a better defined structure as shown in figure 4-24.

Figure 4-24 shows snapshots of the framework after 200 ps of simulation at 100 K and 150 K in the *NPT* ensemble. During this simulation the distance between nickel atoms and the oxygen atoms of the diol groups of the alcohol molecules were constrained. The structure of the original framework is evident in both in a way that was not apparent in figure 4-21, although some disorder of the pores is seen at 150 K.

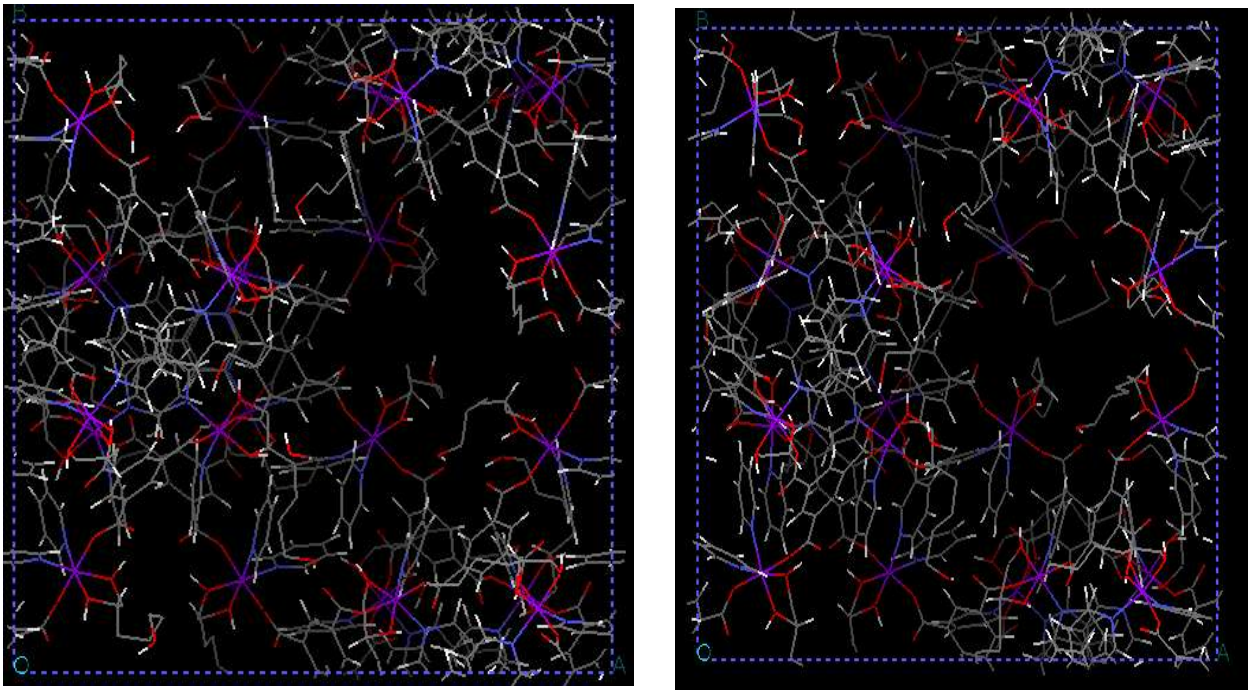

Figure 4-24 Snapshot of the framework when simulated at a) 100 K (left) and b) 150 K (right) in the NPT ensemble for 200 ps.

Table 4-6 shows the cell parameters obtained after these simulations at 100 K and 150 K. These cell parameters were averaged over 200 ps of simulation.

	simulated cell parameter /Å
100 K	27.83
150 K	27.63

Table 4-6 Cell parameters obtained at 100 K and 150 K in the NPT ensemble.

Table 4-6 shows that for the simulated framework at 100 K, the difference between the simulated cell parameter and the original cell parameter is now 3.4 %. At 150 K, the difference is 4 %. This shows that by constraining the nickel-oxygen distance, it has been possible to get a much better match between the simulated and the original cell parameter.

Figure 4-25 shows the evolution of the mean square displacement of nickel atoms of this metal-organic frameworks for simulations performed at 100 K and 150 K in the *NPT* ensemble.

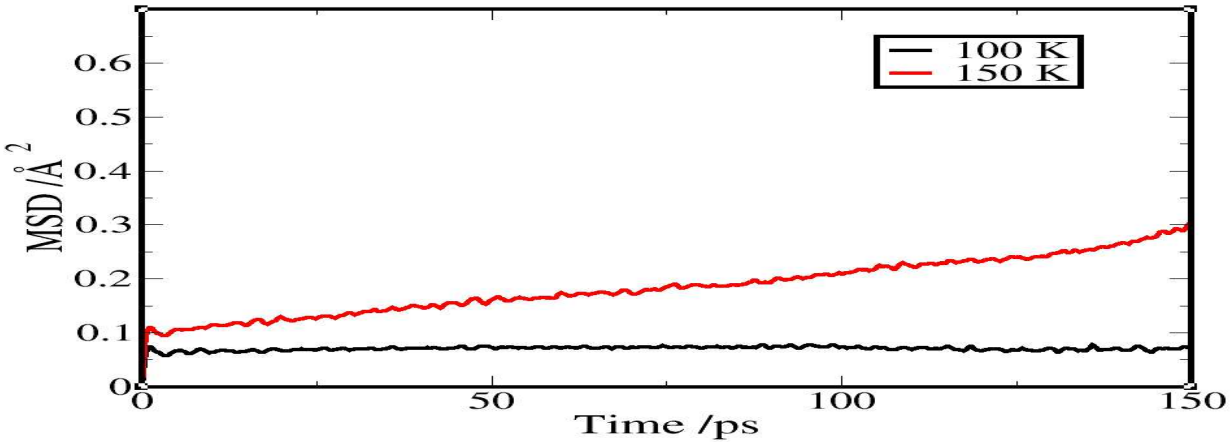

Figure 4-25 Evolution of the mean square displacement of Ni ions with time at 100 K and 150 K in the NPT ensemble.

It is clear from figure 4-25 that the position of nickel atoms during the simulation at 100 K are practically fixed. Indeed, the curve representing the evolution of the mean square displacement of the nickel atoms with time is roughly horizontal and the value of the mean square displacement fluctuates around 0.06 Å^2. At 150 K, the value of the mean square displacement of the nickel atoms stays also very low even though some fluctuation in the position of the nickel atoms can be deduced from figure 4-25. This increased root mean square displacement compared to the values obtained at 100 K results from vibration of the nickel atoms induced by the increased temperature (thermal motion). Figure 4-25 shows therefore that at both 100 K and 150 K, the atomic positions of nickel atoms stay practically fixed. Therefore, it is possible to conclude that at both these temperatures, the framework stayed stable.

Since during the course of these simulations, a constrained bond distance has been imposed between nickel atoms and the oxygen atoms of the diol groups of the alcohol molecules, it is

possible that this constraint partially fixed the position of nickel atoms. Therefore, to corroborate the conclusions drawn from figure 4-25, the evolution of the mean square displacement of other atoms than nickel with time have been performed.

Figure 4-26 shows the evolution of the mean square displacement of C atoms, which represent the carbon atoms of the carboxylic groups of BTC molecules, with time for simulations performed at 100 K and 150 K in the *NPT* ensemble.

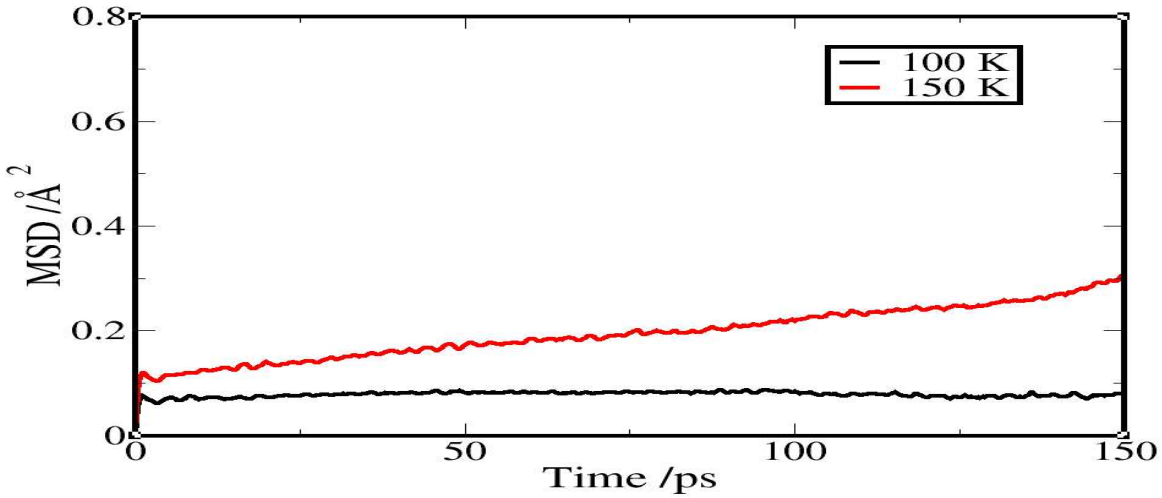

Figure 4-26 Evolution of the mean square displacement of C atoms with time at 100 K and 150 K in the NPT ensemble.

Figure 4-26 corroborates exactly the conclusions drawn from figure 4-25. The study of the evolution of the mean square displacement of other atoms with time also leads to the same conclusion. This metal-organic framework stays stable at 100 K and 150 K. One can make the comparison of the values of the mean square displacements obtained in figures 4-25 and 4-26 with the values obtained in figure 4-22 where the nickel-oxygen (of the alcohol ligands) bond distances were not constrained. Indeed, when this bond is constrained the values of the mean square displacements obtained do not exceed 0.06 Å^2 at 100 K while in the case where this bond is not constrained the values of the mean square displacements obtained are much higher. This shows that constraining this Ni-OT bond distance significantly stabilize the framework thus leading to cell parameters obtained after simulation that are in reasonable agreement with the cell parameters of the original crystal structure.

Conclusion

This study shows that this force field is also appropriate for the study of the metal-organic framework with 1,2,6-hexanetriol as its alcohol ligand in the *NPT* ensemble. However, for the force field to reproduce well the experimental cell parameter, the distance between the nickel atoms and the alcohol oxygen atoms that are initially bound to them have to be constrained. Indeed, if this nickel-oxygen bond distance is not constrained, one of the oxygen atoms initially bound to the nickel gets away from it. This results in this nickel-oxygen bond being broken and subsequently, the framework being destabilized. When this force field is used with this nickel-oxygen bond distance constrained, good agreement is obtained between the original cell parameter and the cell parameter obtained after simulations at 100 K and 150 K in the *NPT* ensemble. However, it has not been possible to reproduce experimental data when this framework is simulated in the *NST* ensemble. Indeed, simulations in the *NST* ensemble led to cell parameters significantly smaller that the cell parameters of the original framework. We believe that this failure of the force field is explained by the fact that it does not reproduce well the interactions involving the terminal oxygen atom of the triol molecules. It might also be the case that the absence of a carbon chain at one side of the diol group of the alcohol molecules has affected the stability of the framework. Indeed, it is likely that the side chains of the alcohol ligands stabilize the framework. That would also be verified by the fact that the metal-organic framework with 4,5-octanediol as its equatorial ligand was more stable, and that it was easier to find a suitable force field for this system than for the metal-organic framework with 2,3-butanediol as its alcohol ligand.

5 Investigation of the potential enantioselective properties of these helical metal-organic frameworks.

5.1 Introduction

In chapter one the possibility of using chiral MOFs for catalysis, gas storage or enantioselectivity was explored. We suggested that modelling could be a very powerful tool for exploring the scope for this, but only once suitable force fields had been developed. In chapter three and four we described the development and testing of a force field and showed it could give an acceptable (though not yet definitive) description of this class of MOFs. In this chapter we therefore return to the question of chiral discrimination.

In this chapter we present the initial results of a study of chiral discrimination within chiral MOFs. It represents a scoping study into the possibility of exploiting chiral MOFs for applications in chiral selection, and is intended to identify fruitful avenues for future research. The focus is on a very important potential property of helical metal-organic frameworks, namely enantioselectivity.

Homochiral crystals of these helical metal-organic frameworks have been synthesized and it is in our interest to investigate the enantioselective properties of such materials. For that purpose a set of MD simulations have been performed. The metal-organic framework used for these simulations is based on the formula $Ni_3BTC_2alc_3pyr_6$ (alc = 4,5-octanediol). The solvent molecules used are also 4,5-octanediol molecules. The use of the same molecules for the solvent and the alcohol ligand is important since these solvent molecules are believed to act simultaneously as template for the formation of the helical structure and as ligand molecules for the framework with possibility of interchange between ligand and solvent molecules. The alcohol used as equatorial ligand for the metal-organic framework is of the (S,S) enantiomeric form in all our simulations. The first set of MD simulations were performed by adding, twenty solvent molecules of the (S,S) alcohol into the

cavities in the MOF. A second set of simulations was then performed with twenty (R,R) alcohol molecules instead. Finally, a racemic mixture consisting of ten (R,R) and ten (S,S) alcohol molecules was added to the unsolvated framework. The force field used is the FF-1 force field of table 3-9. For consistency, the same van der Waals parameters and the same partial charges were used for the alcohol ligand molecules and the alcohol solvent molecules (of both enantiomeric versions) though we note the conclusions of chapter four that this might overstate framework-solvent interactions and it might have been more accurate to take into consideration polarizability effects when assigning partial charges to the alcohol ligand molecules. However, for the reasons described in chapter 3, polarizability effects between the different constituents of the framework were specifically ignored in this work.

5.2 Simulation details

For the computation of the long ranged electrostatic interactions, The Ewald summation method was used. All hydrogen atoms were assigned a mass of 2 u to get better energy conservation by decreasing the frequency of vibration of hydrogen atoms. Simulations were performed in both the *NPT* and *NST* ensembles. The Hoover thermostat was used with a time relaxation constant of 0.1 ps for the thermostat and 1 ps for the thermostat in the *NST* ensemble. In the *NPT* ensemble, the time relaxation constant used for the thermostat is 0.5 ps and 1ps for the barostat. For each system, simulations were performed for a minimum of 500 ps before analysis. To check for reproducibility of the behavior of the solvent molecules inside the framework, different starting configurations of the solvent molecules have been added to the framework. To get these different starting configurations of the solvent molecules inside the MOF, simulations were performed on bulk solvent systems. For both the systems with enantiomerically pure solvent molecules and for the system containing a racemic mixture of solvent molecules, the solvent molecules were successively heated at 4000 K and then cooled at 200 K (in cycles) for different lengths of time before being added to the MOF. The heating of these solvent molecules in bulk systems at very high

temperatures led to random configurations of solvent molecules inside these bulk solvent systems. Configurations of solvent molecules taken at different time intervals were then added to the empty MOF ensuring that each system contained a different arrangement of solvent molecules. Because of overlap between solvent atoms and MOF atoms when solvent molecules are first added to the system (using SOLVADD as described in section 3-4 of this thesis), a time step of 0.1 fs was initially used while freezing the framework atoms of the MOF to allow the system to relax. This was done to allow solvent molecules to move away from the framework and find more stable configurations so that the insertion process did not artificially stress the framework. Simulations were performed on the fixed MOF for a further 40 ps using a 1 fs time step, before allowing the framework atoms to move according to the forces they experienced. Then, simulations on the flexible MOF were then performed for 500 ps at 150 K and 0.1 kbar.

For these simulations, initial cubic boundary conditions were used to mimic an infinite system. However, for simulations in the *NST* ensemble, even though the original cell prior to simulations is cubic, it was allowed to change shape during the course of the simulation.

5.3 Results

In the first instance, simulations performed on the metal-organic framework containing only one enantiomeric version of the solvent molecules inside their pores, either the R,R or the S,S version, will be analyzed to determine whether there is a preference by the framework for a specific solvent enantiomer. As it will be shown that there is some discrimination, results with the racemic solvent will then be discussed to determine whether a chiral separation might be effected.

Since there is no (R,S) meso form of the alcohol molecules present in the systems studied, for the rest of this chapter, the (S,S) enantiomeric form will be referred to as the S form and the (R,R) enantiomeric form will be referred to as the R form.

5.3.1 Enantiomerically pure solvents

MD simulations containing the pure R-R, or the pure S-S, form of the solvent alcohol were performed, as described above. The cell volume for each system is reported in figure 5-1, and is shown to be stable over the 500 ps production run.

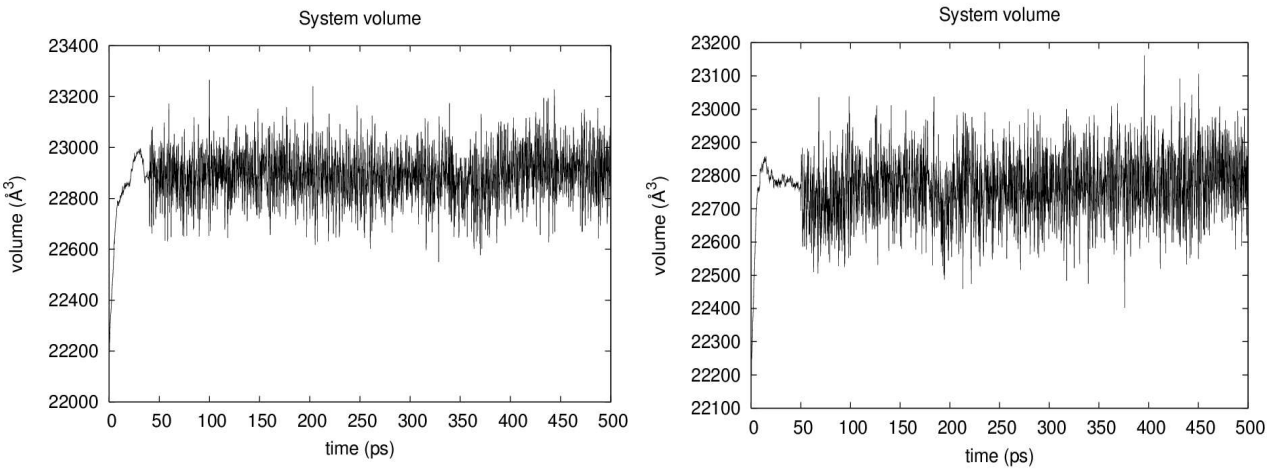

Figure 5-1 Evolution of the system volume with time for a system containing a) the (S,S) alcohol solvent (left) and b) the (R,R) alcohol solvent (right). Simulations were performed for 500 ps in the NST ensemble at 150 K and 0.1 kbar. The number of solvent molecules used for each system is 20.

Table 5-1 shows the cell parameters averaged over 500 ps of simulation in the *NST* ensemble at 150 K and 0.1 kbar when the framework contains either the R enantiomeric form of the solvent molecules or the S one.

	***a* /Å**	***b* /Å**	***c* /Å**	***α* / °**	***β* / °**	***γ* / °**	***Volume* /Å^3**
simulated structure with the S solvent	28.467 +/- 0.11	28.289 +/- 0.11	28.539 +/- 0.11	89.19 +/- 0.36	90.58 +/- 0.36	91.13 +/- 0.36	22893 +/- 80
simulated structure with the R solvent	28.511 +/- 0.11	28.631 +/- 0.11	27.894 +/- 0.11	89.69 +/- 0.36	90.15 +/- 0.36	89.76 +/- 0.36	22766 +/- 80
original crystal structure	28.804 +/- 0.11	28.804 +/- 0.11	28.804 +/- 0.11	90.00 +/- 0.36	90.00 +/- 0.36	90.00 +/- 0.36	23898 +/- 80

Table 5-1 Cell parameters averaged over 500 ps of simulation in the NST ensemble at 150 K and 0.1 kbar for a system containing 20 solvent molecules of the S enmantiomeric form and a system containing 20 solvent molecules of the R enantiomeric form compared to the cell parameters of the original crystal structure.

The cell parameters, and consequently the volume, of the MOF is essentially independent of whether the R- or the S- alcohol is used as solvent. Similarly, the configurational energy (table 5-2) shows little difference between the two solvents: the difference of 0.1 % is well within the statistical uncertainty of the calculations. This suggests that the MOF framework is not significantly affected by the enantiomeric form of the solvent at these solvation levels.

	configurational energy /kcal.mol^{-1}
Framework containing the S solvent	-17375
Framework containing the R solvent	-17354

Table 5-2 Configurational energy averaged over 500 ps of simualtion in the NST ensemble at 150 K and 0.1 kbar for a system containing 20 solvent molecules of the S enantiomeric form and a system containing 20 solvent molecules of the R enantiomeric form.

Interaction energies between the framework and solvent molecules were also determined for the system containing the R-alcohol solvent as well as for the system containing the S-alcohol solvent. This was performed to determine if there is a “preference” by the framework for a specific

enantiomeric form of the solvent molecules.

The interactions energies between the framework and the solvent were determined using equation 5-1:

$$E_{inter} = E_{frame+solv} - (E_{frame} + E_{solv})$$

Equation 5-1

Where E_{inter} represents the interaction energy between the framework and the solvent, $E_{frame + solv}$ the configurational energy of the system containing both the framework and the solvent, E_{frame} the configurational energy of the system containing only the framework and E_{solv} the configurational energy of the system containing only the solvent.

Table 5-3 presents the interaction energies obtained for a system containing the S-solvent and a system containing the R-solvent.

These interaction energies were obtained after 500 ps of simulation in the *NST* ensemble at 150 K and 0.1 kbar.

	Interaction energy /kcal.mol^{-1}
Framework containing the S solvent	-4637.84
Framework containing the R solvent	-4579.24

Table 5-3 Interaction energy averaged over 500 ps of simulation in the NST ensemble at 150 K and 0.1 kbar for a system containing 20 solvent molecules of the S enantiomeric form and a system containing 20 solvent molecules of the R enantiomeric form.

It is observable from table 5-3 that the contribution of the interaction energy to the total energy is higher for the framework containing the S solvent (same enantiomeric form as the alcohol framework molecules) that it is for the framework containing the R solvent (opposite enantiomeric form to the alcohol framework molecules).

This suggests that the framework has a stronger interaction with the S solvent which is the solvent of the same enantiomeric form as the alcohol framework molecules than it has with the solvent of the opposite enantiomeric form to the framework alcohol molecules.

The mean square displacement of nickel atoms in the two systems is shown in figure 5-2.

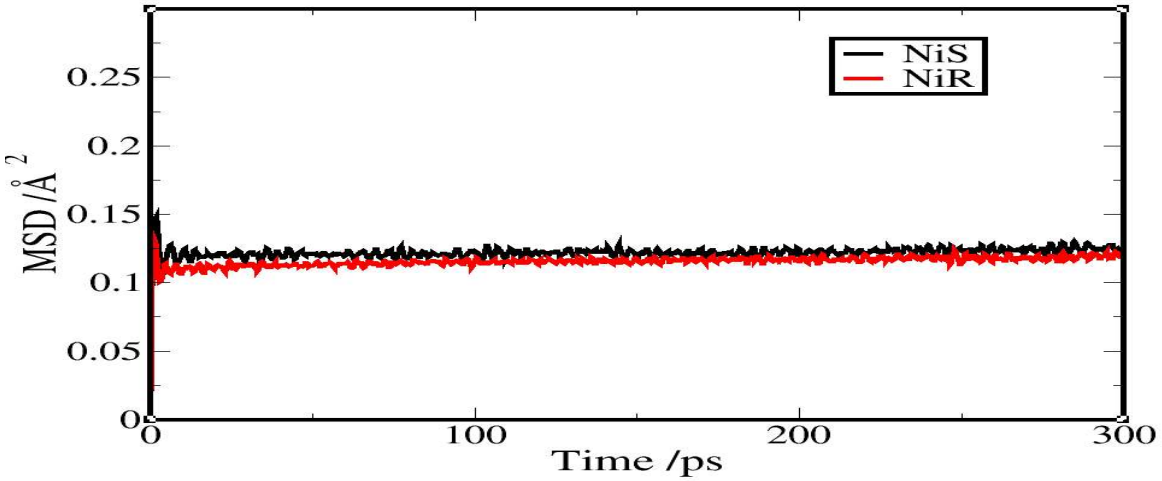

Figure 5-2 Evolution of the mean square displacement of nickel atoms of the framework containing on one hand the R enantiomeric version of the solvent molecules (represented by the NiR curve) and on the other hand the S enantiomeric version of the solvent molecules (represented by the NiS curve).
The simulation was performed for 500 ps in the NST ensemble at 150 K and 0.1 kbar.

There is no evidence of any motion other than lattice vibrations in either system. The amplitude of vibrations is very similar in both, although the amplitude is consistently smaller with the R solvent. Furthermore, the study of the orientational distribution of the aromatic BTC rings constituting the MOF showed no significant differences depending on whether the framework pores were occupied by the S or the R solvent molecules. This is another indication that the framework stays stable independently of which enantiomeric version of the solvent is present inside its pores.
All these analyzes therefore show that, both the framework containing the R solvent and the framework containing the S solvent are stable and that there is no energetically more favorable enantiomeric form of the solvent molecules for the framework.

Figure 5-3 shows selected RDFs for the two systems. The alcohol framework molecules constituting the metal-organic framework are of the S enantiomeric version. In these graphs the label S relates to the alcohol solvent molecules of the S enantiomeric version (therefore same enantiomeric version as the alcohol framework molecules) while the label R relates to alcohol

solvent molecules of the R enantiomeric version (opposite enantiomeric version to the alcohol framework molecules).

These radial distribution functions represent distances between framework atoms and solvent atoms. For example, in the OT-OT RDF, the first OT represents the oxygen atoms of the alcohol framework molecules while the second OT represents the oxygen atoms of the relevant solvent alcohol.

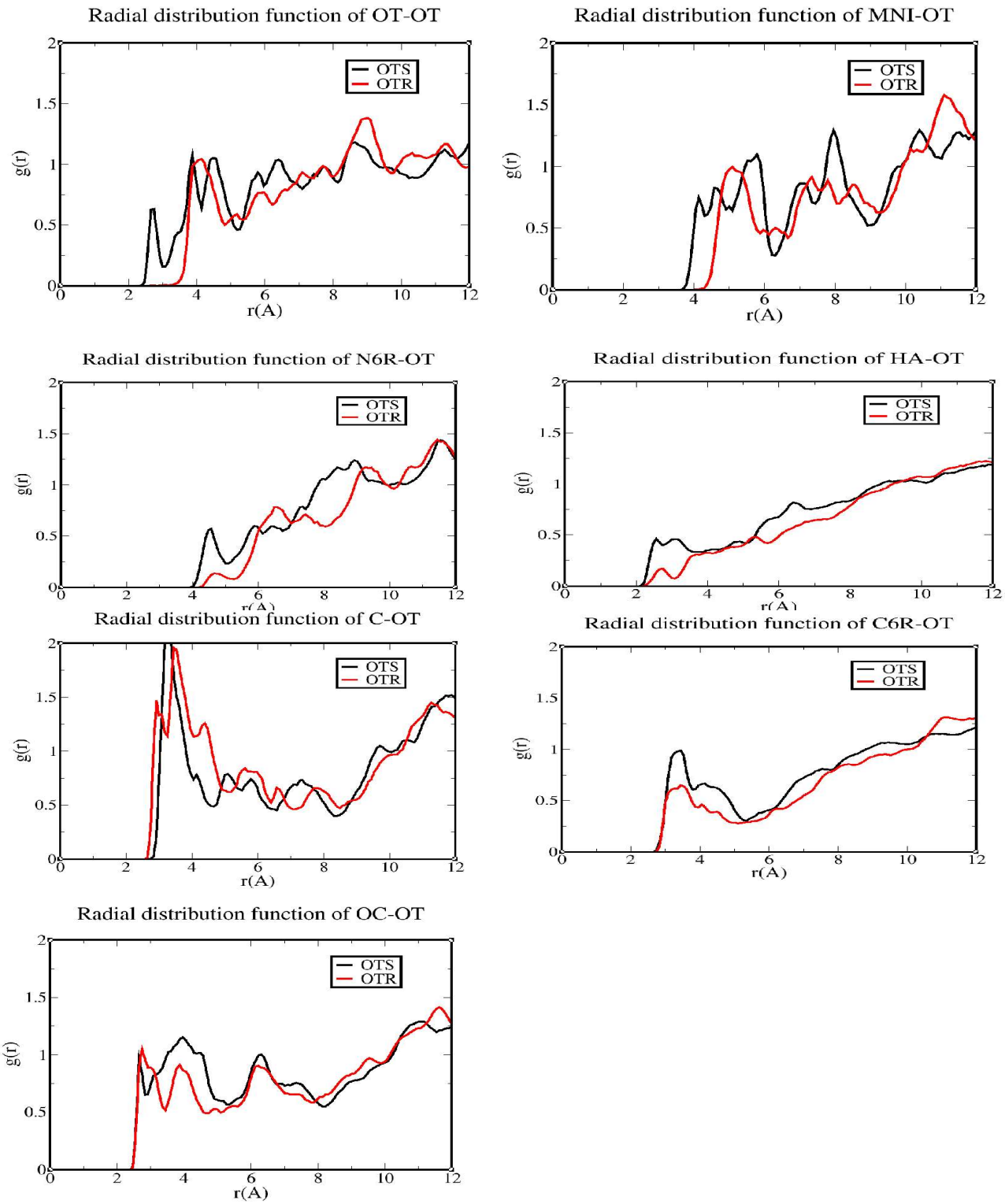

Figure 5-3 Radial distribution functions averaged over 500 ps of simulation in the NST ensemble for systems with enantiopure sovents, containing 20 solvent molecules at 150 K and 0.1 kbar.

In the title of each RDF, the first atom label represents atoms constituting the framework while the second atom label (OT) represents the oxygen atoms of the solvent molecules. OTS represents the oxygen atoms of the S alcohol solvent while OTR represents the oxygen atoms

In figure 5-3, N6R-OT, HA-OT, C-OT, OC-OT, and C6R-OT RDFs represent distances between the oxygen atoms of the alcohol solvent molecules and atoms belonging to the pyridine and BTC ligands of the MOF. It is clear from these RDFs that the S solvent experiences much closer interactions with the framework than does the R solvent. The effect is probably most significant with the framework alcohol, since $g_{OT\text{-}OT}$ reveals an H-bonding peak with the S solvent that is completely absent with the R solvent. Closer interactions with the S solvent are also observed in Ni-OT, although in this case the closest approach is at about 4 Å, and so this is likely to be a secondary effect of the differences already noted for OT-OT. The RDFs reveal strong evidence of other discriminations too. Although first peak positions are similar for R and S solvent in all the other RDFs shown, the height of this peak is much greater for the S solvent in N-OT, HA-OT and C6R-OT. This clearly shows that there is a "preference" by the framework towards the interaction with S solvent molecules over the R solvent molecules. This "preference" is demonstrated by the fact that S solvent molecules get closer to the alcohol framework molecules than the R solvent molecules. The preference is strongest with the framework alcohol, to the extent that they form hydrogen bonds with the S solvent but not with the R. It is not confined to the framework alcohol, however, as discrimination is also evident with the pyridine and Ni.

This study therefore shows that this helical MOF displays substantial enantioselective properties for at least one guest solvent, demonstrating an increased affinity for the guest molecules of the same handedness as that incorporated into the framework (in this case the (S,S)). This affinity is expressed by the formation of hydrogen bonds between the alcohol framework molecules and the solvent molecules of the same enantiomeric form as well as other close contacts between framework and solvent.

The conclusions reached above were found to be independent of the initial solvent configuration. RDFs from the separate simulations are presented in figures 5-4 and 5-5, and, although some variations are evident, the difference in first peak heights and positions is seen in every case.

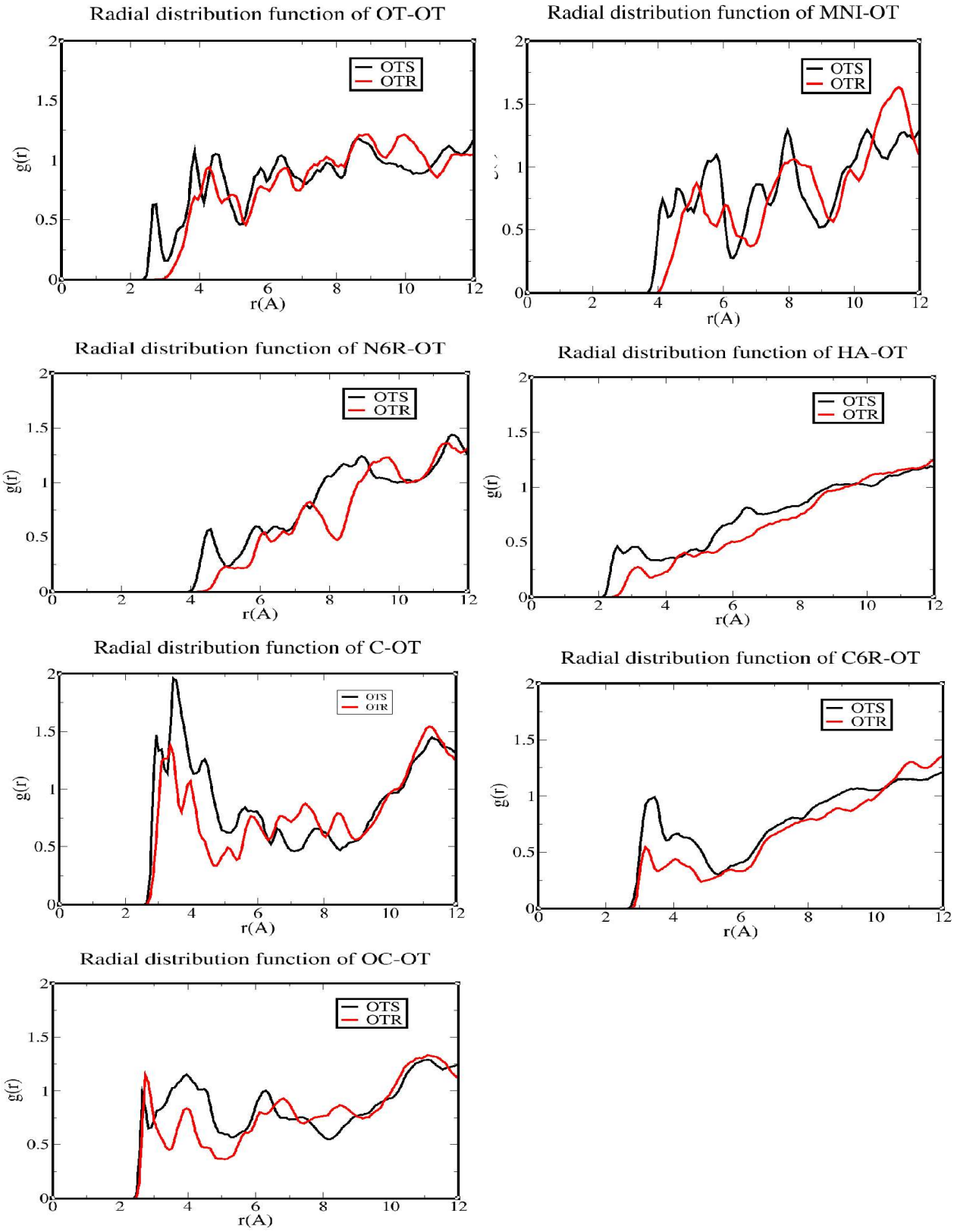

Figure 5-4 Radial distribution functions averaged over 500 ps of simulation in the NST ensemble for systems with enantiopure sovents, containing 20 solvent molecules at 150 K and 0.1 kbar using different starting configurations of solvent molecules.

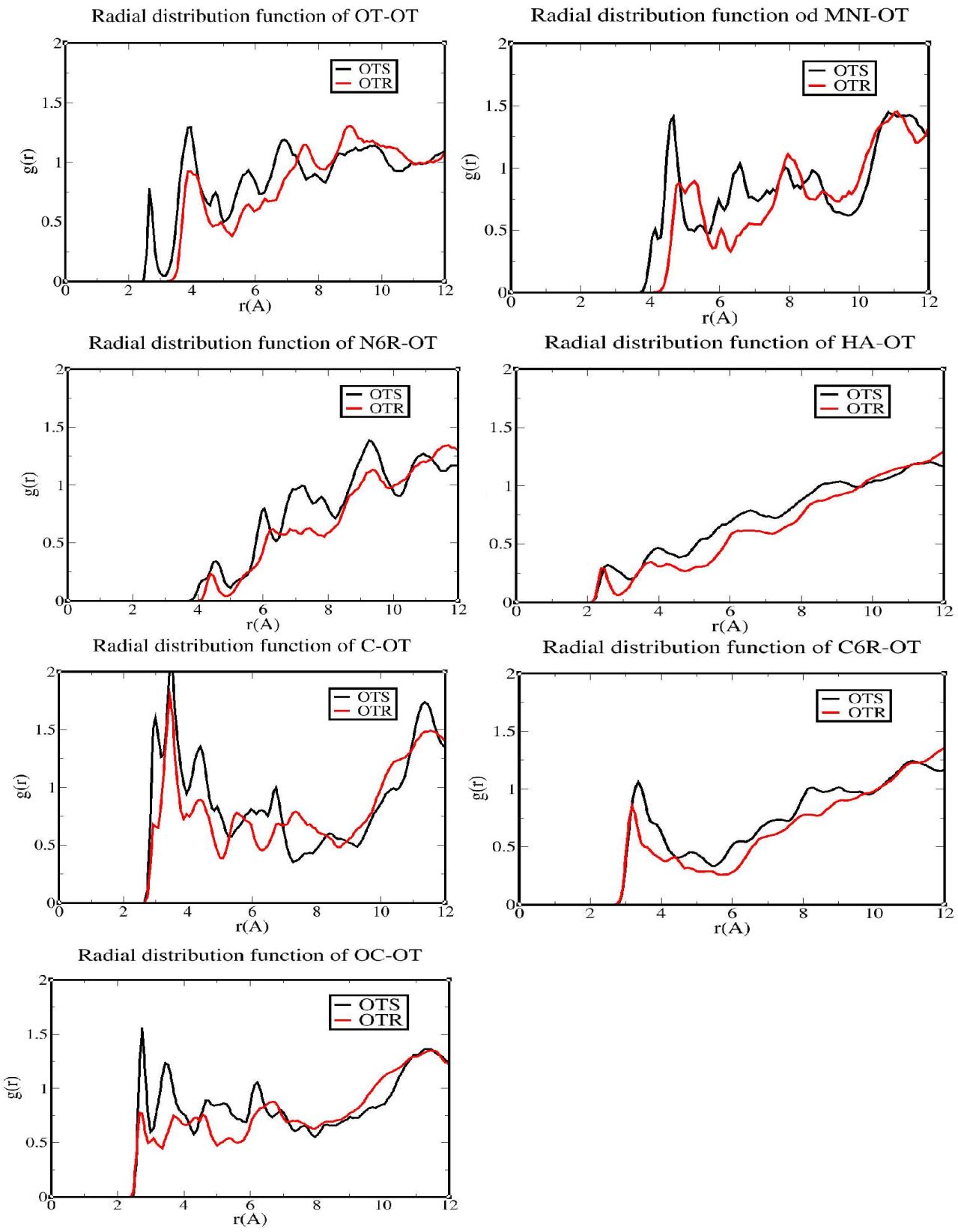

Figure 5-5 Radial distribution functions averaged over 500 ps of simulation in the NST ensemble for systems with enantiopure sovents, containing 20 solvent molecules at 150 K and 0.1 kbar using a third set of starting configurations of solvent molecules.

Figure 5-4 and figure 5-5 show that the position of the first peak of the OC-OT, C6R-OT, HA-OT, N6R-OT and C-OT RDFs are roughly identical whether it is the S solvent molecules that are present in the system or the R ones. This shows that the closest distances between the solvent oxygen atoms and the BTC and pyridine atoms of the framework are similar whether it is the S or the R solvent that is considered. This demonstrates that the framework does not exert any enantiomeric discrimination at the BTC and pyridine sites of the framework. However, similarly to what has been observed in figure 5-3, it is clear from figure 5-4 and figure 5-5 that for the Ni-OT and OT-OT RDFs there is a significant difference between the positions of the first peak of the RDFs depending on whether the oxygen atom belongs to the R or the S version of the solvent molecules. Indeed, it is clear from figures 5-4 and 5-5 that, for both starting configurations of the solvent molecules inside the framework, the oxygen atoms of the S solvent molecules get much closer to the oxygen atoms of the alcohol framework molecules that those of the R solvent molecules. The closest distance (position of first peak) between the oxygen atoms of the S solvent molecules and the oxygen atoms of the alcohol framework is 2.7 Å while, when it is the R version of the solvent molecules which is added to the system, this distance becomes 4 Å. The fact that for all three different starting configurations of solvent molecules (the ones described in figure 5-3, 5-4 and 5-5), the oxygen atoms of the S solvent molecules get as close as 2.7 Å to the oxygen atoms of the alcohol framework molecules indicates that there is hydrogen bond formation between the alcohol framework molecules and the S solvent molecules. The Ni-OT RDFs also show that for all three starting configurations of solvent molecules, the oxygen atoms of the solvent molecules of the S enantiomeric form get closer to nickel atoms than those of the R enantiomeric form.

This second RDF study verifies the conclusion that this helical metal-organic framework displays enantioselective properties with a “preference” for the guest molecules of the same enantiomeric form as the enantiomeric form of the alcohol framework molecules. This selectivity is expressed through the formation of hydrogen bonds between these solvent molecules and the alcohol framework molecules.

5.3.2 Racemic solvent

Since a chiral discrimination was observed in the last section, the next question is whether this is strong enough to effect a chiral separation. To investigate this possibility, the MOF containing simultaneously both enantiomeric forms of solvent molecules has been simulated. Simulations were performed in the *NST* ensemble at 150 K and 0.1 kbar, and using the same relaxation protocol described in chapter 5.2.

Figure 5-6 presents RDFs obtained from these simulations. The RDFs were averaged over 500 ps.

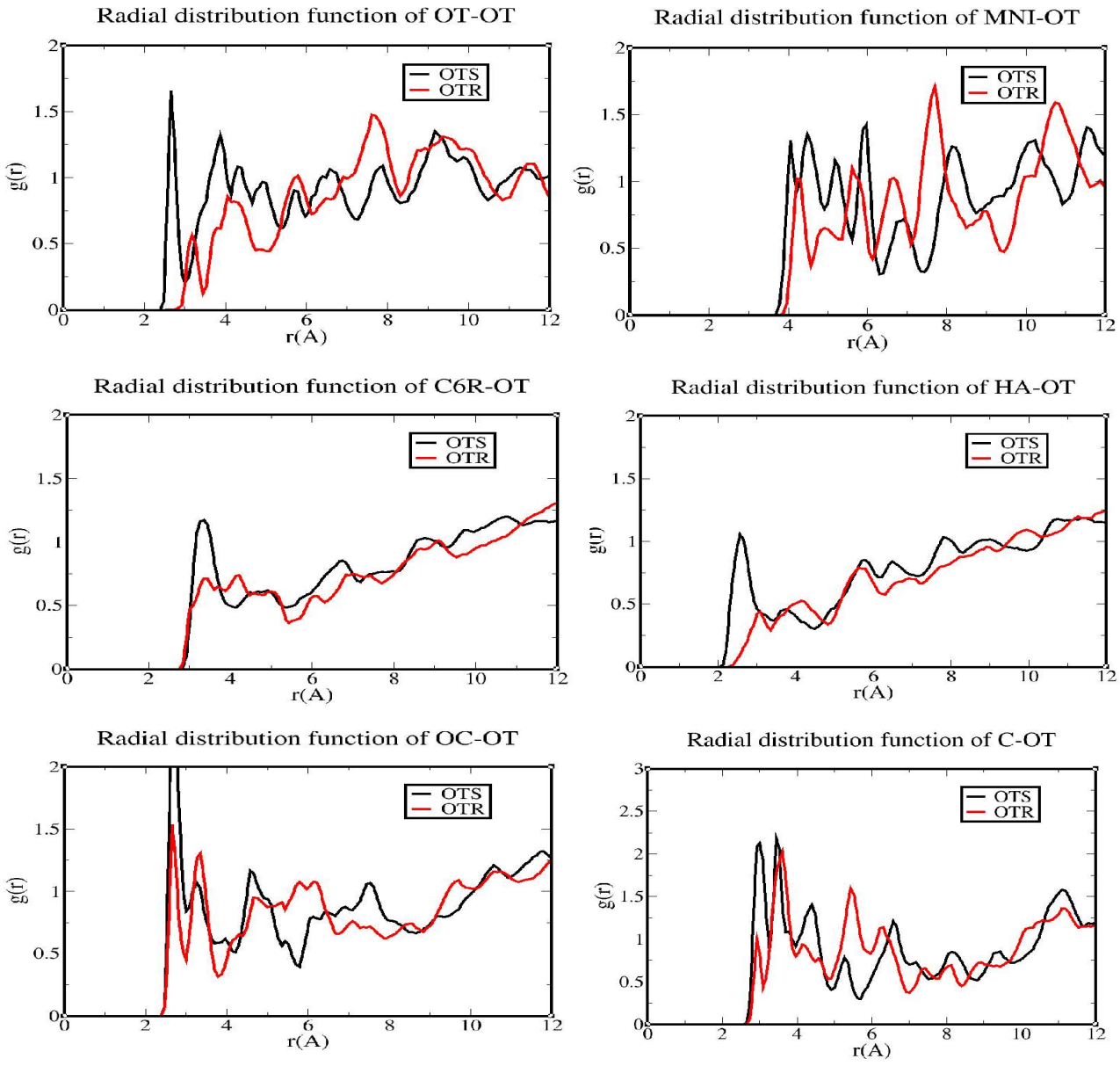

Figure 5-6 Radial distribution functions averaged over 500 ps of simulation in the NST ensemble for a system containing a racemic mixture of 20 solvent molecules at 150 K and 0.1 kbar.

RDFs, which have been calculated separately for each solvent enantiomer, are given in Figure 5-6. The curves show that, for the OC-OT, C-OT and C6R-OT RDFs there is no significant differences between the positions of the first peak of the OTS and the first peak of the OTR curves. This shows that the solvent oxygen atoms of both enantiomeric versions get equally close to the pyridine and BTC molecules of the framework. Therefore, it is deductible from these RDFs that at the positions of BTC and pyridines molecules, the framework does not demonstrate any “preference” towards a

specific enantiomeric version of the solvent molecules. In the case of Ni-OT and OT-OT RDFs, however, it is clear from figure 5-6 that the position of the first peak of the RDF is significantly different depending on whether the solvent is of the R or the S enantiomeric form. Indeed, it is clear from the OT-OT RDFs that the oxygen atoms of the S solvent molecules get much closer to the oxygen atoms of the alcohol ligands of the framework than the oxygen atoms of the R solvent molecules. Indeed, it is observable from the OT-OT RDFs that the first peak of the OT-OTS RDF representing the closest distance between the oxygen atoms of the S solvent molecules and the oxygen atoms of the alcohol framework molecules is centered at 2.7 Å while the first peak of the OT-OTR RDF which represents the closest distance between the oxygen atoms of the R solvent molecules and the oxygen atoms of the alcohol framework molecules is centered at 3.4 Å. Therefore the oxygen atoms of the S solvent molecules get 0.7 Å closer to the oxygen atoms of the alcohol framework molecules than the oxygen atoms of the R solvent molecules. This is a significant difference which shows that for the system containing a racemic mixture of solvents, the "preference" of the framework for one enantiomeric form of the solvent molecules which is exerted through its alcohol ligands is clear even though this difference is less pronounced than what is observed for systems containing enantiopure solvent molecules. Indeed, when the systems containing enantiopure solvent molecules are considered, the oxygen atoms of the S solvent molecules get 1.3 Å closer to the oxygen atoms of the framework than the oxygen atoms of the R solvent molecules. Similarly to what is observed for the OT-OT RDFs, the Ni-OT RDFs show that there is a significant difference between the position of the first peak of the RDF depending on the enantiomeric version of the solvent molecules. Indeed, the Ni-OTS RDF shows a first peak centered at 4 Å while the Ni-OTR RDF shows a first peak centered at 4.4 Å. This corroborates the fact that the S solvent molecules get significantly closer to the framework (since nickel atoms are the centers of mass of the SBU constituting the framework) than the R solvent molecules. It is likely that the fact that the S solvent molecules get closer to nickel atoms is due to the fact that they get closer to the alcohol ligands of the framework in the first place.

In the OT-OTS RDF, the peak at 2.7 Å representing the closest distance between the oxygen atoms of the S solvent molecules and the oxygen atoms of the alcohol ligands of the framework shows

that, similarly to what is observed for the systems containing enantiomerically pure solvent molecules, these alcohol framework molecules form hydrogen bonds with the solvent molecules of the S enantiomeric form.

We conclude that the chiral discrimination in the solvent structure observed with the pure enantiomers is also present with the racemic solvent. The differences are a bit more blurred in the mixed solvent, but are none-the-less still visible. The S form of the solvent gets closer to the framework than the R enantiomer, and forms hydrogen bonds with the framework diol that are simply not seen with the R enantiomer. We therefore expect to see preferential adsorption and/or different diffusion rates when a racemic mixture of the diol is passed through the MOF. This enantioselective discrimination is exerted most clearly at the diol ligand sites of the framework, but is also seen at other framework sites. It is therefore not clear whether this preference is affected by the extended helicity of the framework, or arises purely from the inclusion of chiral sites within it.

5.3.3 Solvent diffusion

To study the behavior of the solvent molecules in the different systems, the study of the evolution of the mean square displacement of the solvent oxygen atoms with time in these systems has been performed.

Figure 5-7 presents the evolution of the mean square displacement of solvent oxygen atoms with time for the systems containing enantiopure solvent molecules and the system containing a racemic mixture of solvent molecules. Simulations were performed for 500 ps at 150 K and 0.1 kbar in the *NST* ensemble.

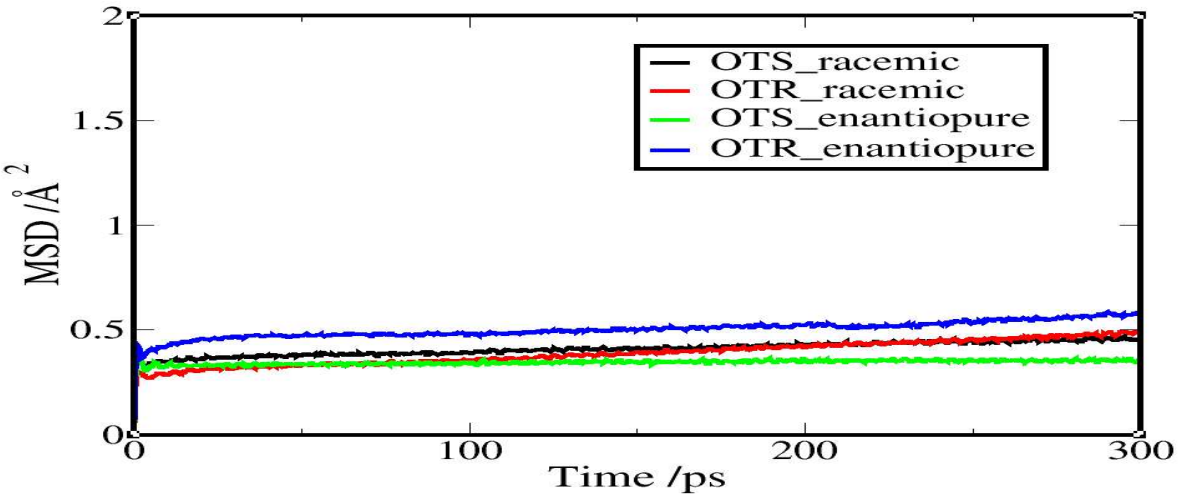

Figure 5-7 Evolution of the mean square displacement of the oxygen atoms of the solvent molecules with time for systems simulated for 500 ps at 150 K and 0.1 kbar in the NST ensemble.
OTS_enantiopure refers to the oxygen atoms of the solvent molecules when the system contains the enantiomerically pure solvent of the S form. OTR_enantiopure refers to the oxygen atoms of the solvent molecules when the system contains the enantiomerically pure solvent of the R form. OTS_racemic and OTR_racemic refer respectively to the oxygen atoms of the S solvent molecules and the oxygen atoms of the R solvent molecules when the system contains a racemic mixture of solvent. For all the three systems studied, the number of solvent molecules present is 20.

The mean square displacement of the solvent oxygen atoms when the system contains a racemic mixture of solvent molecules is limited with values averaging 0.5 Å^2 for both the S and the R solvent molecules. These low values of mean square displacements can be explained by the fact that both the S solvent molecules and the R solvent molecules get adsorbed to the framework. Indeed, it is noticeable from figure 5-6, as explained previously, that the oxygen atoms of the S solvent molecules form hydrogen bonds with the oxygen atoms of the alcohol framework molecules. Therefore, the alcohol framework molecules constitute an adsorption site for the S solvent molecules. This means that for specific periods of times these S solvent molecules form hydrogen bonds with the alcohol framework molecules that "lock" them at specific positions on the framework and impedes them from experiencing the extensive motion that would be expected from solvent molecules that are freely moving inside the framework pores. Furthermore, it is also

noticeable from figure 5-6 that the oxygen atoms of the alcohol framework are not the only adsorption sites for the S solvent molecules. Indeed, it is noticeable from these figures that in the case of OC-OT RDFs the position of the first peak is centered at 2.7 Å. As was shown and extensively described in chapter 3, this 2.7 Å distance between the oxygen atoms of the S solvent molecules and the oxygen atoms of the BTC molecules are characteristic of a hydrogen bond formation between these two molecules. The fact that the peak representing this OC-OT RDF centered at 2.7 Å is sharp and well defined shows that this hydrogen bond interaction is relatively strong. Therefore, it is deducible from the OC-OT RDFs that the O atoms of the BTC molecule represent a second set of adsorption sites for the S solvent molecules. Therefore, another explanation for the limited mean square displacement of the oxygen atoms of the S solvent molecules is that, in the same way the position of these oxygen atoms get "locked" by forming hydrogen bonds with the oxygen atoms of the alcohol framework, their positions get also "locked" by forming hydrogen bonds with the BTC oxygen atoms. The fact that the value of the mean square displacement of the oxygen atoms of the S solvent molecules in the racemic mixture is relatively low can therefore be explained by the fact that most of the 10 S solvent molecules present in the system get adsorbed to either the oxygen atoms of the BTC molecules or the oxygen atoms of the alcohol framework molecules.

The fact that the oxygen atoms of the R solvent molecules in the system containing a racemic mixture of solvent display limited values of the root mean square displacement can also be explained by the fact that, as shown by figure 5-6, the oxygen atoms of the R solvent molecules in this system form hydrogen bonds with the oxygen atoms of BTC molecules. Indeed, it is observable from figure 5-6 that the OC-OTR RDF shows a first peak centered at 2.7 Å which is characteristic of a hydrogen bond formation between a hydroxyl group and an oxygen atom. The limited values of the mean square displacement of the oxygen atoms of the R solvent molecules in the system containing a racemic mixture of solvent can therefore be explained by the fact that most of the 10 R solvent molecules present in the system get adsorbed to the oxygen atoms of BTC molecules and that this impedes these solvent molecules to experience extensive free motion inside the pores of the MOF. It is also observable from figure 5-7, that as it was the case for the system containing a

racemic mixture of solvent, the solvent molecules in the system containing enantiopure solvent display limited motion of the solvent molecules with values of the mean square displacement of the oxygen atoms of these solvent molecules not exceeding 0.6 $Å^2$. This limited movement of solvent molecules is observed for both the system containing S solvent molecules and the system containing R solvent molecules. This is explained by the fact that in both systems, the solvent molecules adsorb to the MOF. In the case of the system containing S solvent molecules, their adsorption sites are the oxygen atoms of BTC and alcohol framework molecules while for the system containing the R solvent molecules, the adsorption sites are the oxygen atoms of the BTC molecules only. These limited motions of solvent molecules can also be explained by the fact that for the different systems studied only 20 solvent molecules were incorporated in the unit cells and as was described in chapter 3, this solvent content is the minimum solvent content necessary to effectively stabilize the framework. Therefore, it was predictable that most of these solvent molecules would adsorb to the framework to stabilize it. However, to get limited motions of solvent molecules, previous simulations (to the ones that led to the values of mean square displacements described in figure 5-7) had to be performed to give time to solvent molecules to stabilize (by getting to the adsorption sites). Indeed, the analyzes of these previous simulations (which were also run for 500 ps) led to high values of mean square displacement therefore displaying extensive motions of solvent molecules.

The fact that as shown in figure 5-7, in the systems containing enantiopure solvent molecules, the oxygen atoms of the S solvent molecules experience less motion than the oxygen atoms of the R solvent molecules can be explained by the fact that, as described previously, the S solvent molecules adsorb to more adsorption sites than the R solvent molecules and that they seem to adsorb to the framework more strongly than the R solvent molecules. Indeed, it is observable from figures 5-3 to 5-5 that the first peak of the OC-OTS and OT-OTS RDFs is sharper that the first peak of the OC-OTR RDF suggesting that the OC-OTS and OT-OTS interactions are stronger than the OC-OTR one.

5.4 Conclusion

This study shows that for both the MOF containing enantiopure solvent molecules and the MOF containing a racemic mixture of solvent molecules, there is a tendency of the framework to "prefer" solvent molecules of the same enantiomeric form to that of the alcohol framework molecules. This shows that these helical metal-organic frameworks display enantioselective properties that are expressed through the alcohol ligands of the MOF. Indeed, these alcohol ligands form hydrogen bonds with the solvent molecules of the same enantiomeric version to theirs. This is an important result, since it suggests that these helical MOFs do have the potential to be used for their enantioselective properties. Materials displaying such enantioselective properties are of particular interest, for example, in the medical sector to select the specific enantiomeric form of a molecule that will be active in the biological systems. However, this is a first hand investigative study and more work will need to be performed to confirm the enantioselective properties of these MOFs.

6 Conclusion

This study represents the first simulation study of a flexible chiral Metal-Organic Framework (MOF). As described in chapter1, only two simulation studies have been published on flexible metal-organic frameworks thus far, and this within the last twelve months. The MOFs considered in those studies consisted of isoreticular metal-organic frameworks (IRMOFs) based on the topology of MOF-5. These IRMOFs are not chiral and their topology consists of a primitive cubic net. This thesis, however, presents a detailed molecular dynamics study of a series of chiral metal-organic frameworks of much more complex topology. These frameworks have a topology consisting of the interpenetration of two (10,3)-a nets resulting in a helical structure. As described in chapter 1, these chiral metal-organic frameworks are of particular interest for their potential enantiselective properties and thus could be used, for example, in the medical sector for chiral separation of potential drugs.

Since no suitable force fields had been reported for MOFs, we began in chapter 3 by reporting the development of a force field for modeling non-rigid MOFs. We began by benchmarking an existing organic force field, CHARMM22, against the framework with 4,5-octanediol as its alcohol ligand. CHARMM22 was shown to produce a stable MOF, but the extent of stability depended on conditions. Without solvent the framework structure changed between 150 K and 200 K. In contrast, with solvent present the framework was stable up to a temperature of 500 K, at least on the simulation timescale. However, it was demonstrated in chapter 3 that a minimum number of solvent molecules was required to effectively stabilize the framework. This number was found to be twenty solvent molecules per unit cell. Indeed, simulations with a number of solvent molecules per unit cell lower than twenty led to simulations that displayed a significant shrinkage of the crystal suggesting loss of the original framework at temperatures as low as 250 K. The associated radial distribution functions (RDFs) of the framework showed that one of the more important interactions that stabilized the solvated framework were the formation of hydrogen bonds between the hydroxyl

groups of the solvent molecules and the “free” (not bound to nickel) oxygen atoms of BTC molecules.

However, even though this CHARMM22 force field led to a stable framework, there were still some important inadequacies with the simulated structure. In particular, the RDFs showed that the Ni-O and Ni-N bonds had an amplitude of vibration that was far too large (~ 1 Å), while the simulated Ni-O and Ni-N bond distances were too small (by up to 0.43 Å). These simulations also showed that the CHARMM22 force field did not reproduce the cell parameters of the original crystal structure adequately. Indeed, a difference in cell length of around 4 % was observed between the simulated and the original structure. Therefore an improved force field was required and a refinement process undertaken.

A series of independent refinements were attempted, targeting different aspects of the structure. The first was to fit bond lengths by adjusting the relevant σ and ε parameters of the Lennard-Jones potentials, particularly those associated with Ni, to reproduce the structure of the secondary building unit (SBU). The aim of getting bond distances that reproduced the bond distances observed in the original crystal structure was successfully achieved. However, the study of the evolution of the cell volume with time, the evolution of the mean square displacements with time and the study of the orientational distribution of molecules in the system showed that the framework underwent a phase change during the course of the simulations and therefore that this force field was not an appropriate force field to use to model this framework even though it reproduced accurately the interatomic distances within each secondary building units. Indeed, the phase change of the framework in this case is explained by the fact that the refined force field obtained did not reproduce accurately long range interactions within the framework (interactions between the different secondary building units).

After this first refinement attempt which led to a phase change of the framework after few picoseconds of simulation at 150 K and 0.1 kbar in the *NPT* ensemble for a system containing 20 solvent molecules, a second more careful refinement of the nickel-ligand and ligand-ligand Lennard-Jones parameters of the CHARMM22 force field was performed (this was a different

refinement process from the first one). The resulting force field led to simulated bond lengths and cell parameters that better reproduced the bond lengths and cell parameters of the original crystal structure than the CHARMM22 force field. Indeed, this refined force field led to a simulated cell parameter that had a difference of only 2.63 % with the original cell parameter while the CHARMM22 force field led to a simulated cell parameter in the *NPT* ensemble that had a difference of around 3.85 % with the original cell parameter. However, this 2.63 % difference along with the the fact that this force field did not reproduce exactly the Ni-O bond lengths of the original crystal structure led us to consider that this refined force field was still not good enough to model this MOF and therefore could further be improved. Therefore, the next stage of the refinement process was to improve the description of the electrostatic interactions using ab initio electronic structure calculations on appropriate fragments of the crystal structure. Initially, attempts were made to perform UDFT and UMP2 calculations on the $NiBTC_2pyr_2alc$ secondary building unit (SBU) but they were proven to be far too computationally expensive. Indeed, it was not possible to get the SCF cycles to converge even when effective core potentials like SDD or LANL2DZ were used for the nickel atom and the 6-31G basis set was used for the other atoms of the SBU. Thus, calculations were performed on separate ligands instead. These were performed using the UMP2 and UDFT methods and a series of basis sets. Partial charges on each atom were determined using the ESP electronic structure calculation method. Therefore a limitation of the force fields obtained through these quantum mechanical calculations is that they do not take into consideration the polarization effects taking place in the SBU. However, force fields that reproduce accurately the experimental crystal structure were still obtained using the partial charges obtained from quantum mechanical calculations on isolated ligand molecules. The first of these,FF-1, consisted of the refined Lennard-Jones parameters obtained during the refinement process just described previously (the second refinement attempt of Lennard-Jones potentials), the partial charges on BTC molecules obtained from the CHARMM22 force field and partial charges on alcohol and pyridine molecules obtained from quantum mechanical calculations using the UMP2 method and the 6-311G basis set. This FF-1 force field led to a simulated cell parameter that differed from the original cell parameter by only 1.6 % when simulated at 150 K in the *NPT* ensemble. Good agreement between the

simulated and original cell parameters was also observed for simulations in the *NST* ensemble. Indeed, for simulations in the NST ensemble, a difference of around only 1.3 % was achieved between the simulated structure and the original one. The FF-1 force field also reproduced accurately the bond distances of the original crystal structure. Indeed, simulations in the *NST* ensemble led to a Ni-N bond that exactly reproduced the Ni-N bond of the original crystal structure (compared to a difference of 0.234 Å when the CHARMM22 force field is used), to a Ni-OC (OC = Oxygen atoms of BTC molecules) bond that differed by 0.17 Å with the Ni-OC bond of the original crystal structure (compared to 0.41 Å when the CHARMM22 force field is used) and a Ni-OT (OT = Oxygen atoms of alcohol molecules) bond that differed by 0.26 Å with the Ni-OT bond of the original structure (compared to 0.46 Å when the CHARMM22 force field is used). Therefore, this force field was proven to be a good force field to model the MOF with 4,5-octanediol as its alcohol ligand. To get an even better reproduction of crystallographic data, in a third refinement stage, this force field was modified by increasing the strength of the hydrogen bond between the oxygen atoms of BTC molecules and the hydroxyl hydrogen atoms of alcohol molecules. The resulting force field was labeled FF-3 and it led to a simulated cell volume that better reproduced the original cell volume than the FF-1 force field. In fact, out of all the force fields developed in chapter 3, the FF-3 force field is the force field that best reproduced the original cell volume. This suggests that the hydrogen bond between the oxygen atoms of the BTC molecules and the hydroxyl groups of the framework alcohol molecules plays an important role in stabilizing the framework. Another force field that was extensively described in chapter 3 is the FF-2 force field. This force field consists of Lennard-Jones parameters and partial charges on BTC molecules obtained from the CHARMM22 force field and the partial charges on alcohol and pyridine molecules obtained from quantum mechanical calculations using the UMP2 method and the 6-311G basis set. Therefore, the only difference between the FF-1 and FF-2 force fields is the Lennard-Jones parameters, the partial charges being the same in both force fields. This FF-2 force field also led to simulated cell parameters that accurately reproduced the cell parameters of the original crystal structure showing that this FF-2 force field is an appropriate force field to use to model the MOF with 4,5-octanediol as its alcohol ligand.

The transferability of these force fields was tested in chapter 4 by using them to model two different, but related MOFs for which experimental crystal structures have been reported. These were the MOF with the formula $Ni_3(BTC)_2(pyridine)_6(2,3\text{-butanediol})_3$ (called MOF4) and the MOF with the formula $Ni_3(BTC)_2(pyridine)_6(1,2,6\text{-hexanetriol})_3$ (called MOF 6). FF-2 was found to be the best of the force fields for MOF4, and did give an adequate description of its known structural properties.

The simulation of the unsolvated MOF with 2,3-butanediol as its alcohol ligand using the FF-2 force field led to cell parameters obtained after simulations that matched well the cell parameters of the original crystal structure. The difference in cell parameters with the original structure being around 1.8 % for both simulations in the *NPT* and *NST* ensembles and at 10 K and 100 K. A phase change at about 150 K was observed with this force-field for the unsolvated MOF. Greater thermal stability was observed in the presence of solvent, however, with the phase change occurring at about 400 K when 40 solvent molecules occupied the pore space in the simulation cell. This study also suggested that there was a hydrogen bond competition taking place between the alcohol ligand and alcohol solvent molecules to form a hydrogen bond with the "free" (not bound to nickel) oxygen atoms of the BTC molecules. Indeed, the study of the RDFs showed that both the oxygen atoms of the framework alcohols and the oxygen atoms of the solvent alcohols formed hydrogen bonds with the BTC oxygens. This hydrogen bond competition was found to lead to some limited rotation of the aromatic BTC rings of the framework since the relative orientation of these BTC rings was better defined in the unsolvated system (showing little motion) than in the solvated one. We therefore concluded that the inclusion of solvent molecules led to the limited motion of BTC rings due to hydrogen bond competition between the framework alcohol molecules and solvent alcohol molecules to form hydrogen bonds with BTC molecules.

It has also been shown in this work that it was a lot more difficult to find an appropriate force field for the MOF with 2,3-butanediol as alcohol ligand than it was for the MOF with 4,5-octanediol as alcohol ligand. One possible explanation for this and for the fact that the 4,5-octanediol based MOF seems to be thermally more stable than the 2,3-butanediol MOF is that the side chains of the 4,5-

octanediol molecules form stabilizing interactions with the rest of the framework, most likely the BTC molecules since they are the molecules to which these side chains get the closest.

The study of the MOF with 1,2,6-hexanetriol as alcohol ligand showed that to reproduce the experimental cell parameter accurately, our force field had to be supplemented by constraining the distance between nickel atoms and the oxygen atoms of the alcohol molecules that are initially bound to them. Without this constraint one of the Ni-OT bonds of each SBU broke therefore destabilizing the structure. However, when this Ni-OT bond was constrained, reasonable agreement was obtained between the simulated cell parameter in the *NPT* ensemble and the cell parameter of the original crystal structure; a difference of 3.4 % was observed between the simulated and the original cell parameter when the simulation was performed at 100 K and a difference of 4 % when it was performed at 150 K. However, it has not been possible to reproduce the original cell parameter for simulation in the *NST* ensemble using any of the force fields developed in chapter 3. Simulations in the *NST* ensemble led to a significant decrease in simulated cell volume at temperatures as low as 10 K. Also, it has not been possible to reproduce experimental data when simulating the solvated 1,2,6-hexanetriol based MOF. We think that in the case of 4,5-octanediol and 2,6-butanediol based MOFs, the presence of a carbon chain at both sides of the diol group impedes any "attack" by solvent molecules of the nickel centers. Indeed, it is possible that these carbon chains act as a shield protecting the metal centers. This would partly explain, for example, why it has been easier to find appropriate force fields for the 4,5-octanediol based MOF than the 2,3-butanediol based one. Indeed, the 4,5-octanediol ligand has side carbon chains consisting of 3 carbon atoms while the 2,3-butanediol ligand has side carbon chains consisting of only one carbon atom. Therefore in the 4,5-octanediol based MOF, it is likely that these longer side carbon chains protect the nickel centers and therefore the overall structure. Furthermore, it is also possible that these side carbon chains form stabilizing interaction with the rest of the framework (most likely BTC molecules). This would also explain why the longer the side carbon chain, the more stable the MOF. We think that the presence of the terminal oxygen of the triol ligand along with the fact that the stabilizing carbon chain is absent at on side of the diol group (leaving the nickel atoms

unprotected) are the reasons why it is so difficult to model the 1,2,6-hexanetriol based MOF. Therefore, more work will need to be performed to develop a force field that would accurately reproduce experimental data for the 1,2,6-hexanetriol based MOF for simulations performed in the *NST* ensemble and for both unsolvated and solvated systems. For this purpose it would be interesting, for example, to include polarization effects within the SBUs to get partial charges of the framework alcohol molecules that are different from the partial charges of the alcohol solvent molecules.

Finally, it has been shown in chapter 5 that chiral MOFs can display enantioselective properties. Simulations of the MOF with the formula $Ni_3(BTC)_2(pyridine)_6(4,5\text{-octanediol})_3$, containing enantiomerically pure solvent molecules or a racemic mixture of solvent showed that the solvent molecules of the same enantiomeric form as that incorporated into the framework interacted much more strongly with the framework, and even formed enantiomer-specific hydrogen bonds with the framework. These interactions were strongest with the framework alcohol, but structural differences were also observed in solvent-BTC, solvent-Ni and solvent-pyridine geometries. It was not possible to determine whether these were secondary effects of the solvent-alcohol interaction, or direct interactions, and so it was not possible to determine whether the chiral discrimination arose from the helical framework, or from the incorporation of a helical site within the framework.
In summary, this MOF does exert a chiral discrimination, most strongly through its alcohol ligands which form hydrogen bonds with the solvent molecules of the same enantiomeric form. The study of these chiral frameworks is of particular interest because of their potential applications in the biological and medical sectors where the synthesis or separation of enantiomerically pure substances is essential.

This work therefore represents a considerable contribution to the field of molecular simulation of porous materials in general and hybrid organic-inorganic materials in particular for which the amount of data available in the literature is limited. This work represents the first step in the development of force fields for helical metal-organic frameworks. It also represents the first

simulation study of the effect of temperature and solvation on these helical metal-organic frameworks. Finally this work showed that these helical metal-organic frameworks exhibit enantioselective properties and therefore could be of interest for the medical sector in particular.

Appendix

CHARMM22 force field for the MOF with the formula $Ni_3(BTC)_2(pyridine)_6(4,5\text{-octanediol})_3$.

- **Partial charges:**

Ni: +2*e*

BTC molecule (number of atoms = 18):

Atom type	***Partial charge /e***
C	0.550
C6R	-0.137
C6R	-0.266
HA	-0.007
OC	-0.570
OC	-0.570
C6R	-0.137
C	0.550
OC	-0.570
OC	-0.570
C6R	-0.266
C6R	-0.137
C	0.550
OC	-0.570

Atom type	*Partial charge /e*
OC	-0.570
C6R	-0.266
HA	-0.070
HA	-0.070

Pyridine molecule (number of atoms = 11):

Atom type	*Partial charge /e*
C6R	0.228
HA	0.108
C6R	-0.152
HA	0.108
C6R	-0.152
HA	0.108
C6R	-0.152
HA	0.108
C6R	0.228
HA	0.108
N6R	-0.540

Alcohol molecule (number of atoms = 14):

Atom type	*Partial charge /e*
CT	-0.040
HC	0.110
CH2E	0.060
CH2E	0.060
CH3E	0.060
OT	-0.650
HO	0.400
CT	-0.040
HC	0.110
CH2E	0.060
CH2E	0.060
CH3E	0.060
OT	-0.650
HO	0.400

- **Lennard-Jones parameters:**

Atom pair		*ε/ kcal.mol^{-1}*	*σ /Å*
MNI	MNI	0.50000E-01	1.7818
C6R	C6R	0.50000E-01	3.6349
C6R	HA	0.45830E-01	3.0023

HA	HA	0.42000E-01	2.3698
MNI	C6R	0.50000E-01	2.7083
MNI	HA	0.45826E-01	2.0758
C6R	N6R	0.67080E-01	3.4478
HA	N6R	0.61480E-01	2.8152
N6R	N6R	0.90000E-01	3.2607
MNI	N6R	0.67082E-01	2.5212
CT	CT	0.90300E-01	3.2072
CT	HC	0.67060E-01	2.1382
CT	CH2E	0.10155	3.5948
CT	CH3E	0.12788	3.5324
CT	OT	0.11719	2.9845
CT	HO	0.15000	2.6727
HC	HC	0.49800E-01	1.0691
HC	CH2E	0.75410E-01	2.5257
HC	CH3E	0.94970E-01	2.4633
HC	OT	0.87030E-01	1.9154
HC	HO	0.49800E-01	1.2116
CH2E	CH2E	0.11420	3.9823
CH2E	CH3E	0.14381	3.9199
CH2E	OT	0.13179	3.3720
CH2E	HO	0.75410E-01	2.6682
CH3E	CH3E	0.18110	3.8576
CH3E	OT	0.16597	3.3097
CH3E	HO	0.94970E-01	2.6059
OT	OT	0.15210	2.7618
OT	HO	0.87030E-01	2.0580
HO	HO	0.49800E-01	1.3542
MNI	CT	0.67194E-01	2.4945
MNI	HC	0.49900E-01	1.4254
MNI	CH2E	0.75565E-01	2.8821
MNI	CH3E	0.95158E-01	2.8197
MNI	OT	0.87207E-01	2.2718
MNI	HO	0.49900E-01	1.5680
C6R	CT	0.67194E-01	3.4211
C6R	HC	0.49900E-01	2.3520
C6R	CH2E	0.75565E-01	3.8086
C6R	CH3E	0.95158E-01	3.7462
C6R	OT	0.87207E-01	3.1983
C6R	HO	0.49900E-01	2.4945
HA	CT	0.61584E-01	2.7885

HA	HC	0.45734E-01	1.7194
HA	CH2E	0.69256E-01	3.1761
HA	CH3E	0.87214E-01	3.1137
HA	OT	0.79926E-01	2.5658
HA	HO	0.45734E-01	1.8620
N6R	CT	0.90150E-01	3.2340
N6R	HC	0.66948E-01	2.1649
N6R	CH2E	0.10138	3.6215
N6R	CH3E	0.12767	3.5591
N6R	OT	0.11700	3.0112
N6R	HO	0.66948E-01	2.3074
C	C	0.14100	3.3320
C	C6R	0.83960E-01	3.4834
C	HA	0.76950E-01	2.8509
C	OC	0.14978	3.1449
C6R	OC	0.89190E-01	3.2963
HA	OC	0.81740E-01	2.6638
OC	OC	0.15910	2.9578
MNI	C	0.83964E-01	2.5569
MNI	OC	0.89191E-01	2.3698
N6R	C	0.11265	3.2963
N6R	OC	0.11966	3.1092
CT	C	0.11284	3.2696
CT	OC	0.11986	3.0825
HC	C	0.83796E-01	2.2005
HC	OC	0.89012E-01	2.0134
CH2E	C	0.12689	3.6571
CH2E	OC	0.13479	3.4700
CH3E	C	0.15980	3.5948
CH3E	OC	0.16974	3.4077
OT	C	0.14644	3.0469
OT	OC	0.15556	2.8598
HO	C	0.83796E-01	2.3431
HO	OC	0.89012E-01	2.1560